Low spatial resolution thermal monitoring of volcanoes from space

Thesis

UNRESTRICTED

LOW SPATIAL RESOLUTION THERMAL MONITORING OF VOLCANOES FROM SPACE

A thesis presented for the degree of Doctor of Philosophy

by

ANDREW JOHN LANG HARRIS

BA (Hons) Exeter, MSc Dundee

Date of submission: 27 June 1996

Date of award: 3 September 1996

Department of Earth Sciences,

The Open University.

1996

ProQuest LLC.
789 East Eisenhower Parkway
P.O. Box 1346
Ann Arbor, MI 48106 – 1346

"Since the startling announcement was made that tiny football-sized objects are to be launched into space, everyone has wanted to know: What are these objects? How will they work? What will they do? And how will they affect my life."

Satellite! Erik Bergaust & William Beller (1957)

Abstract

Low spatial resolution thermal data from the Advanced Very High Resolution Radiometer (AVHRR) have been available for any cloud-free sub-aerial volcano at least 4 times a day since 1979. Although extensively used to monitor ash plumes injected into the atmosphere by volcanic eruptions, this cheap, directly and regularly available data source has never been thoroughly examined to determine its utility for real-time monitoring of high temperature volcanic activity occurring at the surface. This thesis is therefore concerned with developing techniques to locate, measure and monitor high temperature volcanic phenomena in AVHRR data.

To locate high temperature phenomena, I develop an automated thresholding algorithm which roams an image flagging thermal anomalies. The major advantage of this technique over existing thresholding techniques developed for fires is that it requires no manual input. By running the algorithm on 90 images acquired during the 1991 to 1993 effusive eruption at Mount Etna, pixels containing active lava or high temperature open vents were located, with the program completing within 1 second. This permitted lava flow location to within ±1 km of known topographic features, roads and towns. The flexibility of the thresholding algorithm to detect other high temperature sources, over a variety of regions and seasons, was demonstrated by applying the algorithm to images containing wild-fires burning along the east coast of Australia during January 1994.

For quantitative analysis, I develop a new approach capable of estimating the size and temperature of at least three sub-pixel thermal components. This approach enables lava flow area and thermal flux to be constrained more accurately than is possible using established techniques which allow measurement of just two thermal components.

Using the area and thermal flux results, I refine an algorithm to estimate lava effusion rates. This in turn allows calculation of lava flow field cumulative and total volumes. Application to data for effusive activity at Etna during 1985 and between 1991 and 1993 gives mean effusion rates of <8 m^3 s^{-1} during both eruptions, building flow fields of 16-29 x 10^6 and 220-300 x 10^6 m^3 respectively. Both volume estimates are in good agreement with ground-based estimates of 19 x 10^6 and 235 x 10^6 m^3 respectively. In both cases, time series of area, thermal flux, effusion rate and cumulative volume data reveal phases of waxing and waning eruptive activity, in close agreement with those observed from the ground.

I also present simple approaches which use spectral radiance from the volcanic source to monitor volcanic activity through time and to distinguish between different types of volcanic phenomena. At Stromboli, troughs and peaks in a spectral radiance time-series respectively correlate with periods "normal" explosive activity and less frequent effusive events. A scatter plot of spectral radiances from the volcanic source acquired in two thermal wavebands, one in the mid-infrared and one in the thermal infrared, allows lava lakes, flows and open vents to be distinguished according to their position in the scatter.

I use a number of case studies, drawn from effusive activity at Etna, Krafla, Fogo, Cerro Negro and Erebus, as well as pyroclastic and degassing activity at Lascar, Vulcano, Etna and Stromboli, to show how AVHRR can be used to measure and monitor high temperature volcanic phenomena. If data analysis were carried out on reception, regular location and monitoring of on-going effusive eruptions, as well as persistent high temperature phenomena, would be possible.

Acknowledgements

Hundreds of people helped this thesis. Huge thanks to all co-authors and scientists who spent much time and effort contributing to papers contained herein. Their efforts are gratefully acknowledged at each chapter end (and in Table 1.2). Thanks also to Luke Flynn, Arlin Krueger and Ian Sprod for input to Chapter 8, and to Geoff Wadge and Steve Drury for a thorough examination. Here I thank an otherwise unmentioned, but essential crowd, whose help, support and encouragement kept me moving.

Dave's supervision was perfect. His enthusiasm, guidance and advice kept things happy. The speed and thoroughness with which he critically reviewed all work is much appreciated. Unfortunately his jokes finally forced me to submit early. Elric, Rhino, Linda, Phil, Ben, Jugs, Adam, Paul and Jane were fine friends, always available for chats, supportive, social or scientific, as well as being a hard-working and dedicated bunch. Elric was the driving force behind Warp Toilet™, Beatrice (until he drove her into a Vauxhall) and several fashion disasters; Rhino pioneered the way in bike crash survival; Linda provided the knee of much entertainment and chicken of many maggots; Phil did good stuff with fried onions, convincing me of my own cooking crisis; Paul would surely have taken us far beyond the bounds of science had beer not taken his memory. Although a survivor of several Craufurd encounters, gravity defeated Röllin at many party's, in spite of help from supporting structures including Jane. His beer cordial continues to defy all laws of science. Ant, Beto, Treez, Martin and Dick were valued image consultants. Many thanks to Ant who spent much time on my initial image; Beto who contributed head-banging cocktails; Martin's Hawaiian car-balancing tricks and spectrometer juggling were astonishing; Dick was crucial, never failing to solve any thesis ending problem, and helping fight the evil and random forces of T-format. Jez created VAST which slashed processing time from 14 hours to 10 seconds. Pete and Ed were ideal house-mates and

responsible for keeping me sane these last few months. Thanks also to Bill, Mike, Roberto, Emma, Franchi, Morsey, Angela, Fiona, Russ, Yvette, Mark D., Babbs, Gus, Malc, Ribena and Pies for helping.

Within the department I am grateful to Steve Blake, Steve Drury, Peter Francis, John Murray, Hazel Rymer and John Stix for helpful discussions and encouragement, and to Andy Lloyd, John Taylor, John Holbrook, Rita Quill and Janet Dryden for making life much easier. In the field Tanya, Chris and Alina were good people to get cooked with and Nick Rogers helped me overcome an irrational fear of chicken milk pudding. Laurie designed the portable bed-frame which allowed us to reach those parts of a lava flow that other thermocouples cannot reach. I am extremely grateful to John Murray for field time and introductions to Etna and Landrover-mechanics, proving, with Dave Renouf, that gear sticks and brakes are not essential. Excellent times were spent with Nicki and Adam on Stromboli and Vulcano, Nicki carried heavy things up steep slopes, keeping herself alive only with bizarre sun deflecting devices and lumps of raw pig fat; Adam showed me how to dismantle a volcano and carry it home in dodgey card-board boxes. Dave Pieri, Scott Rowland and Peter Mouginis-Mark were fine hosts at JPL and Honolulu.

Biggest thanks to Butts. She was my best mate, taught me loads and put up with far too much. She saved me from scurvy, encouraged Gus in his battle against starting, tolerated him in his moments of Mondeo hate, and made him see reason when he went off the road. She did much the same for me too. Mum and dad deserve special mention for backing me unquestioningly and loaning me more money to buy this here writing machine. The support and encouragement of the whole Harris-Munt-Hearn-Byde-Davis network has been crucial, and will always be appreciated and remembered.

Why do cows chase trains?

H, June 1996

Table of contents

List of figures

List of tables

Chapter 1. Space-borne volcano monitoring: capabilities and principles

1.1. Introduction

Plans to launch earth orbiting satellites carrying instruments designed to measure electromagnetic radiation emitted and reflected by the Earth's surface began during the 1940s (Bergaust & Beller, 1957). By 1960 the first weather satellite, TIROS-1, was providing coarse views of cloud patterns and the Earth's surface (Lillesand & Kiefer, 1987).

During these decades, devastating eruptions at two previously unknown and unmonitored volcanoes, Parícutin (Mexico) and Mount Lamington (Papua), clearly demonstrated the hazard posed by effusive and explosive eruptions. At Parícutin an eruptive vent, opening in a maize field in 1943, built a 410 m high cone, effused a 24.8 km^2 lava flow field and ejected up to 6 x 10^6 m^3 d^{-1} of pyroclastic material during a 9 year eruption (Rees, 1979). Impact on the immediate environment and economy was catastrophic, leaving 2 villages completely buried and 3 partially abandoned (combined population 5916). Residents were relocated in refugee settlements and suffered a number of

"sociocultural hazards" including psychological breakdown (Nolan, 1979). Adverse agricultural effects extended ~50 km, with all vegetation within ~6 km totally destroyed and at least 5000 cattle and horses killed (Rees, 1979). At Mount Lamington in 1951 a Pelean eruption sent ash clouds up to 15 km and fed nuée ardentes which, moving at speeds >350 km h^{-1}, devastated more than 230 km^2 of land killing 2942 people (Taylor, 1958). Prior to this eruption the area had no volcanic history, Mount Lamington itself was not even considered a volcano (Fisher, 1958).

An average of 60 eruptions occur every year from a total of 1511 potentially active volcanoes. Between 1976 and 1994, 414 events produced fatalities and 101 necessitated evacuations (Simkin & Siebert, 1994). In spite of this, many volcanoes remain inadequately monitored due to deficiencies in economic resources, scientific funding or political desire (Tilling, 1989). Consequently many devastating eruptions still occur at poorly monitored volcanoes. Even at Mount St. Helens, although intensive monitoring occurred after initial phreatic events in March 1980, lack of prior funding thwarted attempts to set up base-line monitoring, and such monitoring as did exist was inadequate for making short-term forecasts or eruption predictions (Tilling, 1989; 1995). However, satellite remote sensing potentially offers a regular, safe and cheap means of monitoring all of the worlds sub-aerial volcanoes.

Reviews by Francis (1979), Mouginis-Mark *et al.* (1989), Rothery (1989), Mouginis-Mark & Francis (1992) and Rothery & Pieri (1993) have outlined the benefits that satellite remote sensing offer volcano monitoring. These being:

(1) Global coverage. By repeatedly orbiting while the Earth rotates beneath them, polar orbiting satellites build up coverage of the entire globe (Barrett & Curtis, 1992). In the case of Landsat's Thematic Mapper (TM) and NOAA's Advanced Very High Resolution Radiometer (AVHRR), global coverage is achieved in 18 days and 6 hours respectively. This permits observation of all the world's sub-aerial volcanoes if they are cloud-free at the time of over-pass. Francis & De Silva (1989) demonstrated this capability by using 29 images to cover the entire central Andean volcanic province. This regional

study resulted in the identification of >60 potentially active volcanoes, in comparison with the previously catalogued 16.

(2) Repeat capability. Repeated passes allow regular monitoring. In the case of geostationary satellites, all volcanoes within the satellite's field of view can be monitored once every 30 minutes. This permits baseline and time-series monitoring, as achieved by Glaze *et al.* (1989) and Oppenheimer *et al.* (1993) at Lascar volcano, using 15 TM images acquired between 1984 and 1992. Airborne and ground observations, being dependent on availability of aircraft, safety, funds or manpower are often irregular and infrequent. Repeated satellite observations may thus allow identification of otherwise unobserved events, as shown by Rothery *et al.* (1988) who used a January 1985 TM image to suggest a lava lake at Mount Erebus re-established 10 months earlier than could be proved from ground observations.

(3) Synoptic perspective. The satellite view allows the whole of a feature to be analysed using a single image, including areas that are remote or dangerous. The size of a volcanic ash plume (>1000 km^2) or temperature of an active lava flow (>900 °C) make such targets difficult to monitor from any other perspective: manpower requirements and hazard posed preclude ground-based whole feature analysis. Many published images of pyroclastic and effusive eruptions spectacularly illustrate the whole-feature space-borne perspective (e.g. Rothery & Francis, 1990; Rothery *et al.*, 1992; Stephens, 1993; Stephens, 1995; Denniss *et al.*, in press).

(4) Spectral capabilities. Satellite sensors measure emitted or reflected radiation at selected wavebands across the electromagnetic spectrum. Spectral measurements allow: (a) Analysis of volcanic structure, mapping, identification of units and reconstruction of events (e.g. Baker, 1981; Munro & Mouginis-Mark, 1990; Wadge *et al.*, 1995). (b) Ash plume tracking and detection of hot-spots (e.g. Robock & Matson, 1983; Holasek & Rose, 1991; Harris *et al.*, 1995c). (c) Measurements of ash plume or lava flow temperature and constraint of various parameters, including altitude and velocity of plume tops and radiative flux and core temperature of lava flows (e.g. Pieri *et al.*, 1990; Oppenheimer, 1991a;

Holasek & Self, 1995). (d) Quantification of eruptive sulfur dioxide (e.g. Krueger *et al.*, 1990; Bluth *et al.*, 1994; Schnetzler *et al.*, 1994). (e) Analysis of environmental impacts of ash and aerosol deposition (e.g. Jeyaseelan & Thiruvengadachari, 1993; Tucker & Matson, 1985). (f) Measurements of ground deformation (e.g. Massonnet *et al.*, 1995).

(5) Continuity of data acquisition. Data are provided in a standard, calibrated format providing a globally consistent data set. This allows application of standard analysis techniques producing comparable results for all volcanoes or of a single volcano over a long time-span. AVHRR data have been available for any volcano since 1979.

(6) Safe, re-usable platform. Satellites orbit between ~800 and 36000 km, protecting them from destruction or damage by the phenomena monitored. Continuously recording in situ instruments are liable to destruction during violent events, breakdown in harsh, corrosive, volcanic environments or vandalism (e.g. Moxham *et al.*, 1972; Connor *et al.*, 1993; Lesage *et al.*, 1995). Receiving stations are also distanced from the target, allowing collection and examination of data in safety.

1.2. Thermal measurements and volcanic activity

During quiescent periods, thermal observations have been shown capable of identifying and monitoring pre-cursory eruption activity. Even prior to the lethal 1902 eruption of Mount Pelée, a precursory increase in fumarolic activity was observed between 1889 and 1902 (Chrétien & Brousse, 1989). Although surface temperatures do not always increase prior to eruptions (Neumann Van Padang, 1963), fumarole, crater lake and surface temperature variations have been related to eruptive or magmatic activity at many volcanoes (e.g. Suwa & Tanaka, 1959; Naboko, 1960; Yokoyama, 1964; Rose & Stoiber, 1969; Menyailov, 1975; Archambault *et al.*, 1979; Menyailov *et al.*, 1986; GVN, 1990a; Bonneville & Gouze, 1992; Ruapehu Surveillance Group, 1996). Temperature data for fumaroles and geothermal fields may also be used to estimate valuable volcanic system parameters, including heat flux (Sekioka & Yuhara, 1974), magma chamber volume (Rose & Stoiber, 1969), chamber depth (Stevenson, 1993) and gas flux (Connor *et al.*, 1993).

Thermal measurements of active lavas allow derivation of surface thermal structure and heat loss (Head & Wilson, 1986; Crisp & Baloga, 1990; Oppenheimer, 1991a). Such thermal measurements are essential inputs for models of lava flow rheology, emplacement and cooling (Danes, 1972; Pieri & Baloga, 1986; Dragoni, 1989; Dragoni, 1993; Hardee, 1993; Dragoni *et al.*, 1995; Keszthelyi, 1995). Derived parameters include cooling rates, effusion rates and heat loss from lava tubes. These can in turn be related to flow length, area and morphology (Walker, 1973; Wadge, 1978; Pieri & Baloga, 1986; Kilburn & Lopes, 1988; Pinkerton & Wilson, 1994; Keszthelyi, 1995), or used to develop flow simulation models (e.g. Young & Wadge, 1990; Barca *et al.*, 1993). All are crucial in predicting the future course of a flow and hazard posed to down-flow communities (e.g. Barberi, 1990; Barberi *et al.*, 1993a). Mass eruption rates and thermal energy release are also important in constraining models of magma supply and magma system operation (e.g. Wadge *et al.*, 1975; Wadge, 1981; Francis *et al.*, 1993).

1.3. Thermal monitoring of volcanoes from space: principles

At a given instant a satellite radiometer receives radiance from an area of the Earth's surface defined by the sensor's instantaneous field of view (IFOV). Usually, rotation of a scanning mirror and forward movement of the satellite build up the image in the along- and cross-scan directions respectively (Figure 1.1). Radiance reaching the sensor is separated into discrete spectral bands. These are directed onto detectors, where an electronic signal or voltage is produced, normally proportional to spectral radiance. An analogue to digital converter transforms the voltage to a pixel digital number (Schwalb, 1978; Foote & Draper, 1979; Mather, 1987; Lillesand & Kiefer, 1987; Barrett & Curtis, 1992). Calibration allows digital number (DN) to be related to radiance by

$$R_\lambda = S_\lambda \, DN_\lambda + I_\lambda \qquad (1.1),$$

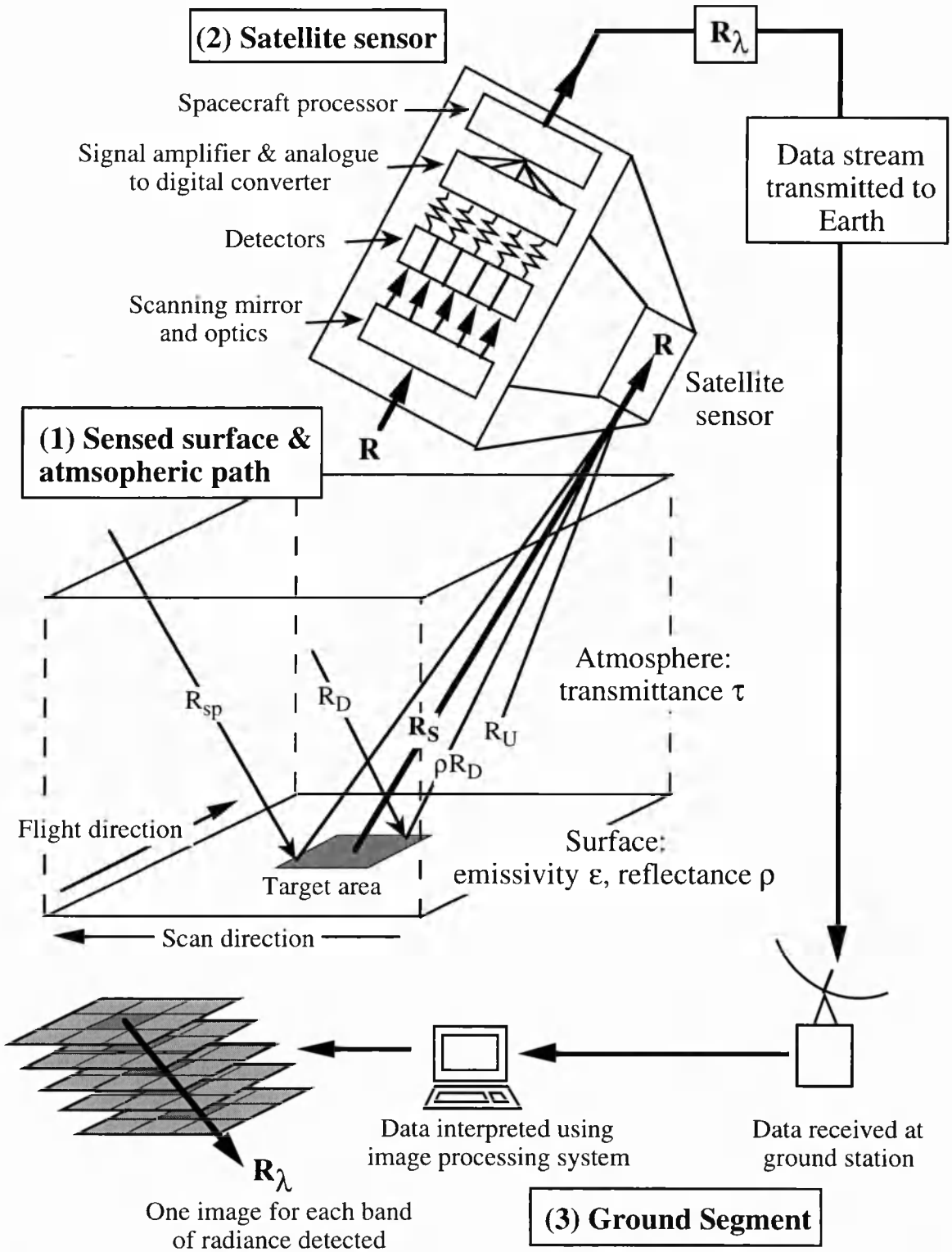

Figure 1.1. *Schematic diagram showing how radiance (R) from discrete areas on the Earth's surface reaches the sensor, is split into spectral radiance (R_λ), converted to DN, transmitted and displayed as pixel R_λ. R depends on surface emissivity and atmospheric transmissivity and will be the sum of radiance emitted by a surface, down welling radiance reflected by the surface, up welling atmospheric and space radiance (R_S, ρR_D, R_U & R_{sp}).*

in which R_λ, DN_λ, S_λ and I_λ are the at-satellite radiance, DN, slope and intercept for a spectral band with central wavelength λ. Total at-satellite radiance can be written as (Cracknell & Hayes, 1991; Hurtado *et al.*, 1996)

$$R_\lambda = \tau_\lambda(\varepsilon_\lambda R_{\lambda S} + \rho_\lambda R_{\lambda D}) + R_{\lambda U} + R_{\lambda sp} \qquad (1.2),$$

where τ_λ, ε_λ and ρ_λ are atmospheric transmissivity, emissivity of the surface and spectral reflectivity of the surface at wavelength λ respectively, $R_{\lambda S}$ is surface radiation, $R_{\lambda D}$ and $R_{\lambda U}$ are the down- and up-welling atmospheric radiances, and $R_{\lambda sp}$ is the space contribution (Figure 1.1). The space contribution is due to the background temperature of space (3 K), which passes down through the atmosphere and is reflected by the surface to the sensor (Cracknell & Hayes, 1991). Since the radiance equivalent of 3 K is vanishingly small between 1 and 14 μm, the contribution of $R_{\lambda sp}$ is insignificant at these wavelengths. At ~11.0 μm the contribution of $\rho_\lambda R_{\lambda D}$ is also negligible and, although not entirely negligible, $R_{\lambda U}$ is of little importance. Towards 3.0 μm $R_{\lambda U}$ becomes very small, but $\rho_\lambda R_{\lambda D}$ rises to ~10 % of R_λ for environmental temperatures (Singh & Warren, 1983; Cracknell & Hayes, 1991).

Detector band-widths are placed in atmospheric "windows", portions of the spectrum within which the atmosphere is relatively transparent to radiation. These occur in the visible and short-wave infrared (SWIR: 0.4-2.5 μm), mid-infrared (MIR: 3.0-5.5 μm) and thermal infrared (TIR: 8.0-14.0 μm). For a blackbody at temperature T, the distribution of spectral radiance emitted with wavelength is given by the Planck function

$$H(\lambda T) = c_1 \lambda^{-5} [\exp(c_2/\lambda T) - 1]^{-1} \qquad (1.3),$$

in which c_1 and c_2 are constants with the values 3.742×10^{-16} W m^2 and 1.4388×10^{-2} m K (Figure 1.2). The wavelength at which a blackbody temperature curve reaches a maximum (λ_m) is defined by Wein's Displacement Law:

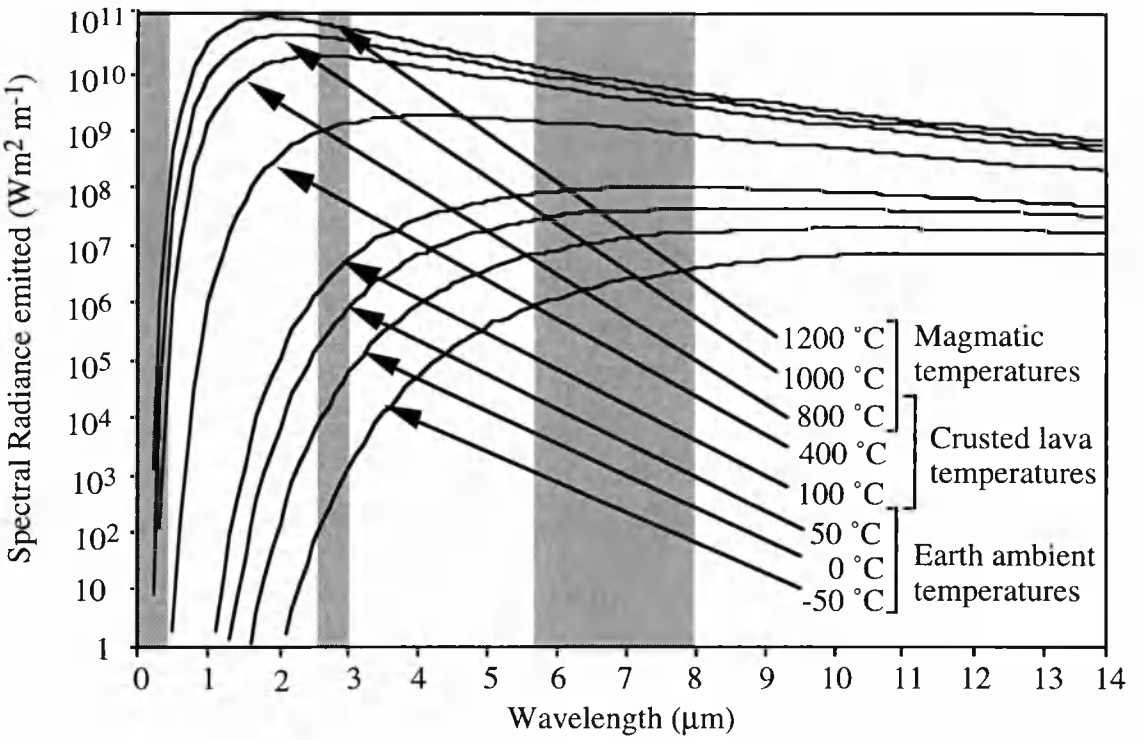

Figure 1.2. *Planck curves for blackbodies at typical magmatic, active crusted lava surfaces and Earth ambient temperatures. White areas give the broad locations of atmospheric windows within which atmospheric transmission is >70 %, within grey zones transmission falls sharply to ~13 %.*

$$\lambda_m = c_3 T^{-1} \qquad (1.4),$$

constant c_3 having a value of 2.898×10^{-3} m K.

These relationships mean that in SWIR wavebands $R_{\lambda S}$ will make a significant, measurable contribution to R_λ only if T is at-least ~120 °C. Coincidence of the SWIR window with λ_m for bodies at magmatic temperatures (800 to 1200 °C) mean that these bodies will contribute measurable $R_{\lambda S}$ (Figure 1.2). However reflectance peaks occurring at ~1.6 to 2.2 μm (Lillesand & Kiefer, 1987) make $\rho_\lambda R_{\lambda D}$ by far the largest contributor, swamping or contaminating $R_{\lambda S}$ by day (Oppenheimer *et al.*, 1993; Harris *et al.*, 1995c). Coincidence of the TIR window with λ_m for bodies at typical Earth ambient temperatures, and negligible contribution of $\rho_\lambda R_{\lambda D}$, makes this waveband useful for measuring $R_{\lambda S}$ from ambient surfaces. Bodies at ambient temperatures also contribute measurable amounts

of $R_{\lambda S}$ in the MIR (Figure 1.2). Coincidence of the MIR window λ_m for bodies at ~250-700 °C makes these wavebands extremely sensitive to thermal emittance from high temperature bodies, such as lava lakes or fires (Wiesnet & D'Aguanno, 1982; Matson *et al.*, 1984). However, day-time measurements are complicated by the contribution of $\rho_\lambda R_{\lambda D}$.

1.3.1. Satellite-derived temperatures over a volcanic hot-spot

At-satellite spectral radiance (R_λ) is related to temperature by

$$R_\lambda = L(\lambda T) = H(\lambda T) / \pi \qquad (1.5).$$

Pixel brightness temperature (T*) can therefore be estimated by re-arranging Equation 1.5 to give

$$T^* = c_2 / \lambda \ln ([c_1 \lambda^{-5} / \pi R_\lambda] + 1) \qquad (1.6).$$

However, T* will not be the temperature of the ground surface occupying the pixel (T_s). To obtain this, $R_{\lambda S}$ (Equation 1.2) must be estimated and substituted into Equation 1.5, to give $R_{\lambda S} = L(\lambda T_s)$. This can be achieved by estimating and removing all other parameters in Equation 1.2 to isolate $R_{\lambda S}$. Various procedures have been designed to estimate and remove the unwanted atmospheric, reflectance and emissivity contributions, allowing accurate, ±0.1 to ±3 °C (McClain *et al.*, 1985; Cooper & Asrar, 1989), surface temperature estimation (e.g. Singh, 1984; McClain *et al.*, 1985; Sobrino *et al.*, 1991; Oppenheimer *et al.*, 1993; Hurtado *et al.*, 1996).

The relationship given in Equation 1.5 assumes that the surface occupying a pixel is isothermal and can be described by a single temperature, T (Figure 1.3a). Over an active lava this assumption is unrealistic. Following the two-thermal component lava flow model

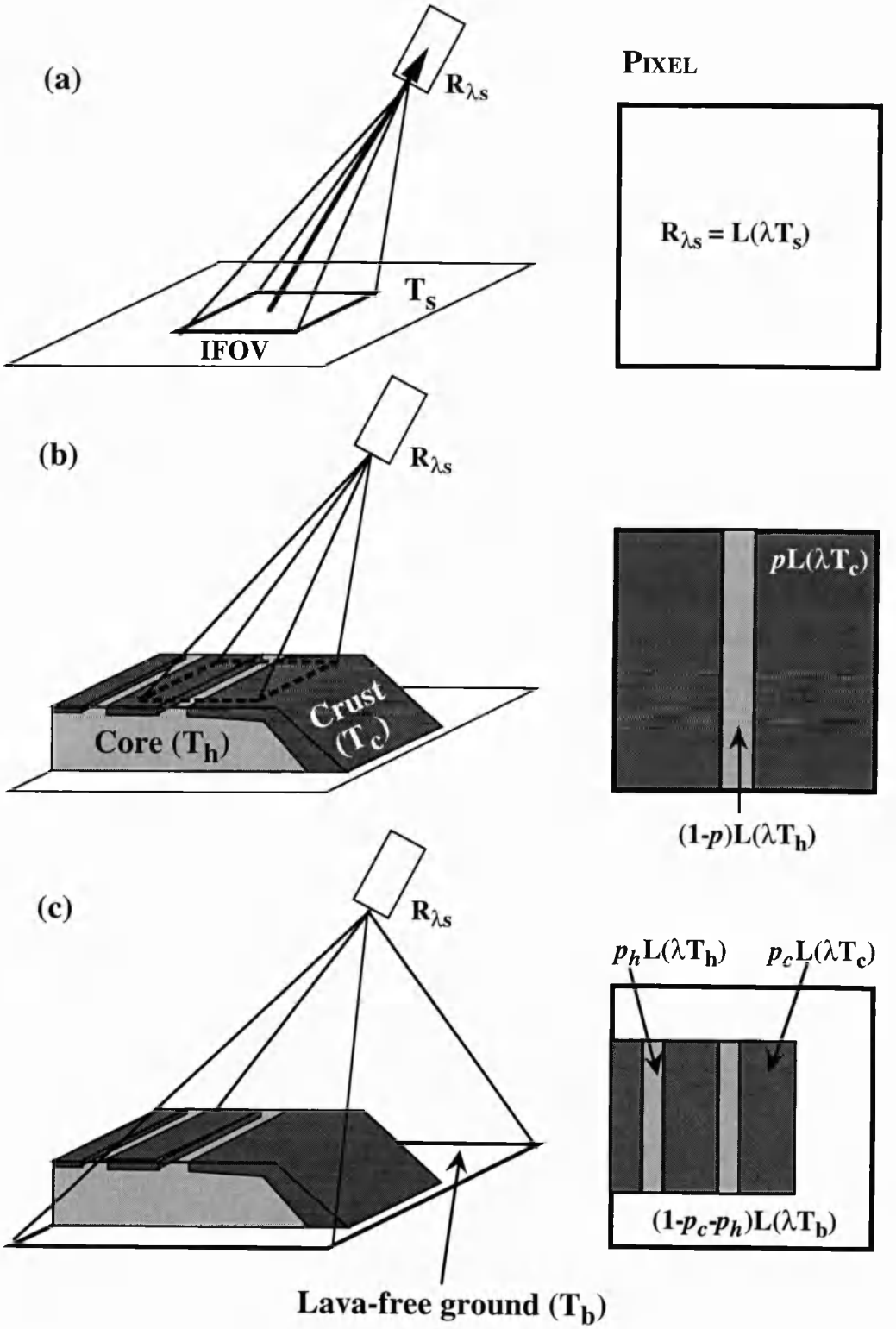

Figure 1.3. *Thermal surface of (a) a pixel occupied by a surface of uniform temperature T_s, (b) a pixel entirely filled by a Crisp & Baloga (1990) model lava surface, where the molten core at T_h is exposed at cracks in a chilled crust at T_c, and (c) a pixel where the two thermal component lava body is of sub-pixel dimensions.*

given by Crisp & Baloga (1990), a pixel over an active lava will be occupied by at least two thermal components: a chilled crust at temperature T_c occupying portion p of the pixel and smaller areas where the molten core at temperature T_h is exposed (Figure 1.3b). Applying the terminology of Rothery *et al.* (1988), a pixel entirely filled by such a surface will have a "pixel-integrated radiance" described by

$$R_{\lambda S} = pL(\lambda T_c) + (1 - p)L(\lambda T_h) \qquad (1.7).$$

Alternatively, T_h may be the temperature of an isolated volcanic hot-spot such as an active degassing vent or high temperature fumarole, in which case T_c will become the temperature of the cooler ambient background surrounding that isolated feature. As explained by Rothery *et al.* (1988), derived "pixel-integrated temperatures" will be "considerable underestimates of the true surface temperature" of the hot-spot since although the hot feature is much smaller than the pixel its radiance is integrated over the whole pixel area.

Dozier (1981) provided the "dual-band method", which allows each of the terms in Equation 1.7 to be estimated. The method requires thermal radiance measurements at two widely separated wavebands, λ_i and λ_j, and the assumption or a priori knowledge of any one of the three unknowns T_c, p or T_h. The remaining unknowns can then be estimated by graphical or numerical solution of the simultaneous equations

$$R_{\lambda iS} = pL(\lambda_i T_c) + (1 - p)L(\lambda_i T_h) \qquad (1.8a)$$

$$R_{\lambda jS} = pL(\lambda_j T_c) + (1 - p)L(\lambda_j T_h) \qquad (1.8b).$$

The method was initially applied by Matson & Dozier (1981) to estimate the size and temperature of sub-pixel industrial hot-spots and gas-flares in AVHRR data. Applicability to volcanic hot-spots was first demonstrated using TM data by Rothery *et al.* (1988), and this volcanic application was subsequently developed by numerous studies

(e.g. Pieri *et al.*, 1990; Oppenheimer, 1991a; Oppenheimer *et al.*, 1993; Flynn *et al.*, 1994).

Oppenheimer (1993) and Harris *et al.* (1995c) point out that in cases where the lava body is of sub-pixel dimensions, the thermal structure given by Equation 1.6 becomes an oversimplification (Figure 1.3c). A more realistic model requires inclusion of a third component, lava-free ground at an ambient temperature of T_b, to give

$$R_{\lambda S} = p_c L(\lambda T_c) + p_h L(\lambda T_h) + (1 - p_h - p_c)\, T_b \qquad (1.9),$$

with p_c and p_h being the pixel portions occupied by the crusted and molten lava surfaces respectively (Figure 1.3c). This creates five unknowns. Consequently, solution by simultaneous equations requires either (1) thermal radiance at two widely separated wavebands and assumption of three unknowns or (2) thermal radiance at four widely separated wavebands and assumption of one unknown. Oppenheimer (1993) showed how the more realistic three component model can be constrained using three bands of thermal data available from the airborne Thematic Mapper Simulator. Emitted radiance has, occasionally, been observed in three bands of satellite data, as during eruptions at Etna, Kilauea and Krafla (Rothery *et al.*, 1992; Flynn & Mouginis-Mark, 1994; Harris *et al.*, 1995c). However, in all observed cases one or two of these bands have been saturated and therefore unusable, precluding application of this more realistic approach.

1.3.2. Analysis of low temperature anomalies

Bonneville *et al.* (1985), Bonneville & Kerr (1987) and Bonneville & Gouze (1992) have shown that over low temperature anomalies, such as ground heated by permeable convection over an intrusion, the most important atmospheric effect in the TIR is due to adiabatic cooling with altitude (Figure 1.4). The strong inverse relationship between altitude and surface temperature obscures subtle variations in heat flux. Therefore, to remove surface temperature variations caused by cooler air temperatures at higher altitudes

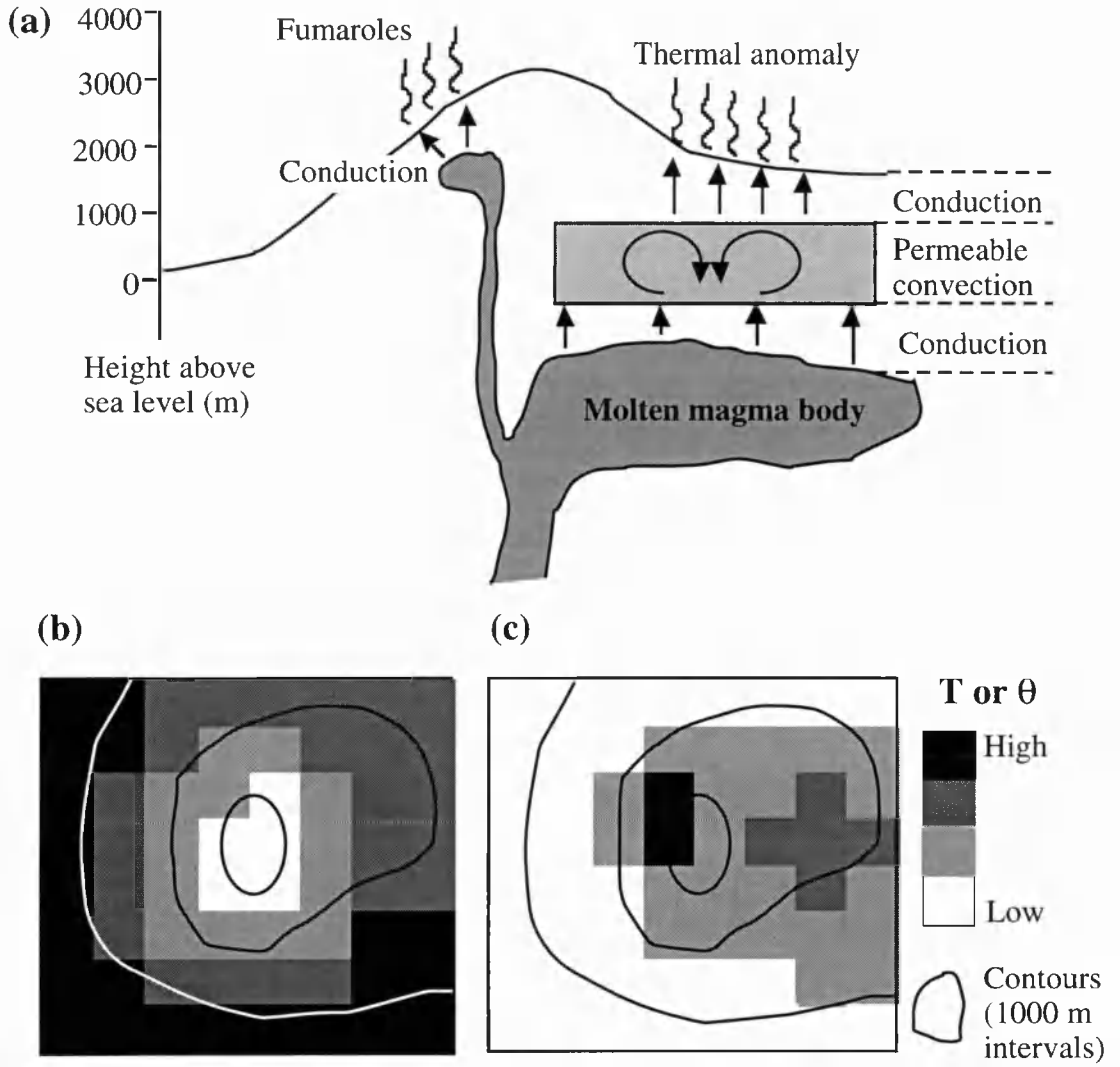

Figure 1.4. *Effect of adiabatic cooling on low temperature anomalies. (a) Model for heat flow from shallow magma bodies given by Hardee (1982). (b) Idealised temperature image for surfaces above the model showing the dominant effect of surface cooling with altitude. (c) Corrected temperature image (θ) showing suppression of altitude effects, enhancing low temperature anomalies due to heat flow from sub-surface magma bodies.*

and distinguish low temperature anomalies, a height independent, corrected temperature (θ) is calculated for each pixel

$$\theta = T_S + (\partial T/\partial z)z \qquad (1.10),$$

in which z is surface altitude and $\partial T/\partial z$ is the adiabatic gradient (Figure 1.4).

1.4. High spatial resolution thermal monitoring from space

Between 1987 and 1988 a series of papers showed how TM's SWIR bands were capable of detecting and monitoring thermal emittance from active lava flows, lakes and domes (Francis & Rothery, 1987; Rothery & Francis, 1987; Rothery *et al.*, 1988). For bodies in excess of ~160 °C, TM not only provides thermal radiance measurements in two wavebands, but also a high (30 m pixel) spatial resolution, allowing constraint of the thermal surface (Rothery *et al.*, 1988; Rothery & Oppenheimer, 1991).

Following these initial observations, numerous studies developed techniques to extract useful volcanological information from TM data (e.g. Oppenheimer 1991b). Some concentrated purely on detecting volcanic hot-spots and application of the dual-band method to estimate sub-pixel temperatures, as during effusive activity at Barren Island in 1991 (Bhattacharya *et al.*, 1993; Gupta & Badarinath, 1993; Reddy *et al.*, 1993). Other studies used dual-band method results to estimate thermal flux (Glaze *et al.*, 1989; Oppenheimer, 1991a; Oppenheimer *et al.*, 1993), derive lava flow core temperature and constrain models of flow cooling (Pieri *et al.*, 1990), or calculate crustal boundary layer thickness (Oppenheimer, 1991a). Single images have been used to map and analyse the spatial distribution of thermal areas across active flows and domes (Oppenheimer, 1991a; Oppenheimer *et al.*, 1993; Flynn & Mouginis-Mark, 1994), and time-series have been used to monitor variations in thermal flux over time (Glaze *et al.*, 1989; Oppenheimer *et al.*, 1993; Andres & Rose, 1995). The time-series studies of Glaze *et al.* (1989) and Oppenheimer *et al.* (1993) showed how variations in thermal flux from the lava dome at Lascar volcano could be related to eruptive cycles.

The TM's TIR band has a pixel size of 120 m, precluding its use in the dual-band method with the smaller SWIR pixels. However it has been used to evaluate crater lake temperature (Oppenheimer, 1993), measure heat flux from fumarole fields and Strombolian vents (Gaonac'h *et al.*, 1994) and detect geothermal areas (Jaskolla & Arnason, 1989).

Analysis of other high resolution satellite data sources for thermal monitoring has been less productive. Chorowicz *et al.* (1992) used 10 m SPOT pixels to identify visible

changes at Sabancaya in 1986 due to ice-melt caused by reactivated fumarolic activity, a precursor to an eruption in 1990. However, since all three SPOT wavebands are less than 0.89 μm in wavelength, detection of thermal emission is unlikely. With four 18 m pixel wavebands in the SWIR, data from JERS-OPS offered great promise (Oppenheimer, 1991b). Unfortunately degradation of the data by severe noise problems has made the data useless except for qualitative analysis of volcanic hot-spots (Denniss *et al.*, in press).

1.5. Low spatial resolution thermal monitoring from space: the AVHRR

The ease with which active lava bodies could be detected using 1 km MIR pixels from the AVHRR was demonstrated as early as 1982, when an image showing a hot spot due lava lake activity at Mount Erebus was published (Wiesnet & D'Aguanno, 1982). During the 1980s a number of studies also demonstrated how, using processing techniques first applied by Bonneville *et al.* (1985) and given here in Section 1.3.2, AVHRR could be used to identify low temperature volcanic thermal anomalies. At Mount Etna, a 50 km^2 area of elevated surface temperatures evident on Very High Resolution Radiometer images (AVHRR's predecessor) between 1978 and 1979 was assumed to relate to shallow level magma storage (Archambault *et al.*, 1979; Smithsonian Institution, 1989). Similar low temperature anomalies were observed prior to effusive eruptions in 1983 and 1986, in both cases coincident with the subsequent eruption site (Bonneville & Kerr, 1987; Bonneville & Gouze, 1992).

In spite of these promising results, prior to the start of this PhD (September 1993) few attempts had been made to build on these studies. Those that had been carried out generally took a limited or negative approach, not attempting to solve any problems encountered. Scorer (1986) published a series of images illustrating thermal anomalies in AVHRR data due to active lava flows during the December 1985 Etna eruption. He was, however, more interested in meteorological phenomena stating, "the eruption was not exciting but there are many points of meteorological interest". Oppenheimer (1989) re-

examined the Erebus image, as well as images of Stromboli, Vulcano and Etna. His result was a list of reasons why "AVHRR is clearly not an ideal tool for thermal monitoring of volcanoes". Problems included: (1) the unrealistic nature of applying the 2 component model assumed by the dual-band to a 1 km pixel, (2) smearing of radiance from the hot-spot pixel into adjacent non-hot spot pixels, (3) contamination by sub-pixel cloud or plume and by sunlight in day-time MIR images, (4) confusion with fires or industrial hot spots, (5) differential atmospheric absorption in the MIR and TIR channels, and (6) failure to detect transient explosive activity at Stromboli on 3 out of 4 images examined or the low temperature Vulcano fumarole field on any of his images.

1.5.1. AVHRR: potential for real time thermal volcano monitoring

Considering the genuine capabilities of the AVHRR in terms of volcano monitoring, it is surprising that no rigorous study has yet examined whether AVHRR can provide anything more than a visual identification of volcanic hot-spots. In fact AVHRR can offer the following:

(1) Thermal capability. As demonstrated by Wiesnet & D'Aguanno (1982), the AVHRR MIR channel (channel 3: 3.55-3.93. μm) is extremely sensitive to high temperature volcanic features. The availability of two bands of TIR data (channels 4: 10.3-11.3 μm, and 5: 11.5-12.5 μm) mean that development of approaches for analysis of high and low temperature anomalies are feasible (Section 1.3). The lack of use of AVHRR thermal data by the volcanic community is even more mystifying when the large body of work carried out by the fire community is examined. Successful applications include fire detection (Flannigan & Vonder Haar, 1986; Lee & Tag, 1990; Langaas, 1993), fire area derivation (Flannigan & Vonder Haar, 1986; Matson & Holben, 1987; Cahoon *et al.*, 1991; Cahoon *et al.*, 1992), time series analysis, fire growth monitoring and fire mapping (Langaas, 1992; Dousset *et al.*, 1993; Chuvieco & Martin, 1994; Arino & Melinotte, 1995).

(2) Temporal capability. The return period of the NOAA satellite on which the AVHRR is flown is 12 hours. Since 1979, NOAA has maintained at least 2 satellites in orbit at any one time, ensuring coverage of any sub-aerial point at-least 4 times a day (Mather, 1987). This coverage improves towards the poles where satellite tracks converge: images from ~10 passes per day are currently received at the University of Dundee receiving station (R. Vaughan, personal communication). When compared with the 16-, 26- and 44- day return periods of TM, SPOT and JERS-OPS, this greatly improves the chances of a pass coinciding with a cloud-free interval or short duration (<1 week) transient event.

(3) Real time monitoring capability. Data can be received directly by the user and analysed on receipt. This capability is essential if effective monitoring of a dynamic feature, such as a developing lava flow or dome, is to be achieved. At the University of Alaska Fairbanks, visual analysis of images on reception allows communication of volcanic hot-spot observations within 5-10 minutes of a satellite pass (K. Dean, personal communication). Automated processing also provides rapid results: automated fire detection techniques take between 30 seconds and 1 hour to run on 512 x 512 pixel AVHRR images (Flasse & Ceccato, 1996). TM data, however, must be ordered from the supplier and can take more than 2 months to arrive (Rothery *et al.*, 1992), making real time monitoring impossible.

(4) Low cost monitoring capability. Data are freely available at cheap to install receiving stations (Gower, 1992). System costs vary depending on sophistication (Table 1.1), but the cheapest are generally equivalent to the cost of a single TM or SPOT image (~US$ 4000 and 15000 respectively based on 1993 prices from the UK's National Remote Sensing Centre Limited). Minimum costs are also considerably less than the US$ 35000 lost when the 1991 eruption of Pinatubo destroyed the entire seismic network installed there (Lesage *et al.*, 1995). In the absence of a station, image costs are <US$ 30 (based on 1996 prices for a 600 line sub-scene ordered from the Dundee University Receiving Station).

System Hard- & soft-ware details	Company Address	Cost Date of quote
Bradford University Research Limited	Bradford University, Bradford, UK	US$ 2700 upwards (1994)
Hardware:	Motorised antenna to track satellite, cable to PC, PC card to convert data to PC readable format (HRPT and SEAWiFs compatible).	
Software:	Automatic tracking and reception software included.	
System installed at Institute of Ocean Sciences	Inst. Ocean Sci., Sidney V8L 4B2, Canada	US$ 4750 (Gower, 1992)
Hardware:	PC interface board, receiver feed, combiner & pre-amplifier/downconverter, PC, 1.2 m dish, antenna steering device.	
Software:	Real time display of central strip of image and data archiving (Chinese Feng-Yun satellite FY-1 compatible).	
Timestep PROsat II system	Timestep, Newmarket CB8 8XB, UK	US$ 4800 (1995)
Hardware:	486 PC, 170 Mb hard drive, HR colour monitor, dish antenna with all cables and associated hard- & soft-ware, GOES/Meteosat capability.	
Software:	Live display, saves full pass in full resolution, calibration, georeferencing, satellite track prediction, image processing.	
SeaSpace TeraScan system	SeaSpace, San Diego CA92126, USA	>US$ 20000 (1995)
Hardware:	1.0 m antenna, 1.5 m protective dome (survival -30 to +55 °C, 162 km h^{-1} winds, 22 kg m^{-2} ice), amplifier & downconverter, cable, Sun-4/50 SPARCstation, DAT archive tape drive.	
Software:	Antenna control & data acquisition (includes automatic unattended operation), calibration, geo-location, cloud-screening, image processing.	
Dartcom winHRPT system	Dartcom, Yelverton PL20 6SP, UK	US$ 38000-62000 (1996)
Hardware:	Pentium PCI, 1 Gb fast SCSI II hard disk, archiving drives, FST monitor, 1.2-1.8 m antenna (survival -35 to 63 °C and 210 km h^{-1} winds), downconverter & receiver, built-in GPS.	
Software:	Antenna control, image acquisition & quick look, image processing including reflectance & temperature calibration and geo-location.	

Table 1.1. *Costs and capabilities of commercially available AVHRR receiving systems.*

(5) Large area analysis capability. A single AVHRR image covers an area of ~3000 x 6000 km and all volcanoes therein, allowing simultaneous real time monitoring of all volcanoes on a regional scale. At the University of Alaska Fairbanks this large area view permits analysis of >50 active volcanoes across Alaska, the Aleutian Islands and Kamchatka (C. Wyatt, personal communication).

Since 1993 six studies have indicated that this vast, cheap, directly available and largely untapped data source could provide a reliable means of volcano thermal monitoring. First, Harris (1992), Harris & Vaughan (1993), Harris *et al.* (1995c) showed how the temporal resolution of the AVHRR could be used to monitor the evolution of a large fissure fed eruption. Then Mouginis-Mark *et al.* (1994) showed how AVHRR viewing geometry may be used to distinguish different volcanic thermal features in off-nadir images. Also in 1994, Flynn & Mouginis-Mark (1994) reported on the observation of a thermal anomaly on an AVHRR SWIR (channel 2: 0.725-1.1 μm) night-time image during effusive activity at Kilauea in 1992. They concluded "night-time AVHRR Band 2 images could be used to detect extremely vigorous lava flows that represent the greatest local hazards."

1.6. Aims and structure of this thesis

Has a potentially valuable data-set capable of eruption monitoring been largely ignored, or are the potential benefits offered by the AVHRR negated by the poor spatial resolution? The main aim of this study will be to answer this question through analysis of the AVHRR's spatial, spectral and temporal capabilities.

(1) Analysis of spatial and spectral capabilities. Data covering a range of active volcanic thermal phenomena are analysed to define (a) the detection and monitoring limits of the AVHRR, and (b) what reliable volcanological information can be extracted.

(2) Analysis of temporal capabilities. If variation in time series can be shown to relate to variations in dynamic volcanic thermal phenomena, then such an approach offers a valuable monitoring tool. Construction of AVHRR time series enable the value of such an approach to be assessed.

(3) Real time monitoring capabilities. Rapid data analysis and dissemination of results is best achieved by reliable automation. Techniques are defined using algorithms capable of inclusion in an automated ground segment for rapid, real-time, on-reception, analysis. Digital data provided by the AVHRR are ideally suited to such an approach.

(4) Improved spatial, spectral and temporal resolution using multiple data-sets. Lillesand & Kiefer (1987) define "multistage sensing" where satellite data are analysed in conjunction with aircraft data and ground observations. Each data source offers differing but complementary spectral, spatial and temporal characteristics, providing a complete thermal data set. Such an approach is considered, where it is anticipated that AVHRR will fulfil the detailed temporal needs of a multistage volcano thermal sensing data set.

Lillesand & Kiefer (1987) define ground reference data as serving "any or all of the following purposes: 1. To aid in the analysis and interpretation of remotely sensed data. 2. To calibrate a sensor. 3. To verify information extracted from remote sensing data." Ground reference data plays a central role in this study. If extracted information agree with reference data then the technique and results are accepted as valid, otherwise the technique is plainly in error and must be amended accordingly or rejected. Ground reference data allows techniques, developed and tested on ground reference events, to be applied with reasonable confidence to similar, but poorly observed, phenomena.

While performing this study, I have taken advantage of opportunities to work with several colleagues based at The Open University and elsewhere. Except for the concluding chapter, each of the remaining Chapters is reprinted from a paper that is published, in press or under review, with only minor editorial changes. Some repetition is therefore inevitable, but it means that any chapter can be read without reference to others. Most papers were written in collaboration with co-authors; however I was senior author on each of them. Table 1.2 indicates thesis structure and the amount of co-author input to each chapter. Papers presented as Appendices are either peripheral to the main study, or were written with too great a co-author contribution to be included in the main body of the thesis.

Chapter/ Appendix	Content & Co-author contribution
1	Introduction
2	Defining and understanding an unexpected response of the AVHRR thermal channels over high temperature targets. ~10-20 %: mainly fire data and discussions/details regarding sensor operation.
3	Design, implementation and testing of an automated algorithm for location of volcanic hot spots, and definition & filtering of point spread function and sensor recovery pixels. ~20-30 %: writing of Excel macro and C++ software to execute the procedure, this is given more fully in Appendix B.
4	Application of automated thresholding and various thermal analysis techniques designed for volcano data to a data set containing fires. No co-authors.
5	Techniques and results from analysis of a times-series of data for a ground reference event (a major effusive eruption at Etna). ~20-30 %: Figure 5.1 used Stevens field-data & SPOT image, and the flow outline derived by her, Blake provided input into Section 5.8.
6	Analysis of a "multistage" data set for Strombolian and fumarolic activity, where AVHRR provides the temporal resolution, and air-borne and ground data the spatial resolution and validation. ~10-20 %: Stevenson provided model for magma depth estimation, implications of results are given more fully in Appendix D.
7	Demonstration of all techniques, designed to allow near-real time, reliable monitoring, on a variety of well and poorly ground referenced events (fissure & vent fed lava flows, pyroclastic flows, lava lakes, pyroclastic flows and degassing/Strombolian open vents). ~20-30 %: provision of Cerro Negro data and details of the reception, calibration and processing systems. Butterworth made a major contribution to the geometry section.
8	Conclusions
A	Review of remote sensing studies to date, specifically for Mount Etna volcano
B	Details of automated software for processing AVHRR sub-images containing volcanoes
C	Constraints on the shallow magmatic system at Stromboli
D	Constraints on the magma systems at Vulcano and Stromboli

Table 1.2. *Thesis contents and co-author contribution.*

Chapter 2. Non-zero saturation of the AVHRR thermal channels over high temperature targets: evidence from volcano data and a possible explanation

---

A.J.L. Harris, D.A. Rothery, R.W. Carlton, S. Langaas, and H. Mannstein

Published in the International Journal of Remote Sensing, 16(1), 189-196, 1995.

2.1. Abstract

Our AVHRR volcano and fire data are in agreement with Setzer and Verstraete (1994), showing that when channel 3 saturates the digital number (DN) recorded is greater than zero. The radiance at which this occurs varies within a single radiometer, and from platform to platform. It appears that non-zero saturation has affected all the thermal channels on all AVHRR instruments to date and may be due to the design of the analogue-to-digital converter circuits. Since the exact relationship between non-zero DN and spectral radiance is not known, we suggest that all DN over high temperature targets that are less than or equal to the non-zero saturation DN cannot be trusted to be reliable measurements of spectral radiance[a].

2.2. Introduction

Although the Advanced Very High Resolution Radiometer (AVHRR) flown aboard the TIROS-N (NOAA) satellites was not designed to monitor high temperature features, the sensitivity of channel 3 (3.55 - 3.93 μm) to high temperature sources has allowed heat sources such as fires, lava lakes and lava flows to be detected and measured (e.g. Rothery, 1992; Langaas, 1993; Pereira & Setzer, 1993; Harris *et al.*, 1995c).

In channels 3, 4 (10.3 - 11.3 μm) and 5 (11.5 - 12.5 μm) the relationship between radiance and digital number (DN) is inverse, with increased radiance resulting in decreased DN. A cut-off in the conversion from analogue signal to DN, here termed saturation, occurs when the spectral flux from a pixel exceeds an upper limit. This occurs at a channel 3 pixel integrated temperature that varies, depending on the platform, from 49 °C to 58 °C

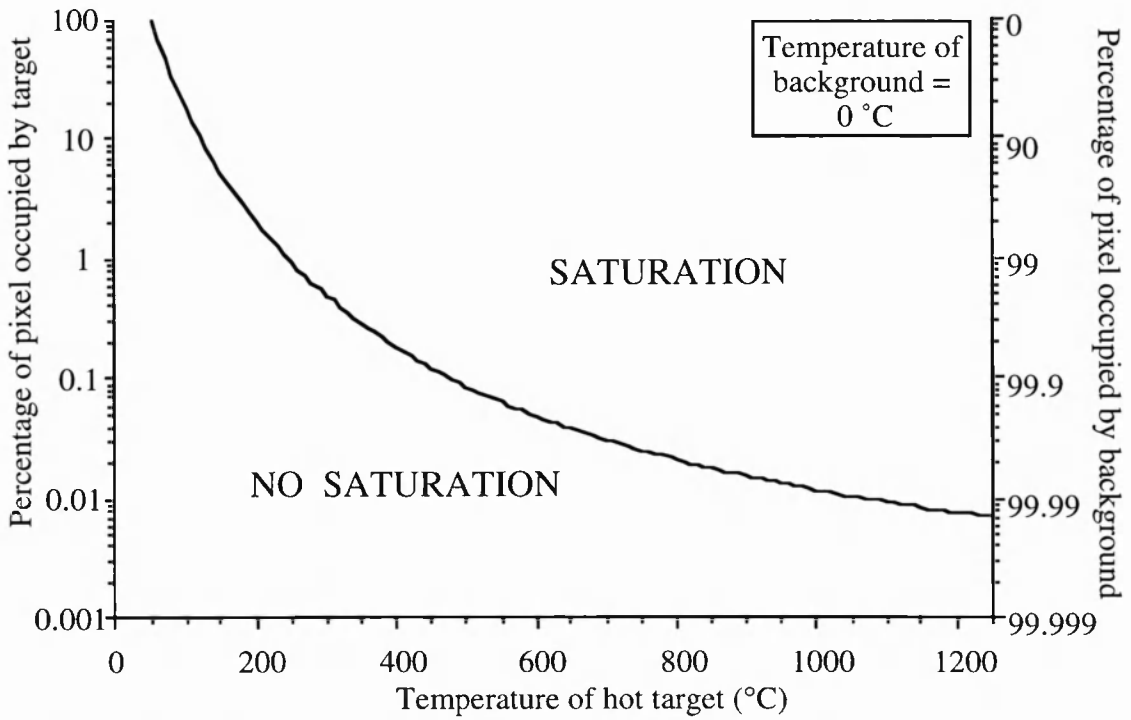

Figure 2.1. *Plot of the minimum pixel portions that need to be occupied by hot targets in order to saturate an AVHRR channel 3 pixel, assuming a background temperature of 0 °C, a saturation temperature of 50 °C and no atmospheric contribution.*

(Robinson, 1991). Images analysed here and by Setzer and Malingreau (1993) show that the pixel integrated temperature at which the channel 3 sensor saturates also varies with time by 3 - 5 °C within a single radiometer.

To achieve saturation temperatures in channel 3, only a small fraction of a pixel needs to be occupied by hot material, see Figure 2.1 and Table 2.1. An active lava flow,

Temp. (°C)	% of pixel occupied	Area (m)	
1200	0.008	10 x 10	Maximum eruption temperature for basaltic lava (Cas & Wright, 1987)
1080	0.01	11 x 11	Temperature in lava channel at Etna (Barberi *et al.*, 1993a)
1000	0.01	12 x 12	Minimum eruption temperature for basaltic lava (Cas & Wright, 1987)
900	0.015	14 x 14	Maximum eruption temperature for rhyolite lavas (Cas & Wright, 1987)
790	0.02	16 x 16	Maximum lava crust temperature calculated by multi-component modelling of spectro-radiometer data for the Kupaianaha lava lake (Flynn *et al.*, 1993)
700	0.03	19 x 19	
600	0.05	24 x 24	
500	0.09	32 x 32	
400	0.2	47 x 47	Range of possible temperatures of lava crusts
300	0.5	77 x 77	
200	2	157 x 157	
100	18	472 x 472	
80	34	638 x 638	Minimum lava crust temperature calculated by multi-component modelling of spectro-radiometer data for the Kupaianaha lava lake (Flynn *et al.*, 1993)

Table 2.1. *Minimum portion of a pixel that must be occupied by hot material, at a variety of lava flow temperatures, in order to saturate a channel 3 pixel, and the minimum area that the temperature source must attain to achieve saturation at nadir. Calculations assume a pixel is occupied by two temperature components: lava at a specified temperature, surrounded by lava-free ground at an ambient temperature (assumed to be 0 °C for this model).*

lake or dome should saturate channel 3 quite easily. Even a lava flow covered by a comparatively cool 100 °C crust occupying 0.5 x 0.5 km within a pixel at nadir should result in channel 3 saturation.

Studies that have used channel 3 data to monitor active lava lakes and flows, for example at Mount Erebus (Antarctica) and Krafla (Iceland), have found that these high temperature targets which should saturate channel 3, giving a DN of zero, have instead given non-zero DN (C. Oppenheimer, personal communication; Harris *et al.*, 1995c; Harris & Vaughan, 1993). A similar phenomenon has been found in channel 3 data for savannah fires in Senegal and The Gambia and other channel 3 fire data sets (e.g. Pereira & Setzer, 1993; Setzer & Verstraete, 1994).

Here we present AVHRR data for volcanoes, in an attempt to further illustrate and understand the "non-zero saturation" problem, and propose an explanation.

2.3. Non-Zero saturation at Krafla and Etna

The September 1984 eruption at Krafla (Iceland) and December 1991 to March 1993 eruption at Etna (Sicily) produced active lava flow fields of sufficient size and temperature that channel 3 should have been saturated. We estimate that at Krafla the lava flow field should have saturated between 21 and 45 channel 3 pixels, creating an area of saturation of up to 4 pixels (scan direction) by 13 pixels (cross-scan direction). At Etna about 15 channel 3 pixels should have been saturated, forming an area of saturation of 7 - 8 pixels by 2 - 3 pixels. However, examination of the channel 3 DN (Figures 2.2a and 2.2b) shows that where saturated DN of zero are expected, non-zero DN occur.

The pattern of non-zero DN in Figures 2.2a and 2.2b, with a central core of uniform DN and lower DN at the periphery, is typical of all images examined for the eruptions at Etna (a total of 60 images) and Krafla (7 images in all), and is similar to the DN variation across areas of sunglint described by Setzer and Verstraete (1994).

(a)

835	827	817	790	785	800	792	788	806	804	800
833	808	734	432	9	467	644	726	762	809	786
859	938	38	47	47	47	45	101	703	785	793
830	834	917	45	47	47	47	47	28	765	780
820	795	785	687	594	574	504	36	457	757	776
809	799	815	809	774	744	726	755	773	759	771

(b)

799	739	589	360	294	512	679	728
796	695	461	13	36	34	482	651
742	585	197	37	38	38	88	812
697	404	34	37	38	38	38	937
615	225	37	38	38	38	38	858
535	92	37	38	38	38	38	324
493	10	37	38	38	38	37	818
378	33	37	38	38	38	36	739
218	36	38	38	38	38	16	816
139	36	38	38	38	38	184	883
276	33	37	38	38	38	34	953
393	0	36	38	38	38	35	1019
531	275	36	38	38	38	997	878
615	509	273	37	37	190	738	744
643	621	562	357	277	542	712	771

(c)

507	503	510	519	517	514	508	500
508	501	506	514	504	504	506	500
509	502	500	490	369	409	505	505
508	499	495	417	11	125	486	510
506	489	476	325	37	20	470	504
505	485	458	127	39	37	444	505
506	489	465	59	39	4	484	500
505	489	430	34	38	280	500	497
502	484	231	39	38	381	503	496
507	488	267	39	38	400	505	494
512	498	436	34	38	315	504	491
510	503	475	7	38	305	505	492
508	507	490	210	73	434	501	493
510	508	503	451	422	489	501	500
516	512	507	499	497	502	505	503

Figure 2.2. *Typical channel 3 and 5 DN distribution at the Etna and Krafla lava flow fields, showing non-zero saturation. (a) NOAA-11 AVHRR channel 3 image of the active December 1991 to March 1993 flow field at Etna acquired on 2 January 1992 at 13:51 GMT. (b) NOAA-7 channels 3 and (c) 5 images of the active Krafla September 1984 flow field acquired on 5 September 1984 at 04:47 GMT.*

At Krafla on 5 September 1984 the temperature of the active lava flow field was high enough to cause a 26 pixel thermal anomaly in channel 2 (Harris *et al.*, 1995c). Thermal emittance in channel 2 (0.725 - 1.1 μm) indicates a pixel integrated temperature of at least 550 °C, well in excess of the temperature necessary to saturate channel 3. At Etna on 2 January 1992 an open lava channel 10 to 15 m wide was radiant in the Landsat Thematic Mapper band 4 (0.76 - 0.90 μm) for 700 m downstream from the source (Rothery *et al.*, 1992), and was measured in the field as 1080 °C (Barberi *et al.*, 1993a). If the lava channel were centred in an AVHRR channel 3 pixel, with the remainder of the pixel at an ambient temperature of 0 °C, the pixel integrated temperature would be around 210 °C, well in excess of the temperature necessary to saturate a channel 3 pixel. It can therefore be safely assumed that the uniform cores of channel 3 DN of 38 (NOAA-7) and 47 (NOAA-11) represent a non-zero saturation level. Thus conversion of these non-zero saturation DN to spectral radiances, using the linear relationship of Kidwell (1995), will give a minimum feasible (often unrealistically low) radiance for the pixel.

For one NOAA-7 Krafla image, acquired on 5 September 1984, we have evidence that the non-zero saturation problem affects channels 4 and 5. Pixels central to the anomaly have near uniform DN, between 30 and 32 in channel 4 and between 38 and 39 in channel 5, with lowest DN peripheral to this central core, Figure 2.2c. All of the central core pixels were also radiant in channel 2, indicating pixel integrated temperatures well in excess of that necessary to saturate channels 4 and 5. We therefore suggest that the non-zero saturation problem also affects channels 4 and 5, and that non-zero saturation will occur in these channels if the pixel integrated spectral radiance is high enough.

2.4. Variation in non-zero saturation level between instruments

Setzer and Verstraete (1994) suggest that the non-zero saturation problem may affect multiple AVHRR instruments. Our volcano data (10-bit) confirm that it has affected

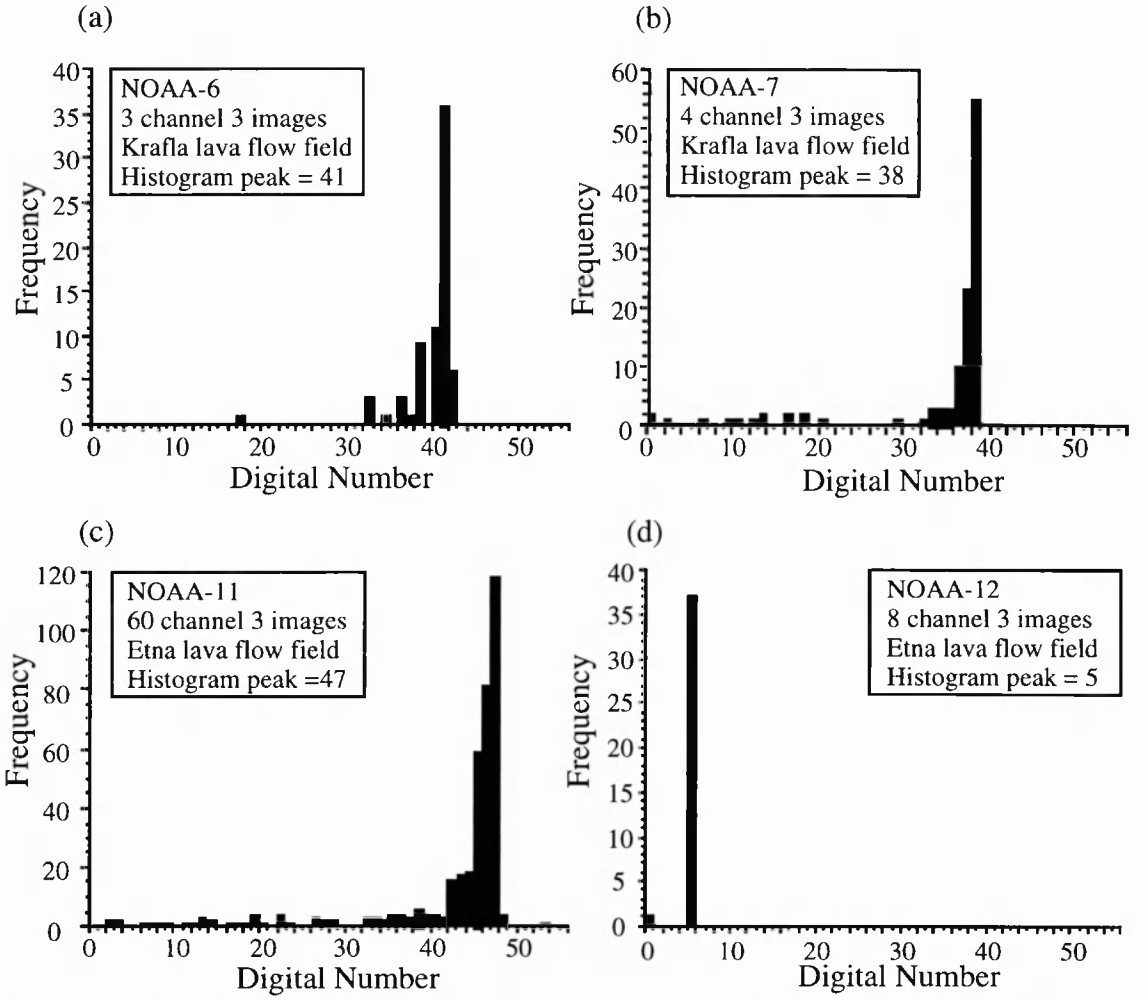

Figure 2.3. *(a) to (d) digital number frequencies for channel 3 lava flow pixels for the entire NOAA-6 (a), -7 (b), -11 (c) and -12 (d) datasets, illustrating the vicinity of the non-saturation DN for each AVHRR instrument.*

the AVHRR aboard NOAA-6, -7, -11, and -12, and is illustrated by the clearly defined peaks in all of the histograms for these NOAA data sets (Figures 2.3a to 2.3d). We observe similar peaks in composite histograms for NOAA-10 and -11 Senegalese fire data (8-bit), with non-zero saturation causing a clear peak at a DN of 8 for NOAA-10 and at a DN of 10 for NOAA-11. Variations in the position of the histogram peaks between each of the histograms indicate that for each instrument the level of non-zero saturation was different. Since Pereira and Setzer (1993) show non-zero saturation of the NOAA-9 AVHRR for fires in the Amazon region, it seems reasonable to assume that non-zero

saturation affects all the thermal infrared sensors of the AVHRR, each sensor having a different non-zero saturation level.

2.5. Non-zero saturation - a possible explanation

Pre-flight testing of the AVHRR thermal channels at ITT Aerospace was based on spectral radiances within or only slightly exceeding the analogue-to-digital converter (A/D) dynamic range and has never revealed the non-zero saturation problem (Roy Galvin, personal communication). However, data here and in Setzer and Verstraete (1994) show that spectral radiances strongly in excess of the DN=0 equivalent radiance will give a non-zero saturation DN. Since the A/D count is not required to have any specific value when the scene is in excess of its brightest dynamic range, i.e. "below" a count of 0, (Roy Galvin, personal communication) we suggest that the problem lies in the design of the A/D circuits, as indicated by Setzer and Verstraete (1994).

Setzer and Verstraete (Fig. 5, 1994) postulate that beyond a threshold radiance, increasing radiances are transformed into increasing "spurious" DN. The left skew we have found in all except the NOAA-12 frequency distributions, Figures 2.3a to 2.3d, supports this hypothesis. The histogram peaks reveal the true DN cut-off of the channel 3 sensor.

Until the sensor is tested on a calibrated high temperature target, the relationship between "spurious" DN and spectral radiance is likely to remain undefined. Fortunately, the AVHRR/3 instrument (due for launch aboard NOAA-K in September 1995) will have an A/D circuit designed such that over-range signals are all mapped to 0 counts (Roy Galvin, personal communication). It is therefore unlikely that non-zero saturation will affect these instruments.

DAY-TIME IMAGES					NIGHT-TIME IMAGES			
Pnad.	NZS	Image Date	Image Time	Cloud?	Pnad.	NZS	Image Date	Image Time
13	47	04/01/92	1328		891	46	03/05/92	0318
21	47	03/03/92	1335		905	46	09/02/92	0311
61	47	07/02/92	1329		907	46	22/05/92	0315
147	47	26/12/91	1332		921	46	11/05/92	0322
201	47	30/01/92	1323		925	46	06/01/92	0309
231	47	23/04/92	1330		927	46	20/12/92	0309
259	47	06/02/92	1341		937	46	30/03/92	0321
289	47	04/03/92	1323		941	46	17/02/92	0317
297	47	03/01/92	1339		947	46	24/04/92	0324
431	47	11/01/92	1346		951	46	31/01/92	0317
505	47	24/04/92	1319		955	45	13/03/92	0322
557	47	02/01/92	1351		961	44	14/01/92	0316
601	46	09/02/92	1306	Cloud	965	46	28/12/91	0315
631	47	13/02/92	1359		967	45	07/04/92	0326
661	47	24/12/91	1356		969	45	25/02/92	0323
693	46	28/04/92	1411	Cloud	981	45	08/02/92	0323
703	47	25/04/92	1307		981	45	21/03/92	0327
747	47	15/12/91	1400		991	45	22/01/92	0322
751	47	01/01/92	1402		993	46	15/04/92	0331
809	44	14/05/92	1420	Cloud	993	45	10/05/92	0334
823	47	23/12/92	1407		995	45	05/01/92	0321
825	47	09/01/92	1409		1007	45	16/02/92	0329
883	46	14/12/92	1412	*	1013	43	23/04/92	0336
885	47	03/02/92	1416		1015	45	30/01/92	0329
887	47	31/12/91	1414					
915	47	24/04/92	1426					
925	47	13/05/92	1432					
935	47	08/01/92	1421					
953	46	26/04/92	1435					
961	44	16/01/92	1427					
979	44	02/02/92	1426					
985	47	30/12/91	1426					
995	45	07/01/92	1433					
1023	46	10/02/92	1434					

Pnad. = Position of lava flow field in the scan (given as pixels from nadir)

NZS = non-zero saturation DN observed for the image

* pass coincided effusion of 2 small, <1km long, flows prior to the main eruption.

Table 2.2. *NOAA-11 day- and night-time images acquired during the Etna 1991 to 1993 eruption, listed in order of increasing distance from nadir.*

2.6. Variations in non-zero saturation between images acquired by the same instrument

The histogram for NOAA-11, Figure 2.3c, shows a peak at 47, agreeing with the non-zero saturation level of 47 described for the 2 January 1992 image. However, this is a composite histogram for 60 images, and masks the fact that the level of non-zero saturation varies from image to image. This is demonstrated by Table 2.2, where the variation

appears to be related to one or more of the following four factors: distance from nadir, whether the image is acquired by day or night, dimensions of the heat source, and cloud contamination. Similar variations in the non-zero saturation level were also found by Setzer and Malingreau (1993). The level of the non-zero saturation DN seems to be determined by factors other than simply the intensity of the heat source.

2.7. Conclusion

It appears that the design of the AVHRR/1 and AVHRR/2 A/D circuits causes the thermal channels to saturate at a non-zero level, a problem which has affected all the AVHRR detectors to date. Until the sensor is tested on a calibrated high temperature target, channel 3 DN of less than or equal to the non-zero saturation levels for areas of high temperature sources must be assumed to relate to a minimum feasible radiance for the pixel[a].

2.8. Acknowledgements

A.J.L. Harris is supported by a PhD grant from the Open University. We are grateful to Peter Bayliss and the NERC Dundee ground station for supplying the AVHRR data used in this study, and to Roy Galvin (ITT Aerospace), Dr. Nagaraja Rao (NOAA/NESDIS) and Katherine Kidwell (NOAA/NESDIS) for their valuable advice.

---

[a]The use of saturated data in quantitative analysis

When radiance from the surface reaches or exceeds the AVHRR saturation point (i.e. at the radiance equivalent of DN=0), the maximum radiance that the instrument is capable of recording is given (Figure 2.4). Therefore, the same radiance will be given whether surface radiance equals the saturation level or greatly exceeds it. For example, converting radiance to temperature, if the saturation temperature is 50 °C and the temperatures for two pixels are 50 °C and 1000 °C respectively, a temperature of 50 °C will be given for both pixels. Saturation radiances must therefore be regarded as the minimum possible for a pixel, and since it is likely that actual surface radiance is greater than the saturation radiance, cannot be trusted to

be a reliable measurement of true surface radiance. Consequently, such radiances should not be used for further quantitative analysis.

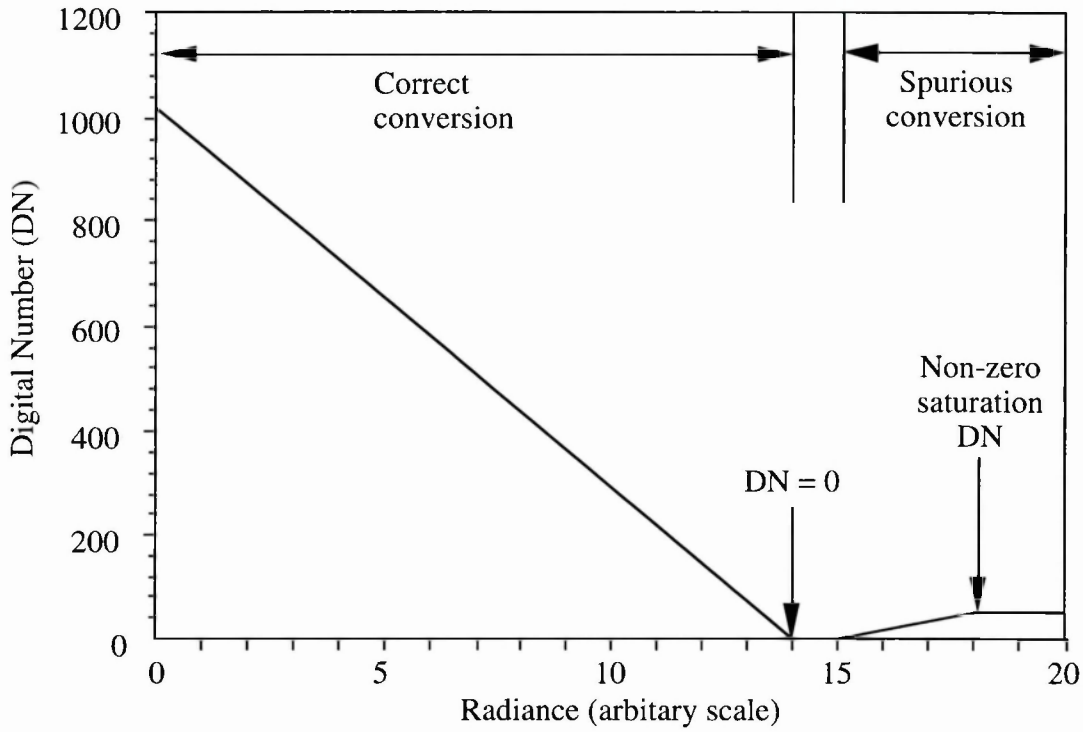

Figure 2.4. *Hypothetical conversion of DN to radiance taken from Setzer & Verstraete (1994). Two conversions exist: a correct conversion where decreasing DN convert to increasing radiance, and a spurious conversion where increasing DN convert to increasing radiance. There is currently no way of defining whether values falling within the DN range to which both conversions apply should be subject to the correct or spurious conversion. Radiances derived from DN within this range should therefore be regarded as saturated, thereby giving the minimum possible, and thereby untrustworthy, radiance for a pixel.*

Chapter 3. Automated thresholding of active lavas using AVHRR data

---

A.J.L. Harris, S.E.J. Swabey and J. Higgins

Published in the International Journal of Remote Sensing, 16(18), 3681-3686, 1995.

3.1. Abstract

An automated algorithm for thresholding hot pixels in AVHRR data is presented. The algorithm, applied to cloud-free sub-images of channel 3 minus channel 4 brightness temperature, compares each target pixel with its immediate background and then compares this difference with the natural variation in the surrounding region. Application to images of Mount Etna identified thermally anomalous pixels containing active lava or vents.

3.2. Introduction

Simkin and Siebert (1994) list 186 volcanic eruptions between 1990 and 1993, 32 of which resulted in fatalities or evacuations. Consequently, volcano monitoring is essential for civil protection as well as for scientific research. However, due to remoteness, inaccessibility or lack of funding, many volcanoes are wholly or partly unmonitored. Satellite data, being capable of providing a regular, synoptic view of all sub-aerial volcanoes, offer considerable benefits to volcano monitoring. These benefits, together with

the frequent repeat cycle, low data cost and near-real-time capabilities of the Advanced Very High Resolution Radiometer (AVHRR), make the AVHRR a valuable tool for volcano monitoring (Mouginis-Mark *et al.*, 1994; Harris *et al.*, 1995c). At the Alaskan Volcano Observatory observations of volcanic hot spots on AVHRR images within ~10 minutes of a satellite pass, and their inclusion in reports to various affiliated institutions (K. Dean, personal communication), have demonstrated how an AVHRR receiving station installed at a volcano observatory can be used for near-real-time volcano monitoring. Reliable automation of techniques increases the efficiency and rapidity of data analysis and information dissemination. We present an automated method for identifying hot pixels at a volcano, which is tested by comparing the results from images of the December 1991 to March 1993 eruption at Mount Etna, Sicily, with ground reports.

3.3. Automated hot pixel thresholding

Since the locations of most sub-aerial volcanoes are known (Simkin & Siebert, 1994), a sub-image covering the volcano of interest can be extracted from the image to minimise processing. For Etna a 50x50 pixel sub-image centred at 37.73°N, 15.00°E would cover the ~32x43 km volcano. The threshold is then applied to the sub-image only.

The threshold must be able to distinguish between solar heated and volcanic thermal anomalies. This is a problem over inactive unvegetated lava, where solar heating can elevate temperatures above the channel 3 (3.55 - 3.93 μm) and 4 (10.3 - 11.3 μm) saturation levels. During field-work in June 1994 at Mount Etna we measured surface temperatures >60 °C, compared with channel 3 and 4 saturation temperatures of ~49 °C. This may result in confusion. For example, three pixels, one filled by a solar heated surface at a uniform 43.8 °C, one containing a solar heated anomaly at 60 °C occupying 40% of the pixel, and one containing active lava at 1080 °C occupying ~0.0047%, with the remainder of the pixel at 25 °C in each case, will all have identical channel 3 brightness temperature (T_3) of 43.8 °C. However, since channel 3 coincides with the peak spectral exitance from blackbodies at ~500 °C and channel 4 with that of blackbodies at ~0 °C,

channel 3 has greater sensitivity to sub-pixel hot spots compared with channel 4 sensitivity. As a result, channel 4 brightness temperature (T_4) for the three pixels given above are 43.8, 40.1 and 25.2 °C respectively. These three pixels can therefore be distinguished using $T_3 - T_4$ (=ΔT), which gives ΔT of 0, 3.7 and 18.6 °C respectively. Thus, we use ΔT to distinguish solar heated and volcanic anomalies, where, on cloud-free day-time images of Etna, we observe ΔT of ~1 to 8 °C for normal ground, including solar heated surfaces, and $\Delta T > 10$ °C for unsaturated pixels containing active lava. This relationship may fail for saturated pixels. In the above example, increasing the size of the lava flow to occupy 0.75% of the pixel gives T_3 of 224 °C and T_4 of 48 °C, however, T_3 now exceeds the channel 3 dynamic range, and so will saturate and show its maximum T_3 of ~49 °C, giving ΔT of ~1 °C.

Our automated thresholding technique[b] iteratively scans a cloud-free ΔT sub-image, comparing the ΔT for each pixel with its non-active background. The non-active background is described by ΔT_b, the mean ΔT of the other 8 pixels in a 3x3 pixel box centred on the target pixel. Pixels already flagged by the threshold and anomalously cold pixels often encountered at the down scan edge of a thermal anomaly, here termed sensor recovery pixels[c], are excluded from ΔT_b so that

$$\Delta T_b = \frac{\sum_{i=1}^{8} \Delta T_{a_i} - \sum_{i=0}^{n_f} \Delta T_{f_i} - \sum_{i=0}^{n_r} \Delta T_{r_i}}{8 - n_f - n_r} \qquad (3.1).$$

In which ΔT_{a_i} is the ΔT of adjacent pixel i, ΔT_{f_i} is the ΔT of adjacent flagged pixel i, ΔT_{r_i} is the ΔT of adjacent sensor recovery pixel i, and n_f and n_r are the number of adjacent flagged and recovery pixels respectively. Natural variation (ω) is then calculated using $\Delta T - \Delta T_b$ from pixels in a 3 to 5 pixel wide buffer immediately surrounding the sub-image. Wherever the difference between ΔT and ΔT_b is greater than the maximum natural variation around the sub-image (max|ω|) the pixel is flagged as "hot". At Etna flagged pixels are assumed to contain a high temperature volcanic feature.

The algorithm is scanned across the sub-image, working pixel-by-pixel down each column in turn. If the sub-image is scanned only once, pixels with ΔT which is elevated, but lower than that of the hottest pixels, may not be flagged. This is due to the influence of adjacent hotter pixels which have not yet been flagged and thereby excluded from Equation 3.1. The sub-image is therefore scanned iteratively with hot pixels already flagged in a previous iteration being excluded from subsequent iterations. This allows pixels at intermediate elevated ΔT to be included. The process is terminated when an iteration fails to flag any further pixels.

As shown in the above example, saturated pixels which are "hot" may be excluded due low ΔT. Therefore, pixels which are not flagged initially, but are saturated in channel 3 and adjacent to an already flagged pixel, are also flagged at the end of the first iteration.

The algorithm was tested on 90 images acquired during and after the 1991 to 1993 Etna eruption. Comparison with field reports and maps of activity at the lava flow field and summit craters allowed the accuracy of the results to be assessed. On all images, pixels containing active lava flows and summit craters were located, and solar heated anomalies discounted, Figures 3.1a to 3.1c. The first iteration, plus adjacent saturated pixels, gave a pixel area in agreement with the position, shape and size of the anomalies expected from field reports (Calvari *et al.*, 1994a). Subsequent iterations identified peripheral pixels, and gave too large an area. For example, maps of the flow field given by Calvari *et al.* (1994a) suggest a ~8x3 pixel thermal anomaly between January and May 1992. On images acquired during this period, the first iteration approximates these dimensions, but subsequent iterations give too large an area, Figure 3.1a. We suggest that, at lava flow field pixels, the first iteration gives a reasonable indicator of lava pixels, subsequent iterations reveal pixels which appear hot because of the point spread function (falsely anomalous due to radiance being spread into them)[d]. During the eruption, changes in the size and shape of the flagged area match ground observations. Between January and May 1992 lava tubes fed surface flows from secondary vents ~5 km from the active fissure. At the end of May artificial

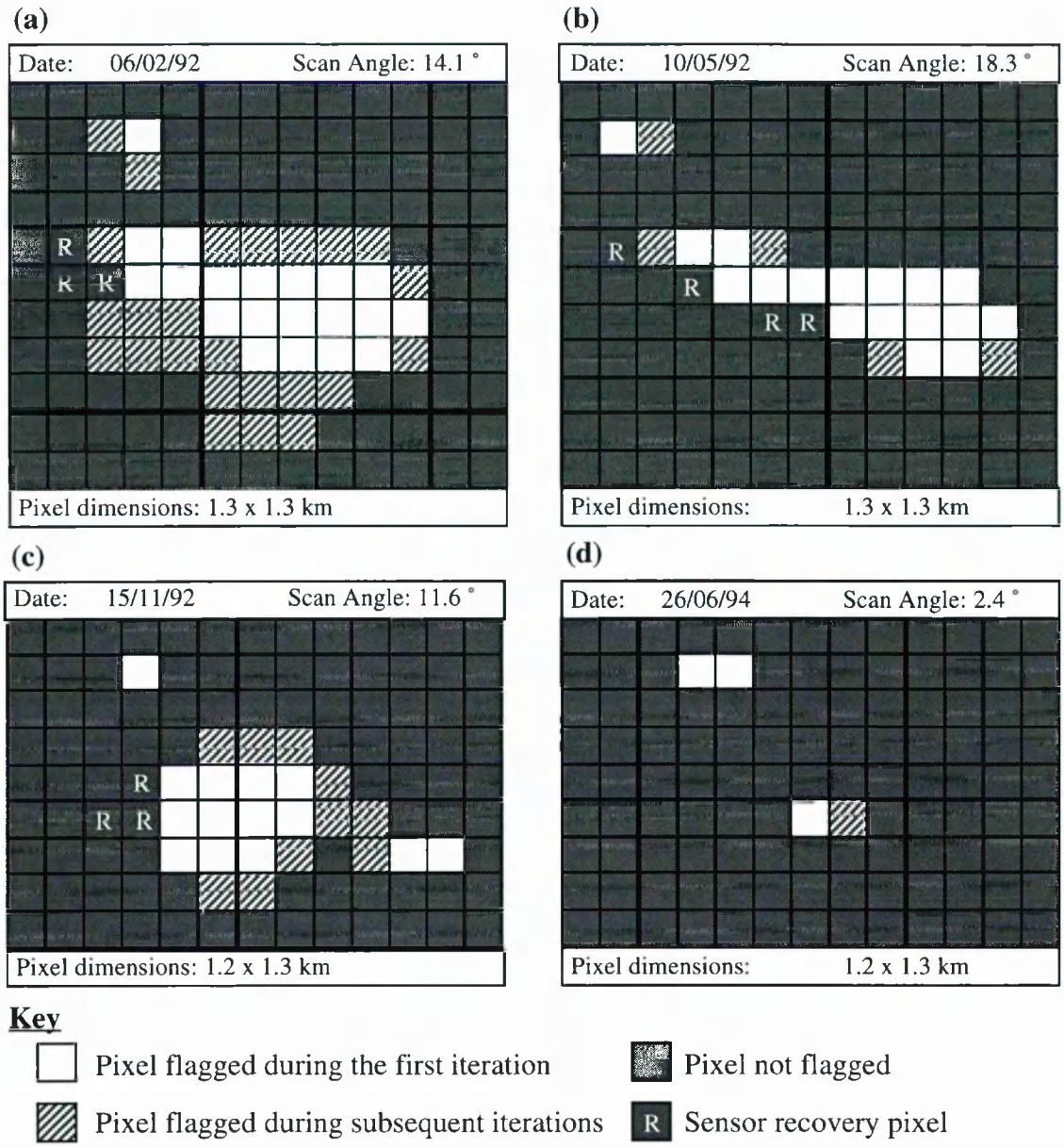

Figure 3.1. *Pixels flagged by the thresholding algorithm on cloud-free sub-images of Etna acquired during (a to c) and since (d) the 1991 to 1993 Etna eruption.*

diversion returned flows to within ~3 km of the active fissure, leaving the toe isolated and cooling ~6 km down flow (Calvari *et al.*, 1994a). The dimensions of the first iteration pixel areas between March and May 1992 (of which Figure 3.1b is an example), and between June 1992 and March 1993 (of which Figure 3.1c is an example), are consistent with these field reports. On all sub-images acquired during the eruption, pixels flagged to the NW of the main flow field locate the active summit craters, Figures. 3.1a and 3.1c, which were

occupied by high temperature degassing vents during June and October 1992 (J. B. Murray, personal communication).

Two anomalies are flagged on the post eruption sub-image, Figure 3.1d. The northern anomaly locates the summit craters, where we observed 3 degassing vents, ~10 m in diameter, at up to 340 °C on 27/06/94. The southern anomaly coincides with the inactive cooling 1991 to 1993 flow field. Although lava flow ceased 14 months prior to this image, we measured temperatures up to 221 °C from widespread fissures on the still cooling flow field on 23/06/94.

3.4. The effect of clouds and fires

The presence of cloud, or volcanic plume, will have three effects: (1) the reflected contribution to the channel 3 radiance will increase ΔT and may set max|ω| too high, thereby excluding some lava pixels; (2) cloud within the threshold area will elevate ΔT causing cloudy pixels to be flagged; and (3) thick cloud will mask anomalous pixels entirely. The algorithm must therefore be applied to cloud-free or cloud masked sub-images only. Where channel 3 radiance shines through thin or partial cloud cover lava pixels can be located. However, cloud contamination will cause "false flags". Flagged cloud pixels can be distinguished from lava pixels using (1) time series analysis, (2) T_3, where lava pixels usually have much higher T_3 than cloud pixels, or (3) a cloud-mask (Figure 3.2).

Fires on the volcano flanks may also cause ΔT to be elevated. This will have two effects. (1) Hot pixels due to fires may cause false flags within the sub-image. (2) Inclusion of pixels containing fires when calculating max|ω| will set max|ω| too high and result in lava pixels being missed. Therefore a fire pixel correction can be applied to max|ω| using the frequency distribution for |ω|, Figure 3.3. This flags lava pixels which are initially excluded (compare Figures 3.1b and 3.3b).

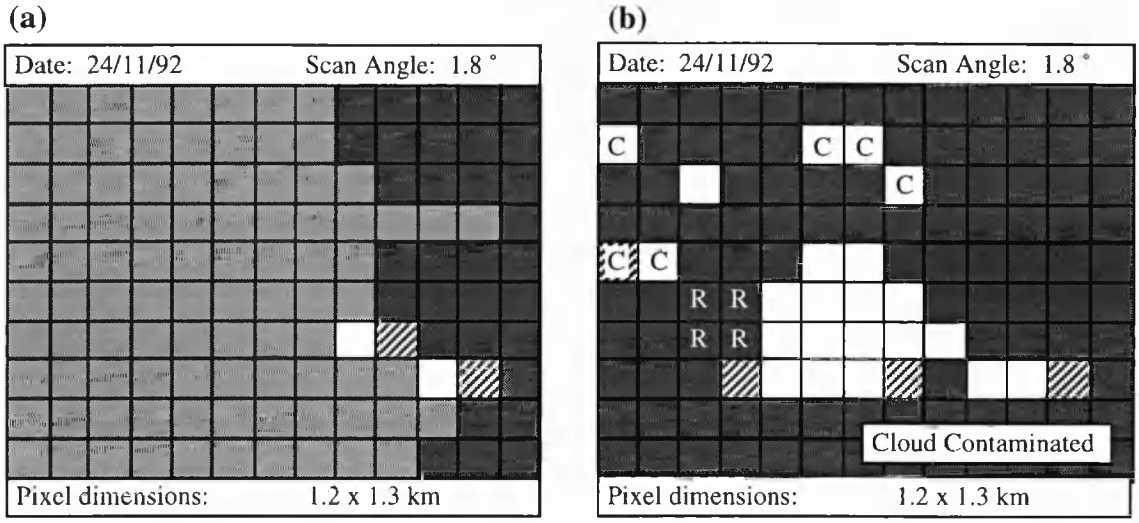

Figure 3.2. *Pixels flagged by the thresholding algorithm on a cloud contaminated sub-image of Etna acquired during the 1991 to 1993 eruption, with (a) cloud contaminated pixels masked and excluded (light grey), and (b) the cloud mask off, but with a "cloud contaminated" warning and false flags due to cloud (labelled "C") identified using time-series data and T_3. Cloud mask is set using Saunders & Kriebel (1988): if $R_2/R_1 > 1.6$ then pixel cloud contaminated, where R_2 and R_1 are the bi-directional reflectances in channels 1 (0.55 - 0.9 μm) and 2 (0.725 - 1.1 μm) respectively. Key as for Figure 3.1.*

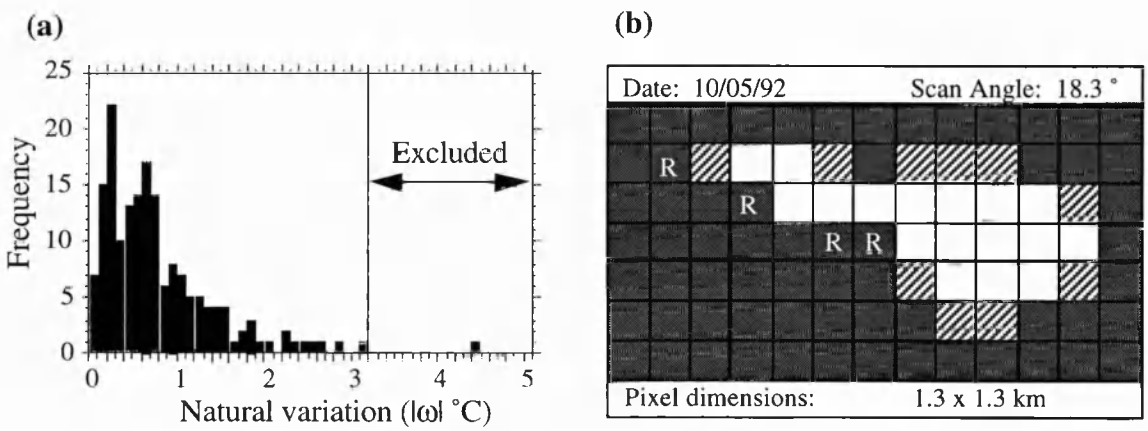

Figure 3.3. *(a) Fire pixel correction to max|ω| using the frequency distribution of |ω|. If max|ω| is significantly detached from the tail of the distribution then it is excluded and max|ω| reselected from the remaining values. (b) The result of applying this correction to the 10/05/92 sub-image.*

3.5. Conclusions

Tests on AVHRR data acquired for Mount Etna indicate that the automated thresholding technique is capable of identifying hot pixels containing active vents or lava, separating lava pixels from solar heated anomalies. Being automated the technique is time efficient, and could be applied for volcano monitoring, or fire detection, using AVHRR or similar data, such as that from the Along-Track Scanning Radiometer or the Moderate Resolution Imaging Spectrometer. Now that the technique is proven, we hope that volcano observatories and civil protection agencies will install such an algorithm in the data processing stream for cheap, frequently available satellite data.

3.6. Acknowledgements

Thanks to Peter Bayliss and the NERC Dundee ground station for supplying data, and to Peter Miller and Steve Groom at the NERC Plymouth Image Analysis Unit for calibration. Dave Rothery, John Murray and Anna Butterworth at the Open University, Ken Dean and Chris Wyatt at the University of Alaska Fairbanks, and Dr. John Price and a number of anonymous referees are gratefully acknowledged for their input. Andy Harris is supported by an Open University PhD studentship.

---

[b] Automated thresholding algorithm

See Appendix B for a further description of the automated thresholding algorithm.

[c] A definition of sensor recovery

Sensor recovery is the term given here for anomalously high DNs (low temperatures) which often occur at the down-scan edge of high temperature thermal anomalies in AVHRR data (Figure 3.4). I have only observed this effect in channel 3. Since sensor recovery has not been defined or examined in any other published study, I assume that sensor recovery is due to faulty response of the sensor down-scan of zones of anomalously high radiance. This faulty response typically affects between 1 and 2 pixels down-scan of the high radiance anomaly (Figure 3.4). Radiances derived from sensor recovery DNs will give a radiance resulting from faulty operation of the sensor, not the true surface radiance. Such data must therefore be

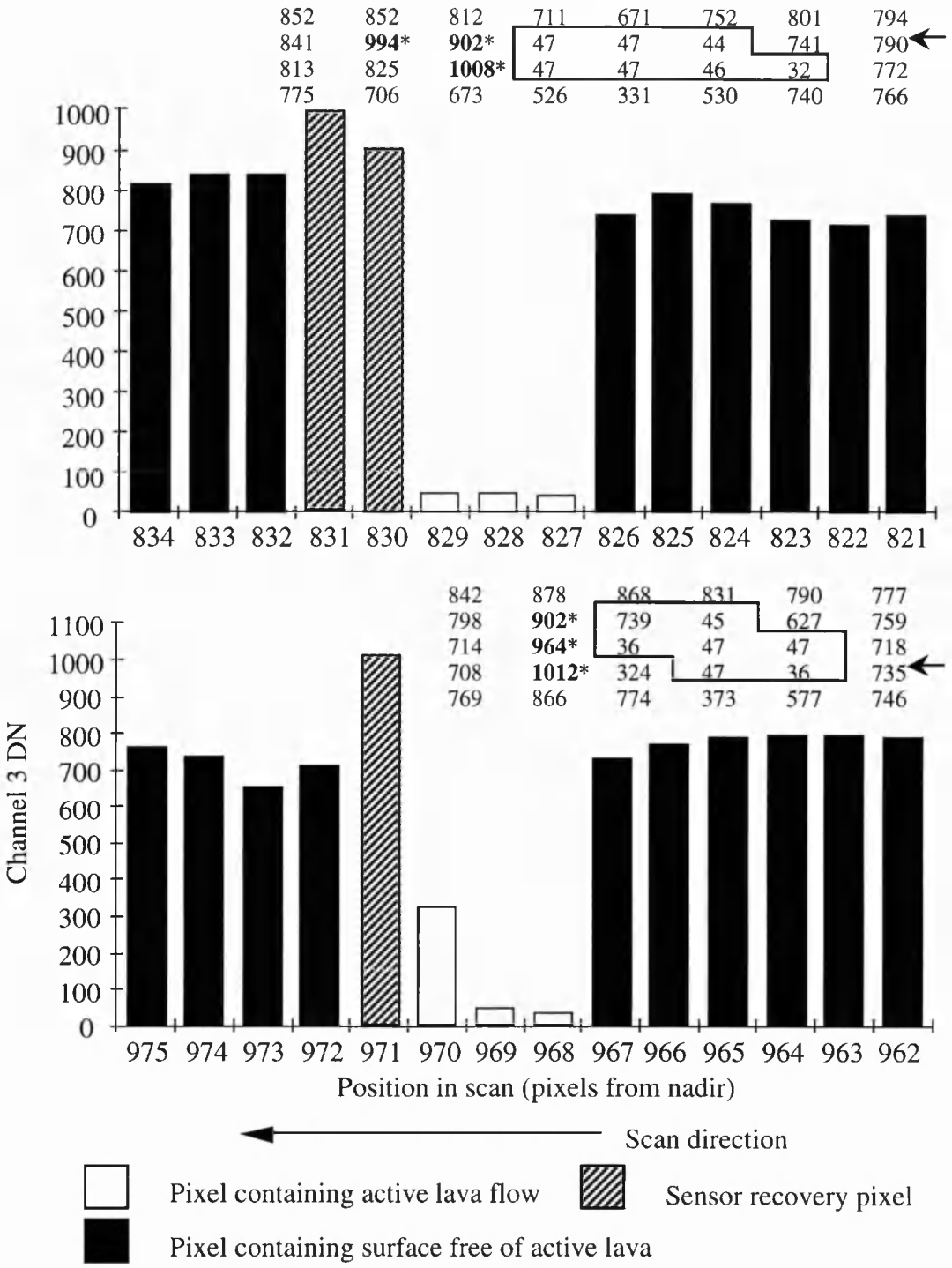

Figure 3.4. *Pixel DN transects taken from two images of Mount Etna acquired during December 1991 and January 1992 showing sensor recovery down-scan of pixels containing active lava flows. In both cases pixel maps of channel 3 DNs for a small portion of each of the images are inset. On each inset saturated DN are outlined, sensor recovery DN are marked by an *, and the scan-line along which the two transects have been taken given by arrows. Pixels containing active lava flows are marked by anomalously low or saturated DN, down-scan of which anomalously high DN associated with sensor recovery are evident.*

identified, masked and excluded from any quantitative analysis. Examination of 10 images of Mount Etna acquired during December 1991 and January 1992 showed that active lava flows caused a thermal anomaly of up to 7 pixels in length in the scan-direction; sensor recovery pixels occurred down-scan of the anomaly on 8 of these images. On the two images where no sensor recovery pixels were apparent, Etna was at the extreme edge of the scan. At the scan edge, greater pixel size (~6 x 2 km pixels, as opposed to ~1 x 1 km towards nadir) will cause the lava flows to occupy a smaller number of pixels (scan edge anomalies were just 2 pixels in length). The occurrence of sensor recovery pixels may therefore be related to the pixel size of the anomaly. Analysis of data for the summit vents at Etna and Stromboli between December 1991 and October 1994 revealed that sensor recovery pixels were not associated with these thermal anomalies (no image analysed showed sensor recovery). At Etna, pixels over the vent area would have contained between 1 and 4 ten metre wide vents at up to 350 °C. At Stromboli pixels would have contained between 5 and 15 four metre wide vents at up to 950 °C. Therefore the occurrence of sensor recovery also appears to depend on the size and/or temperature of the anomaly: small (less than ~100 m^2) and/or low temperature (less than ~350 °C) anomalies do not cause sensor recovery.

d The effect of pixel overlap and point spread function

Pixel overlap and the point spread function cause smoothing of any image and blurring of boundaries (Breaker, 1990; Mannstein & Gesell, 1991; Cahoon *et al.*, 1992). For the AVHRR, pixel overlap occurs vertically, horizontally and diagonally (Mannstein & Gesell, 1991), but the percent overlap remains essentially constant, at ~40%, in the scan direction (Breaker, 1990; Mannstein & Gesell, 1991). In the cross scan direction overlap increases from around 15% to 60% with increasing scan position (Cahoon *et al.*, 1992). Thus, volcanic radiance falling in the pixel over-lap will contribute to the pixel-integrated temperatures of each of the overlapping pixels. The Point Spread Function (PSF) describes the spread of radiance from a point source in a pixel into adjacent pixels. An ideal PSF would spread no radiance between pixels, however the PSF of actual systems is non-ideal, causing radiance to become spread between pixels (Breaker, 1990; Mannstein & Gesell, 1991). The PSF, estimated for the AVHRR by Breaker (1990) and Mannstein and Gesell (1991), will result in the spreading of radiance from a source of intense volcanic thermal radiance centred in one pixel into adjacent pixels which may not contain sources of volcanic radiance. Both effects will cause otherwise non-anomalous pixels to become falsely anomalous (Harris *et al.*, 1995c), and account for the spreading of radiance noted on AVHRR thermal imagery of volcanic activity at Mount Erebus (Oppenheimer, 1989; Rothery & Oppenheimer, 1994) and Krafla (Harris *et al.*, 1995c). Here, comparison of the channel 3 thermal anomaly caused by the 1991 to 1993 lava flow field at Etna with the dimensions expected from field reports, shows radiance to be spread into one, and occasionally two, pixels in all directions. This results in an over-estimation of the dimensions of the anomaly, and causes a ring of lower radiance pixels around a core of high to saturated radiances, where $R_b<R_r<R_c$ in which R_b are low radiances of the non-active background, R_r are PSF/overlap induced radiances at the anomaly periphery and R_c are high radiances of pixels containing active lava at the anomaly

core. This relationship means that core pixels are likely to be located by the first iteration of the algorithm and PSF pixels by subsequent iterations.

Chapter 4. Towards automated fire monitoring from space: semi-automated mapping of the January 1994 New South Wales wild-fires using AVHRR data

---

A.J L. Harris

Accepted for publication in the International Journal of Wildland Fire, 1996.

4.1. Abstract

The Advanced Very High Resolution Radiometer (AVHRR) is capable of providing low cost thermal data in which wild-fires can easily be detected. Data are available for large areas (~3000 x 6000 km) at least 4 times a day, and can be received directly by the user. An automated hot-spot detection technique inserted into the data stream could therefore provide timely fire information for wild-fire monitoring. Here such an automated technique is applied to AVHRR data acquired for the wild-fires that burnt extensive areas in New South Wales, Australia, during January 1994. The technique allows rapid production of fire maps. These revealed a number of major fires burning mainly within the National Parks, impacting on settlements and roads. Such a synoptic view of these fire events would be difficult to obtain using any other means.

4.2. Introduction

Between 27 December 1993 and 16 January 1994 an extended period of extreme fire weather resulted in excess of 800 fires in New South Wales (NSW), Australia. These directly affected 1.2 million hectares of bush land and, at one stage, closed all major roads out of Sydney. Extensive areas were affected particularly in the NSW National Parks, ~98% of the Royal National Park was burnt, and incursion into urban areas, including Sydney, resulted in 4 deaths, 24,864 evacuations and the loss of 188 residential properties (NSW Dept. Bush Fire Services, 1994). As a result of a build-up of flammable material in wild-lands due to changing land management practises, such fire events may become increasingly common and devastating (O'Hanlon, 1995). Consequently, danger to human activities, and effects on flora and fauna are likely to increase. This was illustrated by the October 1991 Oakland-Berkeley Hills fire, U.S.A., and the January 1994 NSW fires. The Oakland-Berkeley Hills fire destroyed or damaged 3,469 homes (Parker, 1992), and the NSW fires made considerable impacts on the environment, including the possible loss of two rare types of flora and severely affecting a local Koala colony (NSW Dept. Bush Fire Services, 1994). Timely detection of such events is extremely important for civil and environmental protection.

Remote sensing offers spatial data capable of detecting, monitoring and measuring fire events. Such data have been used to (1) estimate fire risk (e.g. Paltridge & Barber, 1988; Vidal *et al.*, 1994), (2) locate and measure fire areas in forest and savanna ecosystems (e.g. Matson & Holben, 1987; Langaas 1992; Cahoon *et al.*, 1992; Prins & Menzel, 1992; Kennedy *et al.*, 1994; French *et al.*, 1995; Kasischke & French, 1995; Langaas, 1995) and (3) estimate carbon dioxide and trace gas emissions (e.g. Kaufman *et al.*, 1990; Cahoon *et al.*, 1994). Here I address a fourth potentially valuable application of the data: near-real-time wild-fire monitoring for fire threat assessment. An automated fire detection technique, capable of rapid production of wild-fire threat maps, is presented and used to map the January 1994 NSW fires in relation to vulnerable human and natural features.

4.3. AVHRR for wild fire monitoring

The AVHRR is a scanning radiometer flown onboard the National Oceanic and Atmospheric Administration (NOAA) series of polar orbiting satellites. Data are available at a nominal resolution of 1 km in five channels located in the visible, near-infrared (IR), mid-IR and thermal-IR portions of the spectrum: channels 1 (0.58 - 0.68 μm), 2 (0.725 - 1.1 μm), 3 (3.55 - 3.93 μm), 4 (10.3 - 11.3 μm) and 5 (11.5 - 12.5 μm) respectively.

This spectral resolution offers considerable benefits to fire monitoring. Channels 1 and 2 provide data capable of detecting, monitoring and measuring smoke emissions (Kaufman *et al.*, 1990; Khazenie & Richardson, 1993), but contain no thermal information. However, Kasischke and French (1995) have used a vegetation index calculated from channel 1 and 2 data to locate wildfires: by decreasing the vegetation index, fires are detectable from their fire scars in time series of vegetation index images. French *et al.* (1995) have used this approach to produce a state-wide map of forest fire locations for Alaska in 1990 and 1991. Channel 3 is extremely sensitive to sub-pixel hot spots. For example, a "cool" flame front at 1000 °C, just 5 meters wide and 10 meters long, against an unburnt background at 25 °C will give a channel 3 pixel-integrated temperature (T_3) of 42.2 °C. Thus, the channel 3 signal will be elevated anomalously above its background for fire pixels (Figure 4.1). As a result, this channel is capable of providing data in which fires can easily be detected (e.g. Dousset *et al.*, 1993; Chuvieco & Martin, 1994). Channels 4 and 5 are far less sensitive to sub-pixel hot spots. The fire described above would give a channel 4 pixel-integrated temperature (T_4) of just 25.2 °C, virtually indistinguishable from the background. As a result, fires are far less evident in channels 4 and 5 (Figure 4.1).

The different response of channels 3 and 4 can be used to distinguish between solar heated anomalies and fires (Kaufman *et al.*, 1990; Kennedy *et al.*, 1994). Solar heating of concrete, tarmac, soil or rock can cause hot spots in channels 3, 4 and 5. However, since such solar heated anomalies give similar T_3 and T_4, they can be distinguished from fires using T_3 minus T_4 (= ΔT), where ΔT will be more highly elevated over fires than over solar heated anomalies (Figure 4.2).

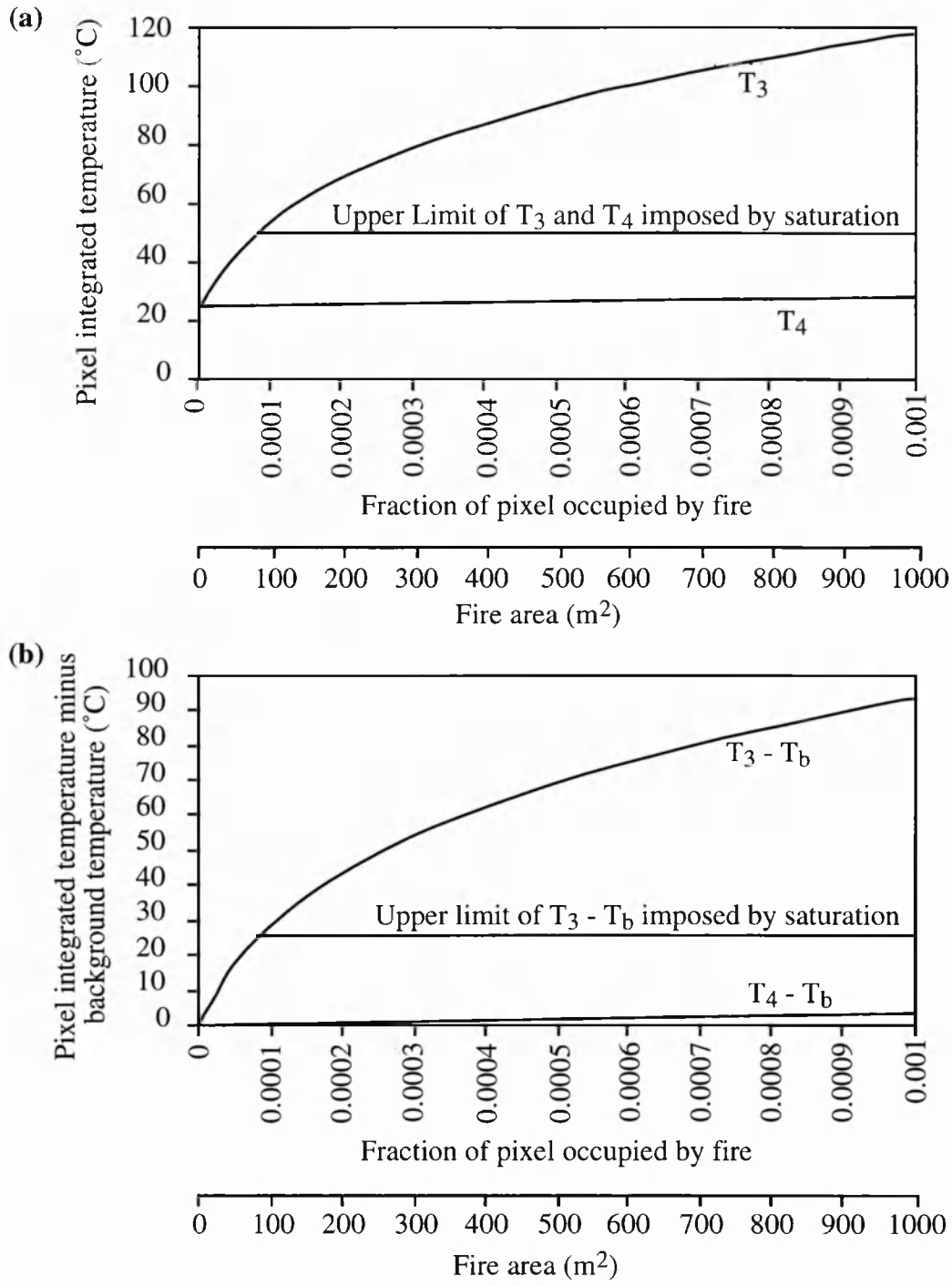

Figure 4.1. *Sensitivity of channels 3 and 4 to small sub-pixel fires. (a) Increase in channel 3 and channel 4 pixel integrated temperatures (T_3 and T_4) for a fire at 1000 °C of increasing size against a fire-free background at 25 °C. In reality, T_3 and T_4 will have an upper limit set by the saturation point of the sensor (~50 °C for the AVHRR). (b) Elevation of T_3 and T_4 above the background temperature (T_b) for the same fire conditions given for (a). The T_3 - T_b difference will have an upper limit set by saturation (in this case 25 °C).*

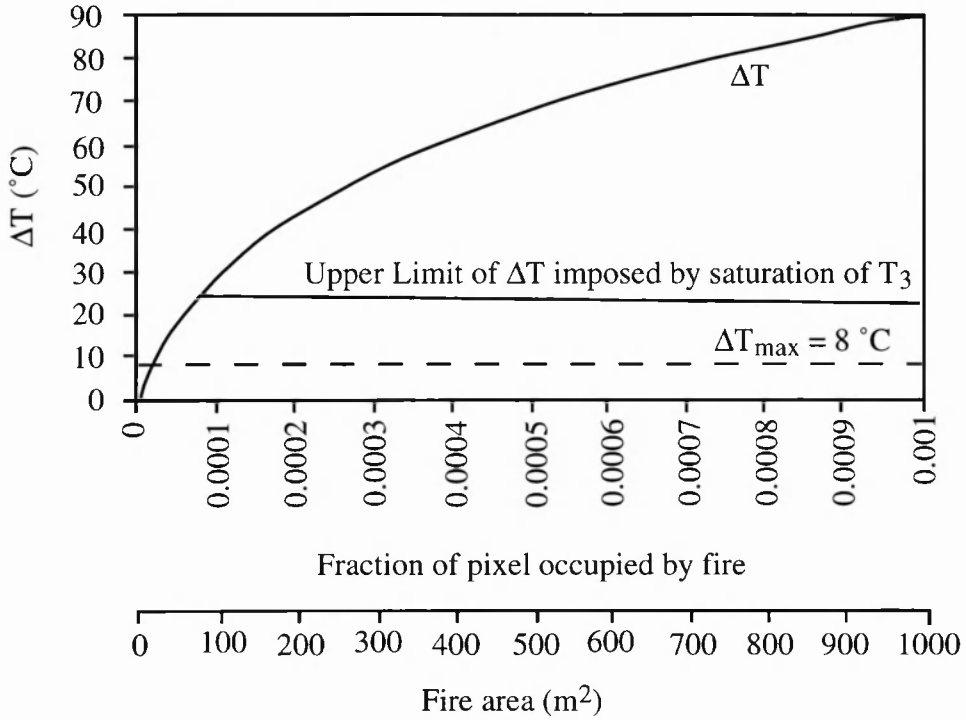

Figure 4.2. *Sensitivity of T_3 - T_4 (= ΔT) to the fire and background conditions given for Figure 4.1. In reality, ΔT will have an upper limit due to saturation of channel 3. At this point T_3 becomes constant at 50 °C. The fire will become distinguishable from the background when its ΔT exceeds the maximum ΔT for non-fire pixels (ΔT_{max}). A ΔT_{max} of 8 °C, obtained from an analysis of 90 images of Mount Etna (Sicily) acquired over an 18 month period, has been used.*

Four further benefits of the AVHRR for fire monitoring are its temporal resolution, image size, near-real-time capabilities and low cost. Each NOAA satellite has a return period of 12 hours at the equator. Since NOAA aims to keep two platforms in orbit at any one time separated by an interval of 6 to 7 hours, a minimum of 4 images a day will be available for any area. Images cover an area of 3000 x 6000 km for an overhead pass, allowing entire regions or countries to be monitored at once. These data are free and immediately available if access to a ground receiving station is possible. Installation of such a facility is relatively cheap, between US$ 4750 and US$ 20000 depending on sophistication. Since data can be viewed and analysed as they are received, near-real-time fire monitoring of large areas is possible. Full or partial automation of analysis will increase efficiency and cut time delays further, allowing fire reports within a few minutes.

To this end an automated fire detection algorithm has been developed and tested, which would be suitable for insertion into the AVHRR data stream at a ground receiving station.

A thorough review of thresholding techniques for fire detection using AVHRR thermal data is provided by Langaas (1995). Many of these use pre-defined temperature rules or thresholds: if the temperature for a pixel is above a defined temperature threshold, or set of thresholds, then the pixel contains a fire. Such an approach was taken by Chuvieco and Martin (1994). They used a diurnal T_3 threshold of 44 °C, nocturnal of 22 °C, along with a forest mask to eliminate sun-heated soils, to produce fire growth maps from a summer AVHRR data set for a Spanish fire. Their results compared well with ground truth. Although successful when applied to the scenarios for which they are designed, such thresholds are region or season specific and will have to be re-defined accordingly. A summer threshold may fail in winter due to lower pixel background temperatures producing lower, possibly sub-threshold, pixel-integrated temperatures over fires. Pre-defined thresholds will also fail to take into account temperature variations across an image due, for example, to altitude, where higher altitudes will result in lower pixel background temperatures, reducing pixel-integrated temperatures over fires. To overcome these problems, contextual algorithms have been developed which use relative rather than absolute thresholds, locating fire pixels by comparing a pixel with its immediate background (e.g. Flannigan & Vonder Haar, 1986; Lee & Tag, 1990; Flasse & Ceccato, 1996). Such algorithms, being self-adaptive, are far more flexible and capable of application over a variety of regions and seasons.

Here I develop such a contextual approach to define whether the pixel is "hot" or not. My intention is to move towards a flexible, automated, globally applicable, algorithm.

4.4. Automated mapping of the January 1994 NSW fires using AVHRR data

On 5 January 1994 there were 150 fires out of control in NSW. This increased to 204 on 8 January when the most intense fire activity occurred. Thereafter fire weather

conditions progressively eased, such that by 16 January the fire fighting operations were scaled down (NSW Dept. Bush Fire Services, 1994). During this 12 day period, 12 cloud-free images are listed as available from the CSIRO Division of Oceanography, Hobart, Tasmania. Two of these images, acquired on 5 and 11 January 1994, were purchased in raw format. To reduce processing time, 200 to 300 km wide sub-images, including Sydney and Newcastle, were extracted from the full images. These were subsequently registered to a map projection to allow accurate spatial location of fires. This geometric rectification was carried out using nearest neighbour resampling to avoid changing any radiance values.

4.4.1. Fire detection algorithm

To locate fire areas automatically the data were run through an algorithm, written in C++, designed to locate pixels which are thermally anomalous because they contain a high temperature source. To distinguish between fire pixels and solar heated anomalies the algorithm is applied to the ΔT image (i.e. T_3 minus T_4). The algorithm calculates the difference in ΔT between a pixel and its immediate background (ΔT_{diff}). The immediate background is determined by centring a 3 x 3 pixel window on the target pixel and taking the mean ΔT of the 8 pixels which surround the target pixel in this window. The ΔT_{diff} is then compared with the sub-image natural variation. Natural variation is the maximum ΔT_{diff} for a fire-free portion of the sub-image, defined using a fire-screened 45 x 45 km area taken from the top NE corner of the sub-image. Fire screening was achieved by rejecting any pixels which were detached from the natural variation frequency distribution tail (Figure 4.3). If ΔT_{diff} is greater than natural variation, then the pixel is flagged as "hot". The algorithm is scanned across the image, working pixel-by-pixel down each column in turn. If the image is scanned only once, hot fire pixels, which are adjacent to even hotter fire pixels, may be not be flagged due to the influence of their higher temperature background. Therefore the image is scanned iteratively, with flagged pixels excluded from subsequent iterations, until no further pixels are flagged. Given the mean

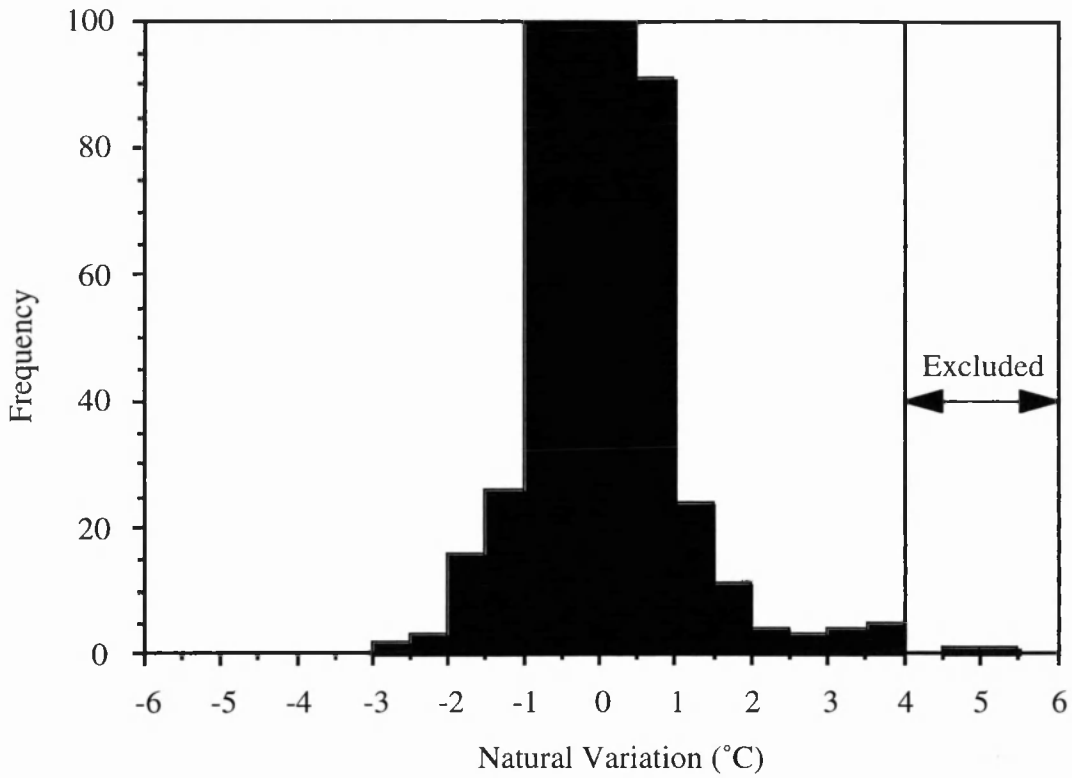

Figure 4.3. *Natural variation frequency distribution for the 5 January 1994 channel 3 sub-image. Pixels are taken from a fire-free portion of the sub-image. Selected pixels are also fire screened by excluding any value detached from the tail of the frequency distribution (natural variation is set to 4 in this example).*

non-fire pixel background temperature for the 5 January 1994 image of 26 °C, a fire temperature of 1000 °C, and a maximum natural variation of 8 °C (from Harris *et al.*, 1995b), theoretically, all fires occupying more than 0.002 % of a pixel should be detected (i.e. ΔT for the fire pixel will exceed 8 °C). For a 1 km^2 pixel, this gives ~20 m^2 as the smallest fire that can be detected using this technique (Figure 4.2).

The resulting fire image was fitted to a map of NSW, allowing the location of fires in relation to major settlements, roads and National Parks (Figure 4.4). Accuracy of fire location varied between 0 and 3 km across the image, and was estimated by overlaying the image with a map and comparing the distance between known ground control points on the

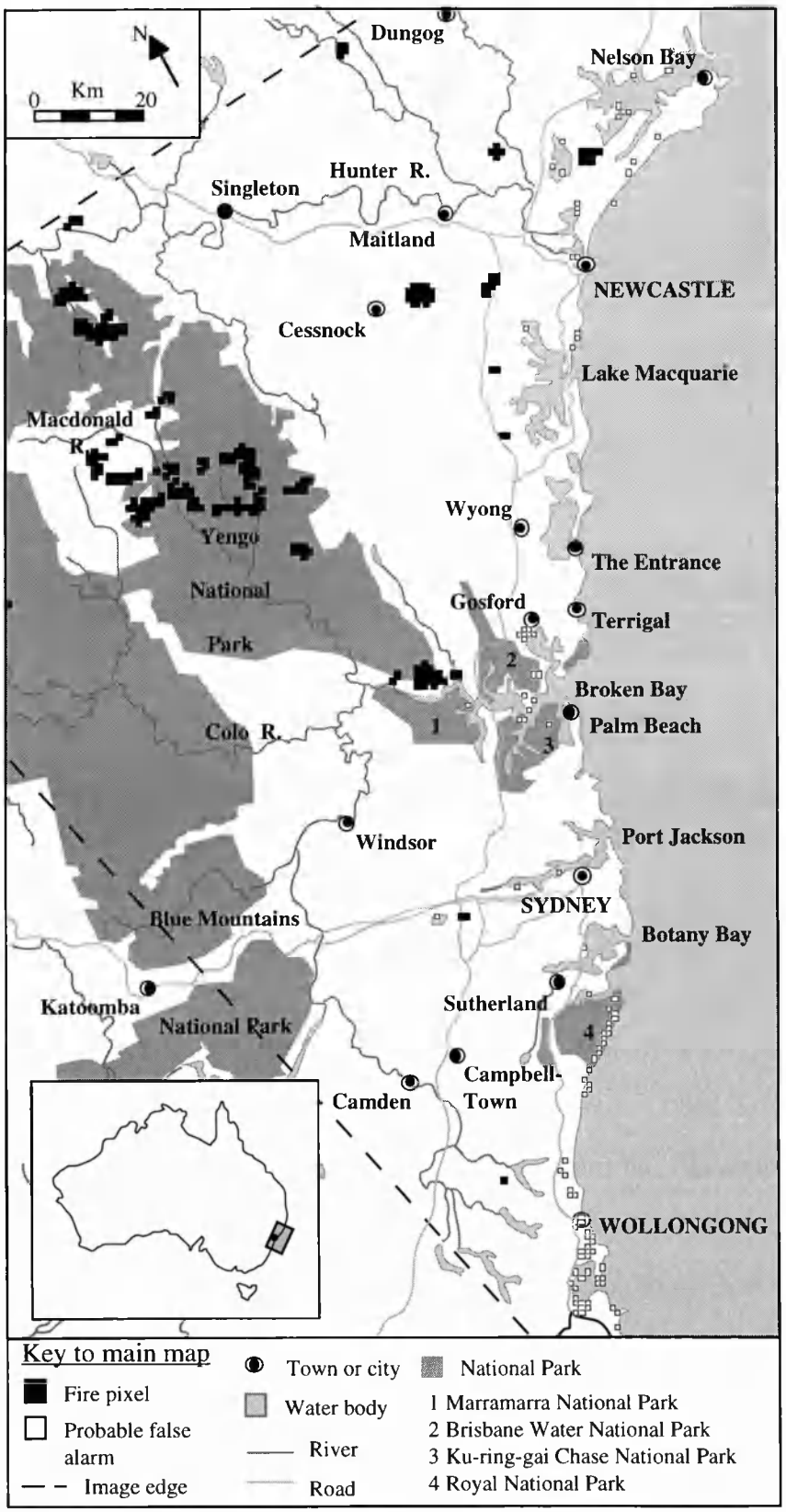

Figure 4.4. *Fire map for the Sydney region on 5 January 1994.*

image and the map. Operationally, automated geometric corrections are capable of 1 km accuracy (Peter Miller, personal communication).

4.4.2. Fire maps for 5 and 11 January 1994

Ground reports (NSW Dept. Bush Fire Services, 1994) spanning these two dates indicate that extensive fires occurred immediately west and north of Sydney. Although Sydney metropolitan fires contributed to most of the house losses, few attained significant size. Of note for their sheer size were a complex of fires north of Sydney, which eventually amalgamated into one continuous belt. A fire in the Blue Mountains also made two

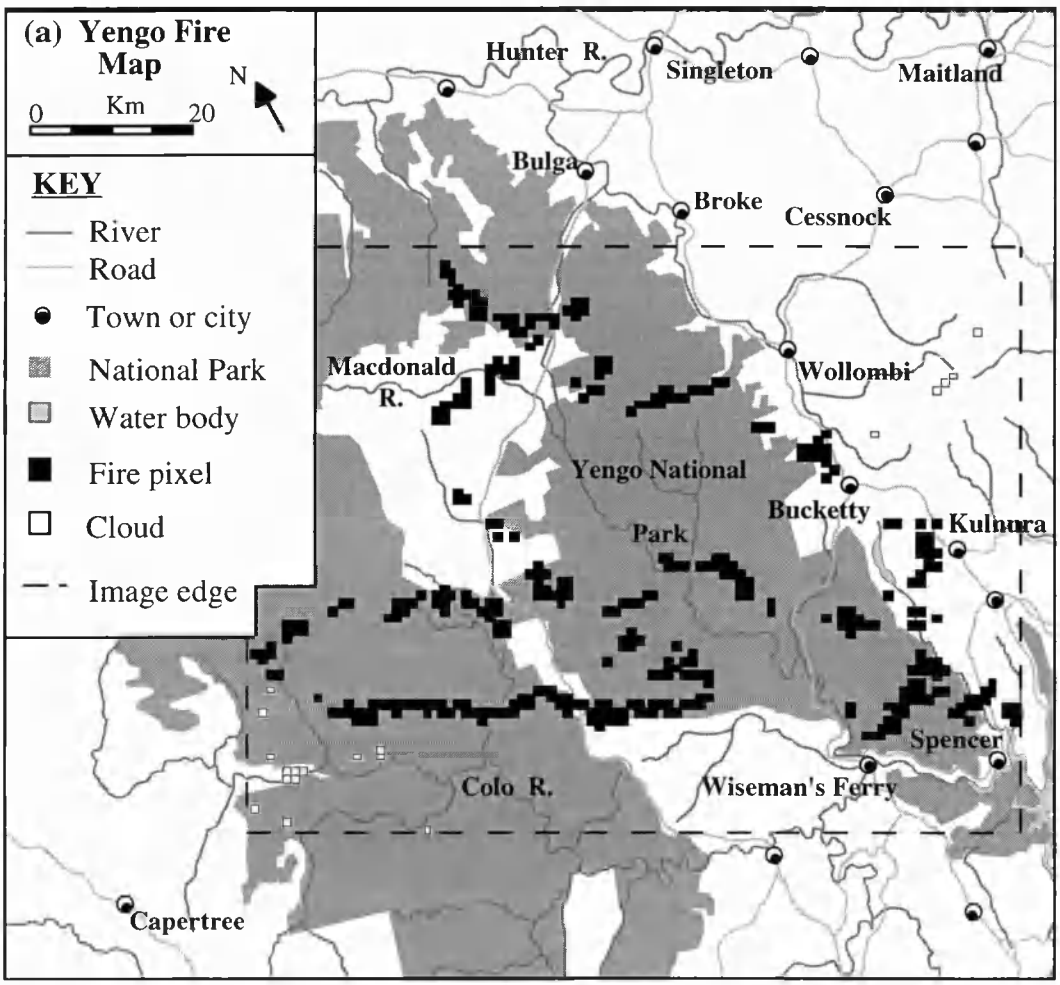

Figure 4.5. *Fire maps for (a) The Yengo National Park, (b) The Broken Bay area and (c) The Blue Mountains on 11 January 1994.*

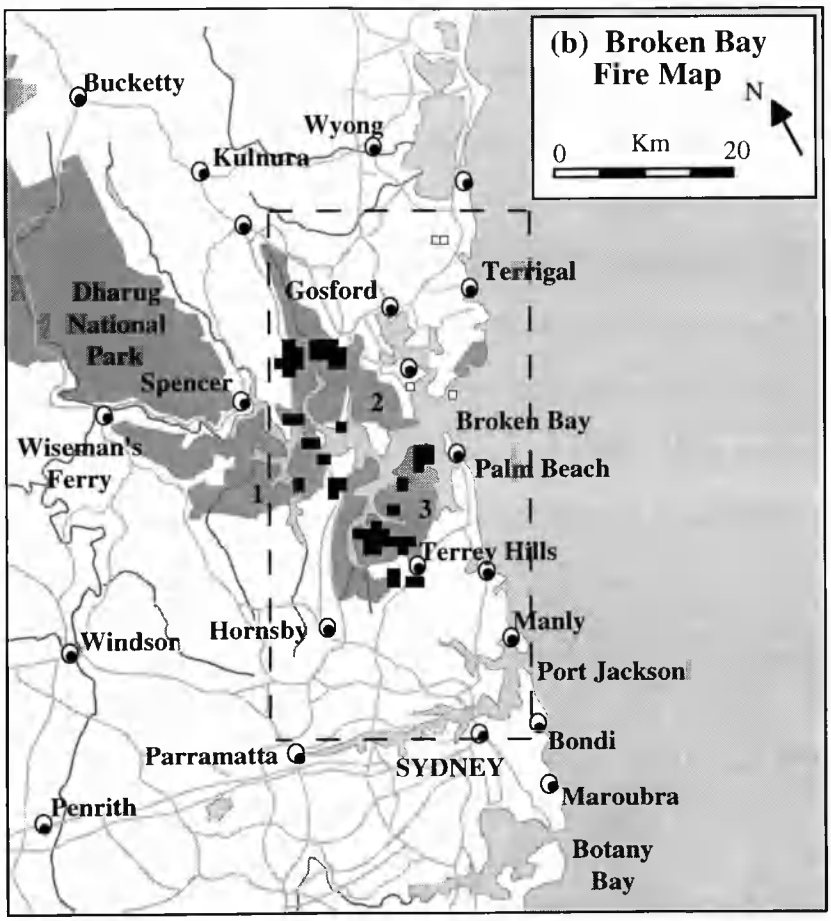
(b) Broken Bay Fire Map
N
0
Km
20
Bucketty
Wyong
Kulnura
Terrigal
Gosford
Dharug National Park
Spencer
2
Broken Bay
Wiseman's Ferry
Palm Beach
1
3
Terrey Hills
Manly
Windsor
Hornsby
Port Jackson
Bondi
Parramatta
SYDNEY
Maroubra
Penrith
Botany Bay

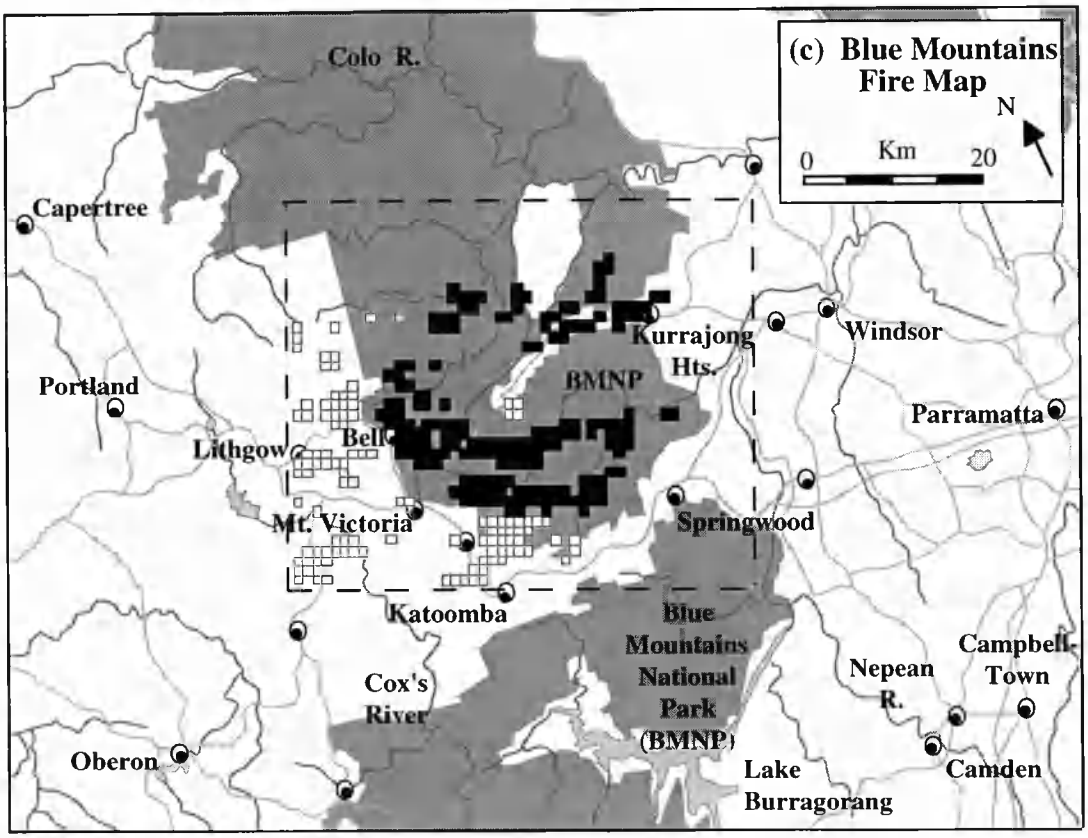
(c) Blue Mountains Fire Map
N
0
Km
20
Colo R.
Capertree
Kurrajong Hts.
Windsor
BMNP
Portland
Parramatta
Bell
Lithgow
Mt. Victoria
Springwood
Katoomba
Blue Mountains National Park (BMNP)
Campbell-Town
Nepean R.
Cox's River
Oberon
Lake Burragorang
Camden

successive major runs under north-south-westerly winds on 7 January and slightly more westerly winds on 8 January (NSW Dept. Bush Fire Services, 1994).

The 5 January and 11 January fire maps are in close agreement with these reported events (Figures 4.4 & 4.5). The 5 January fire map, although not covering all of the Blue Mountains, does show two major fire areas to the north of Sydney, (1) within the Yengo National Park, and (2) west of Gosford (Figure 4.4). A third area of scattered fires is located north and west of Newcastle. Noteworthy for their size are the arcuate, almost continuous, line of fires within the Yengo National Park (Figure 4.4).

On 11 January cloud prevented production of a fire map for the entire area, however fire maps were produced for three relatively cloud-free areas containing major fires: (1) The Yengo National Park (Figure 4.5a), (2) The Broken Bay area (Figure 4.5b), and (3) The Blue Mountains National Park (Figure 4.5c). These maps show a notable increase in the number, size and area of fires. Within the Yengo National Park fires form a number of arcuate, almost continuous lines, north-west of Spencer and Kulnura (Figure 4.5a). This map not only indicates extensive burning of the Yengo National Park, but also threats to Bucketty, Spencer and Wiseman's Ferry, and possible fire impacts along roads south-west of Bulga, north-west of Spencer, and north of Kulnura and Bucketty. A number of fires are evident scattered within the National Parks surrounding Broken Bay threatening Terrey Hills and roads between Gosford to Hornsby (Figure 4.5b). Within the Blue Mountains major fires are burning along continuous fronts south-east of Bell and Mt. Victoria and north-west of Kurrajong Hts., threatening these towns and roads linking them (Figure 4.5c).

4.5. False alarms: causes and solutions

Depending on the size of the image, the algorithm took between 0.4 and 13.4 seconds to run, and successfully distinguished between solar heated anomalies and fires. All fires located visually were located by the algorithm, but false alarms occurred over industrial, coastal and cloud-contaminated areas (Table 4.1).

Image	Image Size (pixels)	Run time (Secs.)	No. of fire pixels located	No. of false alarms	Reason for false alarm	% of pixels misclassified	No. of fire cluxters	Fires missed
05/01/94	48400	13.4	226	101	IHS, HRS	31	28	0
11/01/94								
Yengo	8000	2.2	399	14	C	3	49	0
Broken Bay	1600	0.4	51	4	C	7	14	0
Blue Mts.	2000	0.6	189	120	C	39	13	0
Total			639	138		18	76	0

IHS = Industrial Hot Spot, HRS = High Reflectance Surface, C= Cloud.

Table 4.1. *Summary of fire location results from applying the hot pixel thresholding algorithm to images acquired during the January 1994 NSW fires. Correct location of fire pixels, misclassifications and fires missed were assessed by comparing the algorithm results with a visual analysis of the images.*

Industrial false alarms will occur over high temperature industrial sources, such as steel mills or gas flares, which cause thermal anomalies in channel 3 (Matson and Dozier, 1981; Muirhead & Cracknell, 1984). These were particularly evident around the industrial centres of Wollongong and Newcastle (Figure 4.4). Coastal false alarms are a result of the channel 3 signal being composed of a reflected as well as a thermal component (Flannigan & Vonder Haar, 1986). This causes an apparent rise in T_3, but not T_4. Thus, over reflection anomalies such as white sand beaches, ΔT will be elevated. Industrial hot spots and coastal reflection anomalies were distinguished by placing a mask around all industrial centres and water bodies. All pixels flagged by the algorithm within the masked zones were given a possible false alarm warning (Figure 4.4). Clouds can also result in elevated ΔT and hence false alarms (Harris *et al.*, 1995b). This resulted in false alarms in cloud contaminated areas, for example on the 11 January image (Figure 4.5c). For this image cloud screening was carried out by manual inspection of the image, and possible false alarm warnings were given to fire pixels coincident with areas of cloud (Figure 4.5).

Inclusion of an automated cloud mask in the processing stream (e.g. Saunders & Kriebel, 1988; Gesell, 1989) would cut out this manual step.

Once false alarms had been identified and masked, counts for the total number of fire pixels and fire clusters, i.e. contiguous areas of fire pixels, were produced (Table 4.1). Between 5 and 8 January 1994 there were 150 to 204 fires out of control in NSW. Although conditions eased from the 9 January, fire counts remained high at around 200 until conditions moderated during and after 14 January (NSW Dept. Bush Fire Services, 1994). The fire pixel and cluster counts given in Table 4.1 straddle these ground estimates, but are spread over a wide range. This is not surprising since the pixel count figure will over-estimate the number of fires, with single fires spread over several pixels being counted more than once. Conversely, the cluster count will produce an under-estimate, where clusters containing a number of separate fires will be counted only once.

An easier to validate and reliable test of algorithm accuracy was obtained using 90 images of Mount Etna Volcano, Sicily, spanning all seasons. High temperature volcanic features such as active lava flows present ideal targets on which to test such an algorithm for two reasons: (1) they are far less transient than active fires and (2) accurate ground measurements for their dimensions are usually available against which the algorithm results can be compared. For all 30 x 30 pixel volcano sub-images, analysis was complete within 0.5 seconds, and all pixels containing active lava flows and relatively cool (340 °C) vents as small as 10 m^2 were located. All pixel areas defined were in agreement with the position, shape and size expected from field measurements made simultaneously with image acquisition (Harris & Rothery, 1995; Harris *et al.*, 1995b). Unfortunately no further fire images are available to this study. However, a similar contextual algorithm developed by Flasse and Ceccato (1996) has been tested on a range of ecosystems, detecting 90 % of all fires observed visually (Flasse & Ceccato, 1996).

4.6. Further applications: Local Fire Intensity Maps

As well as hazard monitoring, such fire location maps can be used as a starting point for further analysis. Data can be extracted and used for the production of fire statistics (e.g. Matson & Holben, 1987; Menzel *et al.*, 1991), temporal monitoring of fires (e.g. Langaas, 1992; Chuvieco & Martin, 1994) or estimation of trace gas emissions from fires (e.g. Kaufman *et al.*, 1990; Cahoon *et al.*, 1994). Here, I continue the fire location and monitoring application of the data by producing detailed fire maps for selected fires.

Two fire areas were located by the automated algorithm on the 5 January image burning in the north of the Yengo National Park just south of the River Hunter (Figure 4.4). For these two fires, the thermal data were extracted and used to produce a more detailed local fire intensity map (Figure 4.6). For a pixel containing a fire, the intensity of the thermal signal in channels 3, 4 and 5 will be a function of the size and temperature of the fire: the larger or hotter the fire, the higher the thermal signal or spectral radiance. Therefore a measure of fire intensity is possible using spectral radiance. Fire intensities were estimated using channel 4 spectral radiances, since the majority (33 out of 44) of the channel 3 fire pixels were saturated. First, the spectral radiance attributable to the fire alone was calculated. This was achieved by subtracting the fire-free channel 4 background radiance, estimated using the mean channel 4 radiance of the nearest fire-free pixels in any direction, from that of the fire pixel. The resulting channel 4 fire radiance image was then "sharpened" using the technique given by Harris *et al.* (1995c). Finally a fire intensity image was produced from the sharpened image. Fire intensity was calculated as a relative value, expressed in terms of a percentage of the maximum sharpened channel 4 fire radiance. Fire intensities were assigned a grey scale depending on their magnitude and fitted to a map of the local area (Figure 4.6).

The detailed local fire intensity map shows two fires overlapping the borders of the Yengo National Park to the south of Doyle's Creek and Apple Tree Flats (Figure 4.6). Using the approach given by Cahoon *et al.* (1992) the maximum possible areas for these two fires is estimated by summing the non-overlapping pixel areas for each of the fire

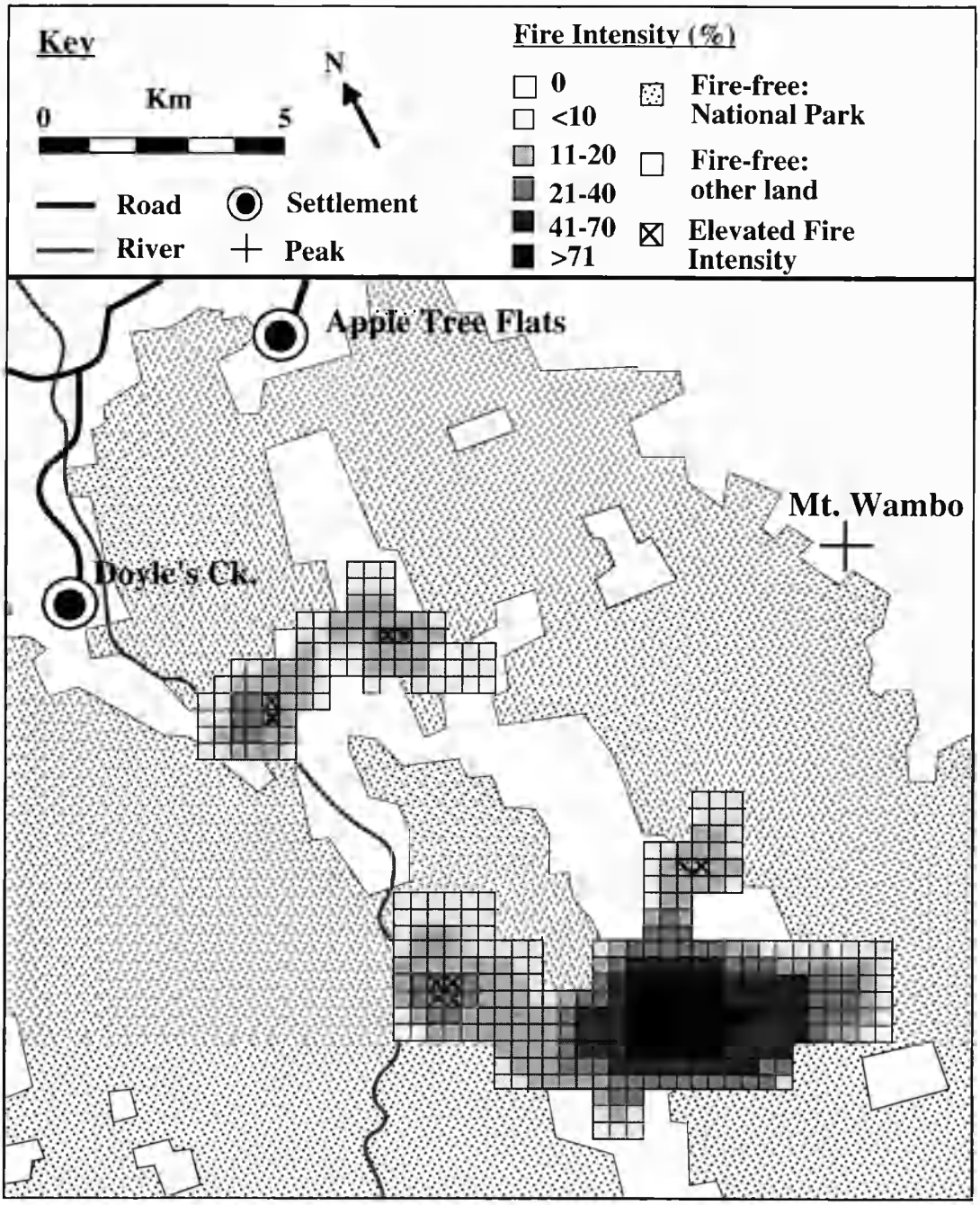

Figure 4.6. *Local fire intensity map for the two fires burning in the north of the Yengo National Park on 5 January 1994 (Figure 4.4).*

pixels located by applying the automated threshold on the un-registered (raw) image. This gives an area (including burning and recently burnt, but still hot, burn scar) of 9.6 km^2 for the northern fire and 30.8 km^2 for the southern fire. Analysis of the fire intensities show that highest intensities occur within the larger southern fire. However, plotting locations

where fire intensities are elevated above those of surrounding fire cells shows that a further four centres of lesser, but elevated, fire intensities exist (Figure 4.6).

Again, the transient nature of, and lack of detailed ground observations for, these fire events makes it difficult to assess the accuracy of this technique using fire data alone. However, application of the technique to data for active lava flows have produced thermal maps in close agreement with ground observations (Harris & Rothery, 1995; Harris *et al.*, 1995c), indicating that the spatial thermal structures identified are accurate.

4.7. Conclusions

The automated algorithm allowed the January 1994 NSW wild-fires to be located and mapped. The technique has also been successfully applied to an 18 month data set of 90 images containing active lavas at Mount Etna volcano. This indicates that the technique is regionally and seasonally flexible, and is capable of automatically locating and mapping hot spots in AVHRR data with reasonable accuracy. The NSW fire maps show the potential of this technique to monitor the threat posed by wild-fires to the environment. Including the algorithm in the data processing stream at an AVHRR receiving station could provide timely fire maps, allowing rapid targeting of potentially destructive wild-fires. This may be particularly useful for monitoring areas which are unmonitored by any other means, such as remote regions, or where large areas must be monitored at once. The aerial coverage provided by the AVHRR means that an entire region could be monitored at once from a centralised headquarters, and near-real-time information disseminated to local fire fighting crews. As well as fire monitoring, the output could serve as a starting point for the collection of fire statistics (e.g. fire counts or burning area estimates) or for further analysis (e.g. trace gas emission estimates).

4.8. Acknowledgements

Images used in this study were purchased using an award from the Remote Sensing Society sponsored by the National Remote Sensing Centre Limited (U.K.). The automated

thresholding software used was written by Jez Higgins (Jez U.K.) and Steve Swabey (O.U.). I am grateful to Anna Butterworth, Dick Carlton and Dave Rothery at the O.U. for their time and input. Thanks also to Sindre Langaas (GRID-ARENDAL), Chris Trevitt (ANU) and Peter Miller (NERC Remote Sensing Data Analysis Service, Plymouth University) for their help and advice. The author is funded by a PhD. grant from the Open University.

Chapter 5. A chronology of the 1991 to 1993 Etna eruption using AVHRR data: implications for real time thermal volcano monitoring

---

A.J.L. Harris, S. Blake, D.A. Rothery, and N.F. Stevens

Paper submitted to Journal of Geophysical Research, April 1995.

5.1. Abstract

Between December 1991 and March 1993 a continuous effusive eruption at Mount Etna built a 7.6 km^2 lava flow-field. Flows extended to within 1 km of the town of Zafferana before a successful artificial diversion was carried out higher up the volcano. During this eruption the space-borne Advanced Very High Resolution Radiometer (AVHRR) acquired 308 images on which the activity could be detected. Since these data can be freely and directly available, such coverage potentially allows regular, real-time monitoring. Ground observations and a flow map that we produced using a SPOT image and Electronic Distance Measurement allowed us to develop and test data extraction techniques. AVHRR radiance maps were consistent with known locations of surface activity. These documented the transition from channel- to tube-fed phases, the changing threat to Zafferana, and flow diversion. Quantitative analysis of the AVHRR data enabled estimation of active lava area, thermal flux, effusion rates and total flow field volume. Our

estimates for eruption rate and total flow field volume, 5.6 to 7.6 m^3/s and 220 x 10^6 to 300 x 10^6 m^3 respectively, are in agreement with trustworthy ground-based estimates of 5.8 m^3/s and 235 x 10^6 m^3. These correlations demonstrate the high degree of confidence that can now be placed in interpretations of AVHRR time series for eruptions where ground-based data are scanty.

5.2. Introduction

In October 1978 the first spacecraft in the TIROS-N series was launched carrying the Advanced Very High Resolution Radiometer (AVHRR) into a polar orbit (Table 5.1). Three years later Weisnet and D'Aguanno (1982) used a NOAA-6 AVHRR image of Mount Erebus to show how the sensitivity of channel 3 could be used to detect active lavas. However, attempts to use AVHRR data to analyse and monitor active lavas were not published until 1993 (Harris & Vaughan, 1993; Mouginis-Mark *et al.*, 1994; Harris *et al.*, 1995c). Lack of frequent data analysis and technique development are surprising for two reasons. Firstly, the return period of the TIROS-N satellites on which the AVHRR is mounted allows a cloud-free sub-aerial volcano to be imaged at least 4 times a day (Table 5.1). Secondly, the data are available to the user via direct down-link at relatively cheap receiving stations (Rothery, 1992; Rothery *et al.*, 1995).

A station installed during 1995 in Managua (Nicaragua) provides a good illustrative example of potential benefits. All hardware and software were installed for US$ 50,000, installation and training taking ~2 weeks (I. Downey, personal communication). Currently, daily analysis of Nicaraguan volcanoes is achieved visually, and during the November to December 1995 eruption of Cerro Negro image data were available to volcanologists within 30 minutes of acquisition (B. van Wyk de Vries, personal communication). These attributes make AVHRR data useful for regular real-time monitoring of volcanoes, particularly those that remain un-monitored from the ground due to financial, logistical or political problems (Tilling, 1989). Although for our study we used archived data from a

TIROS-N satellite series: periods of operation

Satellite	Launch date	Operational date range
TIROS-N	13/10/78	19/10/78 - 30/01/80
NOAA-6	27/06/79	27/06/79 - 05/03/83
		03/07/84 - 16/11/86
NOAA-B	29/05/80	Failed to achieve orbit
NOAA-7	23/06/81	19/08/81 - 07/06/86
NOAA-8	28/03/83	20/06/83 - 12/06/84
		01/07/85 - 31/10/85
NOAA-9	12/12/84	25/03/85 - 07/11/88
NOAA-10	17/09/86	17/11/86 - 16/09/91
NOAA-11	24/09/88	08/11/88 - 11/04/95
NOAA-12	14/05/91	14/05/91 - present
NOAA-13	09/08/93	09/08/93 - 21/08/93
NOAA-14	30/12/94	11/04/95 - present

TIROS-N satellite series: orbital parameters

Altitude:	833 km (NOAA -6, -8, -10, -12) or 870 km (NOAA -7, -9, -11, -13, -14)
Period:	101.58 minutes (833 km orbit) or 102.37 minutes (870 km orbit)
Repeat cycle:	12 hours (maintaining 2 satellites in orbit ensures a 6 hour repeat cycle)
Orbits per day:	14.18 (833 km orbit) or 14.07 (870 km orbit)
Equatorial crossing times (at launch)	02:30 and 14:30 (NOAA -7, -9) 01:30 and 13:30 (NOAA -11, -13, -14) 07:30 and 19:30 (NOAA -6, -8, -10, -12)

AVHRR sensor: band widths (μm)

Channel	TIROS-N	NOAA -6, -8, -10	NOAA-7, -9, -11,-12, -14	NOAA-13
1	0.55 - 0.90	0.58-0.68	0.58 - 0.68	0.58 - 0.68
2	0.725 - 1.1	0.725 - 1.1	0.725 - 1.1	0.725 - 1.0
3	3.55 - 3.93	3.55 - 3.93	3.55 - 3.93	3.55 - 3.93
4	10.5 - 11.5	10.5 - 11.5	10.3 - 11.3	10.3 - 11.3
5	Channel 4 repeated		11.5 - 12.5	11.4 - 12.4

AVHRR sensor: characterisitics

Scan angle from nadir:	±55.4 °
Total swath width:	~3000 km
Radiometric resolution:	10 bits (0 - 1024 counts)
Line rate:	360 lines per minute
Infrared channel NEΔT:	<0.12 K for 27 °C
Visible channel S/N:	3:1 for 50% reflectance
Infrared saturation:	~50 °C
Visible saturation:	100 % reflectance

AVHRR sensor: spatial resolution

Channel	1	2	3	4	5
IFOV (milliradians)	1.39	1.41	1.51	1.41	1.30
Ground resolution at nadir					
Along scan (km)	1.16	1.17	1.26	1.17	1.08
Cross scan (km)	1.16	1.17	1.26	1.17	1.08
Ground resolution at scan edge					
Along scan (km)	6.95	7.05	7.55	7.05	6.50
Cross scan (km)	2.48	2.52	2.70	2.52	2.32

(NEΔT - Noise equivalent differential temperature)
(S/N - Signal-to-noise ratio)
(IFOV - Instantaneous field of view)

Table 5.1. *Instrument characteristics of the NOAA AVHRR.*

remote receiving station, we believe that we have demonstrated ways in which data could and should be exploited in real-time.

Before AVHRR data can be used to monitor active lavas, data analysis techniques and results must be tested at volcanoes for which simultaneous ground observations are available. Harris *et al.* (1995c) used AVHRR data for the 1984 Krafla eruption coupled with ground observations to show how the AVHRR could provide reliable data for Iceland-style fissure eruptions. In this paper we perform a more thorough analysis of AVHRR data covering the 1991 to 1993 eruption at Mount Etna (Sicily) to show that reliable information regarding less-dramatic channel- and tube-fed flow fields can be extracted from AVHRR data.

5.3. The 1991 to 1993 Mount Etna eruption

The 1991 to 1993 Etna eruption, which began during December 1991 and continued until March 1993, built a 7.6 km^2 lava flow field (Calvari *et al.*, 1994a). Channel- and tube-fed flows extended 8.5 km down Etna's east flank to threaten the town of Zafferana Etnea (Figure 5.1). The eruption was well documented by ground observers. Detailed reports appeared monthly in the Bulletin of the Global Volcanism Network and an entire volume of the Italian Volcanological journal, Acta Vulcanologica (volume 4, 1994), is dedicated to the eruption. The wealth of ground observations for activity, flow area, temperatures, effusion rates and volumes makes this eruption an excellent test site for our evaluation of AVHRR data, although (as we specify later) even for such a relatively well-documented eruption there are some revisions and refinements to ground-based estimates suggested by our AVHRR data analysis.

One 10 m spatial resolution SPOT (Satellite Pour l'Observation de la Terre) panchromatic image of the flow field, acquired 28 months after the eruption had finished, was also available to us. This image was used together with results from two Electronic Distance Measurement surveys to map the flow field (Figure 5.1). Using this map and ground observations we define five major eruption phases. This differs from the five phase

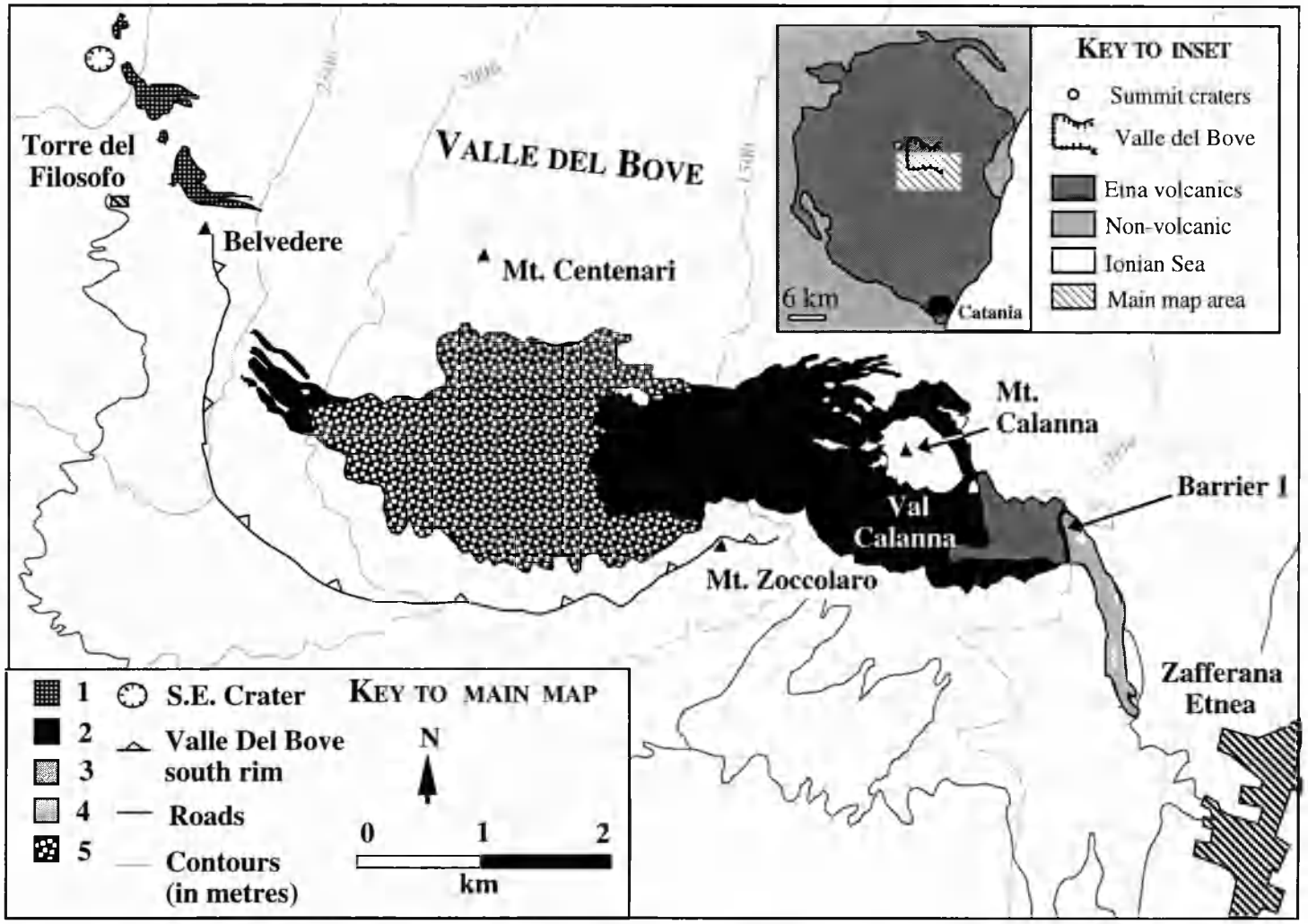

Figure 5.1. *The 1991-1993 flow field produced using EDM and a SPOT image, with lavas from each eruption phase overlain (labelled 1-5 in the key). In the upper flow field lavas from phase 5 cover earlier phase 2 lavas.*

Phase	Duration	Brief description
1	14 Dec 91	Short-lived lava fountaining along an eruptive fissure between the S.E. crater and Belvedere fed flows to the east
2	15 Dec 91 - mid-Jan 92	Predominantly channel-fed flows from a fissure in the W wall of the Valle del Bove extended eastwards into Val Calanna
3	mid-Jan 92 - 8 Apr 92	Tube-fed flows built up a lava flow field within Val Calanna behind a man-made containment barrier
4	9 Apr 92 - 29 May 92	Tube-fed flows overflowed the containment barriers and extended towards Zafferana Etnea
5	30 May 92 - 30 Mar 93	Following a man-made breach of the flow high in the Valle del Bove, flows remained confined within the Valle del Bove, building up a thick lava fan

Table 5.2. *Dates and descriptions of the five phases of activity during the 1991 to 1993 eruption at Etna.*

framework given by Calvari *et al.* (1994a) which applies to flow field development in the Valle del Bove only. Each phase in our framework is identified by changes in surface activity which should be detectable using 1 km resolution thermal data, i.e. major variations in location, area or dimensions of surface flows, or transition from channel- to tube-fed flows (Table 5.2 and Figure 5.1). This provides a reference-frame against which the AVHRR results can be compared.

5.3.1. Phase 1

Following a seismic swarm, an eruptive fissure opened between the S.E. Crater and the Valle del Bove during the early hours of 14 December 1991 (Falsaperla *et al.*, 1994). During this first phase of activity, 300 m high lava fountains fed flows extending

500 m eastwards until around 04:00 GMT on the same day (Calvari *et al.*, 1994a). This phase is identified as "the initial eruptive episode" by Calvari *et al.* (1994a).

5.3.2. Phase 2

The second phase began ~01:45 GMT on 15 December 1991, with lava effusing from the location where the fissure system extending from the S.E. Crater intersected the western wall of the Valle del Bove (GVN, 1991e). Flows, 200-600 m wide, extended 2 km during the first day, 4.5 km by 23 December 1991 and 5.5 km by 2 January 1992 (GVN, 1991e; Calvari *et al.*, 1994a). A Landsat Thematic Mapper image acquired on the 2 January 1992 revealed an extensive flow field, 6.5 km in length, fed by a 10-15 m wide channel (Rothery *et al.*, 1992). During January 1992 a containment barrier was constructed to impede the lava's probable path through Zafferana (Barberi *et al.*, 1993a; Barberi & Villari, 1994; Di Palma *et al.*, 1994).

This phase is divided into two by Calvari *et al.* (1994a), defining flow around the 0.5 km diameter Monte Calanna between the 3 and 10 January 1992 as a separate phase. Since it is not reasonable to expect these Monte Calanna flows to be identifiable in AVHRR data, we do not make this distinction. Hereafter, since activity remained confined to the Val del Bove flow field, our eruption phases agree with the flow-field development phases given by Calvari *et al.* (1994a), with some minor date differences resulting from discrepancies between those given by Calvari *et al.* (1994a) and those given by accounts referenced here.

5.3.3. Phase 3 and 4

Between mid-January and early-March open channels in the upper portion of the flow field progressively sealed up, forming a complex tube system which opened in the lower Val del Bove and Val Calanna feeding flows which built a flow field at the foot of Monte Zoccoloro and in Val Calanna (GVN, 1992a; GVN, 1992c; Calvari *et al.*, 1994a). Lava reached the base of the containment barrier, 2 km from Zafferana, on 14 March

(GVN, 1992c; Di Palma *et al.*, 1994). Phase 4 began on 8 April, when lava spilled over the containment barrier (GVN, 1992c). During this phase the tube system opened at secondary vents within Val Calanna feeding flows which breached three more barriers during April, destroying 2 houses, covering orchards and extending to within 800 m of Zafferana (GVN, 1992c; Barberi *et al.*, 1993a; Di Palma *et al.*, 1994).

5.3.4. Phase 5

Between 27 and 29 May the main lava tube wall high in the Valle Del Bove was destroyed using explosives. This diverted two thirds of the flow into an artificial channel. Total diversion was achieved by blocking the natural channel down-stream of the diversion (Barberi *et al.*, 1993a; Vassale, 1994). Within a few days molten lava was no longer evident in Val Calanna, with the active flow front 6-7 km from Zafferana and within the Valle del Bove (GVN, 1992f). The diversion marked the beginning of the final phase. During this phase, flows extended for no more than 1.5 km, and remained within the Valle Del Bove (Barberi *et al.*, 1993a; Calvari *et al.*, 1994a). By February 1993 overlapping flow units, fed by a forked lava tube, had built up a 2 km wide lava fan (GVN, 1993a). Lava stopped flowing on the south side of the flow field in mid-February 1993. During the second half of March flow declined on the north side. The last active flow was observed during the morning of 30 March 1993 (GVN, 1993b).

5.4. AVHRR data: temporal coverage, advantages over TM, and processing for volcano monitoring

The main spectral, spatial and temporal attributes of NOAA-AVHRR are given in Table 5.1. Data used here were obtained from the AVHRR archive at the University of Dundee (UK), which received images from 648 satellite passes during the eruption. Thermal radiance from the active flows could be detected on 308 of these (Figure 5.2), the remainder being useless because of cloud. This large number of volcano over-passes

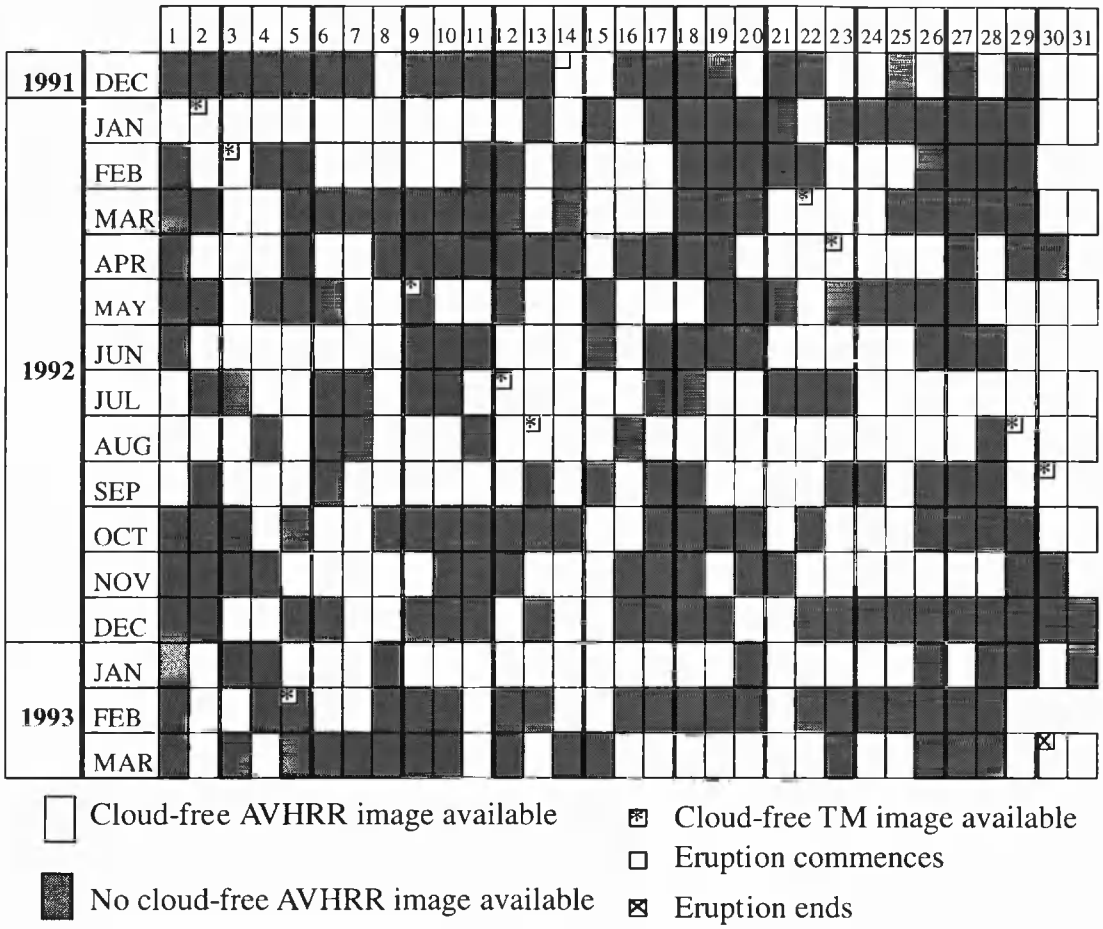

Figure 5.2. *Calendar indicating dates on which the 1991 to 1993 eruption could be detected on AVHRR and TM images.*

demonstrates the value of the AVHRR temporal resolution, allowing daily coverage of the volcano.

During the same period just 10 Landsat-Thematic Mapper (TM) images were available. Since TM data are available in three short wave infrared (SWIR) bands at 30 m resolution, they have been used extensively for quantitative analysis of active lava flows and domes (e.g. Rothery *et al.*, 1988; Pieri *et al.*, 1990; Bhattacharya *et al.*, 1993; Oppenheimer *et al.*, 1993; Flynn *et al.*, 1994; Andres & Rose, 1995). However, the return period of the Landsat spacecraft is 16 days, making even monthly coverage difficult when local weather conditions are taken into account. The percentage of eruption days on which

AVHRR and TM obtained cloud-free images are 52% and 2% respectively (Figure 5.2), highlighting the superior temporal resolution of AVHRR data.

Spectral radiance in AVHRR channels 3, 4 and 5, integrated across each image element or pixel, can be obtained using the calibration procedures given in Lauritson *et al.* (1988), Weinreb *et al.* (1990) and Kidwell (1995). We located pixels containing active lava flows using the automated thresholding technique given by Harris *et al.* (1995b). This technique has been shown capable of distinguishing true lava pixels from pixels at the periphery of the anomaly that are falsely anomalous due to radiance being bled into them from adjacent lava pixels. Bleeding of radiance is a result of pixel over-lap and the non-ideal point spread function of the sensor (Breaker, 1990; Mannstein & Gesell, 1991; Cahoon *et al.*, 1992). Inclusion of such falsely anomalous pixels would give an overly large anomaly pixel area, thereby inducing error, so we discounted these from our analysis. This typically excluded a 1 to 2 pixel wide zone at the periphery of the anomaly and gave an anomaly in agreement with the flow field dimensions (maximum of ~2 x 8 km).

5.5. Derivation of radiance maps

To allow accurate thermal mapping, images were fitted to a map of Sicily, using nearest neighbour re-sampling so as to preserve radiance values. Thermal radiance from the active lava source alone was then estimated in channels 3 and 4 for each pixel by subtracting the mean radiance of the nearest active lava-free pixels from that of the lava pixel.

Widespread saturation, i.e. a default value returned when radiance exceeded the maximum recordable by the sensor, of lava pixels in channel 3 made it impossible to map thermal radiance variations using this channel. However, saturation of channel 4 did not occur on any of the images analysed. This is due to differing sensitivity of these two channels to bodies at typical active lava temperatures, and results from the relationship

given by Planck's law defining radiance emitted by a blackbody as a function of temperature and wavelength:

$$H(\lambda T) = c_1 \lambda^{-5}[\exp(c_2/\lambda T) - 1]^{-1}, \quad \text{and} \quad L(\lambda T) = H(\lambda T) / \pi \qquad (5.1),$$

in which λ is wavelength, T is temperature, c_1 and c_2 are constants with values of 3.742 x 10^{-16} W m^2 and 1.4388 x 10^{-2} m K respectively and $L(\lambda T)$ is the planck function for isotropic radiation. Following the relationship given in Equation 5.1, although bodies at ambient temperatures emit less radiation in channel 3 than in channel 4, bodies at molten lava temperatures will emit more radiation in channel 3 than in channel 4 (Figure 5.3a). As a result, channel 3 becomes saturated very easily, whereas channel 4 remains un-saturated over lava bodies of greater size and temperature (Figure 5.3b). We demonstrate this by assuming the thermal surface predicted by Crisp and Baloga (1990) for a lava flow, with molten material exposed over 0.1 to 10% of the lava surface, and a representative saturation temperature of ~50 °C for both channels 3 and 4 (Table 5.1). If a pixel were occupied by such a flow, with the molten lava at a typical Etnean temperature ~1070 °C (Gauthier, 1973; Tanguy, 1973; Archambault & Tanguy, 1976; Smithsonian Institution, 1989), the remainder of the lava surface at 250 °C, and a lava-free background at 10 °C, channel 3 would reach saturation when the lava body occupied 0.09 to 0.8% of the pixel, but channel 4 would not saturate until it occupied 5.7 to 10%.

Therefore channel 4 lava radiances were used to estimate radiance from the lava source, and the weighted average method given by Harris *et al.* (1995c) was applied. The resulting radiance map was fitted to a topographic base-map of the east flank of Mount Etna, allowing interpretation in relation to topographic features, roads and towns (Figure 5.4). The accuracy of the radiance map to the base map fit has been kept to within 1 pixel, comparable with accuracies of 0.25 to 2 pixels achieved by published automated geometric correction algorithms (Ho & Asem, 1986; Cracknell & Paithoonwattanakij, 1989). The ±1

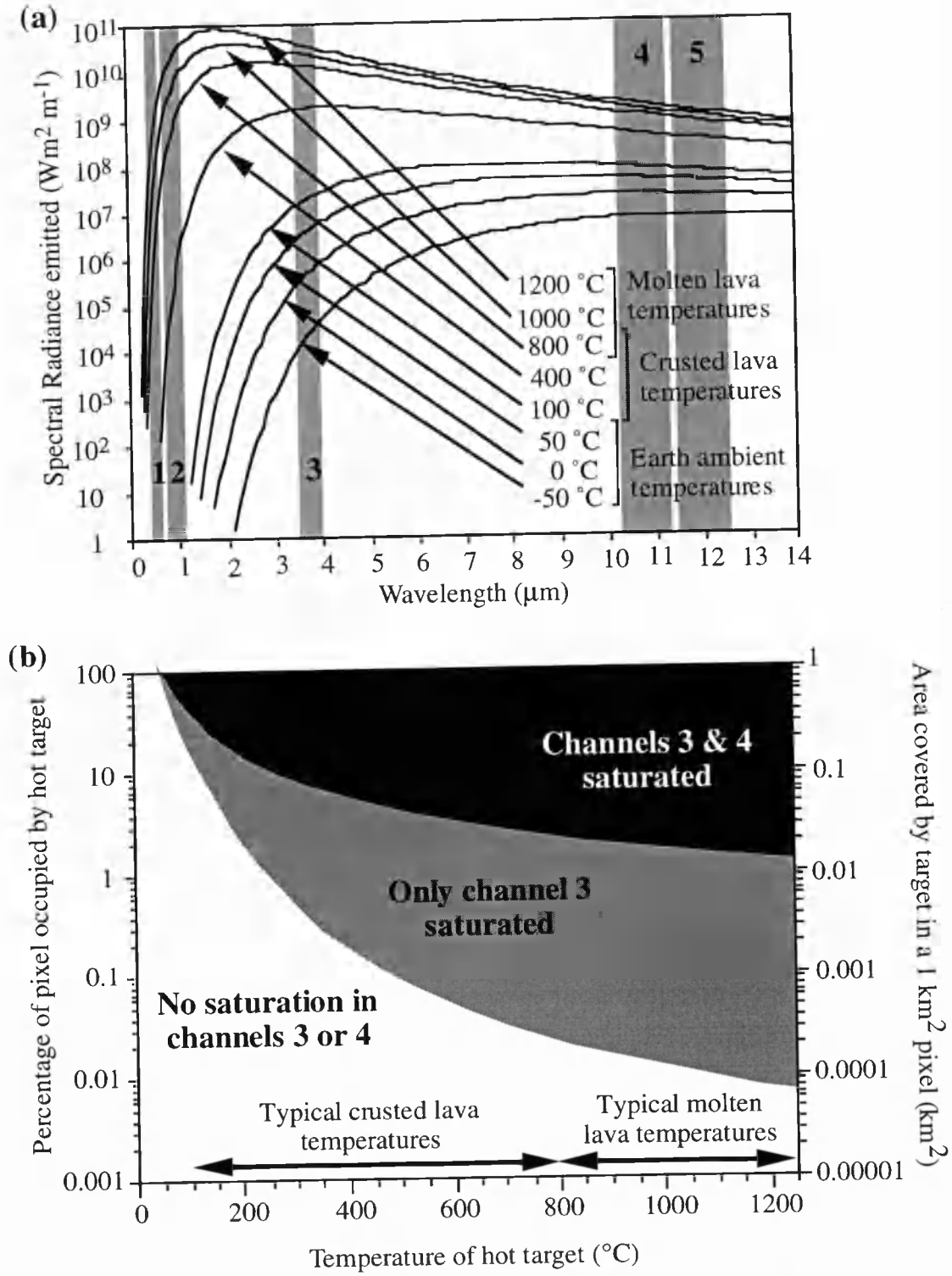

Figure 5.3. *(a) Planck curves for blackbodies at typical magmatic, active crusted lava and Earth ambient temperatures with the AVHRR wavebands shown in grey. (b) Size and temperature of a body necessary to saturate AVHRR channels 3 and 4.*

pixel maximum error results in some anomalous pixels overlapping the southern rim of the Val del Bove by between 0.1 and 1 pixel.

5.6. A chronology of the eruption using radiance maps

Comparison of Figures 5.4a to 5.4k with ground observations shows that these radiance maps identify and locate the main events in each of the eruption phases (Figure 5.1 and Table 5.2), as listed below. We do not claim that interpretation of each radiance map is possible in this detail using AVHRR data alone, merely that the AVHRR-derived radiance maps are consistent with ground reference data.

5.6.1. Phase 1

A cloud-free image obtained on 14 December 1991 showed an anomaly located west of the Central Craters (Figure 5.4a, inset). The anomaly, not being coincident with the Central Craters, and in any case considerably exceeding these in area, suggests association with lava effusion rather than active vents. Ground observations identify the anomaly as due to the lavas from phase 1 activity, which had begun ~12 hours before image acquisition.

5.6.2. Phase 2

A cloud-free image acquired the following day reveal a second anomaly centred on the SW floor of the Valle del Bove, with the phase 1 anomaly still apparent as a separate anomaly W of the Central Craters (Figure 5.4a). The size and location of the new anomaly is consistent with a second lava effusion, presumably beginning sometime during the 24 hours since the previous image. Ground observations confirm this to be coincident with the location of phase 2 lavas. Images acquired until early January (Figures 5.4b and 5.4c)

Figure 5.4. *Time series of radiance maps produced from AVHRR data illustrating the changing location of active flows during the 1991 to 1993 eruption[e].*

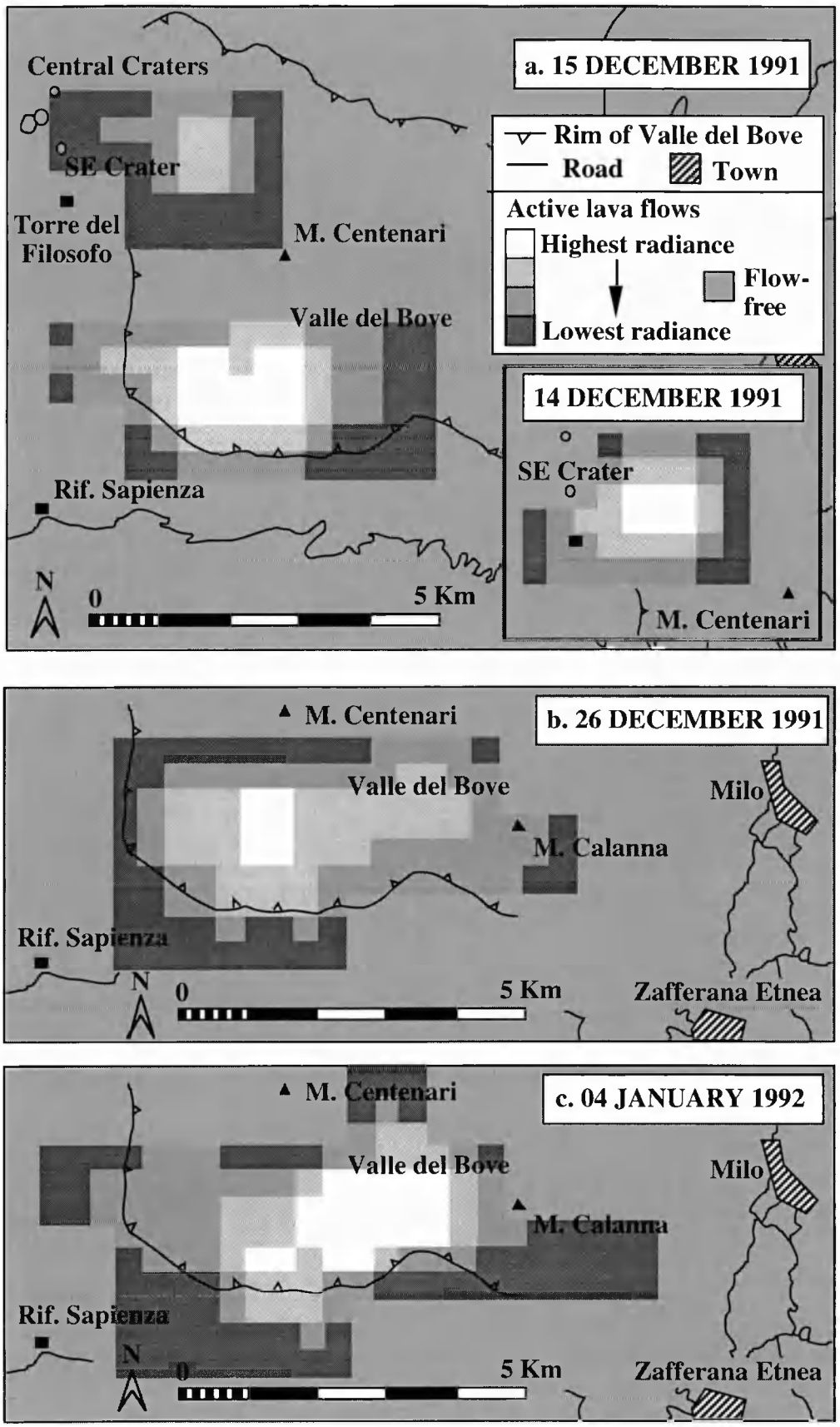
a. 15 DECEMBER 1991
Central Craters
SE Crater
Torre del Filosofo
M. Centenari
Valle del Bove
Rif. Sapienza
Rim of Valle del Bove
Road
Town
Active lava flows
Highest radiance
Lowest radiance
Flow-free
14 DECEMBER 1991
SE Crater
M. Centenari
N
0
5 Km
b. 26 DECEMBER 1991
M. Centenari
Valle del Bove
Milo
M. Calanna
Rif. Sapienza
Zafferana Etnea
c. 04 JANUARY 1992

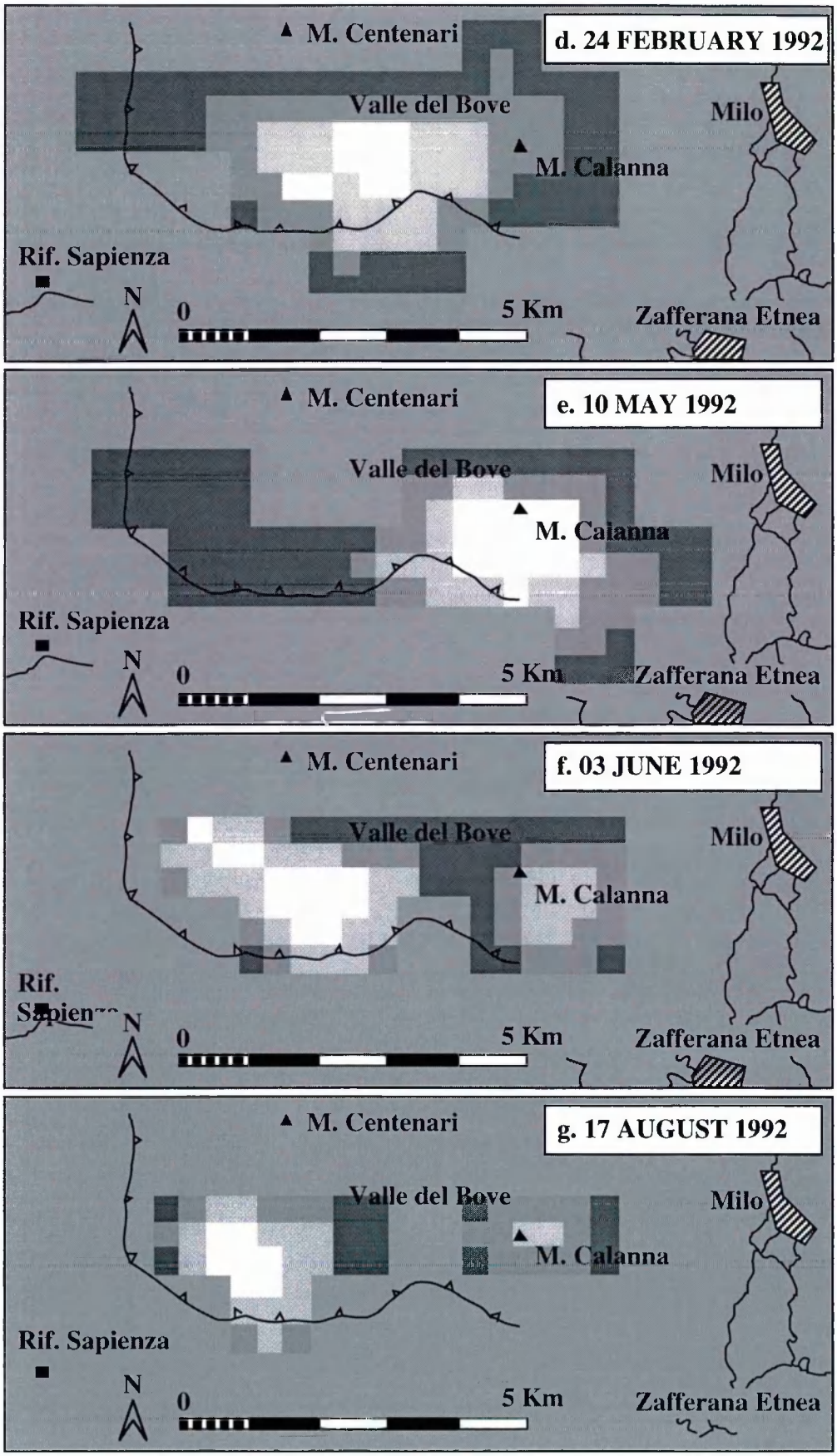
M. Centenari
d. 24 FEBRUARY 1992
Valle del Bove
Milo
M. Calanna
Rif. Sapienza
N
0
5 Km
Zafferana Etnea
M. Centenari
e. 10 MAY 1992
Valle del Bove
Milo
M. Calanna
Rif. Sapienza
N
0
5 Km
Zafferana Etnea
M. Centenari
f. 03 JUNE 1992
Valle del Bove
Milo
M. Calanna
Rif.
N
0
5 Km
Zafferana Etnea
M. Centenari
g. 17 AUGUST 1992
Valle del Bove
Milo
M. Calanna
Rif. Sapienza
N
0
5 Km
Zafferana Etnea

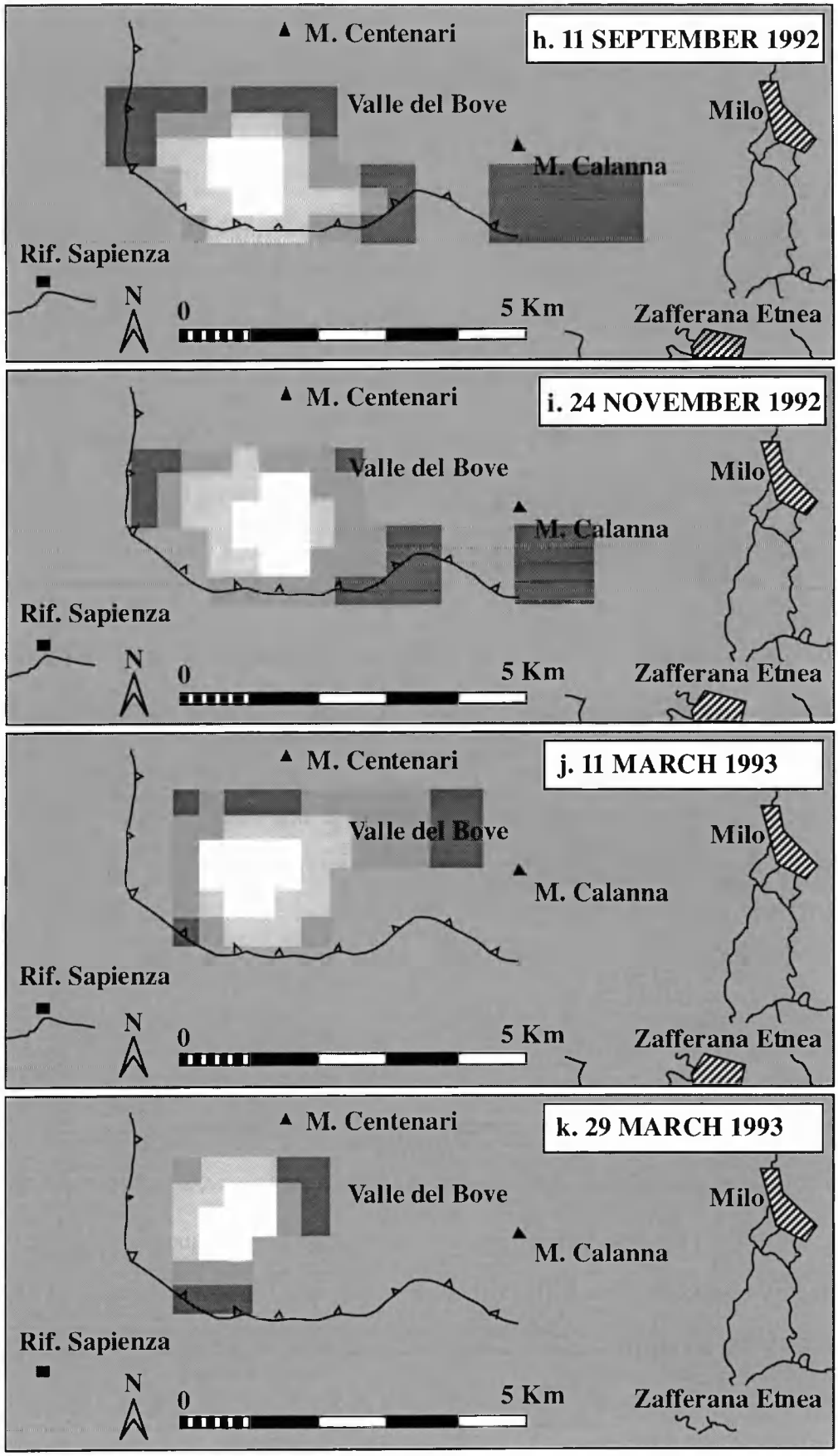
M. Centenari
h. 11 SEPTEMBER 1992
Valle del Bove
Milo
M. Calanna
Rif. Sapienza
N
0
5 Km
Zafferana Etnea
M. Centenari
i. 24 NOVEMBER 1992
Valle del Bove
Milo
M. Calanna
Rif. Sapienza
N
0
5 Km
Zafferana Etnea
M. Centenari
j. 11 MARCH 1993
Valle del Bove
Milo
M. Calanna
Rif. Sapienza
N
0
5 Km
Zafferana Etnea
M. Centenari
k. 29 MARCH 1993
Valle del Bove
Milo
M. Calanna
Rif. Sapienza
N
0
5 Km
Zafferana Etnea

show expansion of the Val del Bove anomaly, conforming with reports of lava flows extending down the Valle del Bove towards and around Monte Calanna during the first three weeks of phase 2. By the end of December the phase 1 anomaly can no longer be distinguished, suggesting anomaly cooling. This is corroborated by the short-lived nature of this phase, which ended during the first day of the eruption, phase 1 flows being inactive and cooling thereafter.

5.6.3. Phases 3 and 4

From January through May, we note a gradual change in structure of the thermal anomaly and in the location of the highest radiance zone. The highest radiance migrates from the west to the east of the anomaly, with the western portion of the anomaly becoming narrower and less radiant (Figures 5.4c to 5.4e). Although individual tube systems cannot be "seen", this change is consistent with reports of gradual roofing over in the Val del Bove (which would have reduced the radiance), while surface flows effused from secondary boccas in the lower Val del Bove and Val Calanna. Gradual extension of the anomaly towards Zafferana between December and May (Figures 5.4a to 5.4e) suggests a potential threat to the town, with the closest radiant pixel ~1 km from the town during phase 4 (Figure 5.4e).

5.6.4. Phase 5

Following the successful diversion, a major change in the location of the highest radiance zone can be noted. An image acquired just 3 days after the diversion shows the zone of highest radiance to have returned to the SW floor of the Val del Bove, coincident with the location of the newly-diverted lavas (Figure 5.4f). Subsequent phase 5 activity is illustrated by Figures 5.4g to 5.4k, with highest radiance remaining confined to the SW floor of the Valle del Bove, which remained the location of active flows until the end of the eruption. Over the same period, the now isolated Monte Calanna anomaly became cooler

and smaller. This is to be expected in the distal portion of this flow field, which was starved of supply, inactive and cooling during the final phase.

From the relationships documented above we conclude that although detailed interpretation of radiance maps requires a degree of corroboration by ground observations, in their absence location of an anomaly to within ±1 km is feasible and qualitative analyses of variations in the intensity and location of radiant sources are possible.

5.7. Estimation of the thermal structure of an AVHRR lava pixel

In 1981 *Dozier* [1981] presented a method to estimate the size and temperature of sub-pixel hot spots in AVHRR data. The method assumes that a pixel is occupied by two thermal components: a high temperature component at temperature T_h occupying portion p of the pixel surrounded by a cooler component at temperature T_b occupying the remainder (1-p) of the pixel. If any one of these three unknowns can be assumed, then the method uses channel 3 and 4 at-satellite radiances (R_3 and R_4) to estimate the remaining two unknowns by solution of simultaneous equations:

$$R_3 = p\, L_3(T_h) + (1-p)\, L_3(T_b) \qquad (5.2)$$

$$R_4 = p\, L_4(T_h) + (1-p)\, L_4(T_b) \qquad (5.3),$$

in which $L_3(T)$ and $L_4(T)$ are the Planck function spectral radiances for a blackbody of temperature T at the channel 3 and 4 central wavelengths. Channel 5 could be used in place of channel 4, but its similar sensitivity to high temperature sources (Figure 5.3a) will result in a similar solution to that obtained using channel 4. The wavelengths of channels 4 and 5 are too close together to allow reliable solution of the simultaneous equations using these two channels together. Note also that channel 5 data are not always available (Table 5.1).

This method has been applied to estimate the size and temperature of industrial hot spots and gas flares using channel 3 and 4 data (Matson & Dozier, 1981). However, it has a number of weaknesses, one being that the model allows only two thermal components (Langaas, 1993). Over an active lava body a 1.1 km pixel will be occupied by at least three components: molten lava at temperature T_h occupying portion p_h of the pixel, chilled crust (which forms rapidly on exposed molten lava) at temperature T_c occupying p_c of the pixel, and lava-free ground at T_b which occupies the remainder $(1-p_h-pc)$ of the pixel. The model also fails to consider the effects of emissivity and atmosphere. We therefore adapt Equations 5.2 and 5.3 to include a third component, and atmosphere and emissivity effects:

$$R_3 = \tau_3 \varepsilon_3 [p_h L_3(T_h) + p_c L_3(T_c) + (1-p_h-p_c) L_3(T_b)] \quad (5.4)$$

$$R_4 = \tau_4 \varepsilon_4 [p_h L_4(T_h) + p_c L_4(T_c) + (1-p_h-p_c) L_4(T_b)] \quad (5.5),$$

in which ε_3 and ε_4 are the emissivities of the surface and τ_3 and τ_4 atmospheric transmissivities in channels 3 and 4. We use ε_3 and ε_4 of 0.96 and 0.9 respectively, which are the maximum spectral emissivities given for basalt by Salisbury and D'Aria (1994), and transmissivities calculated for a standard atmosphere, taking into account pixel altitude and path angle to space, using LOWTRAN 6 (Kneizys *et al.*, 1983). This leaves five unknowns, p_h, p_c, T_h, T_c and T_b. In order to constrain a reasonable model, valid and unique estimates are required for at least 3 of these parameters. We therefore estimate T_b for each lava pixel using the mean channel 4 temperature of the nearest lava-free pixels and assume T_h using in situ observations of typical lava temperatures. During the 1991 to 1993 eruption, although maximum lava temperatures of 1080 °C were obtained at a depth of ~10 cm, at the surface most frequently measured temperatures were ~1000 °C (S. Calvari, personal communication). We therefore set T_h to 1000 °C. Although the 1991 to 1993 flow was predominantly aa, we note a similar relationship in our own measurements of active pahoehoe lobes at Kilauea during October 1995. Although we found core temperatures of

1130 °C, maximum surface temperatures were 1030 °C, with most common temperatures ~1000 °C. This indicates that for basaltic aa or pahoehoe flows, use of core temperature will set T_h too high; in both cases ~1000 °C is more reasonable.

This leaves three unknowns, p_h, p_c and T_c. Field and satellite data show that temperatures for T_c can range over several hundreds of degrees centigrade, making T_c impossible to define using a single value (Oppenheimer, 1991; Flynn & Mouginis-Mark, 1992; Flynn *et al.*, 1993). To avoid error that would be introduced by selecting a single T_c, we choose to solve Equations 5.3 and 5.4 over a reasonable range of T_c to give a range of solutions within which the true solution must lie. Following the results of Oppenheimer (1991) and Flynn *et al.* (1993) we select 100 °C as a reasonable lower limit for the T_c range. T_c will have an upper limit, above which p_h would have to become negative in order to solve Equations 5.4 and 5.5. This approach gave maximum values for T_c typically between 150 and 350 °C, with estimates of up to 470 °C in extreme cases. Few crust temperature measurements are available. However, the range in T_c for this partially crusted basaltic lava flow is in agreement with those calculated by multiple component modelling of spectroradiometer data for the basaltic Kupaianaha lava lake (typically 120 to 390 °C), and with those obtained for the 1989 Lonquimay andesitic flow (<122 to >258 °C) from two component modelling of TM data (Oppenheimer, 1991; Flynn *et al.*, 1993).

Channel 3 radiance cannot be used if it is saturated. Where channel 4 is not saturated, if p_h can be assumed to be very small and its contribution to R_4 negligible, then p_c can be estimated from channel 4 radiance (R_4) alone using:

$$p_c = \frac{[R_4 / \tau_4 \varepsilon_4] - L_4(T_b)}{L_4(T_c) - L_4(T_b)} \qquad (5.6).$$

Where three-component solutions were possible, fractional areas of the flow surface occupied by the molten component, f_h [$= p_h / (p_c + p_h)$], ranged between 0.0001 and 0.01. For such low values of f_h, the assumption that contribution of p_h to channel 4 radiance is

negligible is reasonable. This assumption is also supported by non-saturation of channel 4. To achieve saturation temperature in channel 4, given typical molten and crustal temperatures of 1000 and 250 °C, the contribution of $p_hL_4(T_h)$ to R_4 varies between ~2 and 4%, depending on whether a snow covered (~0 °C) winter- or a solar heated (~40 °C) summer-background is present. Since during all seasons channel 4 radiances were well below saturation, the contribution of $p_hL_4(T_h)$ must be less than 4%. We therefore applied Equation 5.6 if channel 3 was saturated, with saturation defined as in Harris *et al.* (1995a). To solve Equation 5.6, T_b was calculated as for Equations 5.4 and 5.5 and T_c was ranged between reasonable limits to give a range of solutions within which the true solution must lie. The lower T_c limit used to solve Equations 5.4 and 5.5 (100 °C) was used, with an upper limit set at 500 °C, guided by the maximum T_c calculated by Oppenheimer (1991) and Flynn *et al.* (1993).

5.8. Lava flow field area and thermal flux estimates

Surface area and thermal flux are important inputs into lava flow models (e.g. Dragoni, 1989; Crisp & Baloga, 1990; Pieri and Baloga, 1986). Parameters calculated using Equations 5.4 to 5.6 allow us to estimate the area of, and thermal flux from, the active lava. The area of the thermal anomaly or thermally active area for each image (A_{lava}), which we assume equates to the area of active flows at the time of over-pass, is given by

$$A_{lava} = \sum_{x=1}^{n} A_x \left(p_{c_x} + p_{h_x}\right) \qquad (5.7),$$

in which n is the number of lava pixels, p_{c_x} and p_{h_x} are the crusted and molten portions of pixel x and A_x is the area of pixel x. Total radiant flux from active flows for each image (Q_{rad}) is calculated using

$$Q_{rad} = \sum_{x=1}^{n} \left(\sigma \varepsilon A_x [p_{c_x} T_{c_x}{}^4 + p_{h_x} T_{h_x}{}^4]\right) \qquad (5.8),$$

in which σ is the Stefan Boltzmann constant (5.67×10^{-8} Wm^{-2} K^{-4}), ε is emissivity (0.9887, mean emissivity for basalt from Salisbury & D'Aria [1992]) and T_{h_x} and T_{c_x} are the temperatures for the molten and crusted portions of the flow for pixel x.

Area and flux estimates obtained using the cloud-free eruption time series are given in Figures 5.5a and 5.5b respectively. We note highest values during phases 1 and 2,

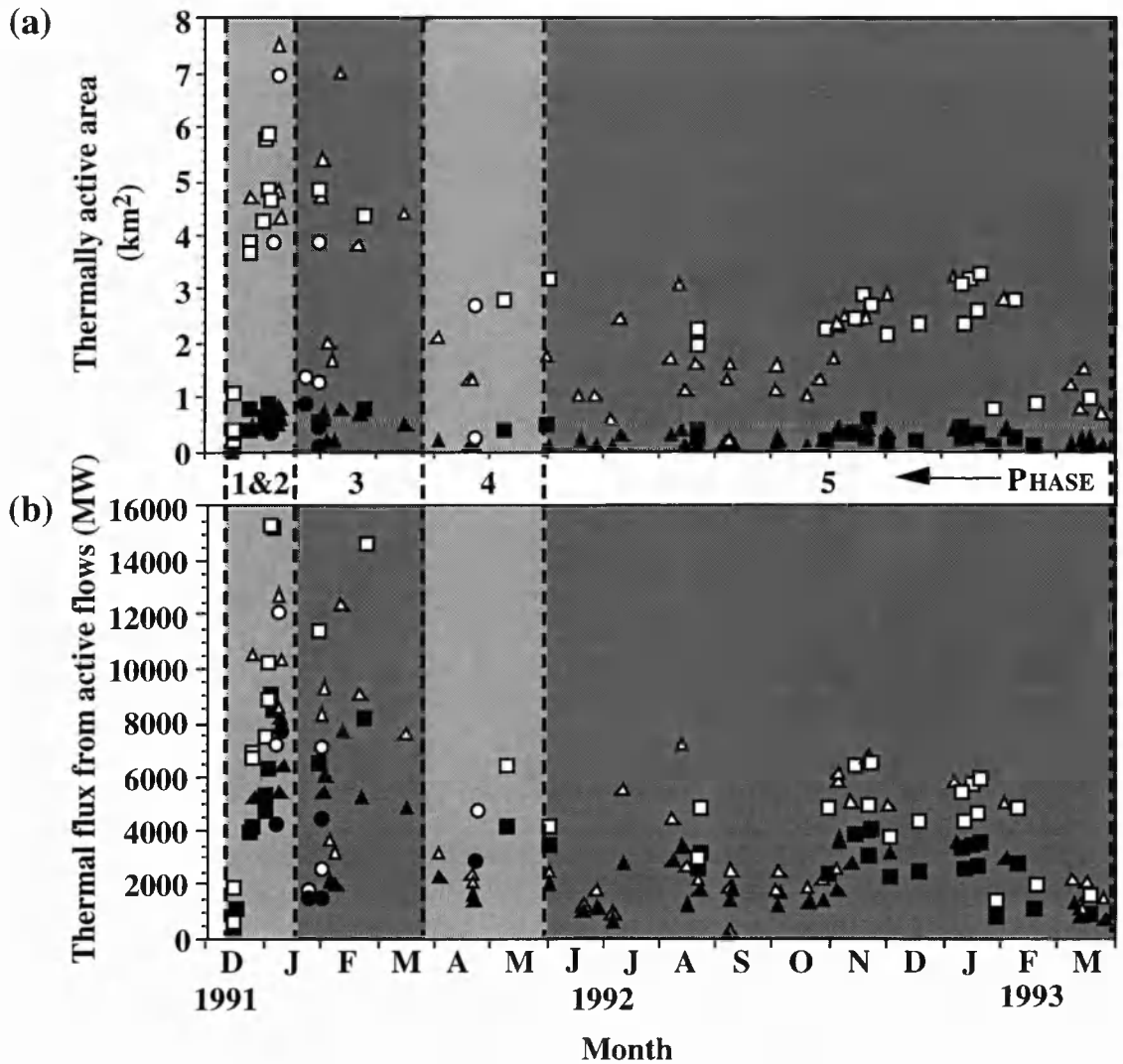

Figure 5.5. *Full eruption time series produced using the cloud-free AVHRR data set in relation to the eruption phases (grey zones) for* (a) *thermally active area and (b) thermal flux, with each eruption phase indicated. In each case a range of possible solutions is delimited by black (lower bound) and white (upper bound) plots. The true solution will lie between these. Data from less trustworthy cloud contaminated and extreme scan angle images are plotted using triangular and circular symbols respectively.*

declining values during phase 3 to lower but steady levels by stage 4, and maintenance of a similarly low and relatively constant level throughout the final and longest phase. We estimate the total radiative flux from active flows during the entire eruption to lie between 1.40×10^{11} and 2.23×10^{11} MJ over 473 days, giving an average flux of 2.96×10^{8} to 4.71×10^{8} MJ/d. A comprehensive estimate such as this can only be obtained from AVHRR, which provided the only time series of thermal radiance measurements spanning the entire Etna eruption (Figure 5.5b).

5.9. Validation, comparison with ground data and error

5.9.1. Validation

We have validated the three-component approach by comparison with the two-component approach, ground observations and TM data. Simultaneous AVHRR, TM and ground observations are available for 2 January 1992. Active flow areas apparent on the TM image (Rothery *et al.*, 1992) covered an area of ~2.8 km^2, in exact agreement with the ground estimate given in Calvari *et al.* (Figure 5, 1994a). We assume that active flow area equates to the thermally active area. Previously, solution of the two component approach (Equations 5.2 & 5.3) has been achieved by assuming a value for T_h (Oppenheimer, 1991; Oppenheimer *et al.*, 1993; Harris *et al.*, 1995c) or for T_b (Matson & Dozier 1981; Pieri *et al.*, 1990; Reddy *et al.*, 1993). Here we apply Equations 5.2 and 5.3 to the AVHRR image first by assuming T_h of 1000 °C, and then using T_b estimated as for Equations 5.4 and 5.5. This gave a thermally active area of 0.002 to 8.2 km^2. This compares poorly with the estimate given by the three component approach (Equations 5.4 to 5.6) of 0.7 to 5.8 km^2, the three component approach providing a tighter constraint in the true active area.

Temperatures derived from applying the two-component approach to AVHRR data for lava flows are considerably less trustworthy than those derived from a three-component approach. Using the 2 January image and assuming a value of 1000 °C for T_h in the two-component approach resulted in a calculated T_b of 14 to 50 °C. However, typical ambient

background temperatures obtained from the image using pixels adjacent to the flow that were free of active lava are 9 to 18 °C, and the expected crustal temperature range is 100 to 500 °C. Thus the T_b range derived by the two-component (14 to 50 °C) approach does not accurately represent either thermal source, i.e. it does not give the temperature of the ambient or the crusted surface. However, the range of T_b calculated using the two component approach is closer to the expected ambient temperature range than the expected crustal range. This could prompt the erroneous and unrealistic conclusion that an entirely molten body at 1000 °C was present against an ambient background, with no crusted surface present. An entirely molten surface is unlikely since crust growth and temperature decline are rapid once magma is exposed to air (see Hon *et al.*, 1994). Flynn *et al.* (1993) and Flynn and Mouginis-Mark (1994) show that the crustal component composes at-least 40-70 % of the total lava surface, even at active lava channels and over-turning lava lakes.

5.9.2. Comparison with ground data

Our more realistic three component estimates for the thermally active areas during the first two and a half months of the eruption span those for total flow field area given by Calvari *et al.* (Figure 5, 1994a) and generally follow the same trend, Figure 5.6a. Over this period, major deviations from the Calvari *et al.* (1994a) time series can be attributed to two factors: cloud contamination and scan angle effects.

Figure 5.6. *Thermally active area estimates made using AVHRR images acquired during the first 2.5 months of the eruption, with active flow areas given by Calvari et al. (1994a) for comparison. In each case a range of estimates are given within which the true value lies: black and white symbols indicate the lower and upper bounds of the three-component model respectively. The true value is located within the grey zone. (a) Gives results using all images on which activity could be detected, (b) excludes anomalous cloud contaminated and extreme scan angle images, indicated by triangular and circular symbols respectively, and (c) gives the maximum value approach, where all images except cloud-contaminated ones are placed into groups of 3 (group A, B, C, etc.) and the trend is plotted through the maximum value of each group.*

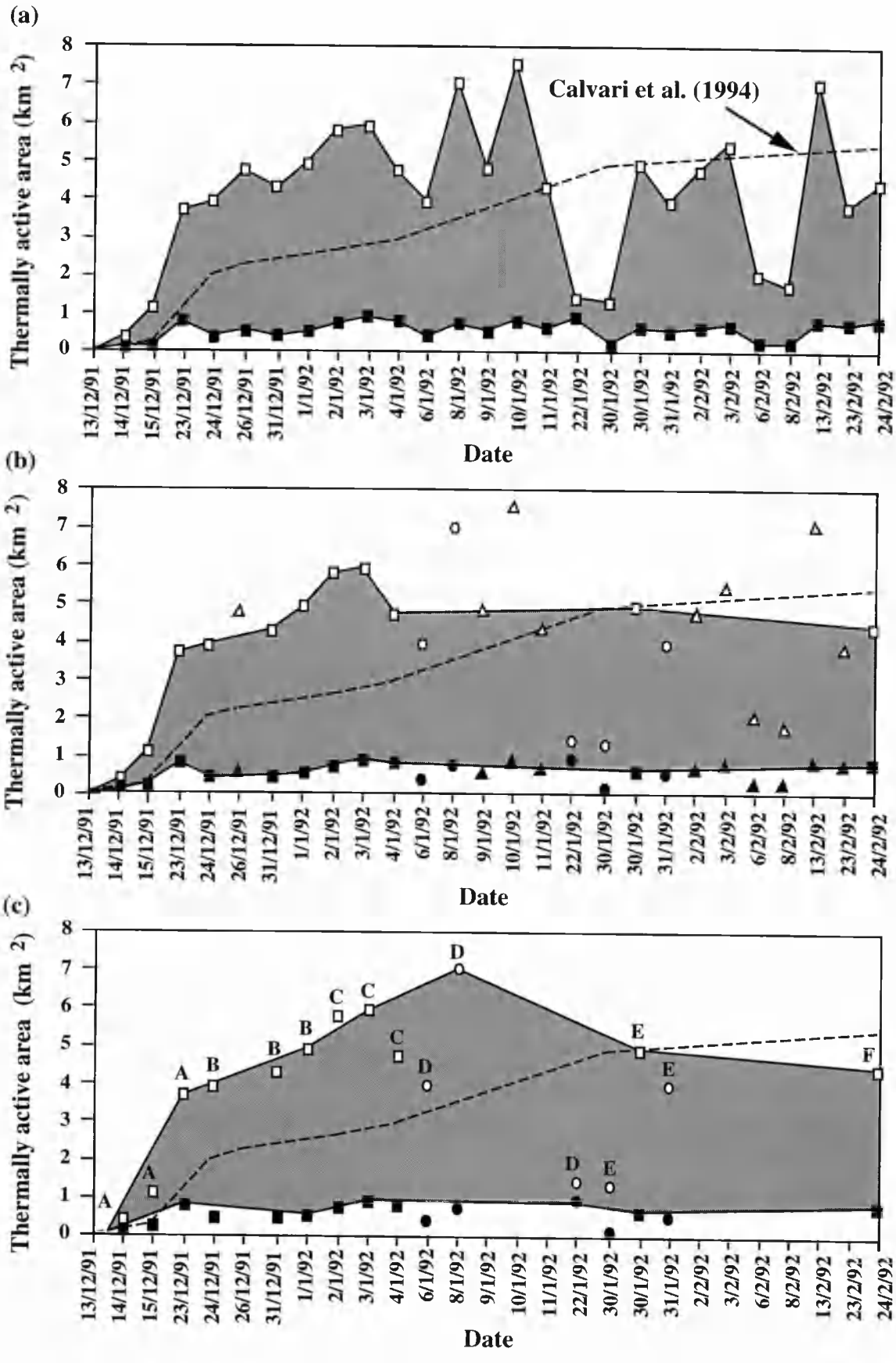
(a)
Thermally active area (km 2)
Calvari et al. (1994)
Date
(b)
Thermally active area (km 2)
Date
(c)
Thermally active area (km 2)
Date

5.9.2.1. Cloud contamination

The intense radiance source presented by the active lava flow is strong enough to be detected through thin cloud in channel 3, or between broken cloud in channels 3 and 4. This allows detection and location of activity even on cloud contaminated images. However, the cloud will contaminate the signal: low warm sub-pixel cloud against snow will increase the pixel-integrated radiance, and conversely high cold cirrus will cause a decrease. It is therefore not surprising that cloud contamination can have conflicting effects on the time series: area estimates for images acquired on 10/1/92 and 13/2/92 being examples of cloud-induced rises, those of 6/2/92 and 8/2/92 showing cloud-induced decline (Figure 5.6a). Cloud-contaminated images must therefore be identified and rejected (Figure 5.6b). This was achieved using standard cloud masking techniques (Saunders, 1986; Sakellariou & Leighton, 1988; Saunders & Kriebel, 1988; Yamanouchi & Kawaguchi, 1992).

5.9.2.2. Scan angle effects

Adverse radiance effects due to off-nadir viewing have been discussed by Tucker *et al.* (1984), Singh (1985) and Goward *et al.*, (1991). Here we find off-nadir views result in anomalously low estimates, the results for images acquired on 22/1/92 and 30/1/92, at scan angles of 50° and 55° from nadir (Figure 5.6a) being good examples. To reduce scan-angle induced effects, sub-scenes at scan angles greater than 30° from nadir have been rejected by Tucker *et al.* (1984) and Goward *et al.* (1991). However, this would have greatly reduced our temporal resolution, leaving just 4 of the remaining 16 cloud-free images in Figure 5.6a. We found that images with a scan angle < 50° gave results in agreement with the trend given by Calvari *et al.* (1994a), and chose to reject only images at scan angles > 50°, in accordance with *Frulla et al.* [1995].

Rejection of images with cloud contamination and extreme scan angles removed anomalous cloud and scan-angle induced peaks and troughs, resulting in area estimates spanning those of Calvari *et al.* (1994a), and following a similar trend (Figure 5.6b). Since

this approach rejects apparently reasonable area estimates obtained from some extreme scan-angle images, for example that of 8 January 1992 (Figure 5.6b), we have investigated an alternative approach which uses all cloud-free images. All cloud-free images in the time series were placed into continuous groups of three, and the maximum for each group used. A similar approach has been applied to reduce cloud, scan angle, sun-angle, shadow, aerosol and water-vapour effects in AVHRR derived vegetation indices (Holben, 1986). The result (Figure 5.6c) gave a trend which fitted that of Calvari *et al.* (1994a) between 14 December 1991 and 6 January 1992. After this time we note that the Calvari *et al.* (1994a) estimate rises through our range, exceeding the upper bound at the end of January. This is a result of the Calvari *et al.* (1994a) estimate being a cumulative one for the entire flow field, active and inactive, whereas ours is for thermally anomalous, active, areas within it.

The maximum value approach was applied to the full cloud-free data set to produce an thermally active area time series for the entire eruption, Figure 5.7. This time series shows a trend in accordance with ground observations and TM-based estimates. Ground observations describe rapid increases in the active flow area during December 1991 and January 1992 to reach a maximum area of ~6 km^2 (GVN, 1992a). Steady tubing over of the flow during the third and fourth phases to feed active surface flows <1-2 km in length, correlates with a steady decline in thermally active area between February and June 1992 (Figure 5.7). Two estimates of the active area in March and August 1992 derived from TM data also fall well within the AVHRR defined range. That the estimates of total flow field area and active area derived from TM data differ after phases 1 and 2, when the TM estimates of active and total area were identical, is compatible with the divergence between our AVHRR-based thermally active estimates and the total flow field estimates of Calvari *et al.* (1994a) after mid-January (Figure 5.7). Between July 1992 and February 1993 thermally active areas remain small, relating to steady eruption of lava at lower effusion rates during phase 5 to produce flows no more than 1.5 km in length (Calvari *et al.*, 1994a). The decline in thermally active area during March 1993 (Figure 5.7) is consistent with a decline in lava effusion observed from the ground at this time (GVN, 1993b).

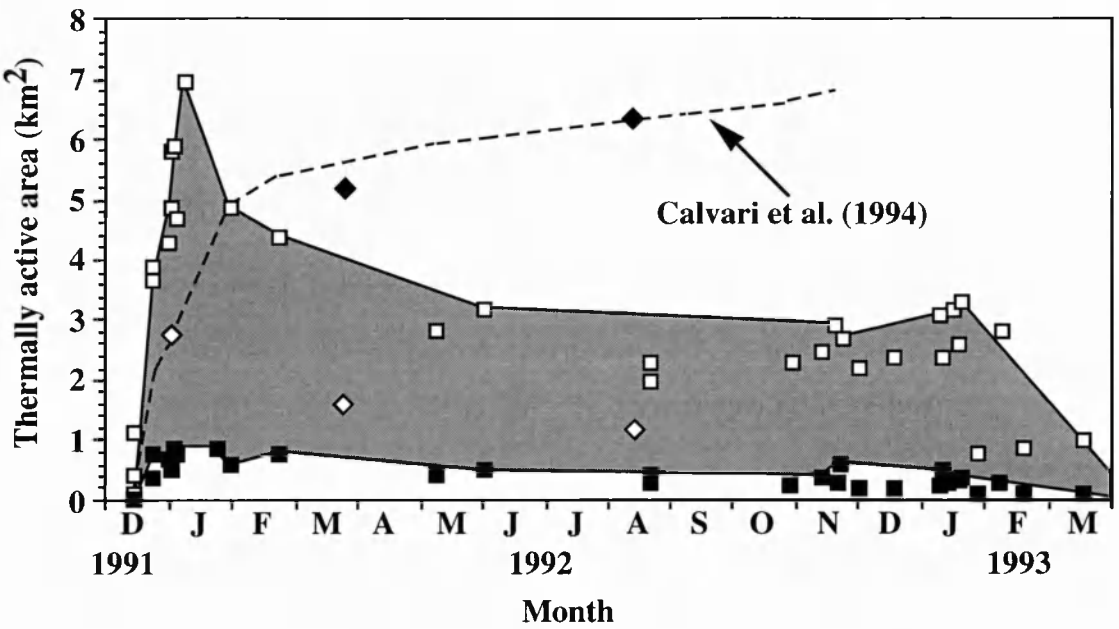

Figure 5.7. *Cloud-free AVHRR time series for thermally active area. Active flow and total flow-field area estimates derived from TM images are given for comparison (white and black diamonds respectively). We assume that thermally active areas should equate to active flow areas. Black and white squares indicate the lower and upper bounds of the three-component model respectively, where the plot has been extrapolated between points obtained from the maximum value approach. The true value is located within the grey zone.*

5.9.3. Errors

We identify three main sources of error: background heterogeneity, non-uniform emissivity and unconstrained atmospheric effects.

5.9.3.1 Background heterogeneity

The use of a single temperature to describe the background may be inappropriate. During measurements of non-active volcanic surfaces at Etna during summer 1994, the typical temperature range across ~100 m^2 areas of uniform surface type at ambient temperatures was ~15 °C. Temperature variations resulted from differences in aspect, exposure to wind and moisture content. Extreme variations occurred where sharp boundaries occurred between two background surface types, e.g. a -1.6 °C snow patch against a 53 °C solar-heated background. We examined possible errors using the 2 January

image. The highest background temperature range from all pixels surrounding the anomaly was 9 to 18 °C, with a mean of 13 °C. We used the mean in the three component approach to estimate pixel portion occupied by active lava ($p_{lava} = p_c+p_h$) for this pixel. Maximum errors were then estimated from scenarios where the pixel is entirely filled by the minimum or maximum temperature surfaces. This gave a maximum error on p_{lava} of ~10%.

5.9.3.2 Non-uniform emissivity

Surface emissivity will depend on background surface type. Background emissivity at 10-12 μm can vary between ~0.95-0.99 for snow (Salisbury *et al.*, 1994), ~0.94-0.97 for vegetation (Salisbury, 1986; Salisbury & Milton, 1988) and ~0.85-0.95 for igneous rocks (Walter & Salisbury, 1989). Emissivity will also vary across a single surface type, Kahle *et al.* (1988) and Realmuto *et al.* (1992) show age-related emissivity variations across flows emplaced within 2 years of each other. We also anticipate a minor emissivity difference between molten and solid lava, but to date this is not been measured. Consequently radiance in channel i over a three component surface is more accurately given by

$$R_i = \tau_i [\varepsilon_{hi} p_h L_i(T_h) + \varepsilon_{ci} p_c L_i(T_c) + \varepsilon_{bi} (1-p_h-p_c) L_i(T_b)] \quad (5.9),$$

where ε_{hi}, ε_{ci} and ε_{bi} are the emissivities of the three thermal components in channel i. Assuming uniform emissivity in the test example given above, with worst case errors estimated using the minimum and maximum possible emissivities, gives maximum error in p_{lava} of ~10%.

5.9.3.3. *Unconstrained atmospheric effects*

Radiance reaching the sensor in channel i is written as

$$R_i = \tau_i[\varepsilon_i L(\lambda T_s) + \rho_i R_{iD}] + R_{iU} \quad (5.10),$$

in which T_s is surface temperature, ρ_i is surface reflectivity in channel i, and R_{iD} and R_{iU} are down- and up-welling atmospheric path radiances. To obtain radiance emitted by the surface [$L(\lambda T_s)$], all other components must be removed. At ~10-12 μm the contribution of $\rho_i R_{iD}$ is negligible, but $\rho_i R_{iD}$ rises to 10-15 % of R_i at wavelengths ~3 μm (Singh & Warren, 1983). We have therefore corrected all channel 3 radiances for this contribution. This has been achieved by assuming the difference between the emissivity and transmissivity corrected channel 3 and 4 temperatures over background pixels is due to this contribution, and subtracting this difference from R_3. Towards 3.0 μm R_{iU} is negligible, and at 10-12 μm is small (<9 % of R_i), though not entirely negligible (Singh & Warren, 1983). Since we have been unable to acquire the atmospheric parameters necessary to calculate and correct for R_{iU}, our estimates remain uncorrected for this effect. Using the test example, maximum error on p_{lava} due to this unconstrained atmospheric effect is 15%.

In a worst case scenario, maximum error due to background heterogeneity, non-uniform emissivity and unconstrained atmospheric effects on p_{lava} is 10-20 % (n.b. errors are not cumulative). All errors will be equally applicable to the two component approach. The presence of such error is implicit in our quoting estimated parameters over ranges, rather than giving specific values. Where the resolution of the sensor is insufficient to constrain background temperature and emissivity variation, use of mean values, set using data from adjacent pixels or prior knowledge of the surface, is the most reasonable approach.

5.10. Effusion rates and flow volume

Effusion rate and flow volume are important controls on lava flow morphological parameters and flow length (Walker, 1973; Wadge, 1978; Malin, 1980; Guest *et al.*, 1987; Kilburn and Lopes, 1988; Pinkerton and Wilson, 1994). Following Pieri and Baloga (1986), assuming that the flow is effectively stationary at the moment of image capture, in a thermally unmixed case effusion rate (E_r) can be written as[f]

$$E_r = \frac{Q_{rad} + Q_{conv}}{\rho\,[C_p \Delta T + \phi c_L]} \qquad (5.11),$$

where Q_{rad} and Q_{conv} are the total radiant heat flux (which we have measured) and convective heat flux respectively, ρ is lava density, C_p is specific heat capacity, ΔT is the average temperature drop throughout the active flow (= initial eruption temperature minus temperature at which forward movement ceases), ϕ is the average mass fraction of crystals grown in cooling through ΔT, and c_L is the latent heat of crystallisation. Pieri and Baloga (Equation 4b, 1986) derive a simpler model in which Q_{conv} and ϕc_L are not considered.

For the 1991 to 1993 flow we have used ρ and C_p of 2600 kg m^{-3} and 1150 J kg^{-1} K^{-1} respectively (Kilburn, 1993). The average temperature drop throughout the active flow (ΔT) is unlikely to be greater than the difference between the eruption temperature and solidus temperature of the lava. We use the maximum temperature measured at the flow, i.e. 1080 °C (S. Calvari, personal communication) for the eruption temperature and, since the difference between liquidus and solidus is 150 to 200 °C for most magmas (Archambault & Tanguy, 1976), we choose a solidus temperature of ~900 °C. The maximum amount of crystallisation (ϕ) is 40 to 50 %, allowing for 30 % initial phenocrysts and 20 to 30 % residual glass in solid lava (Armienti *et al.*, 1994). Latent heat of crystallisation (c_L) is set to 2.9 x 10^5 J kg^{-1} following Huppert and Sparks (1988).

Radiative heat loss, Q_{rad}, is given by Equation 5.8. The free convective heat loss, Q_{conv}, is estimated for the entire active flow surface following Head and Wilson (1986) and Oppenheimer (1991) as

$$Q_{conv} = 0.14\, A_{lava}\, k\, (g\alpha\rho/\mu\kappa)^{1/3}\, \Delta T_s^{4/3} \qquad (5.12),$$

where g is acceleration due to gravity (9.8 m s^{-2}) and $\Delta T_s = T_e - T_{air}$, in which T_e is the effective surface temperature, as defined by Crisp and Baloga (1990) and Pieri *et al.*

(1990), integrated over the entire active flow, and T_{air} is the air temperature. The properties k, μ, κ, α and ρ are thermal conductivity, dynamic viscosity, thermal diffusivity, cubic expansivity and density of air at a mean temperature of $T_{air} + \Delta T_s/2$. Following Oppenheimer (1991), values for k, μ, κ, α and ρ are set from tables in Kays and Crawford (1980) using T_{air} of 0 °C.

Effusion rates derived for active flows during the 1991 to 1993 eruption[g] are in agreement with reliable ground measurements and fill the gap in published estimates between the 200th and 400th day (Figure 5.8a). We note two anomalously high estimates by Barberi *et al.* (1993a) for flow rate through the successful diversion channel. Because of the possibility that this may be affected by the artificial channel dimensions, bottom topography and especially drainage of backed-up lava from the tube system, we regard these as over-estimates of the actual effusion rate from the vent. Our effusion rates give a mean effusion rate over the 473 day eruption, of 5.6 to 7.6 m^3/s. This matches that given by Calvari *et al.* (1994a) for the same period of 5.8 m^3/s.

Eruptions at Etna typically fall into one of two categories: low effusion rate "quiet eruptions" and high effusion rate "paroxysmal eruptions" (Romano & Sturiale, 1982). Mean effusion rates estimated by us and Calvari *et al.* (1994a) for the 1991 to 1993 eruption are all well below the average effusion rate from all historical eruptions at Etna of 25 m^3/s (Romano & Sturiale, 1982), indicating that the 1991 to 1993 eruption was a typical "quiet eruption".

Guest *et al.* (1987) note that a reduction in effusion rate during the 1983 "quiet eruption" at Etna marked the transition between the formation of long flows and the development of a sequence of short flows building a compound flow field, as defined by Walker (1972). From Figure 5.8a, we suggest a similar relationship during the 1991 to 1993 eruption. The reduction in effusion rate given in Figure 5.8a marks the transition between long flows during phases 1 to 2 and shorter flows, building a compound flow field of overlapping units during phases 3 to 5. The compound flow field was extended at

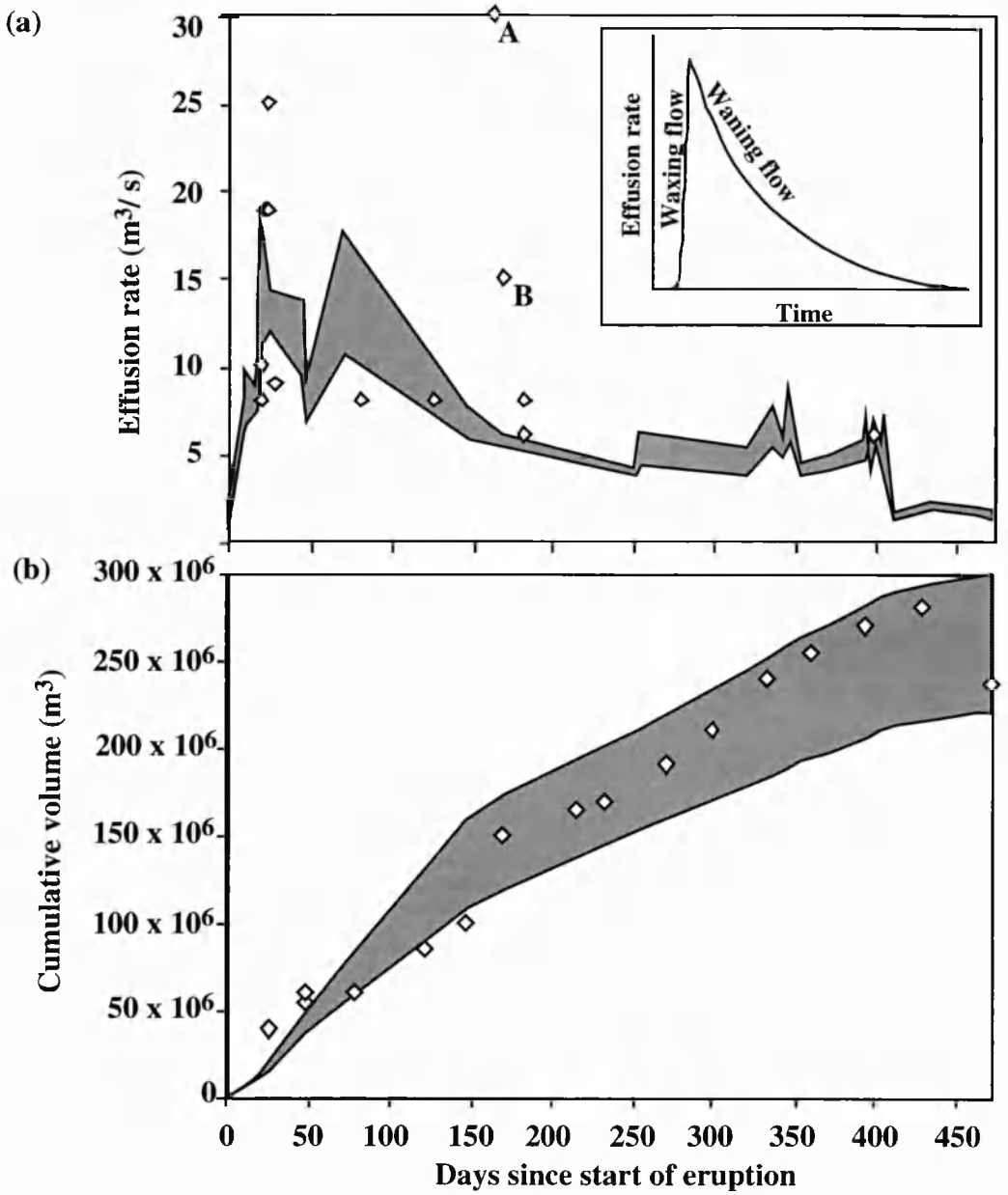

Figure 5.8. *Time series produced from cloud-free AVHRR data for (a) effusion rates, with effusion rate variation for a hypothetical basaltic eruption given by Wadge (1981) inset, and (b) cumulative volume. Ground-based estimates, taken from Calvari et al. (1994a), Barberi et al. (1993a) and all issues of the Global Volcanism Network published during the eruption, are plotted using diamonds. Estimates A and B are those of Barberi et al. (1993a) for flow rate through the diversion channel. Since these may be affected by the artificial channel dimensions, bottom topography and especially drainage of backed-up lava from the tube system, we regard these as over-estimates of the actual effusion rate from the vent. We also note (1) published ground-based effusion rates are fewer than those for cumulative volume, and (2) ground-based volume estimates made during the eruption were in error, as indicated by the lower final value obtained by Calvari et al. (1994a).*

its distal end during phases 3 to 4. After the diversion, low effusion rates and the building of a compound field continued, but construction was shifted to the proximal portion of the flow field. The fall off in effusion rates during the last 40 days of the eruption given in Figure 5.8a correlates with a decline in surface flow activity observed on the ground during the final two months (GVN, 1993a, GVN, 1993b). A similar progressive decline in effusion rate was observed at the end of the 1983 eruption (Guest *et al.*, 1987).

The variation in effusion rate with time approximates that given by Wadge (1981) for a hypothetical basaltic eruption (Figure 5.8a). Wadge (1981) identifies a waxing phase of rapidly increasing effusion rates followed, after maximum effusion rate is reached, by a dominant waning phase characterised by steadily declining effusion rates (Figure 5.8a, inset). In the case of the Etna 1991 to 1993 eruption, a short waxing phase with a peak around 35 days is followed by a longer 438 day waning phase.

By integrating our measured effusion rate over time, we can estimate the cumulative lava flow volume. Our results are in good agreement with ground based volume estimates given in GVN (1991e) to GVN (1993a), Figure 5.8b. We estimate the total volume of the Etna 1991 to 1993 flow to be between 220 x 10^6 m^3 and 300 x 10^6 m^3. This is consistent with the volume of 235 x 10^6 m^3 calculated by Calvari *et al.* (1994a) using GPS measurements, and is well under the estimate, given for 31 October 1992, of 500 x 10^6 m^3 by Barberi *et al.* (1993a). We believe the estimate of Calvari *et al.* (1994a) to be more reliable since it is based on GPS measurements of the total flow field, whereas that of Barberi *et al.* (1993a) is extrapolated from an anomalously high mean effusion rate of ~18 m^3/s (Figure 5.8a).

5.11. Conclusions and implications

For effusive eruptions, data from the AVHRR can provide reliable information in real time. The data are potentially free and directly available at cheap to install receiving stations, allowing daily monitoring of cloud-free volcanoes within 3000 miles of the station. Our software locates lava pixels automatically, providing area and thermal flux

estimates for the located body, and runs in less than 10 seconds on 30 x 30 pixel sub-images containing the volcano. Although we used archived data in this study, data capable of aiding ground-based lava flow monitoring could be in the hands of volcanologists or civil defence agencies within minutes of acquisition by the satellite. Possibly one of the most useful features of the AVHRR data is the ease with which time series for various flow parameters (e.g. area, thermal flux, effusion rate, cumulative volume) can be constructed and used to monitor the development of an effusive eruption.

The use of SPOT images to map the flow field in detail shows the value of using other, more infrequently collected and expensive, satellite or airborne data in conjunction with AVHRR data. Use of multiple, complementary data sources (e.g. AVHRR, Landsat-TM, SPOT, and Synthetic Aperture Radar), allows temporally and spatially more complete analysis. Using the results of a preliminary AVHRR analysis, sites of particular interest may be targeted for more detailed analysis from the ground, air or space.

The good agreement with ground data shows that estimates of active lava flow areas, thermal fluxes, effusion rates and volume derived from AVHRR images can be used to corroborate ground-based estimates, or to fill gaps for periods or locations where no other observations are possible. The value of such information in understanding lava flow morphology, flow field development and effusion rates make them valuable in planning scientific response or hazard mitigation.

5.12. Acknowledgements

We are grateful to John Murray (Open University) for advice and help with the EDM survey, and to Ian Downey (NRI), Sonia Calvari (IIV, Catania), Jez Higgins (Jez UK), Ben van Wyke de Vries, Anna Butterworth and Dick Carlton (all Open University) for their input. Painstaking reviews by Gregg Bluth, Vince Realmuto and Bill Rose did much to improve the clarity of the paper. AVHRR images were supplied by the NERC Dundee University ground station and calibrated courtesy of Peter Miller and Steve Groom at the NERC Plymouth Image Analysis Unit. Field work on Etna and Kilauea was funded

by the Remote Sensing Society's Shackleton Award and a grant from the Overseas Development Agency respectively. Andy Harris' work reported here was funded by an Open University PhD grant.

---

[e] Radiance key for Figure 5.4

For each radiance map given in the Figure 5.4a to 5.4k time series, grey tones have been assigned using the following procedure: (1) For each image, elevated radiance is calculated for each anomalous pixel (see Section 7.7). The resulting pixel values are sharpened as described in Section 7.7. (2) The sharpened image is then density sliced by dividing the range of elevated radiance for all pixels into 4 groups and assigning each group a grey tone (higher ranges are assigned lighter tones). Since this is applied separately to each image in turn, the exact radiance range to which each grey tone relates will differ from image to image. The relationship between grey tone and radiance will thus vary from image to image. Radiant intensity is therefore not comparable between images, and hence the key has not been assigned any values. However, this approach has not been designed to analyse the quantitative variations in radiance from image to image (this is shown by Figure 5.5b), but to highlight changes in the location of the zone of highest radiance.

N.B. Anomalous pixels outside of the Valle del Bove cannot be ignored and must be considered as representing the maximum possible zone covered by lava. A fissure extending along the line of the SE fissure system which fed this eruption and through the topographic barrier presented by the southern wall of the Valle del Bove could feed flows to the south of the Valle del Bove; so this scenario would have to be considered if ground truth were absent. However, the zone given by the lightest tones is likely to represent the most probable centre of surface flow activity.

[f] Derivation of effusion rate

For completeness Equation 5.11 should be written as

$$E_r = \frac{Q_{tot}}{\rho\,[C_p \Delta T + \phi c_L]} \qquad (5.13),$$

where $Q_{tot} = Q_{rad} + Q_{conv} + Q_{cond} + Q_{rain}$, in which Q_{cond} is conductive heat loss through the bottom of the active flow and Q_{rain} is the heat lost by evaporation of rain. Following Danes (1972) Q_{cond} is assumed to be negligible. Heat loss by evaporation (Q_{rain}) can be crudely estimated by adapting Keszthelyi (1995) to give,

$$Q_{rain} = \partial R/\partial t\, A_{lava}\, \rho_{H2O}\, L_{H2O} \qquad (5.14),$$

in which $\partial R/\partial t$ is the rate of rainfall, A_{lava} is the thermally active area, ρ_{H2O} is the density of water (958 kg/m^3 for water at 100 °C following Kays & Crawford (1980)) and L_{H2O} is the latent heat of vaporisation of water (2.5 MJ/kg) plus the heat needed to warm water to 100 °C (~0.3 MJ/kg). Mean annual rainfall for the Valle del Bove is 1000 to 1200 mm, however the most notable characteristic of rainfall in Sicily is its seasonality: in summer it is common for rainfall to amount to less than 5 % of the annual total (Chester *et al.*, 1985). Using a mean rainfall of 1100 mm, Q_{rain} will account for 0.5 to 3.7 % of Q_{tot}, resulting in error in calculation of E_r of between 0.5 and 10.6 % . However, adjusting for seasonality of rainfall means that by summer Q_{rain} may contribute as little as 0.04 to 0.15 % to Q_{tot}, resulting in an error on E_r of <0.2 % (Table 5.3). Obviously, the contribution of Q_{rain} will be more important in wetter climates. Setting rainfall to 3000 mm, the maximum annual rainfall recorded at Kilauea by Keszthelyi (1995), increases the contribution of Q_{rain} to Q_{tot} to 1.7 to 10.3 %, resulting in an error of on E_r of 1.7 to 11.3 %. However, it is noteworthy that uncertainties in ΔT or ϕ are likely to induce more error into the estimation of E_r than uncertainty in Q_{rain} (Figure 5.9). Effusion rates should therefore be estimated over a range set using the minimum and maximum expected ΔT and ϕ. Where daily or monthly rainfall records are not available, as at Etna for the 1991 to 1993 time series, error due to not considering Q_{rain} is likely to be between 0 and 11 %. However, since such errors are implicit in giving effusion rates over a range of values, and are far less than the errors already considered due to uncertainty in ΔT or ϕ, it is anticipated that the inclusion of Q_{rain} would not have a significant effect on the ranges of effusion rates given.

Image date (rainfall, mm)	2/1/92 (1100)	24/8/92 (1100)	24/8/92 (55)
A_{lava}, km^2	0.7 - 5.8	4.4 - 6.3	4.4 - 6.3
Q_{rad}, MW	6420 - 10340	3290 - 4930	3290 - 4930
Q_{conv}, MW	4256 - 3254	1468 - 1860	1468 - 1860
Effusion rates calculated using $Q_{rad} + Q_{conv}$, m^3 s^{-1}	10.02 - 12.75	4.46 - 6.37	4.46 - 6.37
Q_{rain}, MW	69 - 571	39 - 197	2 - 10
Q_{tot}, MW	10745 - 14165	4797 - 7427	4760 - 6800
Effusion rates calculated using Q_{tot}, m^3 s^{-1}	10.07 - 13.29	4.50 - 6.97	4.46 - 6.38

Table 5.3. *Heat fluxes and resulting effusion rates calculated using AVHRR data during the 1991 to 1993 Etna eruption. Two rainfall values are used for the 24/8/92 image: the mean annual rainfall (1100 mm) and an adjusted summer value (55 mm, i.e. 5 % of the annual rainfall).*

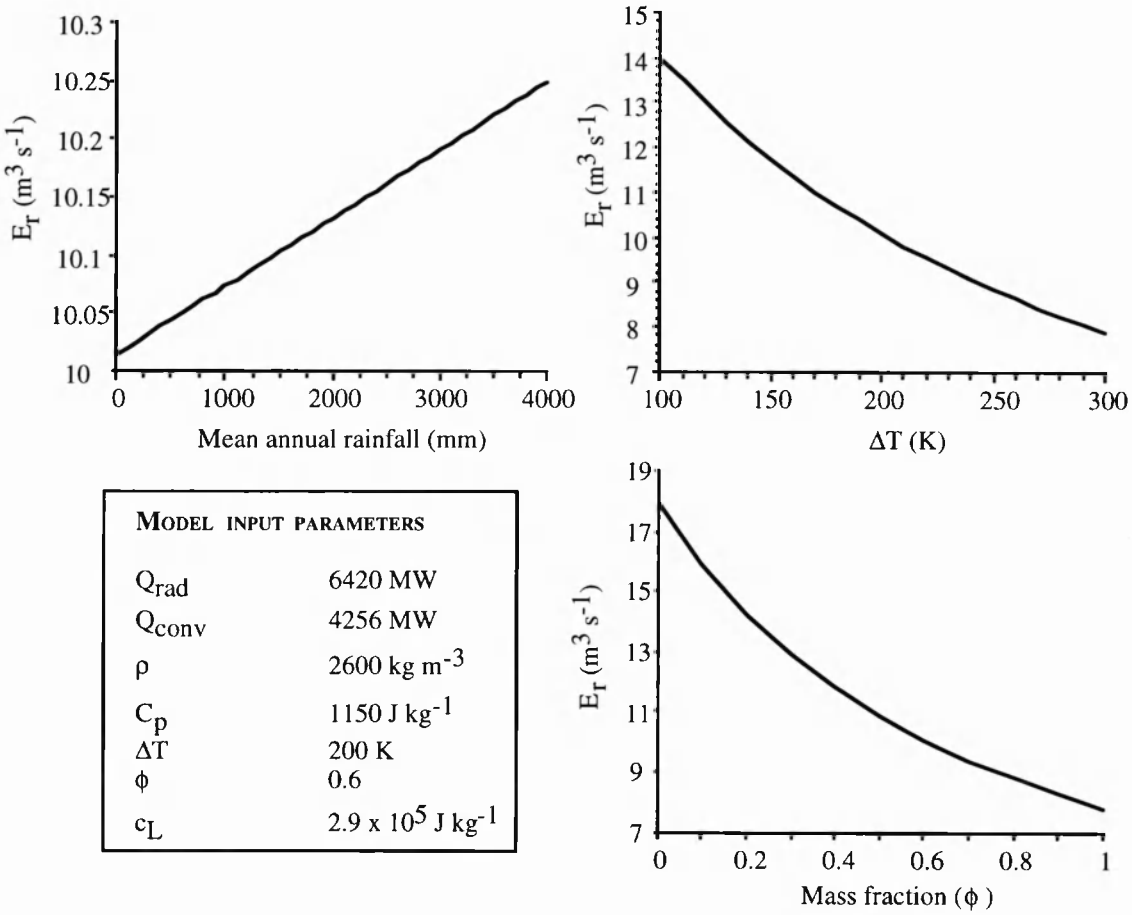

Figure 5.9. *Sensitivity of effusion rate (E_r) to variations in mean annual rainfall, ΔT and ϕ. Note that changes in ΔT and ϕ have a much larger effect on E_r than rainfall.*

g Effusion rates and cumulative volumes for the Etna 1991 to 1993 eruption calculated using AVHRR data

Date	E_r (min) ($m^3\ s^{-1}$)	E_r (max) ($m^3\ s^{-1}$)	Cumul. vol. (min) (x $10^6\ m^3$)	Cumul. vol. (max) (x $10^6\ m^3$)
14/12/91	0.8	0.9	0.03	0.03
15/12/91	1.9	2.3	0.15	0.17
23/12/91	6.3	9.8	2.96	4.35
24/12/91	6.6	8.2	3.52	5.13
31/12/91	7.4	8.8	7.78	10.27
1/1/92	8.4	10.6	8.46	11.11
2/1/92	10.0	12.7	9.25	12.11
3/1/92	12.5	18.2	10.23	13.45
4/1/92	11.2	17.8	11.25	15.00
8/1/92	12.0	14.4	15.26	20.56
30/1/92	9.5	13.7	35.67	47.27
31/1/92	6.9	9.2	36.37	48.26
24/2/92	10.7	17.8	54.59	76.21
10/5/92	5.9	7.7	108.27	158.86
2/6/92	5.4	6.2	119.50	172.68
22/8/92	4.0	4.1	152.61	208.70
24/8/92	4.5	6.4	153.34	209.61
31/10/92	3.9	5.4	177.73	244.16
15/11/92	5.4	7.8	183.72	252.73
22/11/92	4.9	5.9	186.82	256.87
25/11/92	5.7	8.7	188.19	258.77
3/12/92	3.7	4.5	191.45	263.34
20/12/92	4.1	5.0	197.19	270.28
11/1/93	4.6	5.9	205.44	280.59
12/1/93	5.3	7.3	205.87	281.16
13/1/93	4.1	5.4	206.28	281.71
18/1/93	5.5	7.1	208.36	284.42
21/1/93	4.4	5.7	209.65	286.08
22/1/93	5.6	7.3	210.08	286.64
30/1/93	1.3	1.8	212.49	289.79
21/2/93	1.8	2.3	215.47	293.69
20/3/93	1.6	1.9	219.54	298.83
29/3/93	1.2	1.8	220.73	300.46

Table 5.4. *Minimum and maximum effusion rates and cumulative volumes obtained by applying Equation 5.11 to lava flow field data from each of the cloud-free AVHRR images acquired during the 1991 to 1993 eruption at Etna.*

Chapter 6. Thermal observations of degassing open conduits and fumaroles at Stromboli and Vulcano using remotely sensed data

---

A.J. L. Harris and D.S. Stevenson

Paper submitted to Journal of Volcanological and Geothermal Research, June 1996.

6.1. Abstract

For volcanoes characterised by activity from open degassing conduits and fumarole fields, thermal data from remote sensing instruments can provide an integrated data set capable of measuring various volcanic system parameters (e.g. magma depth, thermal flux and vent areas) and of mapping the distribution of vents and other thermal features. At Stromboli such thermal data define a persistent vent system aligned along a SW-NE tectonic line, fed by a shallow (<1 km deep) magma chamber. Total thermal losses from the conduit between the magma surface and vent are ~4 MW for high temperature (900 °C) degassing vents, and ~14 MW for all vents within the crater terrace. At Vulcano, heat from a <4 km deep magma body drives a hydrothermal system feeding a 400-470 m^2 exhalative area. Consistent thermal flux measurements at Vulcano (38.6±2 W m^{-2}) between 1985 and 1995 are validated by detailed ground measurements. Time series constructed from repeated satellite and aircraft over-passes are capable of monitoring fluctuations in activity.

At Stromboli time-series constructed for 1985 to 1995 distinguish phases of intense explosive, lava pond and effusive activity. At Vulcano, a steady level of activity is identified over the same period. The good agreement with ground data suggests that the techniques presented here could be used at other volcanoes characterised by open conduit or fumarolic activity, either where no other data sources are available, or as a reliable supplement to existing commonly used data sources (e.g. seismic and chemical analyses).

6.2. Introduction

At many volcanoes, degassing magma bodies feed open conduits or active fumaroles between eruptions. At the surface, the flow of magmatic gases is manifested by elevated temperatures at and near the vents. By providing a link to the magma system, surface vent temperatures allow qualitative inferences about the magmatic system (e.g. Korzhinsky et al., 1994; Taran et al., 1995; Martini, 1986) and calculations of various system parameters such as magma depth, volume, mass flux or energy budget (e.g. Birnie, 1973; Italiano et al., 1984; Giberti et al., 1992; Connor et al., 1993; Stevenson; 1993). Further, fumarole temperatures have often been observed to increase prior to eruptions or during shallow magma intrusions (e.g. Naboko, 1960; Suwa & Tanaka, 1959; Moxham, 1967; Menyailov, 1975; GVN, 1990a). The potential contribution of vent temperature data for identifying eruption precursors and understanding the volcanic system has resulted in efforts to monitor fumarole temperatures at several volcanoes (e.g. Menyailov et al., 1986; Connor et al., 1993).

Thermal remote sensing offers a safe means of measuring and monitoring vent temperatures on a regular basis using ground-based, air- or space-borne instruments. Ground-based instruments, such as hand-held or tripod mounted radiometers, allow detailed measurements from a safe distance (e.g. Birnie, 1973; Zettwoog & Tazieff, 1972; Oppenheimer & Rothery, 1991; Harris et al., 1996); however, measurements are limited to periods when the volcano can be accessed and are temporally irregular. Automatic recording stations, with a satellite telemetry link to an observatory, allow safer, continuous

monitoring (e.g. Moxham et al., 1972; Brivio & Tomasoni, 1980; Connor et al., 1993); however, on-site stations are liable to break-down, especially due to the extreme volcanic environment, and will be destroyed during eruptions (e.g. Moxham et al., 1972; Connor et al., 1993; GVN, 1990a). Some of these problems are overcome by over-flying vent areas with aircraft-mounted radiometers. This gives a high spatial resolution, multiple waveband, synoptic view, allowing detailed analysis of vent distributions and thermal structure (e.g. Moxham, 1971; Gawarecki et al., 1980; Tabbagh et al., 1987; Bianchi et al., 1990; Oppenheimer, 1993; Oppenheimer et al., 1993; Mongillo & Wood, 1995). Aircraft and helicopter flights may be made during volcanic crises (e.g. Kieffer et al., 1981), but frequent monitoring in this way is logistically and financially unreasonable at many volcanoes. Regular monitoring is possible using satellite-borne radiometers, such as the Thematic Mapper (TM) flown on the Landsat satellite series and the Advanced Very High Resolution Radiometer (AVHRR) flown on the National Oceanographic and Atmospheric Administration's satellites. Multiple waveband data, in which fumarole fields and high temperature vents have been observed (e.g. Gaonac'h et al., 1994; Harris et al., 1995b), are available for any cloud-free sub-aerial volcano once every 16 days for the TM and once every 6 hours for the AVHRR.

Each system offers unique and complementary spectral, spatial and temporal capabilities. As a result, the best thermal monitoring approach is one that integrates ground-based, air- and space-borne data to provide a spectrally, spatially and temporally complete data set, i.e. a data set of increased resolutions. Such an approach is taken here to extract data suitable for regularly measuring, monitoring and interpreting of the thermal flux from the open conduit system at Stromboli and the fumarole field at Vulcano (Aeolian Islands).

6.3. An integrated thermal data set

For this study, an integrated thermal data set was constructed from two ground-based, one air-borne and two space-borne instruments of complementary spectral, spatial and temporal resolutions (Table 6.1).

(a) Ground based

	Compac 3	Cyclops 152
Spectral range (μm)	8 - 14	0.8 - 1.1
Temperature range (°C)	-50 - 500	600 - 3000
Response time (seconds)	0.5	0.13 - 0.45
Spatial resolution	3.8 mm @ 1 m[a] 8.6 m @ 290 m[b]	4.8 mm @ 1m[a] 1.7 m @ 290 m[b]
Instrument dimensions (mm)	90 x 82 x 126	78 x 223.5 x 170
Weight (g)	720	1000
Platform	Hand held or tripod mounted	

[a] Instrument-target distance at Vulcano, [b] Instrument-target distance at Stromboli

(b) Air-borne

	TMS	
Channel	Spectral range (μm)	Temperature range (°C)
1	0.42 - 0.45	1160 - 1620
2	0.45 - 0.52	1020 - 1440
3	0.52 - 0.60	900 - 1290
4	0.60 - 0.62	820 - 1200
5	0.63 - 0.69	780 - 1160
6	0.69 - 0.75	710 - 1090
7	0.76 - 0.90	610 - 950
8	0.91 - 1.05	470 - 760
9	1.55 - 1.75	200 - 410
10	2.08 - 2.35	90 - 260
11	8.50 - 14.0 Low Gain	-30 - 110
12	8.50 - 14.0 High Gain	-5 - 50

Spatial Resolution	Depends on height of aircraft and terrain 8/7/91: 18 x 18 m pixels for Stromboli Crater Terrace 19/7/91: 15 x 15 m pixels for Vulcano Fossa Crater
Image width (km)	~15
Platform	Aircraft (NASA's ER-2)

(c) Space-borne

	TM		AVHRR	
Band/Channel	(μm)	(°C)[c]	(μm)	(°C)
1	0.45 - 0.52	1050 - 1490	0.58 - 0.68	800 - 1350
2	0.52 - 0.60	960 - 1410	0.725 - 1.10	500 - 940
3	0.63 - 0.69	810 - 1170	3.55 - 3.93	-70 - 50
4	0.76 - 0.90	620 - 1000	10.3 - 11.3	-150 - 60
5	1.55 - 1.75	220 - 430	11.5 - 12.5	-150 - 60
6	10.42 - 12.42	-60 - 110		
7	2.08 - 2.35	120 -290		

[c] after Flynn et al. (1994)

Spatial Resolution (m)	30 and 120 (band 6 only)	1100 at nadir
Image width (km)	185	3000
Platform	Landsat satellite	NOAA satellite
Temporal resolution	16 days	12 hours (6 hrs. by maintaining 2 satellites in orbit at once)

Table 6.1. *Data set characteristics*

Ground-based thermal surveys were made at Stromboli and Vulcano during October 1994 and September 1995 using hand-held Minolta/Land Compac 3 and Cyclops 152 radiometers (Table 6.1a). Their use to measure fumaroles and open conduits has been described by Oppenheimer & Rothery (1989; 1991). These instruments have the advantages of being extremely portable and quick to use. However, obtaining a line of sight directly into a high temperature degassing vent may be dangerous or impossible, and field time limits the spatial coverage and repeatability of observations. Consequently important targets or events may be missed.

During July 1991, Stromboli and Vulcano were over-flown by an aircraft carrying the Thematic Mapper Simulator (TMS, Table 6.1b) as part of the NASA MAC Europe '91 campaign. These data complement ground-based measurements by giving a high spatial resolution synoptic view of the whole volcano, revealing all hot-spots visible to the scanner. The use of such data for magma filled vents and active lava flows has been described by Oppenheimer (1993) and Abrams et al. (1994).

Since aircraft flights are sporadic, data from two satellite-borne radiometers, the TM and AVHRR, were selected to improve the temporal capabilities of the data set (Table 6.1c). Although of coarser spatial resolution, use of TM and AVHRR data allows a regular repeat capability. The high temporal resolution of the AVHRR greatly enhances the chances of data acquisition coinciding with short, transient events or cloud-free periods. Using cheap to install receiving stations, AVHRR has the additional advantages of being free, with near-real-time monitoring permitted by direct reception (Harris et al., 1995b, 1995c). Methods to extract thermal data for fumarole fields and craters containing open conduits from TM data have been described by Gaonac'h et al. (1994), and detection of high temperature degassing vents in AVHRR data have been reported by Harris et al. (1995b).

6.4. Remote sensing measurements of surface temperature

Data from the TMS, TM and AVHRR are received in the form of digital numbers (DN). These are converted to at-satellite spectral radiance using the linear relationship

$$R_\lambda = S_\lambda \, DN_\lambda + I_\lambda \qquad (6.1),$$

in which R_λ, S_λ, DN_λ and I_λ are at-satellite spectral radiance, slope, DN and intercept for a channel of central wavelength λ. If not appended to the image as part of a header file, coefficients S_λ and I_λ can be calculated using NASA/AMES (1991) for TMS, Markham & Barker (1986, 1987) for TM, and Lauritson et al. (1988) for AVHRR. Due to the non-linear response of AVHRR channels 4 and 5, R_λ should be corrected for non-linearity using the method and coefficients given by Weinreb et al. (1990) and Kidwell (1995). For measurements in the thermal infrared (8.0-15.0 μm), surface temperature (T) can be calculated from

$$R_\lambda - R_{\lambda U} = R_{\lambda thermal} = \tau_\lambda \varepsilon_\lambda L(\lambda T) \qquad (6.2),$$

in which, $R_{\lambda thermal}$ is thermal radiation emitted by the surface received by the sensor, $R_{\lambda U}$ and τ_λ are up-welling atmospheric path radiance and atmospheric spectral transmissivity, both of which can be estimated using LOWTRAN atmospheric code (Kneizys et al., 1983), and ε_λ is surface spectral emissivity; values used here are shown in Table 6.2. $L(\lambda T)$ is the Planck function for isotropic radiation, given by:

$$L(\lambda T) = c_1 \lambda^{-5} \{\pi [\exp(c_2/\lambda T) - 1]\}^{-1} \qquad (6.3),$$

where c_1 and c_2 are constants with the values 3.742×10^{-16} W m^2 and 1.4388×10^{-2} m K.

Channel/ Band	Spectral range (μm)	Emissivity (ε_λ)	
		Stromboli	Vulcano
TMS			
9	1.55-1.75	0.935	Not available
10	2.08-2.35	0.928	Not available
11 & 12	8.50-14.0	0.956	0.974
TM			
5	1.55-1.75	0.935	Not available
6	10.42-12.42	0.949	0.970
7	2.08-2.345	0.928	Not available
AVHRR			
3	3.55-3.93	0.951	0.965
4	10.3-11.3	0.944	0.977
5	11.5-12.5	0.963	0.984

Table 6.2. *Spectral emissivity (ε_λ) for volcanic surfaces at Stromboli and Vulcano. Emissivities were calculated using the spectral reflectance for scoria taken from within Stromboli's crater terrace and a trachytic-rhyolitic block taken from Vulcano's Fossa crater. Reflectance spectra were measured between 2.08 and 14 μm using a Nicolet system FTIR spectrometer by J. Salisbury (Johns Hopkins University) and between 0.4 and 2.5 μm using a GER IRIS Mk IV spectrometer by A. Denniss (Open University). Spectral reflectances (ρ_λ) were calculated by integrating reflectance spectra over each TMS, TM and AVHRR waveband, and used to calculate ε_λ from Kirchhoff's Law ($\varepsilon_\lambda = 1 - \rho_\lambda$).*

For daytime measurements in the short-wave infrared (0.4-2.5 μm) and mid-infrared (3.0-5.5 μm) the contribution of $R_{\lambda U}$ is not significant, but non-thermal radiation reflected by the surface ($R_{\lambda non\text{-}thermal}$) must be considered, where

$$R_{\lambda non\text{-}thermal} = \tau_\lambda \rho_\lambda R_{\lambda D} \qquad (6.4),$$

in which ρ_λ is the spectral reflectivity of the surface and $R_{\lambda D}$ is down-welling atmospheric path radiance. To obtain surface temperature, $R_{\lambda non\text{-}thermal}$ must be estimated and

removed. Estimation of $R_{\lambda non\text{-}thermal}$ is achieved here for pixels in the 0.4-2.5 μm waveband using the mean R_λ for the nearest pixels which have no thermal contribution. For 3.0-5.5 μm waveband pixels $R_{\lambda non\text{-}thermal}$ is estimated by assuming that the 8.0-15.0 μm minus the 3.0-5.5 μm temperature difference for adjacent non-anomalous pixels is due to the non-thermal contribution. $R_{\lambda non\text{-}thermal}$ is then substituted into Equation 6.2 to give

$$R_\lambda - R_{\lambda non\text{-}thermal} = R_{\lambda thermal} = \tau_\lambda \varepsilon_\lambda L(\lambda T) \qquad (6.5).$$

Hand-held radiometer measurements were corrected for emissivity using the broad-band (8.0-14.0 μm) volcanic rock emissivities given by Salisbury & D'Aria (1992).

6.5. Stromboli: activity, magma system and hazard monitoring

Stromboli has probably been in a state of more or less continuous activity since observations were first made by Aristotle 2000 years ago (Chouet et al., 1974; Giberti et al., 1992). During October 1994 and September 1995 we made detailed observations of current activity within Stromboli's crater terrace (Figure 6.1 and Table 6.3). On both occasions continuous degassing and frequent explosive events occurred from between 5 and 15 open vents, sending gas, incandescent ejecta and ash to heights of up to 300 m. Frequent observations made over the last 100 years show that this has been the typical mode of activity over at least this time (Washington, 1917; De Quervain & Streckeisen, 1927; Abbruzzese, 1937, 1940; Bullard, 1954). Occasionally activity is punctuated by effusive eruptions, the most recent occurring in 1975 and 1985-86 (Nappi, 1976; Capaldi et al., 1978; Rosi & Sbrana, 1988; Nappi & Renzulli, 1989), and paroxysms sending ash

Figure 6.1. *Stromboli's crater terrace in (a) October 1994 and (b) September 1995. (b) is produced using EDM and triangulation measurements, (a) is a sketch map which has been fitted to (b) using common ground control points. Labelled vents were observed as active during the measurements (Table 6.3), unlabelled vents were observed as active during October 1995 (A. Maciejewski, personal communication).*

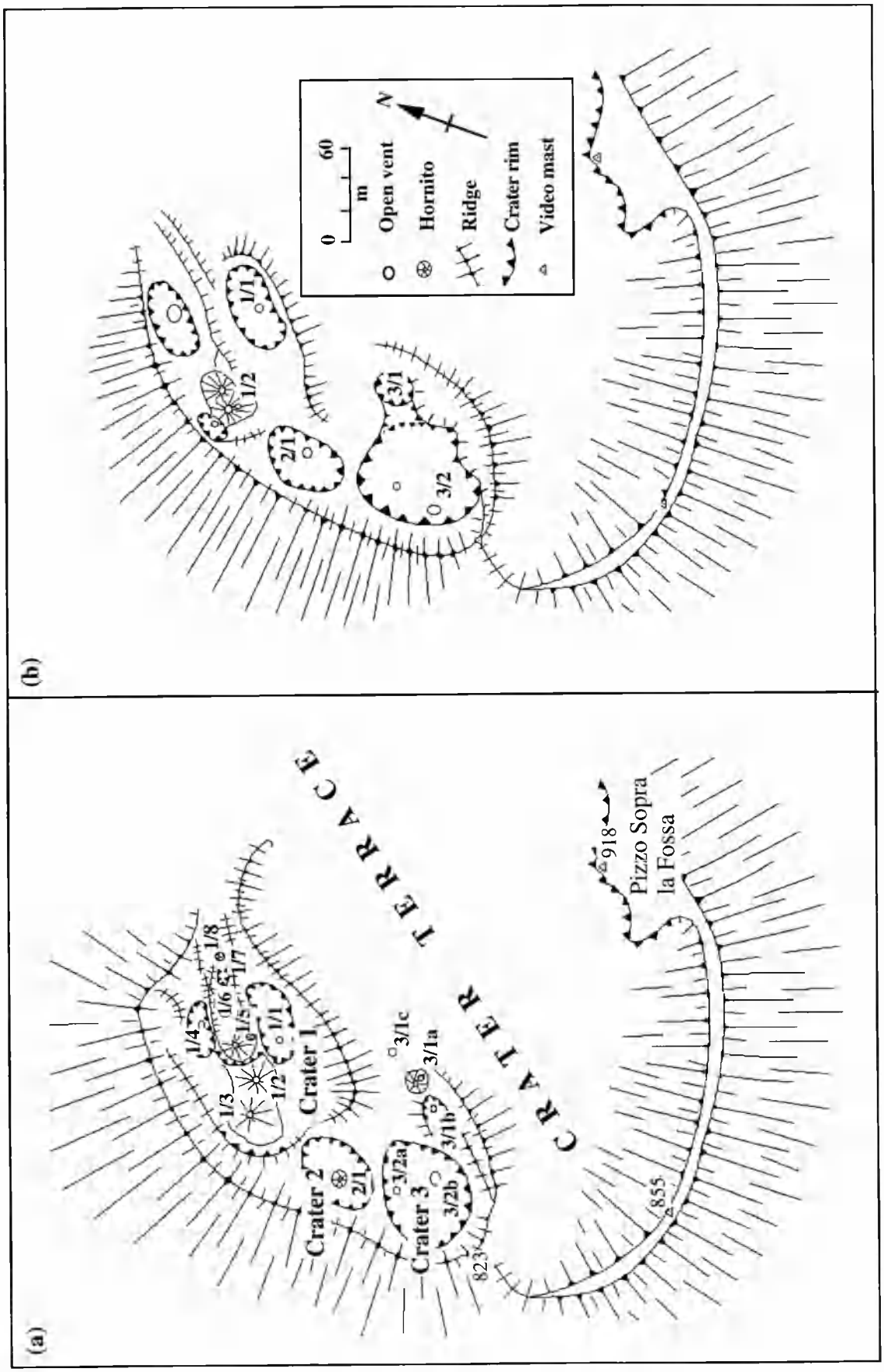
(a)
TERRACE
CRATER
Crater 1
Crater 2
Crater 3
1/1
1/2
1/3
1/4
1/5
1/6
1/7
1/8
2/1
3/1a
3/1b
3/1c
3/2a
3/2b
823
855
918
Pizzo Sopra
la Fossa
(b)
0
60
m
Open vent
Hornito
Ridge
Crater rim
Video mast
N
1/1
1/2
2/1
3/1
3/2

(a) October 1994	Craters 3 and 2						Crater 1									Tot.
Vent	3/1a	3/1b	3/1c	3/2a	3/2b	2/1	1/1	1/2	1/3	1/4	1/5	1/6	1/7	1/8	1/9	15
Night-glow	Y	Y	N	Y	Y	N	Y	N	Y	N	Y	N	Y	N	N	8
Explosions/hour																
Max	0	0	0	0	9	0	5	0	3	2	0	4	3	0	0	17
Min	0	0	0	0	3	0	3	0	1	1	0	0	1	0	0	11
Mean	0	0	0	0	5	0	4	0	1.5	1.5	0	2.3	2.5	0	0	14
Ejecta type	d	d	d	gb	gba	d	gba	d	g	gb	d	gba	gba	d	d	
Estimated ejecta height (m) * oblique ejection	0	0	0	50 TO 300		0	200	0	50	150*	0	200	150	0	0	

(b) Sept 1995	Craters 3 and 2			Crater 1			Tot.
Vent	3/1	3/2	2/1	1/1	1/2		10^x
Night-glow	Y	Y	N	Y	Y		4
Explosions/hour							
Max	0	5	4	5	3		11
Min	0	3	0	3	2		7
Mean	0	3.75	1.8	4	2.8		9
Ejecta type	e	gba	gb	gba	gb		
Estimated ejecta height (m)	10	150	150	150	50		

Key
x: total includes Oct 95 vents
d: continual degassing only
g: gas eruption
b: bombs
a: ash
e: frequent, quiet bomb ejection

Table 6.3. *Summary of activity observed at Stromboli during October 1994 and September 1995. Total vent count for September 1995 includes vents observed as active during October 1995 by A. Maciejewski (Open University).*

up to 10 km above the summit (Barberi et al., 1993).

Explosive activity poses hazards to hundreds of tourists who view the activity from Pizzo Sopra la Fossa each year (Figure 6.3). This area is frequently reached by pyroclasts (Barberi et al., 1993), resulting in injury and access restrictions (SEAN, 1989a; GVN, 1993d; GVN, 1995b). Historic lava flows affect an uninhabited and inaccessible sector of the volcano, however fallout and hot avalanches from paroxysms pose serious hazard, having caused property damage and deaths on at-least 8 occasions since 1900 (Arnaud, 1988; Barberi et al., 1993).

6.5.1. Ground-based vent measurements

Using the Cyclops 152, vent temperatures were measured by gaining a line of sight directly into vent 3/1a in October 1994 and vent 1/2 during September 1995 (Figure 6.1). No lava was visible in either vent, but vent walls were incandescent due to the passage of high temperature gas. Vents 3/1a and 1/2 gave maximum temperatures of 873 and 940 °C respectively. During the 1995 observations, the diameter of vent 1/2 was measured as 4 m using triangulation. This is identical to the visual estimate made for vent 3/1a in 1994, and compares with diameters between 0.5 and 10 m estimated from other visual observations (Chouet et al., 1974; Settle & McGetchin, 1980; Arnaud, 1988; Giberti et al., 1992).

6.5.1.1. Magma depth and feeder system

Stevenson (1993) provides a model which allows magma depth to be estimated if gas temperature at the conduit exit (T_{exit}) and conduit radius (r_c), along with magma surface temperature (T_{magma}), distance to ambient temperatures (r_a) and mass flow rate per unit area are known. Although devised for application to narrow centimetre-radius fumarole pipes, the assumptions on which the model are based are equally applicable to wider, metre-radius, de-gassing conduits. Following Giberti et al. (1992) a T_{magma} of 1000 °C is assumed and the radius of the crater terrace (~100-200 m) used for r_a. By distributing the time averaged total gas flux of 150±90 kg s^{-1} given for Stromboli by Allard et al. (1994) between ten 4 m diameter vents, a mass flow rate of 0.5-1.9 kg s^{-1} m^{-2} is obtained. This puts the top of a shallow magma body at 250 to 1000 m.

This is in good agreement with estimates made from photoballistic, seismic and thermal modelling measurements which place the magma source at 50 to 600 m below the crater terrace (Chouet et al., 1974; Giberti et al., 1992; Neuberg et al., 1994; Ripepe & Braun, 1994). The presence of a small (<100 m wide), shallow (100-600 m deep) magma chamber or feeder dyke to which some vents are linked is postulated to explain relationships in statistical, seismic and thermal data (Settle & McGetchin, 1980; Ntepe & Dorel, 1990; Harris et al., 1996).

6.5.1.2. Thermal flux

Using our measurements of vent temperatures and area we calculate radiative and convective heat losses at the conduit exit (Q_{rad} and Q_{conv}) and heat loss by conduction through the conduit wall between the magma surface and the vent (Q_{cond}).

For a roughly circular conduit of radius r_c,

$$Q_{rad} = \pi r_c^2 \sigma \varepsilon T_{exit}^4 \qquad (6.6),$$

in which σ is the Stefan-Boltzmann constant (5.6697×10^{-8} Wm^{-2} K^{-4}) and ε is emissivity (here assumed to be 0.9887, the broadband emissivity for basalt after Salisbury & D'Aria [1992]). Given T_{exit} of 1143 and 1213 K, and r_c of 2 m, Q_{rad} will be 1.2 and 1.5 MW respectively.

Following Holman (1992), free convective loss can be estimated from

$$Q_{conv} = 0.14 \pi r_c^2 k (g\alpha p/\mu\kappa)^{1/3} (T_{exit} - T_{air})^{4/3} \qquad (6.7),$$

where g is acceleration due to gravity, and k, α, p, μ, and κ are thermal conductivity, density, cubic expansivity, dynamic viscosity and thermal diffusivity for air at a mean temperature of $(T_{air}+T_{exit})/2$. Values for these parameters are given by Kays and Crawford (1980). For both exit temperatures this gives Q_{conv} of 0.2 MW.

Conductive losses will be expressed by

$$Q_{cond} = [2\pi k_w L(T_{gas} - T_{surf})] / \ln(r_a/r_c) \qquad (6.8),$$

in which k_w is the wall rock thermal conductivity (3 Wm^{-1} K^{-1}, Giberti et al. (1992)), L is the conduit exit to magma surface distance, T_{gas} is the gas temperature in the conduit, approximated from $(T_{magma}+T_{exit})/2$, and T_{surf} is ambient surface temperature. This gives

total thermal loss from the conduit $Q_{conduit}$ (= Q_{rad}+Q_{conv}+Q_{cond}) of 4.0±1.5 and 4.3±1.5 MW for the 870 and 940 °C vents. This must be a minimum estimate for total heat loss from the conduit (Q_{tot}) since it does not include heat carried by the gas phase or by ejecta and gas expelled during eruptions, neither of which can be estimated using vent temperature and area data alone (see Harris & Stevenson, 1996).

Although night glow was observed at several other vents (Table 6.3), it was impossible to gain a safe line of sight into these. We therefore took advantage of the synoptic view of the crater terrace provided by TMS to monitor and measure all crater terrace vents.

6.5.2. TMS thermal measurements

July 1991 was characterised by typical explosive activity at Stromboli, with an average of 6 explosions/hour from vents within craters 1 and 3 and gas emission from crater 2 (GVN 1991a, 1991b). On 8 July Stromboli was over-flown by an aircraft carrying TMS. The image showed the whole crater terrace to be marked by anomalously high radiance in bands 11 and 12, within which 5 active vent areas were marked by hot spots in bands 9 and 10 (Figure 6.2a). If the surface occupying a pixel is isothermal and can be described by L(λT) (Equations 6.2 or 6.5), then thermal emittance in bands 10 and 9 indicates surface temperatures of at least 90 and 200 °C respectively (Table 6.1). However, for a 18 x 18 m pixel over a 4 m diameter Strombolian vent the pixel thermal structure will be more accurately described by:

$$R_{\lambda thermal} = \tau_\lambda \varepsilon_\lambda [p\, L(\lambda T_h) + (1-p)\, L(\lambda T_b)] \qquad (6.9),$$

Figure 6.2. *Thermal maps indicating location of high temperature vents on 8 July 1991 produced from (a) TMS spectral radiance in bands 9, 10 and 12 and (b) radiant flux density. Image data have been fitted to the September 1995 crater terrace map (Figure 6.1b) and (b) has been mapped using the procedure given by Harris et al (1995c).*

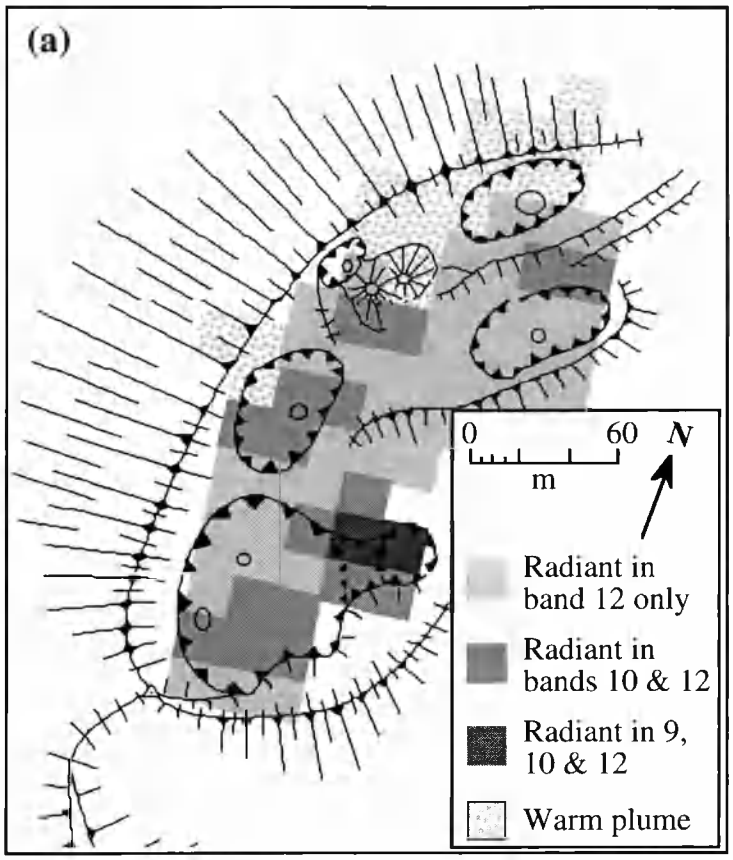
(a)
0
60
m
N
Radiant in band 12 only
Radiant in bands 10 & 12
Radiant in 9, 10 & 12
Warm plume

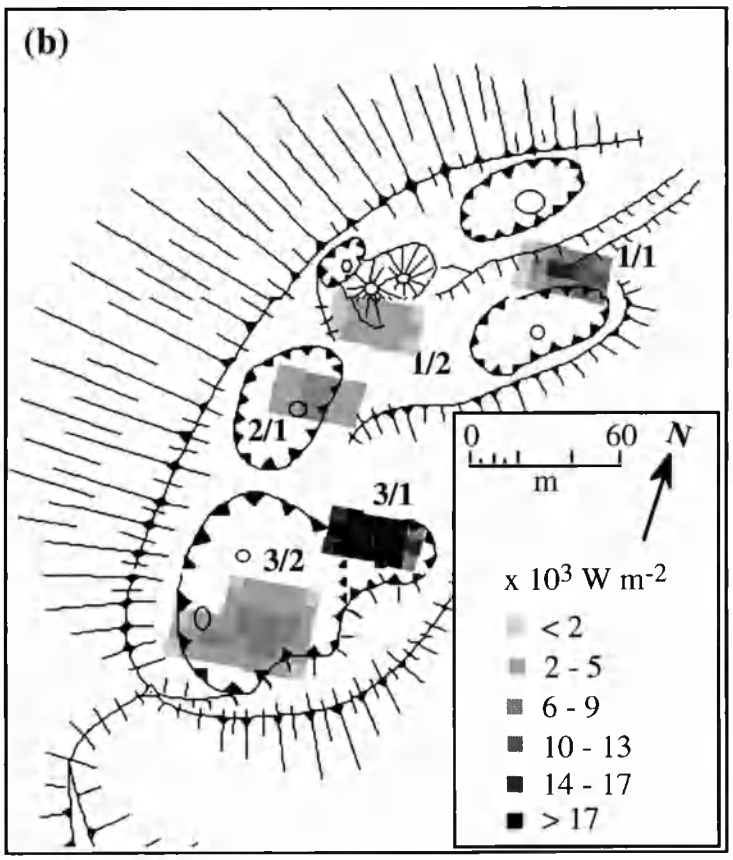
(b)
1/1
1/2
2/1
3/1
3/2
0
60
m
N
x 10³ W m⁻²
< 2
2 - 5
6 - 9
10 - 13
14 - 17
> 17

where the pixel with the integrated radiance $R_{\lambda thermal}$ is occupied by a sub-pixel vent at temperature T_h occupying portion p of the pixel surrounded by a cooler background at T_b occupying the remainder $(1-p)$ of the pixel. In this case, T_h can be much higher than the pixel integrated temperature obtained from Equations 6.2 or 6.5.

Where $R_{\lambda thermal}$ are available at two widely separated wavebands, x and y, the size and temperature of the sub-pixel vent can be calculated by solution of simultaneous equations (Dozier, 1981):

$$R_{xthermal} = \tau_x \varepsilon_x [p\, L(\lambda_x T_h) + (1-p)\, L(\lambda_x T_b)] \quad (6.10)$$

$$R_{ythermal} = \tau_y \varepsilon_y [p\, L(\lambda_y T_h) + (1-p)\, L(\lambda_y T_b)] \quad (6.11).$$

Solution requires a value for one of the three unknowns T_h, T_b and p to be assumed or derived independently. Using the TMS data, p and T_h were estimated using emitted radiance in bands 10 and 11 and a value for T_b taken from the mean band 11 temperature for the nearest non-vent pixels. Solution of Equations 6.10 and 6.11, and assuming a magma depth of 625±375 m, allows estimation of all parameters in Equations 6.6 to 6.8 for all vent areas (Table 6.4) and enables radiant flux density (Q_{rad}/area) to be mapped (Figure 6.2b).

6.5.2.1. Activity

TMS-based estimates for the diameters of vents 1/1, 1/2 and 2/1 (Table 6.4) were between 4 and 8 m, in agreement with ground estimates. However, it is possible that some of the vent areas identified in this way are occupied by more than one vent in which case the area of each vent would be smaller than estimated here, although the total area of vents within each crater would be unaffected. The mapped location of hot-spots (Figure 6.2) coincide with those expected from field-reports during August (GVN, 1991c, 1991d). These show vents 1/1 and 1/2 to be coincident with 150 m high fountain activity from the

Vent	Temp. range (°C)	Vent area (m^2)	Vent radius (m)	Q_{rad} (MW)	Q_{conv} (MW)	Q_{cond} (MW)	$Q_{conduit}$ (MW)
1/1	250-260	60	4	0.3	0.2	2±1	2.5±1
1/2	280-300	30	3	0.1	0.1	1.9±1	2.1±1
2/1	290-370	20	2	0.2	0.1	1.8±1	2.1±1
3/1	460-480	30	3	0.3	0.2	2.2±1.5	2.7±1.5
3/2	260-310	190	8	1.1	0.9	2.6±1.5	4.6±1.5
Total	250-480	330	20	2.0	1.5	10.5±6	14±6

Table 6.4. *Stromboli vent parameters derived from TMS data for the active vent locations given in Figure 6.2b.*

NE of crater 1 and emission of incandescent tephra from a hornito respectively. No explosions were reported on the ground from vent 2/1, but glow from radial fissures and sustained gas emissions were observed (GVN, 1991c, 1991d). Temperatures at these vents are lower than those measured in 1994 and 1995 (Table 6.4), but in the temperature range of 225 and 700 °C obtained in 1988 for an incandescent vent at Stromboli by Oppenheimer & Rothery (1989).

Highest temperatures were obtained for vent 3/1 (Table 6.4, Figure 6.2b). Temperatures approach the upper range expected for a crusted lava lake surface (500-800 °C, Flynn et al. 1993), and may therefore indicate activity at a small lava pond. Ground-based observations during August confirm this, showing the vent to be the source of small, active lava ponds (GVN, 1991d). Persistence of activity in the vent 3/1 area is noteworthy, being the location of high temperature vent 3/1a measured at 873 °C in 1994 and observed to be the site of night-glow in 1994 and 1995 (Table 6.3). Incandescence from a vent in this area has been observed regularly since 1990 (B. Behncke, personal communication), with frequent reports of incandescence or active lava ponds (GVN 1990b, 1993c, 1994a, 1994b, 1994c, 1995a, 1995c).

The large area covered by vent 3/2 (Table 6.4, Figure 6.2b) indicate that this is the site of a cluster of vents rather than a single vent. This was confirmed by observations in

late August which revealed a pit in the SW of crater 3 containing at-least three open vents, of which two were incandescent (GVN, 1991d).

6.5.2.2. Thermal flux

Using the TMS data, $Q_{conduit}$ for all open conduits is estimated as 14±6 MW (Table 6.4). Heat loss due to radiation (Q_{rad}, Table 6.4) is an order of magnitude greater than that previously estimated by McGetchin & Chouet (1979), who used data from the photoballistic study of Chouet et al. (1974) to estimate 0.2 MW.

Although the TMS data allowed analysis of all vents within the crater terrace, there was only one over-flight. To allow a more complete temporal analysis we therefore used the regular thermal data available from Landsat's TM (Table 6.1).

6.5.3. TM thermal measurements

Two cloud-free TM images covering the Aeolian Islands were acquired during July and August 1994. On both images, most of the crater terrace was radiant in band 7, with two active vent areas apparent as hot spots in bands 5 and 7 (Figure 6.3). Assuming an isothermal pixel structure, thermal emittance in bands 7 and 5 implies surface temperatures greater than 120 and 220 °C respectively (Table 6.1). During the August pass, three band 5 pixels were saturated, i.e. the upper limit of the band 5 measurement range had been reached, implying a temperature of at-least 430 °C (Table 6.1). Using emitted radiance in bands 5 and 7 and assuming T_b, calculated using the mean band 6 temperature for the nearest non-vent pixels, vent temperatures and areas were estimated using Equations 6.10 and 6.11. Unfortunately 8 out of 13 pixels in which there was thermal emittance in bands 5 and 7 were saturated in band 7. Saturated pixels cannot be used in Equations 6.10 and

---

Figure 6.3. *Thermal maps indicating location of high temperature vents on (a) 18 July 1994 and (b) 3 August 1994 produced from TM spectral radiance in bands 5 and 7. Image data have been fitted to the September 1995 crater terrace map (Figure 6.1b).*

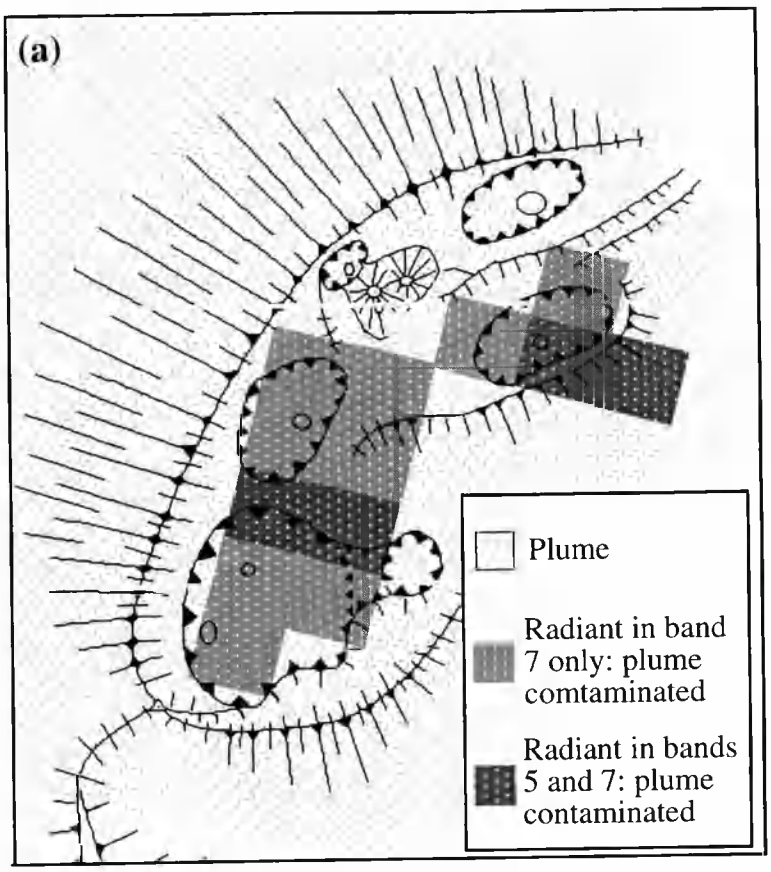
(a)
Plume
Radiant in band 7 only: plume comtaminated
Radiant in bands 5 and 7: plume contaminated

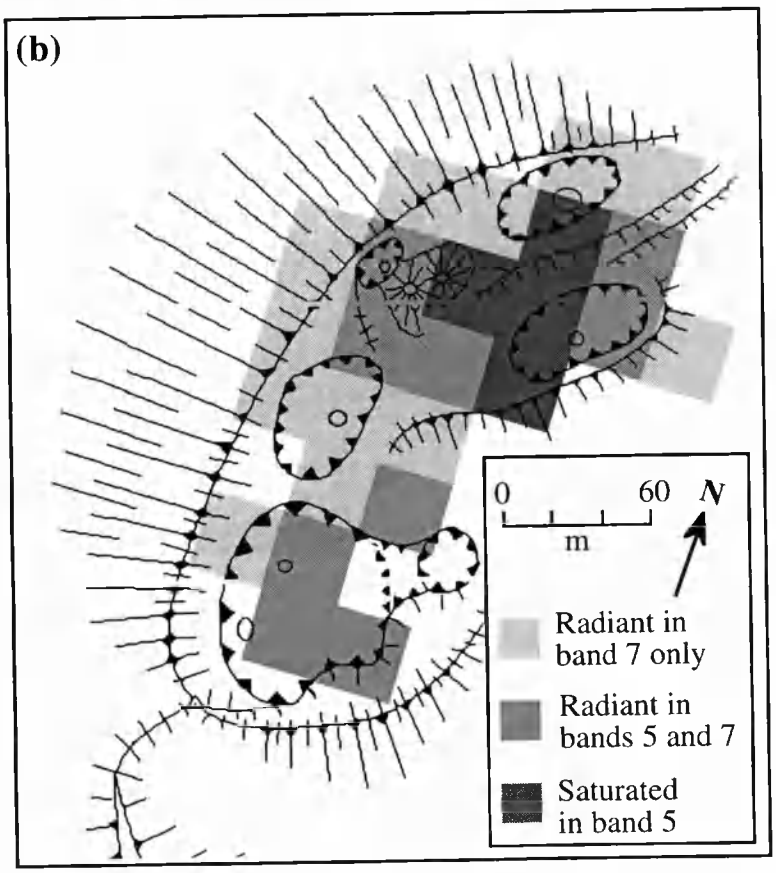
(b)
0
60
m
N
Radiant in band 7 only
Radiant in bands 5 and 7
Saturated in band 5

6.11, and bands 5 and 6 cannot be used as a pair because of the difference in pixel size (Table 6.1).

However, following Gaonac'h et al. (1994) relative radiative flux (Q_{rel}) can be estimated from band 6 alone. To remove surface temperature variations caused by cooler air temperatures at higher altitudes, a height independent, corrected temperature (θ) is calculated for each pixel (Bonneville et al., 1985; Gaonac'h et al., 1994):

$$\theta = T + h\alpha \qquad (6.12),$$

in which T is the satellite derived surface temperature (Equation 6.2), h is surface altitude and α is the adiabatic gradient (0.006 $^{\circ}C\ m^{-1}$). Q_{rel} is then estimated by adapting Sekioka & Yuhara (1974):

$$Q_{rel} = \{4.614\varepsilon[0.52+0.065(e)^{0.5}]\Delta\theta\} \qquad (6.13),$$

where e is vapour pressure and $\Delta\theta$ is the difference between maximum θ within the anomaly and minimum θ from all pixels adjacent to the anomaly (Gaonac'h et al., 1994).

6.5.3.1. Activity and structural control

Temperatures obtained using unsaturated pixels within crater 1 and on the western side of crater 3 were consistent with high temperature degassing vents (~800 $^{\circ}C$). However, temperatures obtained for unsaturated pixels on the eastern side of crater 3 gave ~1000 $^{\circ}C$, revealing the persistence of lava ponds at this location since the 1991 TMS over-flight. As noted, this has been the location of lava activity and incandescence since 1990. During March and May 1994 it was reported as the site of a lava pond displaying almost continuous spattering (GVN, 1994a, 1994b). The saturation of band 5 pixels within crater 1 suggests a concentration of high temperature vents; this is supported by the October ground observations which located 9 open vents within this crater (Table 6.3).

Maps produced from ground, TMS and TM data show a persistence of activity within craters 1 and 3, and to a lesser extent crater 2, with active vents aligned along a SW-NE trend (Table 6.3, Figures 6.1, 6.2 & 6.3). Activity has persisted at these three locations since at-least 1768, with activity at crater 2 being far more intermittent than at craters 1 and 3 (Washington, 1917; Schick & Mueller, 1988). Vent alignment and persistence correlates with a major SW-NE regional tectonic line, the Stromboli-Panarea-Lipari fault system, which crosses the centre of Stromboli. Fumaroles, soil gas emission, hot springs, dyke trends, elongation of the island, parasitic vents and Strombolicchio, an eroded remnant of a pre-Stromboli cone, are also aligned along this axis (Rosi, 1980). Main collapse structures occur on either side of this axial line, including the Sciara del Fuoco collapse which involved ~1.81 km^3 of rock <5000 years ago (Kokelaar & Romagnoli, 1995). This lineament therefore acts as a major control on the location of persistent activity and structural instabilities.

6.5.3.2. Thermal flux and activity

Using a TM band 6 image of Stromboli acquired on 23 October 1986, 6 months after an effusive eruption, Gaonac'h et al. (1994) estimated Q_{rel} from the crater terrace of 29 W m^{-2} distributed across 4.3 x 10^4 m^2. In the present study, plume contamination on the July 1994 image excluded this image from quantitative analysis, but the 3 August 1995 image gave Q_{rel} of 65 W m^{-2} similarly distributed across 4.3 x 10^4 m^2, in other words three band 6 pixels. This doubling of Q_{rel} since October 1986 reflects differing levels of activity on the two dates as indicated by ground observations. Ground reports show that in October 1986 activity was recovering from the effects of the effusive event. During the eruption, activity within the crater terrace was much weaker than normal, resuming during the months following May 1986, and reaching 8-10 explosions/hour by October (Nappi & Renzulli, 1989).

Conversely, 3 August 1994 was during of a period of intense activity. Activity reached a peak of 36 explosions/hour on 19 July, continuing at high levels until 7 August,

with pyroclastics often reaching usual tourist zones (GVN, 1995c). The higher level of Q_{rel} clearly marks this energetic, and dangerous, phase of activity.

Unfortunately, TM images are expensive (US$ 4000 per scene) and cannot be received directly. As a result we were only able to obtain two scenes, with delivery taking ~4 months. To produce a more complete time-series we therefore took advantage of AVHRR data, which are immediately and freely available, and are far more frequent than TM (Table 6.1).

6.5.4. AVHRR thermal measurements

Theoretically, ten 4 m diameter vents at 940 °C against a background of 0 °C centred in a 1 km AVHRR pixel will give channel 3 and channel 4 temperatures (T_3 and T_4) of 52 and 0.6 °C respectively. However, for ground at ambient temperatures T_3 minus T_4 (T_{3-4}) will be close to zero. This difference in sensitivity to sub-pixel hot-spots makes T_{3-4} a valuable tool for locating sub-pixel volcanic hot-spots and distinguishing them from solar heated anomalies (Figure 6.4). Once a volcanic thermal anomaly has been located, the sub-pixel thermal structure can be estimated by using channels 3 and 4 and an assumed T_h in Equations 6.10 and 6.11, with ~900 °C being a reasonable T_h for activity at Stromboli. This allows the T_b and A_h (area occupied by T_h) to be estimated. By substituting A_h and T_h as πr_c^2 and T_{exit} in Equation 6.6, Q_{rad} can be estimated.

Where channel 3 is saturated, but the less-sensitive channel 4 is not, radiance in channel 4 due to the volcanic target (R_{4volc}) can be estimated from

$$R_{4volc} = \tau_4\varepsilon_4 L(\lambda_4 T_v) - \tau_4\varepsilon_4 L(\lambda_4 T_{nv}) \qquad (6.14),$$

where T_v is the temperature for the pixel containing the volcanic source, and T_{nv} is the mean temperature of all non-volcanic pixels immediately adjacent to the volcanic pixel.

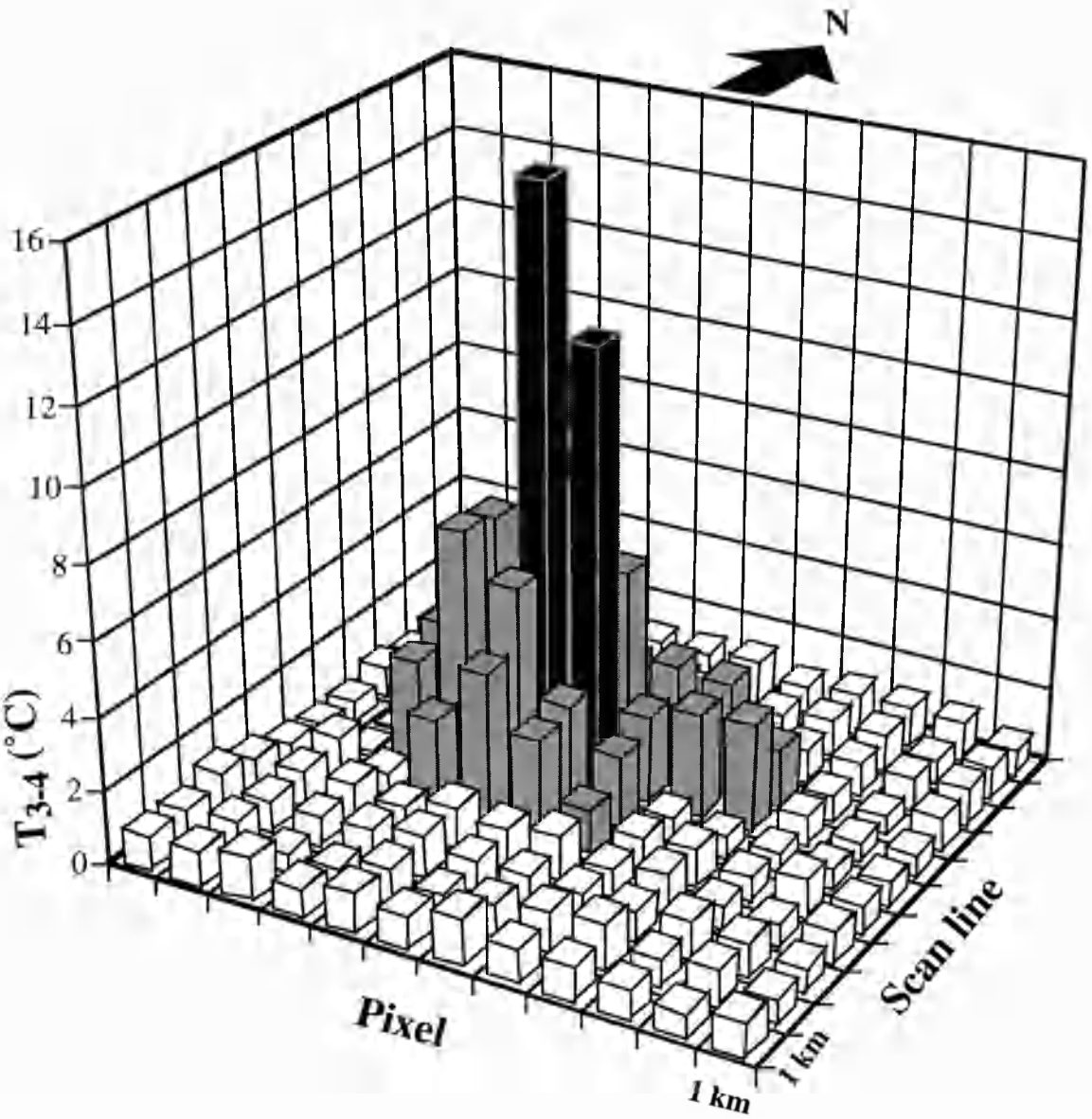

Figure 6.4 *T_{3-4} over Stromboli on an 18 June 1994 AVHRR image. Black pixels contain sub-pixel hot-spots as indicated by highly elevated T_{3-4}, and locate activity at the crater terrace. Grey and white pixels indicate those pixels containing land at ambient temperatures and sea respectively.*

6.5.4.1. Activity and hazard monitoring

Analysis of 34 cloud-free AVHRR images between July 1990 and October 1994 reveals a persistent hot-spot at Stromboli (Figure 6.4). On 14 images the hot spot was sufficiently intense to saturate channel 3. However, unsaturated channel 4 data allow a R_{4volc} time series to be produced (Figure 6.5a). Comparison with ground reports shows

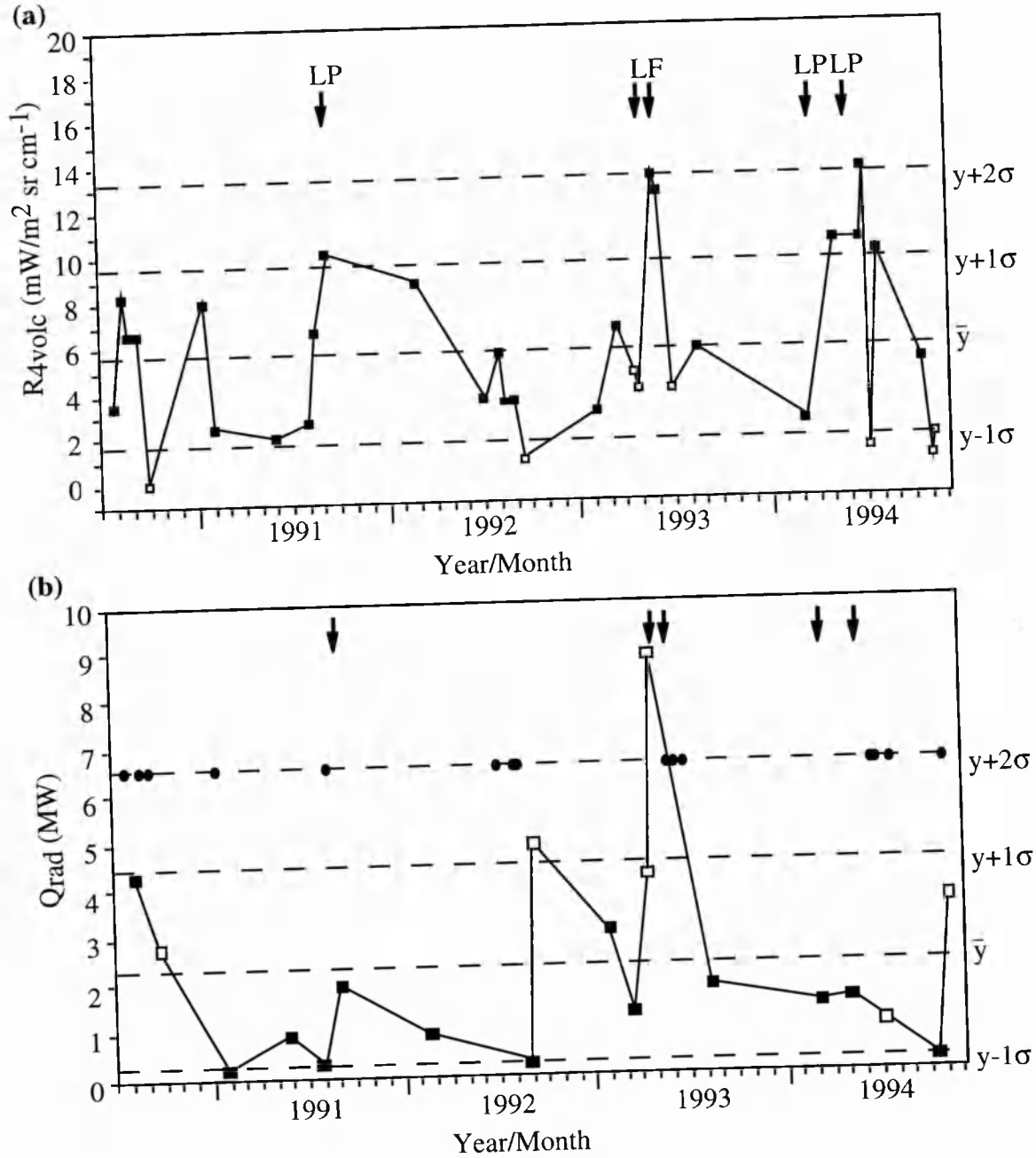

Figure 6.5. *AVHRR 1990 to 1994 times series for (a) R_{4volc} and (b) Q_{rad} at Stromboli. LP and LF indicate ground reports of lava ponds or lava flows. White symbols represent cloud-contaminated data, as indicated by conflicting R_{4volc} and Q_{rad}. Occasions when channel 3 was saturated and Q_{rad} could not be estimated are indicated by black circles, these are plotted for convenience along the 2σ line.*

that the only occasions on which R_{4volc} was elevated by more than one standard deviation above the mean were during three periods when lava activity was reported within the crater terrace. Periods of elevated R_{4volc} in August 1991 and March - May 1994 correlate with lava pond activity (GVN 1991d; GVN 1994a, 1994b) and during May 1993 with short, <30 m long, lava flows (GVN, 1993c).

Given a background temperature of 0 °C, a 1 km channel 3 pixel will saturate if it conatins a body at 900 °C larger than ~200 m^2. As the background rises to 40 °C, so the area that the 900 °C body must occupy in order to cause saturation decreases to ~55 m^2. Since much of Stromboli's summit consists of vegetation free basalt, on which temperatures of 30-52 °C were measured during 1994, channel 3 is frequently saturated and unusable during summer or effusive periods (Figure 6.5b). Leaving those dates aside, Q_{rad} estimated using unsaturated data varied between 0.2 and 8.8 MW, in comparison with 2 MW obtained using TMS.

Existing atmospheric correction procedures allow data to be corrected only for a standard plume-free atmosphere. Therefore, variations in R_{4volc} and Q_{rad} may reflect fluctuations not only in activity, but also the amount of plume contaminating the signal. Differential absorption properties of water vapour at the channel 3 and 4 wavelengths (Singh, 1984) will cause a water vapour laden plume to attenuate the channel 4 signal far more than the channel 3 signal. The effect on the solution of Equations 6.10 and 6.11 of decreasing R_4 with respect to R_3 will be to increase the value of p, and consequently Q_{rad}. Dense plumes therefore explain extreme troughs in the R_{4volc} plot and conflicting R_{4volc} and Q_{rad} plots. Such points are thus regarded as plume contaminated and unreliable (Figure 6.5).

Variation in R_{4volc} and Q_{rad} may also result from changes in vent temperature. However, Harris et al. (1996) showed vent temperature to be stable over a 5 hour period of near-continuous measurements, and our observations show a difference of just 70 °C over 12 months. We therefore assume maximum vent temperatures to be constant at 900±50 °C.

Activity at Stromboli between 1990 and 1994 was typical for non-effusive activity at this volcano. Therefore the mean and standard deviation for the R_{4volc} and Q_{rad} time-series during this period can be regarded as a baseline against which activity during other periods can be assessed. The potential of this approach was assessed using data acquired before, during and after the effusive eruption which began on 6 December 1985, with emission of a hot avalanche and lava flows, and continued until 25 April 1986 covering a 0.16 km^2 area (Rosi & Sbrana, 1988; Nappi & Renzulli, 1989). Using the baseline, the onset of activity was clearly detectable, causing channel 3 to saturate and R_{4volc} to be elevated by more than two standard deviations above the mean (Figure 6.6). R_{4volc} remained at this high level throughout the eruption. Although the presence of cooling lava flows caused R_{4volc} to remain elevated until well after eruption, the end of effusive activity was defined by termination of channel 3 saturation and a decline in Q_{rad}. There are indications of increases by more than 2 standard deviations above the mean before both the 1993 and 1985-1986 effusive events, but unfortunately the points are possibly plume contaminated and unreliable (Figures 6.5b and 6.6b). However, comparison with ground observations shows the baseline to be a reliable tool to detect the onset of effusive activity and distinguish normal, minor effusive/lava pond and major effusive activity at Stromboli.

The global coverage provided by the AVHRR means that this approach could be used to monitor thermal activity at any sub-aerial volcano. Such an approach was suggested by Francis (1979) using repeated airborne surveys, but was viewed as unlikely due to the prohibitive cost of sustained use of aircraft. AVHRR data overcome this drawback, because they are freely available for all volcanoes.

6.6. Vulcano: activity, magma system and hazard monitoring

Activity at Vulcano typically follows a four phase "Vulcanian" cycle: (1) a quiet phase characterised by fumarolic activity, followed by (2) an explosive eruption beginning with a surge phase, developing into (3) a Vulcanian phase, with surge and fall deposits, ending with (4) a lava effusion phase (Frazzetta et al., 1983; Frazzetta & La Volpe, 1991).

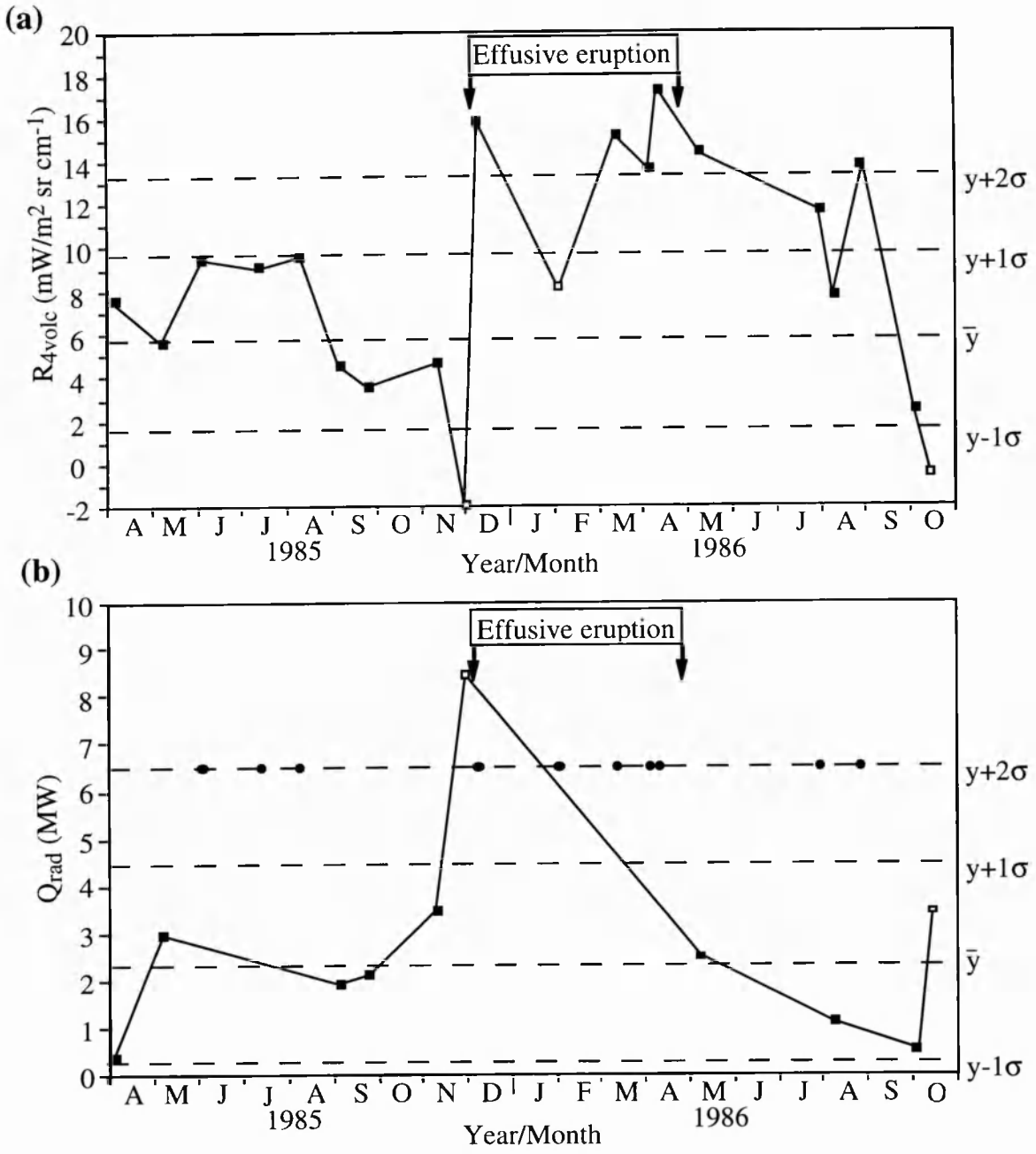

Figure 6.6. *AVHRR times series for (a) R_{4volc} and (b) Q_{rad} at Stromboli between April 1985 and October 1986 spanning a major effusive eruption which began on 6 December 1985 and continued until 25 April 1985 as indicated. The mean and standard deviation are those calculated using the 1990 to 1994 baseline time series given on Figure 6.5. See Figure 6.5 for key.*

This cycle is evident from historical records dating from 475 B.C., which show explosive activity with repose periods of 30-840 years, interspersed with periods of fumarolic discharge (Frazzetta et al., 1984).

During October 1994 and September 1995 we made detailed temperature observations at the main fumarole field within the Fossa crater (Figure 6.7 and Table 6.5). On both occasions, degassing fumaroles at temperatures of up to 530 °C were observed across a 1.63 x 10^4 m^2 zone stretching from the NE crater rim to the crater floor. This is

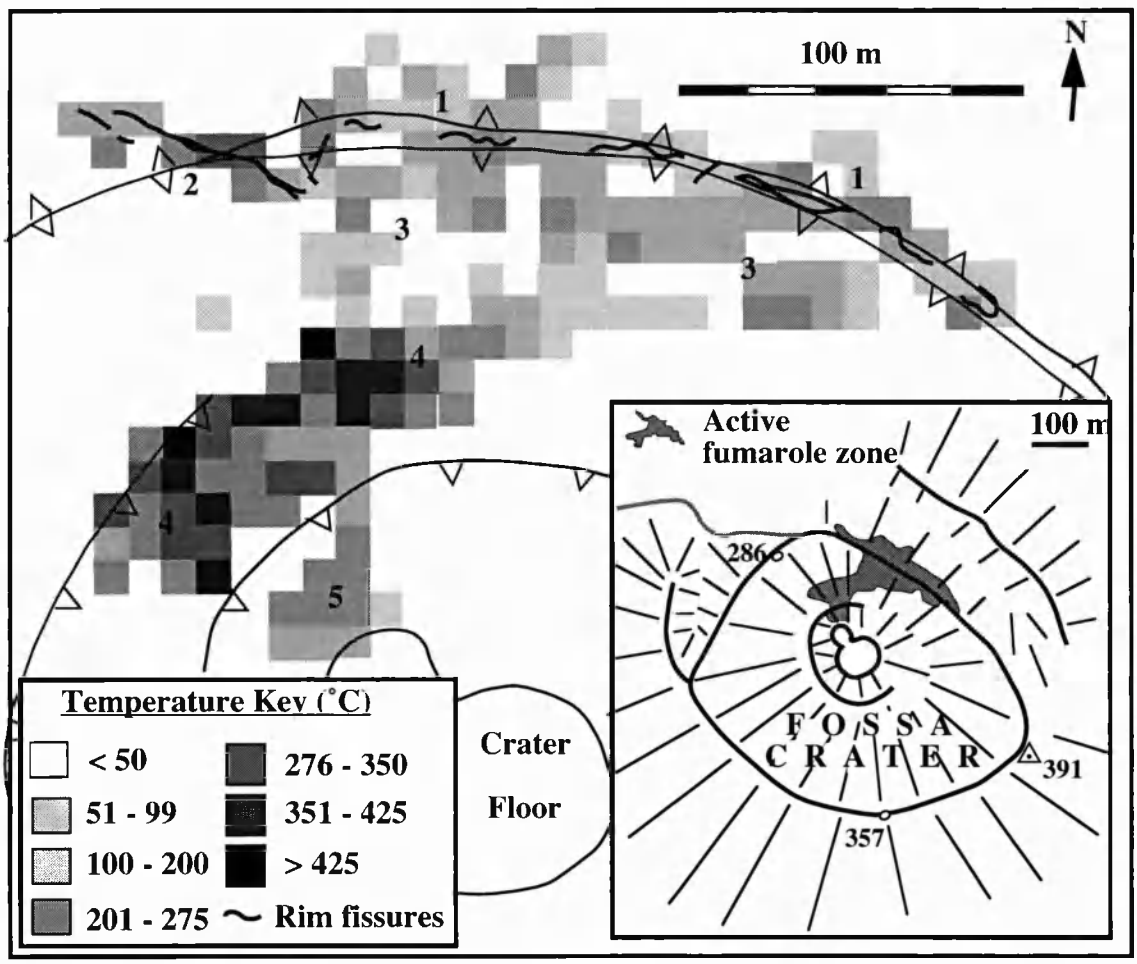

Figure 6.7. *Maximum temperature map for the Vulcano Fossa fumarole field, crater area inset with spot heights in metres, mapped using EDM and ground-based thermal measurements made during September 1995. Temperatures refer to the maximum obtained within each 10 x 10 m cell and cover the entire active area. Fumarole zone key: 1 = crater rim, 2 = rim rifts, 3 = upper crater, 4 = middle crater, 5 = lower crater (Table 6.5).*

Fumarole zone	No. of vents		Max. Temp. (°C)		Mean Temp. (°C)	
	1994	1995	1994	1995	1994	1995
Crater rim	150	96	453	374	171±5	154±7
Rim rifts	64	33	348	348	260±7	237±14
Upper crater	154	223	337	316	176±4	180±4
Middle crater	136	103	510*	531	284±9	284±9
Lower crater	-	68	-	339	-	157±30
			Maximum and mean for all fumaroles measured			
Total field	-	523	-	531	-	196±4
Total without lower crater	504	455	510*	531	214±4	203±4

* = saturation point of radiometer

Table 6.5. *Summary of temperature measurements made at the Vulcano Fossa fumarole field during October 1994 and September 1995 (see Figure 6.7 for location of fumarole zones.*

typical of the current "quiet phase", which has continued at the Fossa crater since the last explosive phase between 1888 and 1890 (Chiodini et al., 1995). However, maximum temperatures at the Fossa fumarole field have fluctuated since 1900, with a low of 110 °C in 1913 increasing to a high of 536-615 °C between 1921 and 1924, followed by a decline to 170 °C by 1937 (Sicardi, 1940). Between 1977 and 1978 the maximum temperature rose from 216 to 291 °C, reaching 330 °C in 1987-1988 and 690 °C in 1993 (Martini et al., 1980; Chiodini et al., 1995; Tedesco et al., 1995). If the typical eruption cycle is followed, the current quiescent period should be interrupted by renewal of explosive activity. The major hazard from such an eruption would be surge activity that would engulf Porto di Levante, a village with a seasonally variable population of 250-15000 lying ~1 km from the Fossa crater (Sheridan & Malin, 1983; Frazzetta et al., 1984; Coniglio & Dobran, 1995).

In view of this, continuous temperature and seismicity monitoring, as well as periodic geochemical and ground deformation monitoring, are in place (Barberi et al., 1991).

As at Stromboli, we took advantage of the unique and complementary spatial, temporal and spectral attributes of the radiometer, TMS, TM and AVHRR data (Table 6.1) to measure and monitor the fumarole field at Vulcano.

6.6.1. Ground-based thermal measurements

During October 1994 and September 1995, we made detailed vent temperature measurements at over 500 fumaroles distributed across the Fossa fumarole field using the Compac 3, or a K-type thermocouple where the Compac 3 saturated (Table 6.1). On the second occasion, measurements were made within 100 m^2 cells centred using Electronic Distance Measurement (EDM), allowing production of a detailed thermal map (Figure 6.7). This gave total fumarole field area (A_{field}) of 1.63 x 10^4 m^2, within which fumaroles typically covered 2.5 % of the surface, giving a 410 m^2 area of exhalation (A_{exhal}). This compares with estimates made between 1985 and 1987 using steam output which give exhalation areas of 232-350 m^2 (Italiano & Nuccio, 1992), to which at-least 50 m^2 must be added due to the growth of a new area since 1990 (Italiano et al., 1994). Maximum temperatures were typically <350 °C, except for a high temperature zone located on the middle inner flank of the crater (Figure 6.7, Table 6.5). This is the site of a fumarole which evolved rapidly between 1988 and 1992, showing a temperature increase from ~400 to 692 °C (Capasso et al., 1994).

6.6.1.1. Vent temperatures and activity

Chiodini et al. (1995) used isotopic and chemical data to propose two scenarios during which eruption risk at Vulcano is high: (1) opening of fractures by seismic activity causing magma degassing to extend to the core of the magma body and an inflow of marine hydrothermal fluids, and (2) rise of magma into wet environments at the periphery of the fumarole field. Both scenarios could result in a "Vulcanian" eruption. In the former case

temperature rises would indicate heat input from the core of the magma body, as occurred at the Fossa crater during regional seismic activity in 1978, 1986 and 1988 (Falsaperla et al., 1989; Chiodini et al., 1992; Bolognesi & D'Amore, 1993). The latter would cause increased fumarole temperatures at peripheral fumaroles. Both scenarios may therefore cause precursory temperature increases. It is noteworthy that the 1888-1890 eruption represented the climax of an episodic increase in fumarolic activity (Keller, 1980).

Temperature data collected during 1994 and 1995 define two general fumarole zones: a zone of highest temperatures extending from the middle of the inner N flank to the crater floor and a cooler zone at the crater rim (Figure 6.7, Table 6.5). Statistical analysis of the 1994-1995 temperature data shows a decline in temperatures at the rim and stable temperatures within the inner flank zone. The temperature decline at the rim accounts for the decline in the mean temperature for the whole fumarole field (Table 6.5). While fumarole temperatures remain stable or decline, eruption risk is low.

Temperature decline at the rim and stability within the inner zone, indicate a shift in activity from the rim, the location of highest temperatures and growing exhalative areas during the 1980's (Table 4, Mazor et al., 1988; Italiano & Nuccio, 1992), to the inner zone. This is consistent with growth of the inner zone since 1989, with increases in exhalative area, stream output and temperature between 1990 and 1991 at this zone (Italiano et al., 1994; Capasso et al., 1994).

6.6.1.2. Magma depth

Using the porous pipe model of Stevenson (1993) to model gas flow at a fumarole field, magma depth can be estimated using the same input parameters as at Stromboli. Following Stevenson (1993) the model is centred on a variable number of vent clusters (N). Between 3 and 10 clusters were identified for Vulcano, 5 of which are indicated on Figure 6.7 (labelled 1 to 5). Input parameters r_a and r_c are calculated from $N\pi r_a^2=A_{field}$ and $N\pi r_c^2=A_{exhal}$, respectively giving 20-40 m and 3-7 m for the Fossa fumarole field in 1995. T_{exit} was set to the maximum vent temperature, this being assumed to have the most

direct link to the deep feeder system, and gas flow rate was estimated at 25±20 kg s^{-1} from Bruno et al. (1994), Chiodini et al. (1994) and Italiano et al. (1994). Given these inputs, depth to magma at 1000 °C [the crystallisation temperature of rhyolites during the 1888-1890 eruption (Clocchiatti et al., 1994)], is 2.1±1.9 km.

This range coincides with evidence from drill holes, where a temperature of >419 °C and steep temperature gradient at a depth of 1360-2050 m suggest that magma may only be a few hundred metres deeper (Faraone et al., 1986). We thus confirm that current activity at Vulcano is driven by heat from a shallow (<4 km deep) degassing magma body. This has been the main premise for models of the volcanic hydrothermal system based on geochemical data (e.g. Martini et al., 1980; Carapezza et al., 1981; Cioni & D'Amore, 1984; Tedesco et al., 1991; Bolognesi & D'Amore, 1993; Tedesco et al., 1995).

6.6.1.3. Thermal flux

For each 10 x 10 m cell identified in Figure 6.7, the area occupied by active fumaroles and mean vent temperature were substituted into Equation 6.6 in place of πr_c^2 and T_{exit} respectively to give Q_{rad} per cell. Summing all cells gives Q_{rad} for all exhaling vents at the Fossa fumarole field of 0.6 MW. Using Equation 6.7 and setting T_{exit} to the mean vent temperature for the whole field (Table 6.5) and substituting πr_c^2 with exhalative area, Q_{conv} of 0.7 MW is obtained. Q_{cond} is estimated assuming a mean gas temperature of 200 °C from an indeterminate number of fumaroles with a combined radius of 10 m. This gives Q_{cond} of 2 to 70 MW depending on the depth of the source.

6.6.2. TMS thermal and reflectance measurements

On 19 July 1991 the Fossa crater was over-flown by an aircraft carrying TMS. Thermal emittance was not detectable in bands 9 and 10, these bands being dominated by reflected solar radiation. Although Solar heating in bands 11 and 12 made the anomaly difficult to distinguish from the background, two hot-spots were apparent (Figure 6.8). These were coincident with sites of persistently high temperature fumaroles observed at the

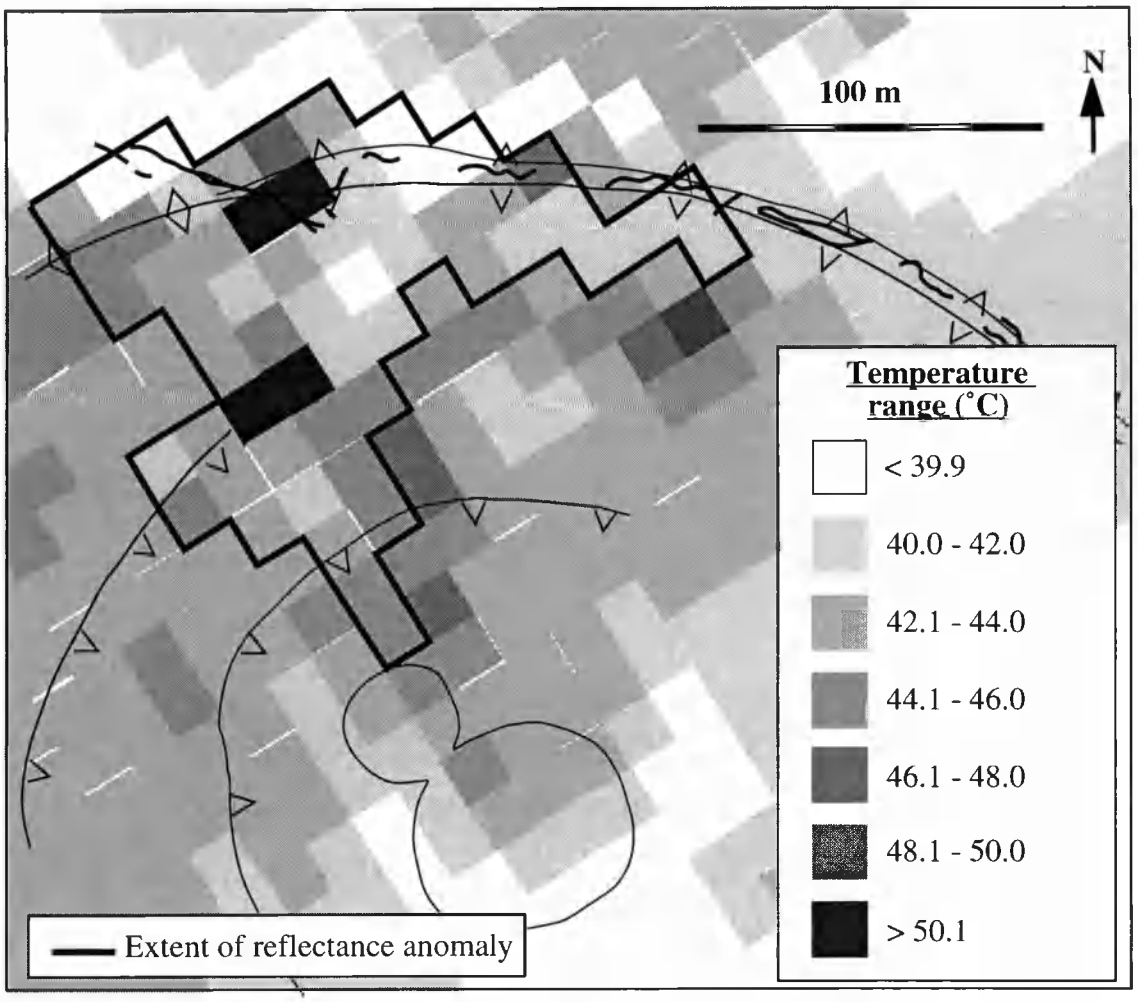

Figure 6.8. *19 July 1991 TMS pixel brightness temperatures within the Fossa crater fitted to the topographic base created using EDM measurements in 1995 (Figure 6.7). Bold line indicates extent of fumarole field mapped using spectral reflectance in bands 5 and 7.*

rim and within middle crater fumarole zone in ground observations. The rim hot-spot coincides with a 25-50 cm wide, 60 m long fissure cutting the N end of the rim fumarole zone (Figure 6.7). This displayed maximum temperatures of 200 to 240 °C in 1988-1989 (Oppenheimer & Rothery, 1991) and 348 °C in 1994-1995 (Table 6.5). The second hot spot locates a fumarole at which increasingly high (400-690 °C) have been measured since 1988 (Capasso et al., 1994) and the zone of highest temperatures in 1995 (Figure 6.7).

Since thermal measurements were only available in one band, Equation 6.13 was applied to give Q_{rel} of 43 W m^{-2}. This is similar to Q_{rel} of 37 W m^{-2} obtained by Gaonac'h et al. (1994) using a TM band 6 image of the Fossa crater acquired on 23 October 1986.

The fumarole field showed up clearly on TMS images as a reflectance anomaly in bands 1 to 10 (Figure 6.8). This is due to the presence of yellow sublimate, which XRD analysis showed to be dominated by sulfur. Although impure sulfur melts between 113 and 150 °C to be replaced by grey-black sublimates, yellow sublimate persists around most fumaroles at Vulcano. The high reflectance of sulfur at all wavelengths, compared with the low reflectance sublimate-free background, causes a bright reflectance anomaly at the fumarole field in all wavebands (Figure 6.9). Using the reflectance anomaly, the fumarole field area was estimated at 1.80 x 10^4 m^2, in agreement with the ground-based estimates.

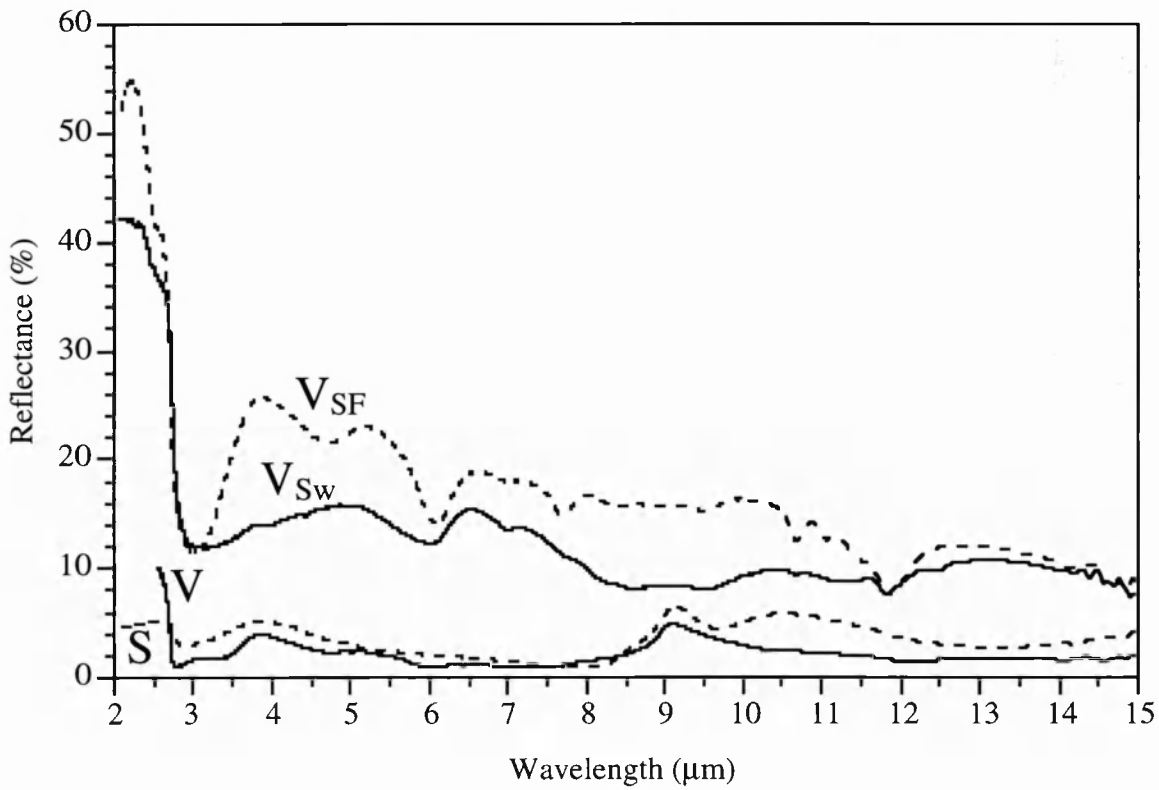

Figure 6.9. *Spectral reflectance of weathered (V_{SW}) and fresh (V_{SF}) yellow sublimate from Vulcano, basaltic scoria from Stromboli (S) and a trachytic-rhyolitic block from Vulcano (V). Note the much lower reflectance of S and V. Spectra were obtained using a Nicolet system FTIR spectrometer by J. Salisbury at Johns Hopkins University.*

6.6.3. TM thermal and reflectance measurements

No emitted radiance was observed in TM bands 5 or 7, but a thermal anomaly in band 6 located the Fossa fumarole field on both the 18 July and 3 August 1994 images. However, solar heating of east facing slopes caused anomalies of equal intensity to the Fossa anomaly (Figure 6.10). Without prior knowledge of the fumarole field location it would have been impossible to distinguish it from the solar heated anomaly. To unambiguously identify low temperature geothermal anomalies in TM band 6 or TMS bands 10-11, night-time data should be used. However, as with the TMS data, the fumarole field was evident as a reflectance anomaly, giving a total fumarole field area of 1.80-1.89 x 10^4 m^2, agreeing with the TMS and ground based estimates.

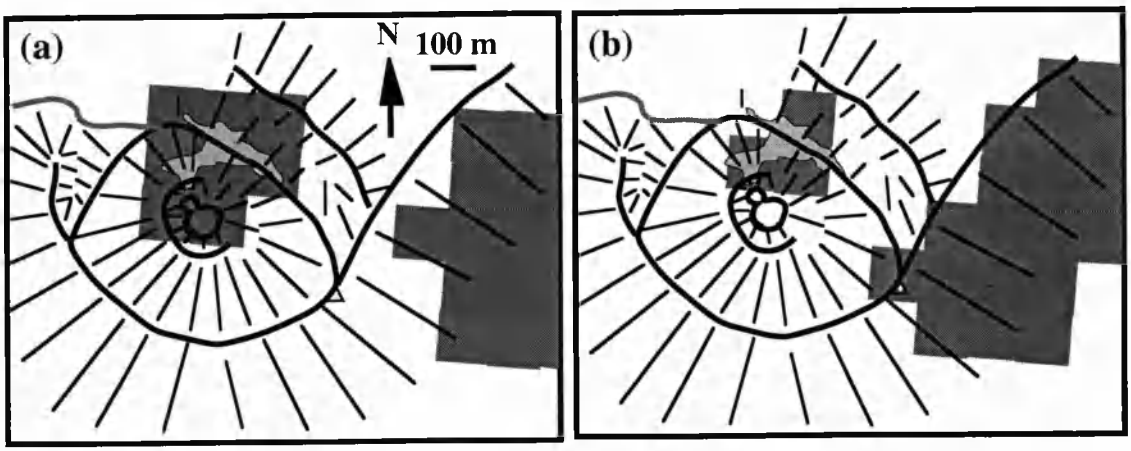

Figure 6.10. *Thermal anomalies, dark grey, in the vicinity of the Fossa crater on TM images obtained on (a) 18 July 1994 and (b) 3 August 1994. The anomaly within the crater locates the fumarole field, that on the outer flank is a Solar-heated anomaly. Images have been fitted to the Figure 6.8 inset map of the crater terrace on which the area of the fumarole field is depicted in light grey.*

Application of Equation 6.13 gives Q_{rel} of 37 and 39 W m^{-2}, nearly identical to the 1986 estimate by Gaonac'h et al. (1994) and the 1991 TMS estimate. The 1994 TM estimate is also validated by the September 1995 ground estimate: Q_{rad} of 0.6 MW distributed over the total 1.63 x 10^4 m^2 fumarole field area gives a Q_{rel} of 37 W m^{-2}.

The stability of the radiated thermal flux between 1986 and 1995 (38.6±2 W m^{-2}) implies that thermal output integrated over the entire fumarole field has remained stable over this period. Assuming Q_{conv} and Q_{cond} have also been constant over this time, to keep the thermal flux stable, the development of the new high temperature zone on the inner flank must therefore have been matched by cooling of the former high temperature zone on the rim, as indicated by the 1994-1995 ground based surveys (Table 6.5). We suggest that decline at the rim is the result of a build up of hydrothermal minerals and clays, which progressively clog these older, established fumaroles. To maintain thermal flux, activity must transfer to new locations, where temperatures increase to balance declining flux from sealing zones.

6.6.4. AVHRR thermal measurements: activity and hazard monitoring

On all 41 AVHRR images of Vulcano analysed between 1986 and 1995, the Fossa fumarole field was located by the highest $T_{3\text{-}4}$ on Vulcano (Figure 6.11). Since the thermal structure of the fumarole field is too complex to be modelled by the two component thermal surface assumed in the application of Equations 6.10 and 6.11, Equation 6.14 was applied to channels 3 and 4.

Stability of thermal flux from the fumarole field between 1986 and 1995 implied from the TM and TMS data is confirmed by the near horizontal best fit line for the R_{3volc} time series (Figure 6.12a). A very slight decline may be the result of the area of maximum temperatures shifting from the rim towards the crater floor, resulting in a reduced signal due to topographic shielding in off-nadir images.

The stability of the radiated thermal flux during this time period suggests that this data set can be used as a baseline against which future fluctuations can be assessed. Analysis of the R_{4volc} time series indicates that random variation means that R_{4volc} must be elevated more than two standard deviations above the mean before any significance is placed on the R_{4volc} rise (Figure 6.12b). Due to the unsaturated data and superior sensitivity provided by channel 3 for this target, a 450 m^2 area at a mean temperature of

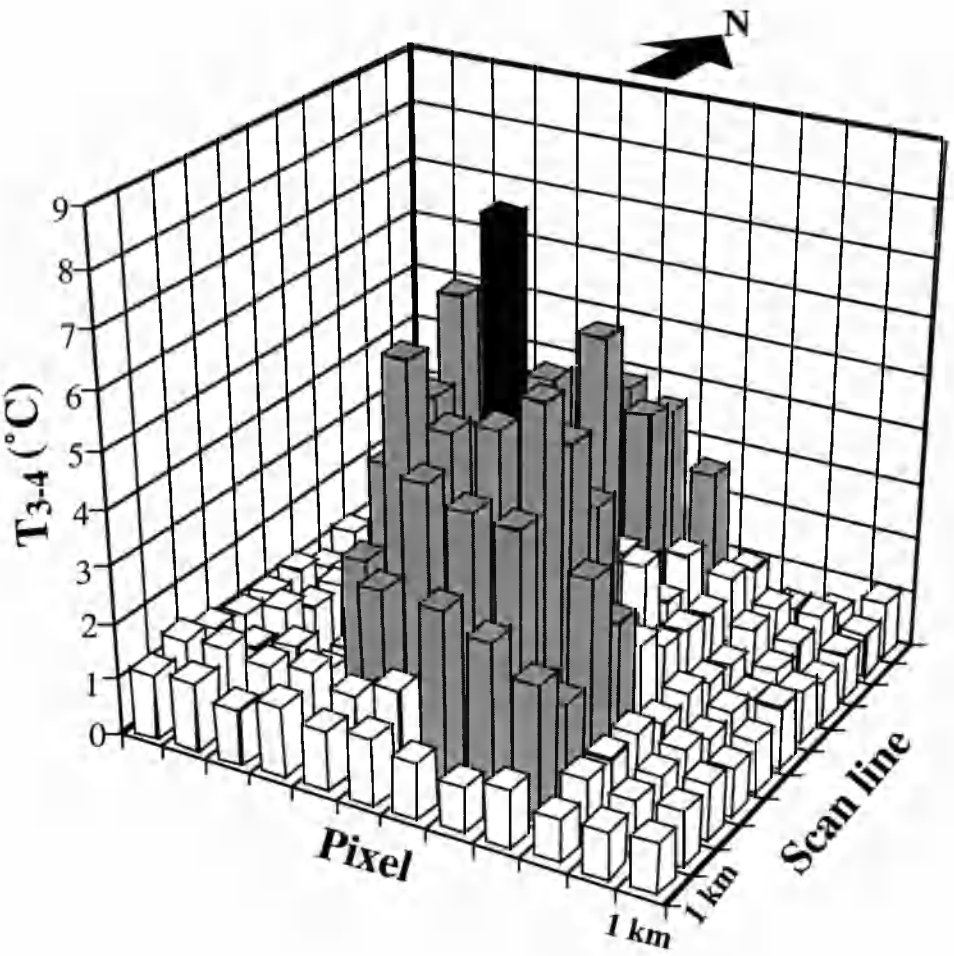

Figure 6.11. *T_{3-4} over Vulcano on an 18 June 1994 AVHRR image. Black pixels contain sub-pixel hot-spots as indicated by highly elevated T_{3-4}, and locate activity at the Fossa crater. Grey and white pixels contain land at ambient temperatures and sea respectively.*

200 °C against a background at 0 °C will raise T_3 and T_4 by 3 and 0.2 °C respectively. It would therefore be more reasonable to use R_{3volc} as a baseline (Figure 6.12a). Following the scenarios given by Chiodini et al. (1995), rises away from the baseline will imply increased eruption hazard.

6.7. Conclusions

Integrating remotely sensed data from a variety of different instruments allows spectrally, temporally and spatially detailed measurements and monitoring of volcanic

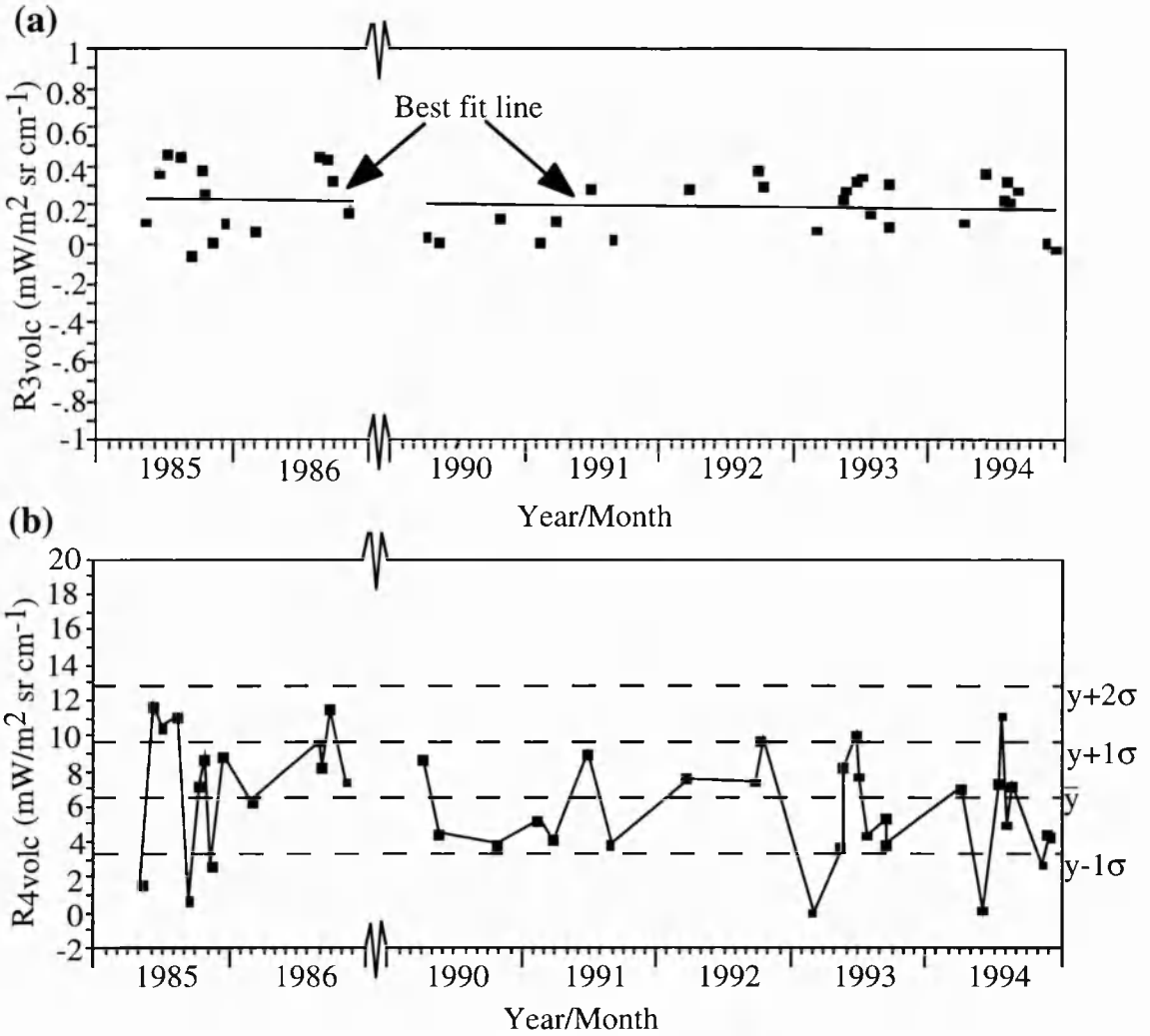

Figure 6.12. *AVHRR times series for (a) R_{3volc} and (b) R_{4volc} from Vulcano's Fossa crater between 1985 and 1994.*

systems that are characterised by activity at open degassing vents and fumarole fields. For Vulcano and Stromboli, thermally derived estimates for various volcanic system parameters, including magma depth, thermal flux, and vent areas, are in good agreement with other published estimates. This excellent agreement with ground data suggests that such thermal data sets can not only be used as a valuable supplement at well-monitored volcanoes, but can also provide a reliable means of defining and monitoring the volcanic system at poorly monitored volcanoes.

Utilising the increasing stream of data available from an expanding array of ground-based, air- and satellite-borne sensors provides a safe, regular and repeatable means of measuring and monitoring volcanic activity, even during dangerous or eruptive episodes.

6.8. Acknowledgements

Nicki Stevens (University of Reading) and Adam Maciejewski (Open University) are gratefully acknowledged for their invaluable help in the field and discussions. Jack Salisbury (Johns Hopkins University) and Ant. Denniss (Open University) are gratefully acknowledged for providing rock spectra, and Tanya Babbs (Leicester University) for XRD analyses. Peter Bayliss and the NERC Dundee Receiving station are thanked for rapid provision of AVHRR data and Peter Miller at the NERC Plymouth Image Analysis Unit for calibration. TM images were provided courtesy of NERC Scientific Sevices. Dave Rothery, Peter Francis, Dick Carlton, Anna Butterworth, Martin Wooster, Kirsta Galloway, the rest of the Open University's Volcano Geophysics Group, Roberto Carniel (University of Udine) and Boris Behncke (GEOMAR) all provided invaluable input and help. Fieldwork was funded by the Remote Sensing Society's Shackleton Award, and research by an Open University PhD grant.

Chapter 7. Low cost volcano surveillance from space: case studies from Etna, Krafla, Cerro Negro, Fogo, Lascar and Erebus

---

A.J.L. Harris, A.L. Butterworth, R.W. Carlton, I. Downey, P. Miller, P. Navarro and D. A. Rothery

Paper submitted to Bulletin of Volcanology, June 1996.

7.1. Abstract

Satellite data provide an ideal means of monitoring sub-aerial volcanoes. Being directly and freely available several times a day, the Advanced Very High Resolution Radiometer (AVHRR) offers great potential for real time monitoring of all volcanoes across large (3000 x 3000 km) areas. Thermal data can detect and locate the onset of activity and distinguish various styles of activity. Here we describe techniques to estimate lava area, thermal flux, effusion rates and cumulative volume. These were first tested on well monitored eruptions at Krafla (1984) and Etna (1991-93), known from ground-based studies to have produced 24 km^2 and 7.6 km^2 flow fields respectively. AVHRR-derived results gave maximum active lava areas of 24 km^2 and 7 km^2, with maximum effusion rates of 120 $m^3 s^{-1}$ and 18 $m^3 s^{-1}$ respectively. Excellent agreement with ground reference data in both test cases indicates that the same techniques can be applied with confidence to

interpret AVHRR data for other eruptions. Low effusion rate (<4.5 m^3 s^{-1}) eruptions are identified at Etna (1985) and Cerro Negro (1995), building 16-29 x 10^6 m^3 and 1.0-1.6 x 10^6 m^3 flow fields respectively, and the magma flux of Erebus' lava lake is estimated as at-least 350 kg s^{-1}. Radiance maps produced for Krafla (1984) were in agreement with ground observations. Those produced from time series data acquired during the 1995 Fogo eruption located flows within the summit caldera impacting on settlements and farmland. Radiance maps and temperatures obtained from AVHRR data acquired during the April 1993 Lascar eruption identified uniform temperature (~120 °C) pyroclastic flows extending 7 km. Time series analysis of Etna's Central Craters defined increased activity since 1993 and an apparent thermal precursor to renewed activity. All these techniques could be incorporated in ground analysis segments of existing, or cheap to install, receiving stations allowing automated real time volcano thermal monitoring on a regional scale.

7.2. Introduction

At least 1200 eruptions have occurred since the first civilian satellite observation of volcanic activity was made at Surtsey in 1967 by Williams & Friedman (1970). During this time, explosive blasts, pyroclastic flows, dome collapse, eruption of lava and generation of mudflows have caused loss of lives and destruction of entire communities, wild-life, habitat, agricultural land, infrastructure and homes. Evacuations have been required in many cases and lava diversion has been attempted (Table 7.1). Continuous monitoring of all volcanoes from the ground has proved impossible due to logistical, financial and political problems. Consequently eruptions have frequently occurred at poorly monitored volcanoes (Tilling, 1989). However, over this same period satellite data have been continuously available for the whole globe, with the potential to observe all volcanoes and eruptions coincident with cloud-free satellite passes from a safe and re-usable platform.

Since 1979 thermal data have been available at least 4 times a day for any sub-aerial volcano from the Advanced Very High Resolution Radiometer (AVHRR) flown aboard the TIROS-N and NOAA satellite series. AVHRR data, and more frequently available (once

Volcano, eruption date & description	*References*
Arenal 1968	*Melson & Saenz (1973)*
Explosive eruption emitting pyroclastic flows & bombs causing 60m diameter impact craters within 5km: ~80 people killed, villages & 12 km^2 tropical rainforest destroyed.	
Vestmannaeyjar 1973	*Thorarinsson et al. (1973); Time-Life (1982)*
Lava flow at 100m^3s^{-1}, 150m high cone built in 1 week: 300 buildings burnt, 5300 people evacuated, water pumped onto lava in attempt to stop blockage of fishing port.	
Nyiragongo 1977	*Smithsonian Institution (1989)*
Draining of a lava lake fed flows which moved downslope at 60km/hr: ~70 people killed, 800 homeless, 1200ha of agricultural land destroyed.	
St. Helens 1980	*Tilling (1989); Smithsonian Inst. (1989)*
Laterally directed blast, eruption column to 19 km: 57 lives lost, mud-flows destroy 123 homes, >1 billion dollars of damage.	
Etna 1981	*Smiths. Inst. (1989); Chester et al. (1985)*
Lava flows extended 5km in 4 hours, covering 6 km^2 in 1 week: ~$10x$10^6$ damage, 2 railways & 3 major roads cut, buildings & orchards destroyed, 250 people evacuated.	
Galunggung 1982	*Hanstrum & Watson (1983); S. Inst. (1989)*
Ash up to >15km, pyroclastic flows extending 5km: villages destroyed, ~68 people killed, 75000 evacuated, 3 passenger aircraft damaged & emergency landings forced.	
El Chichon 1982	*Smithsonian Inst. (1989); Tilling (1989)*
Ash clouds ~17km in height, pyroclastic flows extending 7km: all villages within 7 km destroyed, ~2000 people killed, >10000 evacuated, $55x$10^6$ crop damage.	
Etna 1983	*Colombrita (1984); Chester et al. (1985)*
131 day effusive eruption of 100x$10^6$$m^3$ of lava: cut arterial roads, damaged tourist complex, cable car systems & ski pistes, lava diversion carried out costing 40x10^8 Lira	
Kilauea 1983-96	*Weisel & Stapleton (1992); HVO (1995)*
1.3km^3 of lava, extending up to 12km, erupted by 1995: 181 homes, National park natural, archeological & cultural resources lost, $50x$10^6$ public facility damage.	
Nevado del Ruíz 1985	*Tilling (1989), Smithsonian Inst. (1989)*
Hot ejecta from small volume eruption mixes with snow/ice to feed fast moving mud-flows: 22000 people killed; 5000 injured; 10000 homeless; $212x$10^6$ economic loss.	
Pinatubo 1991	*GVN (1991f), Simkin & Siebert (1994)*
Ash clouds up to 16km high, pyroclastic flows extending 18km & rain triggered lahars: 25000 people evacuated, up to 800 killed, 1.2x10^6 homeless, 10^5 houses destroyed	
Unzen 1991	*Yamamoto et al. (1993)*
Dome collapse fed pyroclastic flows: 43 people killed, zone evacuated, homes burnt.	
Rabaul 1994	*Simkin & Siebert (1994); ABC news*
Explosive eruption causing 1-2m of ashfall: >50000 evacuated, reports indicate 25% of structures in greater Rabaul destroyed (80% in inner zone), 50% significantly damaged.	
Fernandina 1995	*GVN (1995d)*
Effusive eruption sending lava flows ~5km to the sea: wildlife impact, iguanas, birds, & other marine-life killed, largest Galapagos Fur Seal breeding population endangered.	

Table 7.1. *Eruptions causing major damage: selected examples 1967-1996.*

every 30 minutes) geostationary satellite data, have become commonly used to monitor atmospheric ash plumes from explosive eruptions. Such plumes extend rapidly over thousands of kilometres, the April 1982 El Chichon eruption plume encircling the globe in 3 weeks (Robock & Matson, 1983). The regular, synoptic, global satellite perspective has proved the only feasible way to monitor such transient, large scale features, allowing: plume location and tracking; measurements of plume height, velocity and dispersion; and identification of communities impacted by airfall or aerosols and hazards to aircraft (Hanstrum & Watson, 1983; Tucker & Matson, 1985; Sawada, 1989; Holasek & Rose, 1991; Jeyaseelan & Thiruvengadachari, 1993; Casadevall, 1994; Dean *et al.*, 1994; Holasek & Self, 1995).

Detection of active lava on AVHRR thermal images acquired as early as 1980 was first reported by Wiesnet & D'Aguanno (1982), but the use of AVHRR to monitor high temperature volcanic thermal anomalies has been less common than for plume studies. Since the discovery of a thermal anomaly on two 1985 Thematic Mapper (TM) images of Lascar volcano (Francis & Rothery, 1987), interest has instead focused on the use of TM to analyse lava domes and lakes (Rothery *et al.*, 1988; Rothery & Francis, 1990; Oppenheimer *et al.*, 1993; Andres & Rose, 1995), lava flows (Pieri *et al.*, 1990; Oppenheimer, 1991a; Bhattacharya *et al.*, 1993; Flynn *et al.*, 1994), and fumaroles and conduit vents (Abrams *et al.*, 1991; Gaonac'h *et al.*, 1994).

When the 10^6 m^2 and 900 m^2 pixel areas of AVHRR and TM are compared, the dominance of TM in the analysis of high temperature volcanic features is not surprising. However, AVHRR data are freely available at cheap-to-install receiving stations (costing US$ 1000 to 60000, depending on sophistication), compared with costs of up to US$ 4000 for a single TM scene. Once installed, analysis of all cloud-free volcanoes within 3000 km of the station is possible using a single image. Up to 10 images per day are received at the Dundee University receiving station (Scotland, UK) covering all volcanoes in Jan Mayen, Iceland, Italy, Greece and Turkey. Direct acquisition also allows image analysis on reception, permitting real time monitoring, impossible using TM due to

delivery delays of several months. Inspection of AVHRR images as they are received at the University of Alaska Fairbanks allows reports of activity at Alaskan, Aleutian and Kamchatkan volcanoes within 10 minutes of the satellite pass (K. Dean, personal communication).

If reliable information can be extracted from AVHRR data, its cost, availability and real time monitoring capabilities make it an attractive tool for volcano hot spot monitoring. To this end we have developed and tested techniques capable of volcanic hot-spot identification, analysis and monitoring. These are demonstrated using data for lava flows at Etna, Krafla, Cerro Negro and Fogo, a pyroclastic flow at Lascar, the Erebus lava lake and degassing open vents at Etna.

7.3. Volcano hot-spot detection limits of the AVHRR

The AVHRR is a space-borne scanning radiometer which detects reflected and emitted radiation in 5 wavebands (Kidwell, 1995). Channels 1 and 2 are situated in the short-wave red and infrared regions at 0.55-0.90 and 0.725-1.10 μm. By day these two channels are dominated by reflected radiation. By night the coincidence of the channel 2 waveband with the peak spectral exitance from bodies at 800-1200 °C means that radiance from a lava body will be detectable if its size and temperature are sufficient. To be elevated above a noisy channel 2 night-time background, a lava body with high temperature chilled crust (~500 °C) occupying 99% of the lava surface and the remainder occupied by exposed molten lava (~1000 °C), must occupy at least 20% of a pixel or ~0.2 km^2 for a 1 km^2 pixel. This scenario is only likely during major effusive eruptions. Indeed, to date only two instances of thermal emittance from an active lava in channel 2 have been reported, both during major effusive events at Kilauea and Krafla (Flynn & Mouginis-Mark, 1994; Harris *et al.*, 1995c). To be detectable in channel 1, lava at 800-900 °C must fill a pixel, i.e. attain an area of at least 1 km^2. This is highly unlikely during any terrestrial eruption.

In the mid-infrared channel 3 (3.55-3.93 μm), the lower reflected radiation contribution and coincidence of the channel with the peak spectral reflectance from bodies

at 100-1000 °C makes this channel extremely sensitive to active lava by day or night. Only a small portion of a pixel (~0.002 %) needs to be occupied by a lava body to elevate channel 3 radiance above that of the ambient background (Figure 7.1a). However, the maximum recordable temperature in channels 3 to 5, here termed saturation, occurs at a temperature of about 50 °C. To achieve saturation only a small portion of a pixel needs to be occupied by the lava body. The lava body described above for channel 2, against a lava-free background at 0 °C, would saturate channel 3 when its area reached just ~800 m^2. Most active lavas therefore saturate channel 3 quite easily.

Channels 4 and 5 lie in the thermal infrared, at 10.3-11.3 and 11.4-10.4 μm respectively. These wavebands coincide with the peak spectral exitance for bodies at ambient temperatures, and are therefore far less sensitive than channel 3 to high temperature (100-1000 °C) lava bodies. Consequently a much larger portion (>0.1%) of a channel 4 or 5 pixel must be occupied by a lava body to elevate radiance above ambient background (Figure 7.1b). This much lower sensitivity means that channels 4 and 5 usually provide unsaturated data when channel 3 is saturated (Figure 7.1c), the lava body described above for channels 2 and 3 will not saturate channels 4 and 5 until its area reaches ~45000 m^2.

7.4. Locating volcanic hot-spots

Routine night-time observations using channels 1 and 2 to detect effusive activity by means of thermal radiance would miss all but the most exceptional events. However, the sensitivity of channel 3 makes this channel extremely useful for detecting volcanic hot-

---

Figure 7.1. *Elevation above background of (a) channel 3 and (b) channel 4 pixel temperatures for sub-pixel bodies, at a range of typical active lava temperatures, of increasing size; and (c) temperature and size of a sub-pixel body necessary to saturate a channel 3 or 4 pixel given a background temperature of 0 °C.*

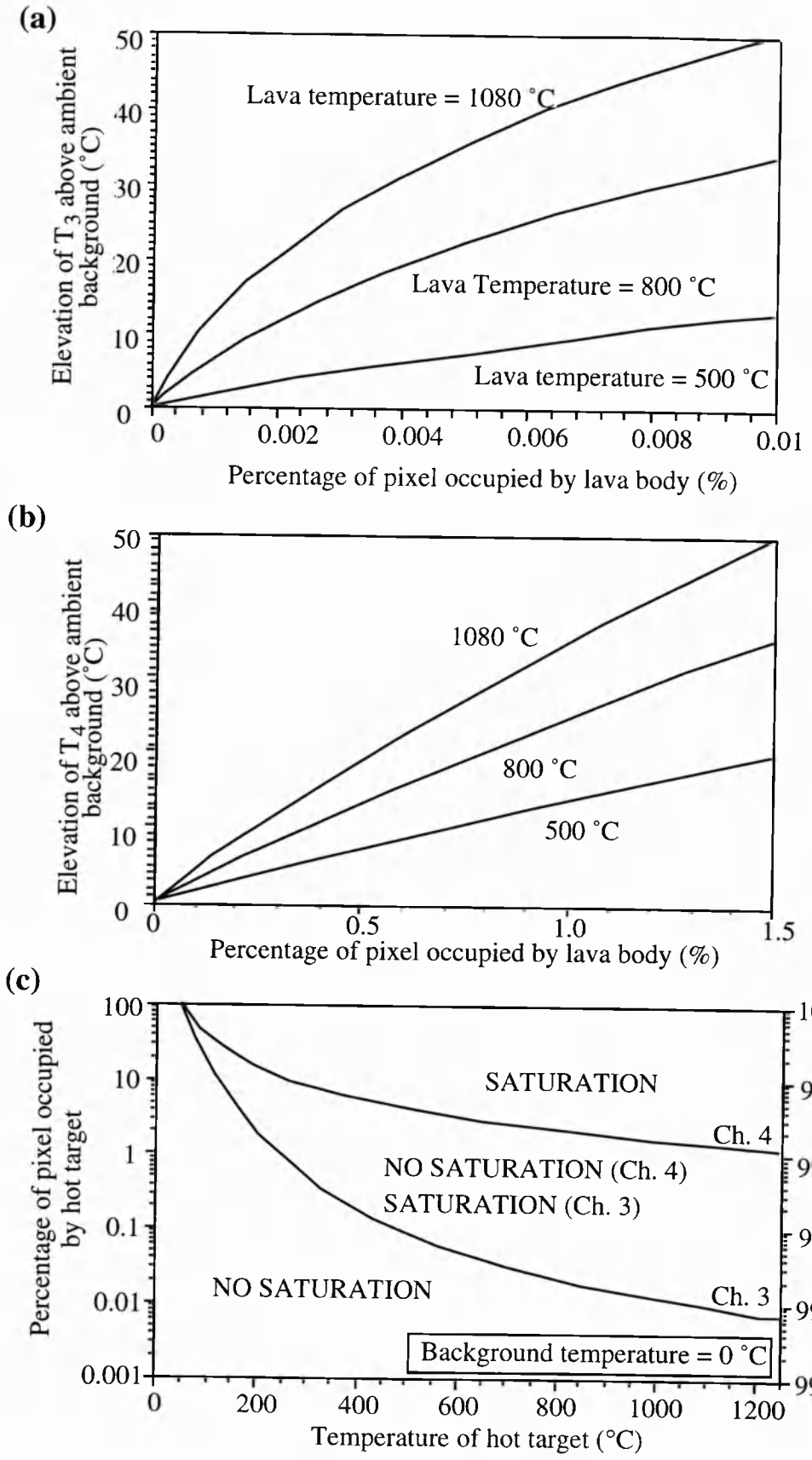
(a)
Elevation of T_3 above ambient background (°C)
Lava temperature = 1080 °C
Lava Temperature = 800 °C
Lava temperature = 500 °C
Percentage of pixel occupied by lava body (%)
(b)
Elevation of T_4 above ambient background (°C)
1080 °C
800 °C
500 °C
Percentage of pixel occupied by lava body (%)
(c)
Percentage of pixel occupied by hot target
SATURATION
Ch. 4
NO SATURATION (Ch. 4)
SATURATION (Ch. 3)
NO SATURATION
Ch. 3
Background temperature = 0 °C
Temperature of hot target (°C)
Percentage of pixel occupied by background

spots if ambient background temperatures are sufficiently cool (Figures 7.2a & 7.3a). However, by day black vegetation-free basaltic surfaces can heat to >50 °C: we measured widespread temperatures of 50-60°C at Etna (Sicily) on sun-heated, inactive, slaby pahoehoe, ash and scoria during summer 1994. This reduces the contrast between the volcanic anomaly and the background, and if the ambient background reaches saturation the anomaly will become indistinguishable using channel 3 alone (Figures 7.2b & 7.3b). Due to the lower sensitivity of channel 4, volcanic hot-spots are far less obvious in this channel (Figure 7.2). However, the difference in sensitivity between channels 3 and 4 is a useful tool for identifying volcanic hot-spots and distinguishing them from solar heating. Channels 3 and 4 are equally sensitive giving similar pixel temperatures (T_3 & T_4 respectively) over sun-heated surfaces, but over sub-pixel volcanic hot-spots the higher sensitivity of channel 3 causes T_3 to be much higher than T_4 (Figures 7.3a & 7.3b). Analysis of 160 images of Etna, Stromboli and Vulcano (Sicily) containing sun-heated anomalies, fumaroles, active degassing vents and lava flows shows the T_3 minus T_4 difference (ΔT) to be at most ~10 °C for surfaces at ambient and solar-heated temperatures, but over volcanic hot spots ΔT was always higher (typically 12-40 °C). Thus, analysis of ΔT allows volcanic hot-spots to be identified even on sun-heated images, and is the basis on which the automated lava thresholding algorithm given by Harris *et al.* (1995b) operates (Figure 7.3c & 7.3d).

7.5. Estimation of surface temperature over volcanic surfaces using the AVHRR

7.5.1. Procedure

For each pixel, the signal from the surface is converted from an analogue signal to a digital number (DN), which, following Lauritson *et al.* (1988), is related to emitted radiance by:

$$R_i = S_i DN_i + I_i \qquad (7.1a),$$

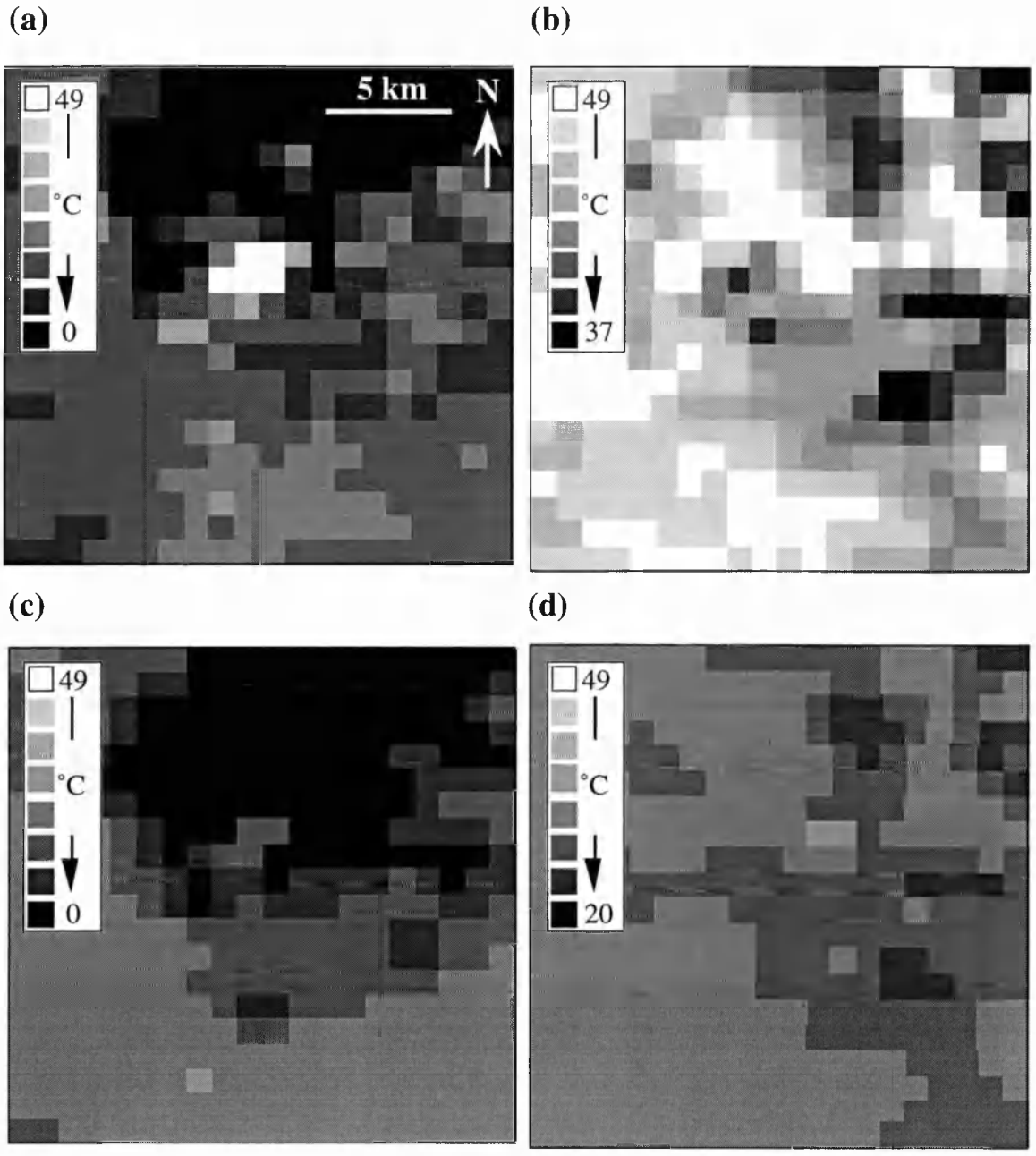

Figure 7.2. *Channel 3 brightness temperature images acquired during the 1985 Etna eruption on (a) 30 March showing a high temperature anomaly due to an active lava flow and on (b) 10 July showing solar heating problems. Channel 4 brightness temperature images for the same days are given in (c) and (d) showing the inferior sensitivity of this channel to bodies at active lava temperatures.*

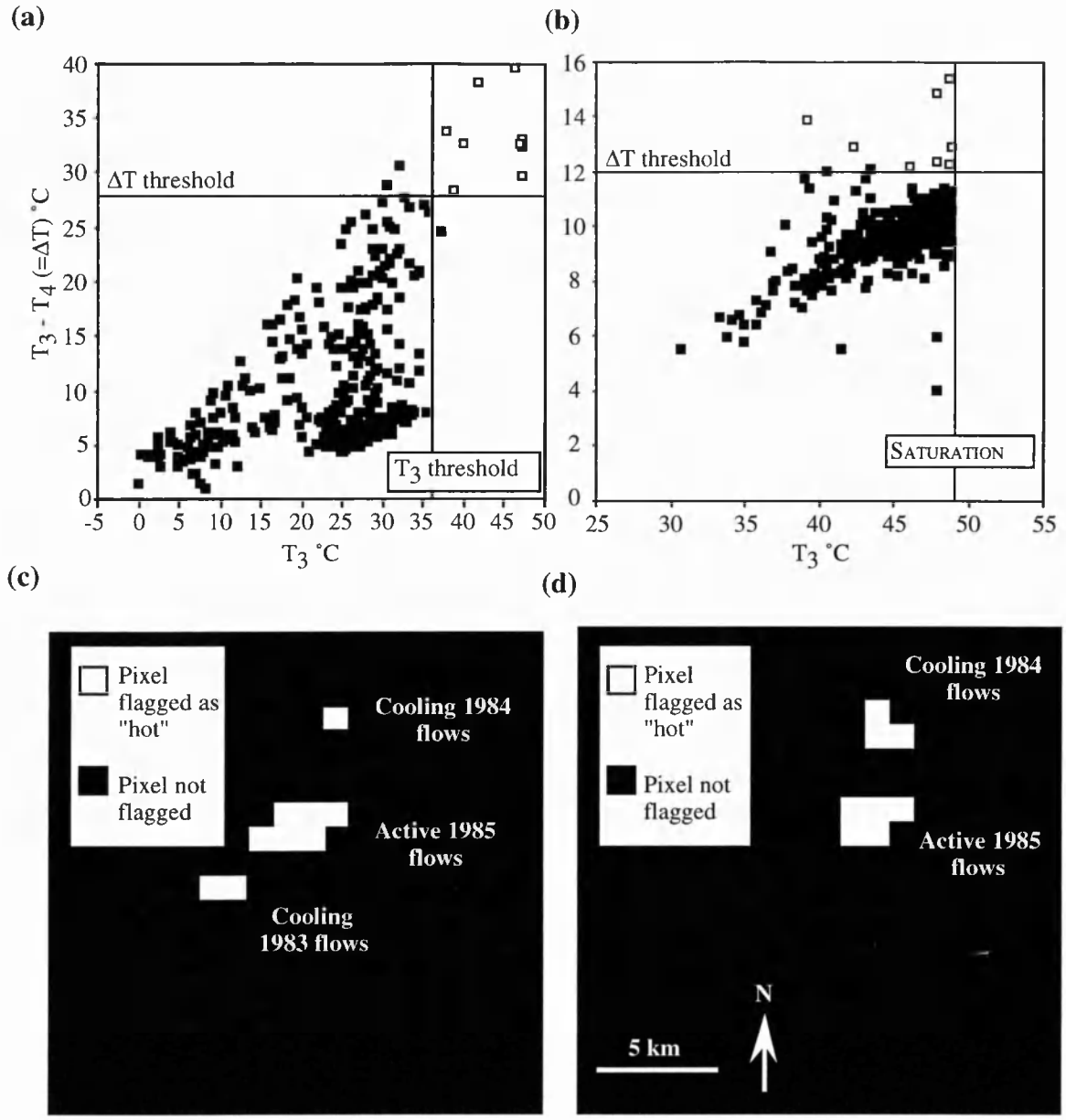

Figure 7.3. *T_3 versus ΔT scatter graphs for (a) the 30 March image and (b) the 10 July image, both given in Figure 2, showing the use of T_3 and ΔT thresholds to distinguish pixels containing active lava (white plots) from those occupied by ambient or solar heated surfaces (black plots). (c) and (d) give results of threshold application to flag "hot" pixels. Results are identical to those obtained by application of the automated thresholding technique given by Harris et al. (1995b).*

in which R_i, DN_i, S_i and I_i are the radiance, DN, slope and intercept in channel i respectively. Radiance can be converted to surface temperature (T) using the Planck function for isotropic radiation, $L(\lambda T)$, and allowing for surface emissivity (ε) and atmospheric transmissivity (τ), whereby

$$R_i = \varepsilon_i \tau_i L(\lambda_i T) \qquad (7.1b).$$

Inversion of the Planck function gives

$$T = \frac{c_2}{\lambda_i \ln ([\varepsilon_i \tau_i c_1 \lambda_i^{-5} / \pi R_i] + 1)} \qquad (7.1c),$$

where λ_i is the central wavelength of channel i, c_1 and c_2 are constants with the values 3.742×10^{-16} W m^2 and 1.4388×10^{-2} m K. Channel emissivities (ε_i) for typical volcanic surfaces are given in Table 7.2 and we obtain channel transmissivities (τ_i) using LOWTRAN 7 atmospheric code (Kneizys *et al.*, 1983). Temperatures derived for channels 4 and 5 must be corrected for the non-linear response of these channels using the procedure and coefficients given by Weinreb *et al.* (1990) and Kidwell (1995).

7.5.2. Accuracy

We assessed the accuracy of AVHRR surface temperature derivation by making surface temperature measurements simultaneous with a cloud-free AVHRR over-pass of Etna on 3 June 1994. Fifty surface measurements were made over a >1 km^2 area of uniform surface type (i.e. scoria field) ~1 km west of the summit craters using a Minolta/Land Compac 3 infrared thermometer. Measurements were integrated over a 1 km^2 area to give a simulated AVHRR pixel temperature of 35.6±0.8 °C. AVHRR surface temperature was obtained from the AVHRR image using the emissivity of scoria (Table 7.2) and a variety of published atmospheric corrections. Results showed that the majority

Sample location	Date collected	Sample description	ε_3	ε_4	ε_5
Etna	09/95	Slaby pahoehoe[b] (1991-93 flow field).	.9436	.9344	.9534
Etna	09/95	Aa clasts[b] (1991-93 flow field).	.9627	.9610	.9676
Etna*	09/95	Scoria[b] (1990 air-fall field).	.9361	.9590	.9687
Stromboli	09/95	Solidifed spatter[b].	.9314	.9404	.9611
Stromboli	10/94	Fresh scoria[b], <1 year old.	.9507	.9442	.9627
Stromboli	10/94	Aa clasts[b] (1985-86 flow field).	.9536	.9474	.9564
Hawaii	10/95	Pahoehoe[b] (smooth glassy surface). (1969-75 flow field).	.9254	.9385	.9399
Hawaii	10/95	Pahoehoe[b] (smooth glassy surface) (1995 flows).	.9001	.8363	.9003
Hawaii	10/95	Pahoehoe[b] (vesicular glassy surface) (1995 flows).	.9495	.8494	.9089
Hawaii	10/95	Ropey pahoehoe[b] (1995 flows).	.9566	.9055	.9313
Hawaii	10/95	Aa clast[b] (1969-75 flow field).	.9532	.9562	.96068
Vulcano	09/95	Trachytic-rhyolitic block coated with fumarolically altered clay.	.9650	.9769	.9836
Vulcano	09/95	Yellow fumarole sublimate, mainly sulfur:			
		fresh surface	.7540	.8615	.8705
		weathered surface	.8634	.9056	.9101
Salisbury & D'Aria (1994)		Obsidian	.9517	.8869	.9452
Salisbury & D'Aria (1994)		Andesite	.9576	.8959	.9478
Salisbury & D'Aria (1994)		Andesite	.8813	.9332	.9654
Salisbury & D'Aria (1994)		Andesite	.9305	.9041	.9582
Salisbury & D'Aria (1994)		Rhyolite	.8358	.9042	.9518

Table 7.2. *Channel 3, 4 and 5 (ε_3,ε_4 and ε_5) emissivities for typical volcanic surfaces. Emissivities were calculated using spectral reflectance measured between 2.08 and 14 μm with a Nicolet system FTIR spectrometer by J. Salisbury (Johns Hopkins University). Spectral reflectances (ρ_i) were calculated by integrating reflectance spectra over each AVHRR waveband, and used to calculate ε_i from Kirchoff's Law ($\varepsilon_i = 1 - \rho_i$). The sample marked * was collected during measurements made with a simultaneous AVHRR over-pass from within the measurement site and [b] denotes basalt.*

of corrections gave surface temperature to ±3 °C of the predicted temperature, many achieving an accuracy of ±1 °C, including LOWTRAN 7 (Figure 7.4).

Since LOWTRAN corrects each channel individually, a temperature is obtained for each of channels 3, 4 and 5 (T_3, T_4 and T_5 respectively). The LOWTRAN mid-latitude summer estimate of T_3 is between -2.3 to -4.6 °C higher than T_4 or T_5 (Figure 7.4), because of the reflected contribution to the channel 3 signal by day. To obtain day-time surface temperatures in channel 3 this reflected component must be removed. For any target pixel, we remove the reflected component from channel 3 by taking the mean T_3 minus T_4 difference for all surrounding non-hot spot pixels, assuming that this was due to the reflected contribution in channel 3, and subtracting this from the T_3 of the target pixel. For 20 images of Etna acquired between 1993 and 1995 this gave corrections typically between -1.0 and -2.5 °C for the summit pixel. This slightly lower correction than predicted is probably because at least 50% of the summit background is composed of rough aa lava, which our spectral measurements (Table 7.2) show to have a lower channel 3 spectral reflectance than scoria (3.7 as opposed to 6.3 %).

7.5.3. Thermal structure of an AVHRR pixel over a volcanic hot spot

Pixel temperatures derived using Equation 7.1 assume that a pixel is occupied by a uniform thermal surface. However, where the pixel is occupied by a sub-pixel hot-spot Equation 7.1b must be rewritten to give

$$R_i = \varepsilon_i \tau_i [pL(\lambda_i T_h) + (1-p)\, L(\lambda_i T_b)] \qquad (7.2),$$

in which T_h is the temperature of the hot spot occupying portion p of the pixel and T_b is the temperature of the cooler ambient background occupying the remaining portion $(1-p)$ of the pixel. Where measurements are available at two widely separated wavebands (i and j), following Dozier (1981) any two of the three unknowns T_h, T_b or p may be estimated by

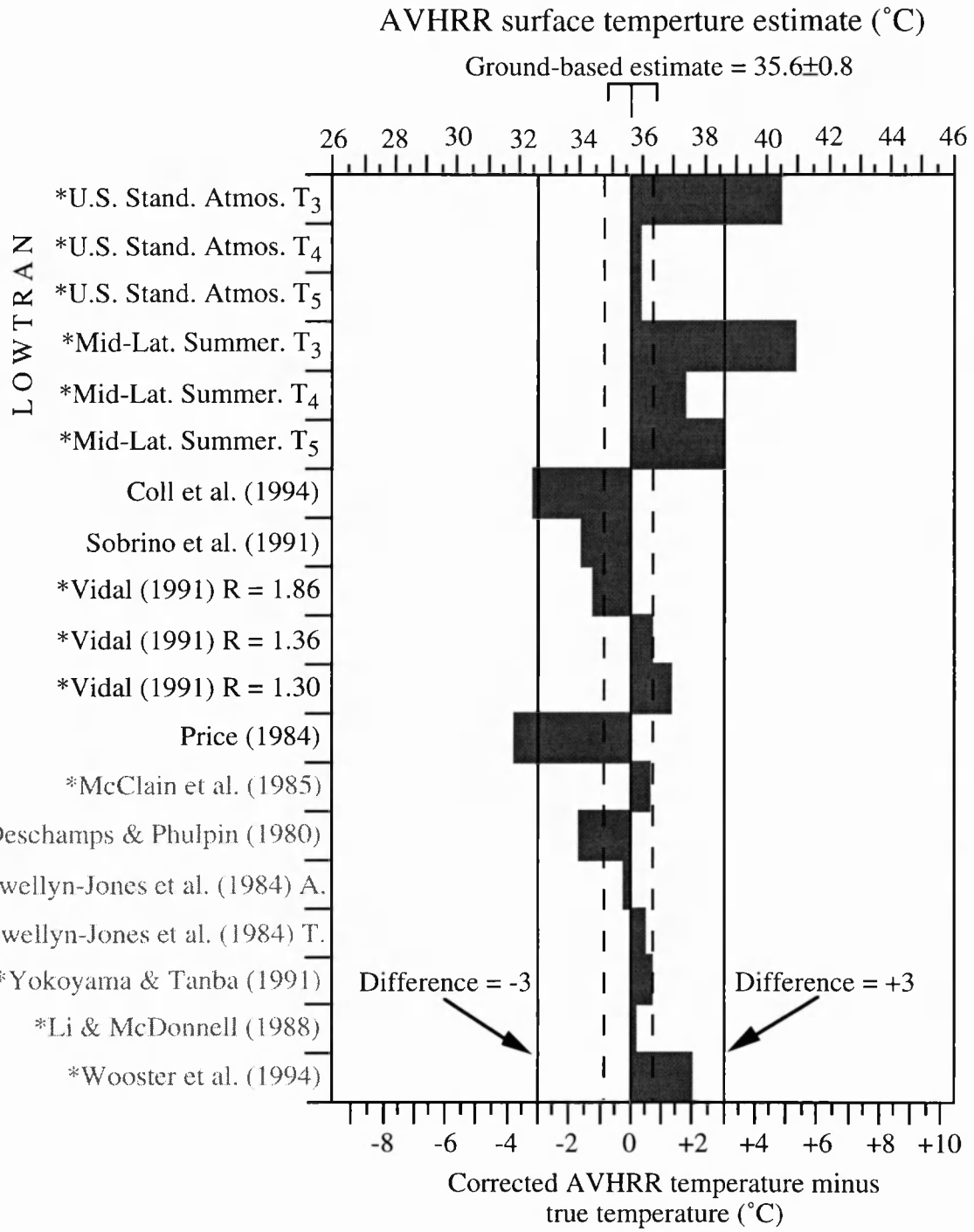

Figure 7.4. *Comparison of AVHRR surface temperature estimated by various atmospheric and emissivity correction procedures with "true" surface temperature obtained by simultaneous ground measurements at Etna. Procedures marked * do not include an emissivity correction and have therefore also been corrected for emissivity [emissivity corrected radiance = $L(\lambda_i T)/\varepsilon_i$]; those given in grey type were initially designed to obtain sea- or lake- surface temperatures within specific latitudinal zones.*

solution of simultaneous equations if the third unknown can be assumed or derived independently:

$$R_i = \varepsilon_i\tau_i\,[pL(\lambda_i T_h) + (1\text{-}p)\,L(\lambda_i T_b)] \quad (7.3)$$

$$R_j = \varepsilon_j\tau_j\,[pL(\lambda_j T_h) + (1\text{-}p)\,L(\lambda_j T_b)] \quad (7.4).$$

Over degassing vents the two component thermal structure generally holds. At Etna in June and October 1994 a degassing vent was present on the floor of one of the summit craters. On both occasions the vent was measured by us in the field at 300-340 °C against a cooler ≤60 °C ambient background. Using three images acquired between March and August 1994 and setting T_b in Equations 7.3 and 7.4 to the mean T_4 from pixels at ambient temperatures surrounding the vent pixel gave T_h of 210-300 °C. Differences between the satellite and ground estimates will be due mainly to contamination of the signal by variable amounts of plume from the degassing vent.

The two component structure will not hold over an active lava. In the most simple case the surface of an active lava is composed of two thermal components: a chilled crust at temperature T_c broken by much smaller areas, typically covering <10% of the lava surface, where molten material at T_h is exposed (Crisp & Baloga, 1990). Within a 1 km^2 AVHRR pixel, lava-free ground at T_b will also be present. Thus, over an active lava, the thermal structure of an AVHRR pixel can be expressed in the most simple case as

$$R_i = \varepsilon_i\tau_i\,[p_h L(\lambda_i T_h) + p_c L(\lambda_i T_c) + (1\text{-}p_h\text{-}p_c)\,L(\lambda_i T_b)] \quad (7.5),$$

in which p_h and p_c are the portions of the pixel occupied by molten and crusted lava respectively. If Equations 7.3 and 7.4 are applied to a pixel containing such a three component surface, the solution will be in error, with the magnitude of the error depending on the relative size and temperature of the three components (Figure 7.5). To avoid error,

Equations 7.3 and 7.4 must be modified to take into account the third thermal component to give

$$R_i = \varepsilon_i\tau_i\,[p_h L(\lambda_i T_h) + p_c L(\lambda_i T_c) + (1\text{-}p_h\text{-}p_c)\,L(\lambda_i T_b)] \quad (7.6)$$

$$R_j = \varepsilon_j\tau_j\,[p_h L(\lambda_j T_h) + p_c L(\lambda_j T_c) + (1\text{-}p_h\text{-}p_c)\,L(\lambda_j T_b)] \quad (7.7).$$

Setting T_b to the mean T_4 of surrounding non-lava pixels leaves 4 unknowns: T_h, T_c, p_h and p_c. To be solvable only two unknowns are allowed, we therefore choose to assume values for T_h and T_c. Our field measurements of active lava flows at Kilauea (Hawaii) during October 1995 gave maximum surface temperatures on exposed molten lava typically ~1000 °C, as opposed to a core temperature ~1100 °C. This is identical to typical maximum surface temperatures measured on active flows at Etna between 1991 and 1993 (S. Calvari, personal communication). We therefore set T_h to 1000 °C. For T_c, our Hawaii field data show that T_c can range from a few degrees less than T_h to ~80 °C, depending on time since the crust formed, agreeing with other field- and satellite-based estimates for crustal temperatures (Oppenheimer, 1991a; Flynn *et al.*, 1993; Flynn & Mouginis-Mark, 1992). This makes T_c impossible to define using a single value. We therefore choose to solve Equations 7.6 and 7.7 over a reasonable range of T_c, with the lower limit set to ~100 °C

Figure 7.5. *(a) False solution of Equations 7.3 & 7.4 by assuming T_h and a two-component model for the 3-component model given. Graphical solution occurs where curves, giving all possible T_b and p_h combinations that give T_3 and T_4, converge. However, in the three-component model the cooler background consists of two distinct sources. Since the source at T_c has much higher temperature than the source at T_b, differing channel 3 & 4 sensitivities cause the integrated background temperature $\{=[p_c/(1\text{-}p_h)]L_i(T_c)+[p_b/(1\text{-}p_h)]L_i(T_b)\}$ to be much higher in channel 3 (T_{b3}) than in 4 (T_{b4}). Thus correct solution will be where $T_{b3}>T_{b4}$, not where $T_{b3}=T_{b4}$. (b) to (e) give errors calculated by holding all model parameters constant except the y axis parameter, which is variable. P_h & P_c are then estimated by assuming T_b and applying a 2-component solution to a number of 3-component models defined by increasing the y axis component through a given range, giving errors resulting from increased (a) T_h (b) T_c (c) p_h and (d) p_c.*

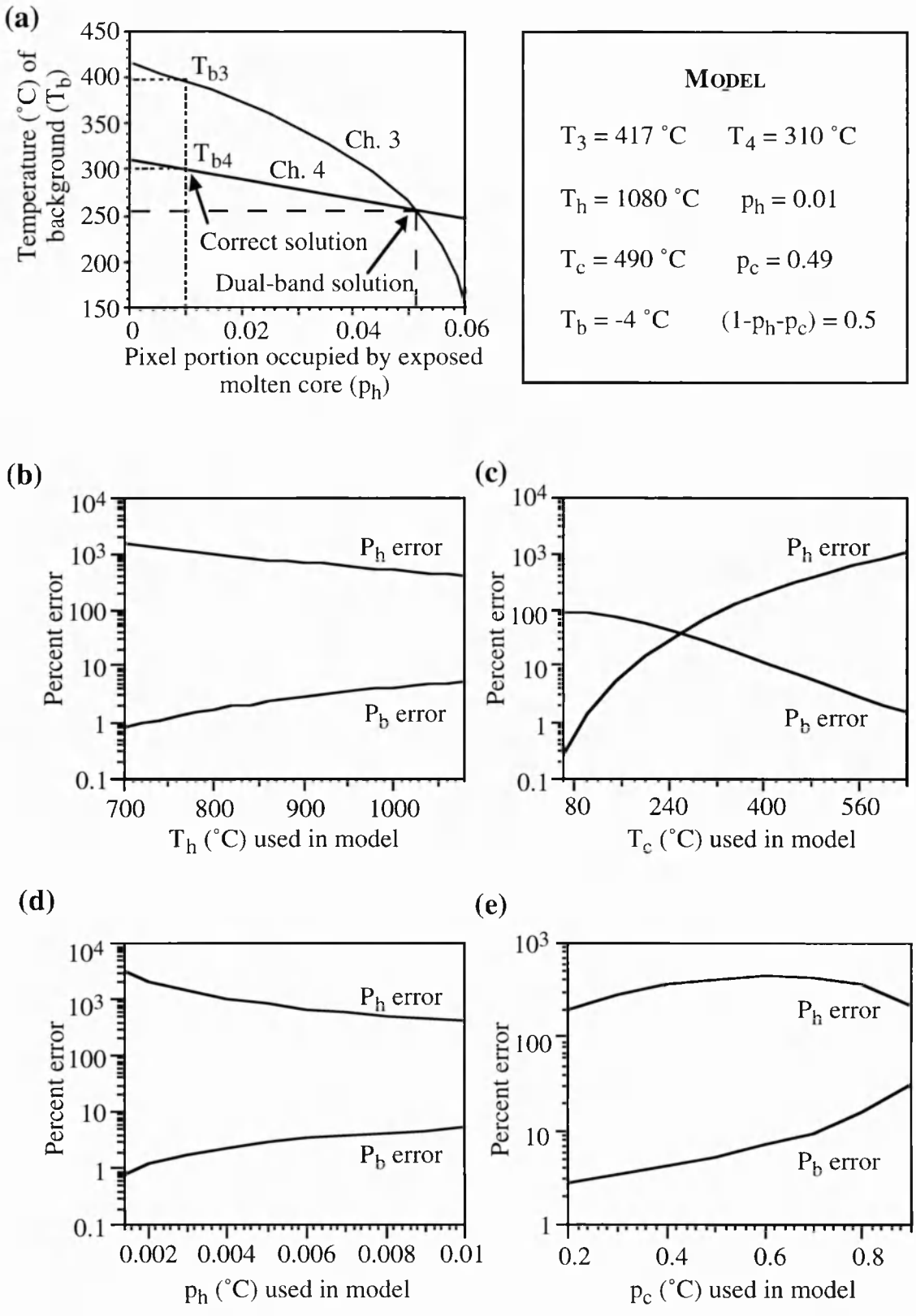
(a)
Temperature (°C) of background (T_b)
450
400
350
300
250
200
150
T_{b3}
T_{b4}
Ch. 3
Ch. 4
Correct solution
Dual-band solution
0
0.02
0.04
0.06
Pixel portion occupied by exposed molten core (p_h)
MODEL
T_3 = 417 °C
T_4 = 310 °C
T_h = 1080 °C
p_h = 0.01
T_c = 490 °C
p_c = 0.49
T_b = -4 °C
$(1-p_h-p_c)$ = 0.5
(b)
Percent error
10^4
10^3
100
10
1
0.1
P_h error
P_b error
700
800
900
1000
T_h (°C) used in model
(c)
Percent error
P_h error
P_b error
80
240
400
560
T_c (°C) used in model
(d)
Percent error
P_h error
P_b error
0.002
0.004
0.006
0.008
0.01
p_h (°C) used in model
(e)
Percent error
10^3
100
10
1
P_h error
P_b error
0.2
0.4
0.6
0.8
p_c (°C) used in model

and an upper limit set by the maximum T_c for which Equations 7.6 and 7.7 are still solvable. However channel 3 radiance cannot be used if it is saturated.

Where channel 3 is saturated and channel 4 is not, if the contribution of $p_h L(\lambda_4 T_h)$ to R_4 (Equation 7.5) can be assumed negligible, and T_b and T_c are known, then p_c can be estimated by re-arranging Equation 7.2. Estimates for p_h derived from Landsat TM data for lava flows, domes and lakes show that p_h typically occupies <0.4 % of the surface (Rothery *et al.*, 1988; Pieri *et al.*, 1990; Oppenheimer *et al.*, 1993; Andres & Rose, 1995). Even given the unlikely scenario of an AVHRR pixel entirely filled by a lava body with 0.4 % of the surface at 1000 °C and the remainder at 500 °C, $p_h L(\lambda_4 T_h)$ contributes ≤1 % of the total radiance (R_4), so the assumption that its contribution is usually negligible is a reasonable one. Setting T_b as for Equations 7.6 and 7.7 and ranging T_c between reasonable limits gives a range of solutions within which p_c must lie, reasonable T_c limits being 100 and 500 °C following the range of T_c derived by Oppenheimer (1991a) and Flynn *et al.* (1993).

7.5.4. Estimation of area

The area of active lava (A_{lava}) can be estimated by multiplying p_h plus p_c by pixel area. This requires accurate calculation of pixel area, since an AVHRR pixel area varies from ~1 to 21 km^2 depending on scan angle, instrument and channel (Table 7.3 & Figure 7.6b). Pixel area is derived using the trigonometric relationships shown in Figure 7.6 and calculated by multiplying the along-scan pixel dimension (P_a) by the cross-scan dimension (P_c), where P_a and P_c obtained from

$$P_a = \{R\,[\sin^{-1}(\Omega \sin\alpha_2) - \alpha_2]\} - \{R\,[\sin^{-1}(\Omega \sin\alpha_1) - \alpha_1]\} \quad (7.8)$$

and

$$P_c = 2\,(\psi \tan\gamma) \quad (7.9),$$

<NOAA> Sat.	Ch	<-----IFOVs------> Scan (mrad)	X-scan (mrad)	<----------Pixel dimensions----------> Pixel (n)	P_a (km)	P_c (km)	Area (km^2)	Pixel (n)	P_a (km)	P_c (km)	Area (km^2)
6	1	1.2995	1.2954	1	1.08	1.08	1.17	1024	6.50	2.31	15.015
	2	1.2751	1.2792	1	1.06	1.07	1.13	1024	6.38	2.28	15.55
	3	1.3299	1.0660	1	1.11	0.89	0.99	1024	6.65	1.90	12.64
	4	1.2448	1.2954	1	1.05	1.08	1.13	1024	6.28	2.31	14.51
7	1	1.443	1.433	1	1.26	1.25	1.575	1024	7.92	2.71	21.46
	2	1.433	1.423	1	1.25	1.24	1.55	1024	7.86	2.69	21.14
	3	1.28	1.463	1	1.11	1.27	1.41	1024	7.02	2.76	19.38
	4	1.423	1.423	1	1.24	1.24	1.76	1024	7.81	2.69	21.01
	5	1.32	1.31	1	1.15	1.14	1.31	1024	7.24	2.47	17.88
8	1	1.36253	1.36665	1	1.13	1.14	1.29	1024	6.81	2.44	16.62
	2	1.35732	1.36338	1	1.13	1.14	1.29	1024	6.79	2.43	16.50
	3	1.38884	1.10897	1	1.16	0.92	1.07	1024	6.95	1.98	13.76
	4	1.21878	1.18863	1	1.02	0.99	1.01	1024	6.10	2.12	12.93
9	1	1.301	1.359	1	1.13	1.18	1.33	1024	7.14	2.57	18.35
	2	1.295	1.370	1	1.13	1.19	1.34	1024	7.10	2.59	18.39
	3	1.067	1.470	1	0.93	1.28	1.19	1024	5.85	2.78	16.26
	4	1.165	1.222	1	1.01	1.06	1.07	1024	6.39	2.31	14.76
	5	1.159	1.257	1	1.01	1.10	1.11	1024	6.36	2.37	15.07
10	1	1.13706	1.34010	1	0.95	1.12	1.06	1024	5.69	2.39	15.60
	2	1.05178	1.27513	1	0.88	1.06	0.93	1024	5.26	2.28	11.99
	3	1.14315	1.22843	1	0.95	1.02	0.97	1024	5.72	2.19	12.53
	4	1.05584	1.28934	1	0.88	1.07	0.94	1024	5.28	2.30	12.14
11	1	1.22	1.26	1	1.06	1.10	1.17	1024	6.69	2.38	15.92
	2	1.30	1.27	1	1.13	1.10	1.24	1024	7.13	2.40	17.11
	3	1.34	1.46	1	1.17	1.27	1.49	1024	7.35	2.76	20.29
	4	1.14	1.24	1	0.99	1.08	1.07	1024	6.25	2.34	14.63
	5	1.197	1.38	1	1.04	1.20	1.25	1024	6.57	2.61	17.15
12	1	1.32	1.34	1	1.10	1.12	1.23	1024	6.60	2.39	15.77
	2	1.32	1.32	1	1.10	1.10	1.21	1024	6.60	2.36	15.58
	3	1.38	1.42	1	1.15	1.18	1.36	1024	6.90	2.54	17.53
	4	1.24	1.28	1	1.03	1.07	1.10	1024	6.20	2.29	14.20
	5	1.32	1.26	1	1.10	1.05	1.15	1024	6.60	2.25	14.85
14*	1	1.40	1.42	1	1.17	1.18	1.38	1024	7.00	2.54	17.78
	2	1.40	1.42	1	1.17	1.18	1.38	1024	7.00	2.54	17.78
	3	1.38	1.48	1	1.15	1.23	1.41	1024	6.90	2.24	18.22
	4	1.28	1.34	1	1.07	1.12	1.20	1024	6.40	2.39	15.30
	5	1.48	1.242	1	1.23	1.03	1.27	1024	7.40	2.22	16.43
Kidwell (1995)											
	1	1.39	1.39	1	1.16	1.16	1.35	1024	6.95	2.48	17.23
	2	1.41	1.41	1	1.17	1.17	1.37	1024	7.05	2.52	17.77
	3	1.51	1.51	1	1.26	1.26	1.59	1024	7.55	2.70	20.39
	4	1.41	1.41	1	1.17	1.17	1.37	1024	7.05	2.52	17.77
	5	1.30	1.30	1	1.08	1.08	1.17	1024	6.50	2.32	15.08

* NOAA-13 was launched on 9 August 1993, but failed on 21 August 1993 before all of the sensors had been turned on.

Table 7.3. *Instantaneous field of view (IFOV) for each AVHRR sensor and channel, with the nadir (pixel 1) and scan edge (pixel 1024) pixel dimensions/areas that these give.*

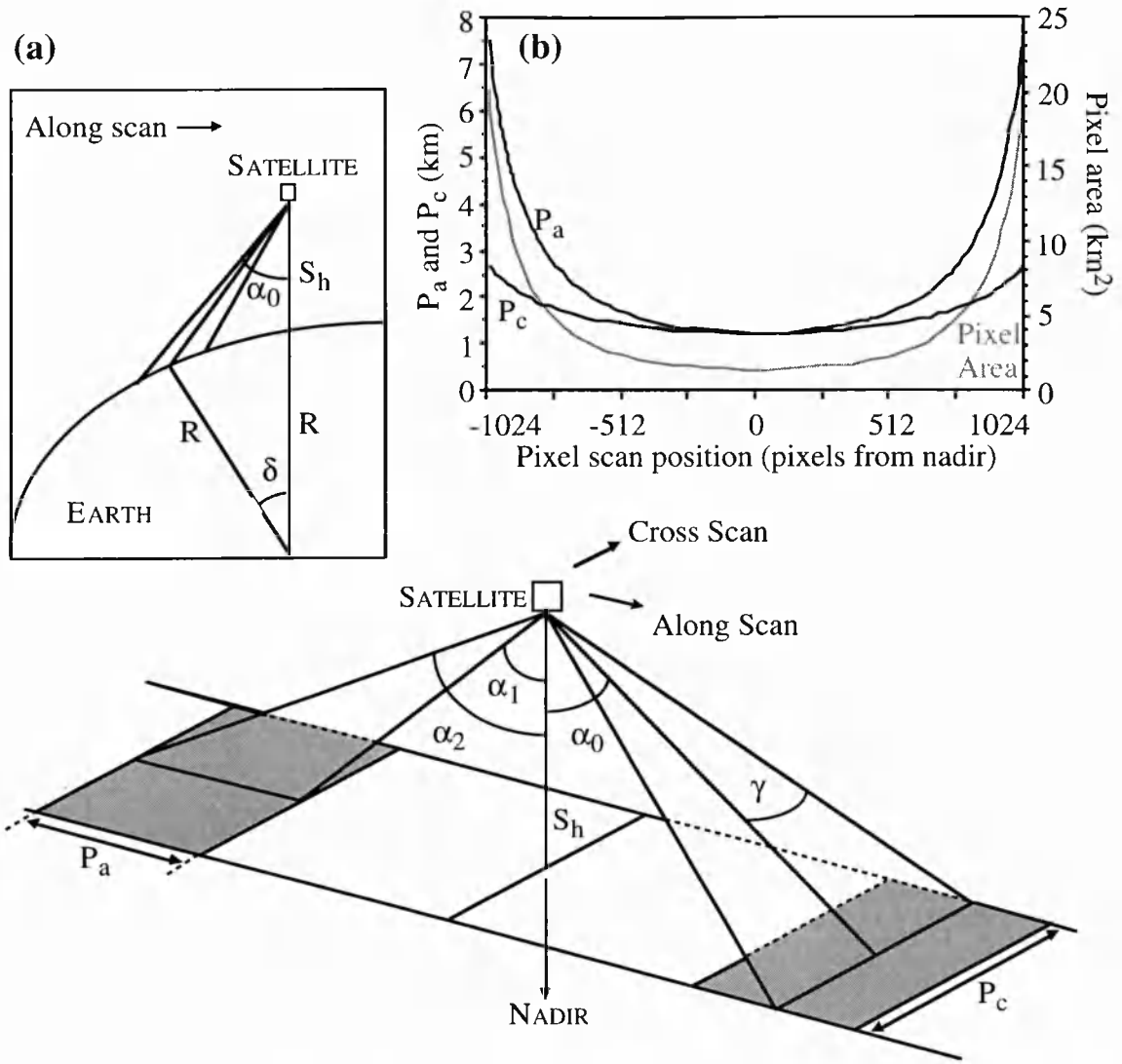

Figure 7.6. *(a) Trigonometric relationships used to estimate along- and cross- scan pixel dimensions (P_a & P_c), and (b) variations in pixel dimensions and area with scan position.*

in which R is the radius of the Earth (6378 km), $\Omega = (S_h+R)/R$, where S_h is satellite height (833 km for NOAA -6, -8, -10, & -12 and 870 km for TIROS-N, NOAA-7, -9 -11, & -13 [K. Kidwell, personal communication]), and α_2 and α_1 are the angles from nadir to the outer and inner edges of the pixel respectively. For a pixel at n pixels from nadir, $\alpha_2(n) = \alpha_0(n)+\beta/2$ and $\alpha_1(n) = \alpha_0(n)-\beta/2$, in which $\alpha_0(n)$ is the angle from nadir to the centre of pixel n, given by $n\theta-\theta/2$, θ being the scan increment angle (0.95×10^{-3} rad), and β is the instantaneous field of view (IFOV) angle. The IFOVs given by the manufacturers of the AVHRR, ITT Aerospace, vary from channel to channel and from platform to platform,

therefore the IFOV used will depend on the platform and channel being considered (Table 7.3). In Equation 7.9, γ is half of the cross-scan IFOV (Table 7.3) and $\psi = (R\sin\delta)/\sin\alpha_0$, where δ is the angle from the centre of the earth to the centre of the pixel, calculated from $\delta = [\sin^{-1}(\Omega\sin\alpha_0)]-\alpha_0$.

Using pixel areas calculated in this way along with p_h and p_c estimated using the three component approach, lava flow areas were estimated during the first month of the 1991 to 1993 eruption at Etna. This effusive eruption, which began on 14 December 1991 and continued until 29 March 1993 producing a 7.6 km^2 flow field (Calvari *et al.*, 1994b), was well monitored from the ground, providing a wealth of ground data against which the satellite based estimates can be compared. The range of area estimates produced by the AVHRR data were in good agreement with the ground-based estimates given by Calvari *et al.* (1994b), straddling them and showing an identical trend (Figure 7.7a).

7.6. AVHRR estimates of flow-wide thermal flux and effusion rates

Total thermal loss (Q_{tot}) from an active lava is given by the sum of the radiative, convective and conductive heat losses ($Q_{rad} + Q_{conv} + Q_{cond}$). Following Danes (1972), heat loss by conduction through the bottom of an active lava flow is assumed to be negligible. This is confirmed by the development of active flows on snow-covered surfaces without phreatic explosions, suggesting rapid development of basal crust providing efficient thermal insulation (Chester *et al.*, 1985). Q_{tot} may therefore be calculated from Q_{rad} and Q_{conv} alone, where

$$Q_{rad} = \sum_{x=1}^{n}\left(\sigma\varepsilon S_x[f_{c_x}T_{c_x}{}^4 + f_{h_x}T_{h_x}{}^4]\right) \qquad (7.10),$$

and

$$Q_{conv} = 0.14\, A_{lava}\, k\, (g\alpha\rho/\mu\kappa)^{1/3}\, \Delta T_s{}^{4/3} \qquad (7.11),$$

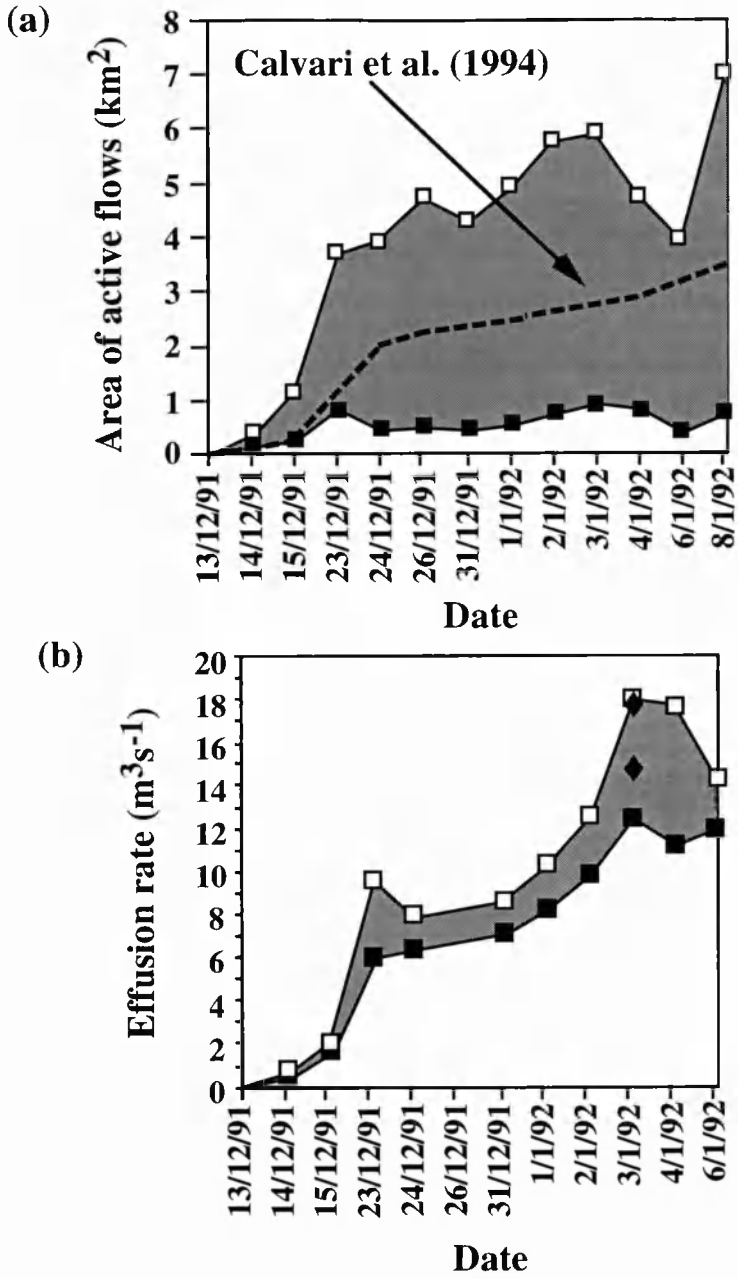

Figure 7.7. *Variation in (a) active flow area and (b) effusion rates during the first 3 weeks of the 1991-1993 Etna eruption. Upper and lower bounds of AVHRR estimates are given by white and black squares, where the true value should lie in the grey zone. Dashed line and diamonds give ground-based estimates.*

in which σ is the Stefan Boltzmann constant (5.67×10^{-8} Wm^{-2} K^{-4}), ε is emissivity integrated across all wavelengths (0.9887, mean emissivity for basalt from Salisbury & D'Aria [1992]), S_x is the lava area in pixel x, T_{h_x} and T_{c_x} are the temperatures for the molten and crusted portions of the lava for pixel x, and n is the total number of lava pixels. Parameters f_c and f_h are the fractions of the lava surface occupied by the crusted and molten components respectively, where $f_c = p_c/(p_c+p_h)$ and $f_h = p_h/(p_c+p_h)$. In Equation 7.11, g is acceleration due to gravity (9.8 m s^{-2}) and $\Delta T_s = T_e - T_{air}$, where T_e is the effective surface temperature [$= (f_h T_h^4 + f_c T_c^4)^{0.25}$, after Pieri *et al.* (1990)] and T_{air} is the air temperature. Properties k, μ, κ, α and ρ are thermal conductivity, dynamic viscosity, thermal diffusivity, cubic expansivity and density of air at a mean temperature of $T_{air} + \Delta T_s/2$, and are taken from tables in Kays & Crawford (1980) using T_{air} of 0 °C.

Following Pieri & Baloga (1986), effusion rates can be calculated by equating Q_{tot} with the heat flux supplied by cooling and crystallisation of the mass of active lava, mass flux rate (M) can be constrained from

$$M = \frac{Q_{tot}}{[C_p \delta T + \phi c_L]} \qquad (7.12a),$$

for an active lava flow, converting mass flux to volume flux, gives effusion rate (E_r)

$$E_r = \frac{Q_{tot}}{\rho\,[C_p \delta T + \phi c_L]} \qquad (7.12b),$$

where ρ is lava density (2600 kg m^{-3}), C_p is specific heat capacity (1150 J kg^{-1} K^{-1}), δT is the average temperature drop throughout the active flow, ϕ is the average mass fraction of crystals grown in cooling through δT and c_L is the latent heat of crystallisation (2.9×10^5 J kg^{-1}). Effusion rates obtained using the December 1991 to January 1992 AVHRR Etna eruption data set were in good agreement with ground-based estimates (Figure 7.7b). This method was also tested on three AVHRR images acquired during the 4-18 September 1984

fissure eruption at Krafla (Iceland). These gave much higher effusion rates of 50-120 $m^3 s^{-1}$. These estimates are consistent with ground-based volume estimates which give 1.2 x 10^8 m^3 of lava erupted in just 14 days (Grönvold, 1987).

7.7. Radiance maps for eruption monitoring

Using the September Krafla 1984 eruption data, Harris *et al.* (1995c) showed how sharpened images could produce radiance maps capable of monitoring the development of an active lava flow field (Figure 7.8). Sharpening improves qualitative visual interpretation of lava flow thermal structure (Figures 7.8a & b), producing radiance maps which at Krafla were in close agreement with ground observations (Harris *et al.*, 1995c). The Krafla radiance map produced from an image acquired just 5 hours after the eruption began late on 4 September clearly locates an eruptive fissure feeding flows in all directions (Figure 7.8b). By the second full day of the eruption, radiance maps indicate shutting down of fissure segments, with activity becoming confined to two areas, one at the northern end of the original fissure and one towards the centre (Figure 7.8c).

Radiance maps are produced by applying the image sharpening technique originally given by Harris *et al.* (1995c) to each hot-spot pixel. The technique divides a pixel into 9 equally sized sub-pixels (Figure 7.8d). New, artificial values are calculated for each sub-pixel, depending on the weighted mean of neighbouring pixels and sub-pixels, by application of Equations 7.13a to 7.13i in the following order:

Figure 7.8. *Thermal maps of the September 1984 Krafla fissure eruption, with ground-based flow field map (Smithsonian Institution, 1989) inset. (a) gives flow field thermal map obtained using a raw image acquired at 04:47 GMT on 5 September 1984, 5 hours after the eruption began and (b) gives the sharpened equivalent. (c) shows the sharpened thermal map for the following day. In each case the image has been fitted to a map of Iceland and the active fissure location overlain, note the shut-down of all bar 2 segments of the active fissure by the second day. (d) shows the partitioning of original pixel (E) to obtain sharpened sub-pixels (spx1 to 9).*

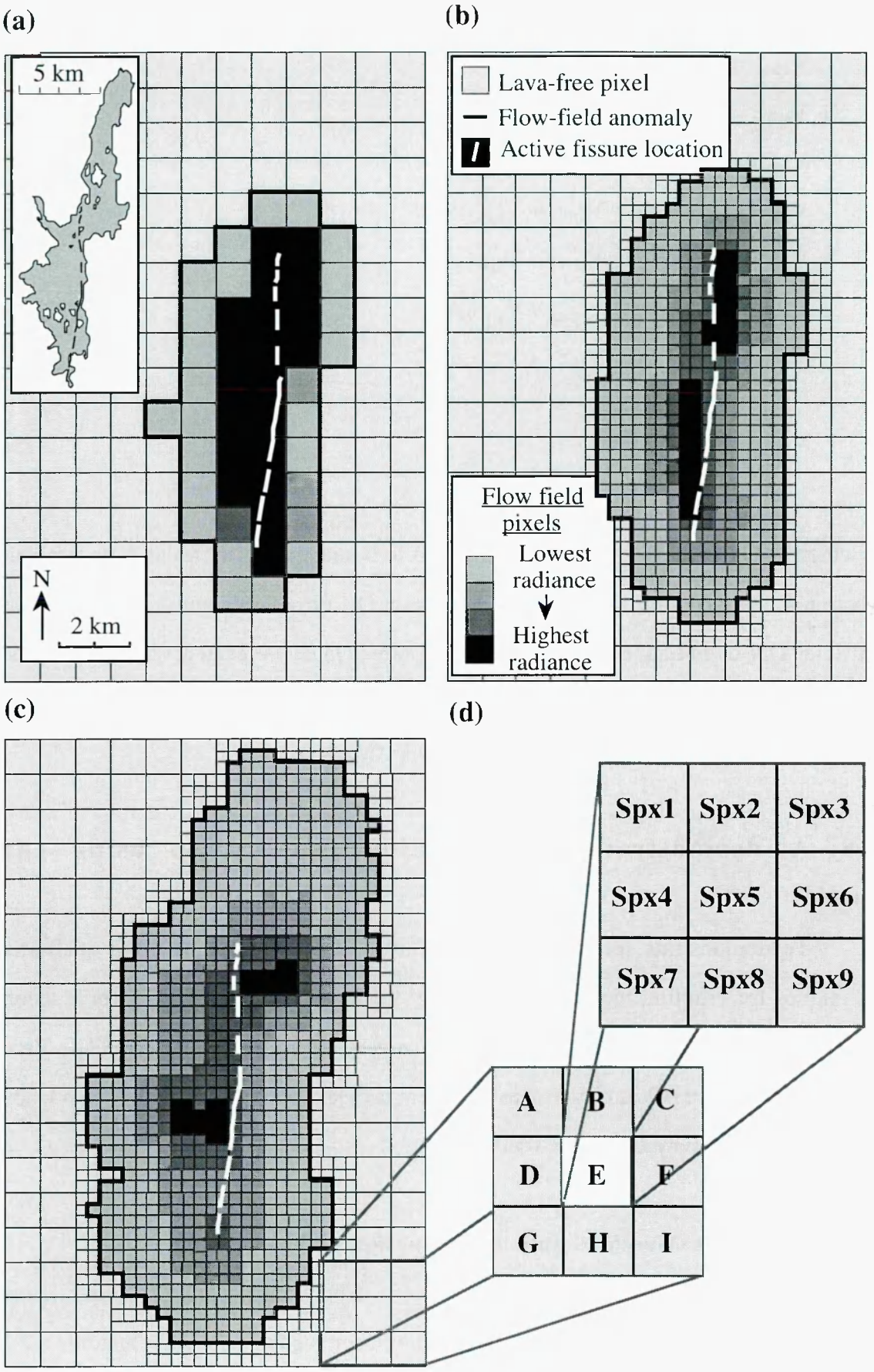
(a)
5 km
N
2 km
(b)
Lava-free pixel
Flow-field anomaly
Active fissure location
Flow field pixels
Lowest radiance
Highest radiance
(c)
(d)
Spx1
Spx2
Spx3
Spx4
Spx5
Spx6
Spx7
Spx8
Spx9
A
B
C
D
E
F
G
H
I

$$V_{spx1} = (V_A + V_B + V_D + V_E)/4 \quad (7.13a)$$

$$V_{spx3} = (V_B + V_C + V_E + V_F)/4 \quad (7.13b)$$

$$V_{spx7} = (V_D + V_E + V_G + V_H)/4 \quad (7.13c)$$

$$V_{spx9} = (V_A + V_B + V_D + V_E)/4 \quad (7.13d)$$

$$V_{spx2} = (V_B + V_E + V_{spx1} + V_{spx3})/4 \quad (7.13e)$$

$$V_{spx4} = (V_D + V_E + V_{spx1} + V_{spx7})/4 \quad (7.13f)$$

$$V_{spx6} = (V_E + V_F + V_{spx3} + V_{spx9})/4 \quad (7.13g)$$

$$V_{spx8} = (V_E + V_H + V_{spx7} + V_{spx9})/4 \quad (7.13h)$$

$$V_{spx9} = \frac{\sum_{spx=1}^{8} V_{spxi}}{8} \quad (7.13i)$$

In which V_i is the value for pixel i, where i = A to B and V_{spxi} is the value for sub-pixel i, where i = 1 to 9 (Figure 7.8d). V_i may be a pixel DN or radiance and V_{spxi} is a derived artificial DN or radiance. We also map two other values: elevated volcanic radiance (R_{ivolc}), calculated by subtracting the mean R_i of the nearest background pixels from the R_i of a located "hot" pixel, and radiant flux density (= Q_{rad}/lava area).

7.8. A demonstration of technique application using case studies

To demonstrate the global applicability of these quantitative and qualitative techniques for eruption monitoring, we apply them to AVHRR data sets for a second eruption at Mount Etna and eruptions at Cerro Negro (Nicaragua), Fogo (Cape Verde Islands), and Lascar (Chile), as well as persistent lava lake activity at Erebus (Ross Island, Antarctica) and activity from open vents at Etna.

7.8.1. The March to July 1985 eruption of Mount Etna

On 12 March 1985 four effusive vents opened between 2490 and 2620 m on Etna's south flank (Smithsonian Institution, 1989). Flows continued until 13 July, building a 2.2

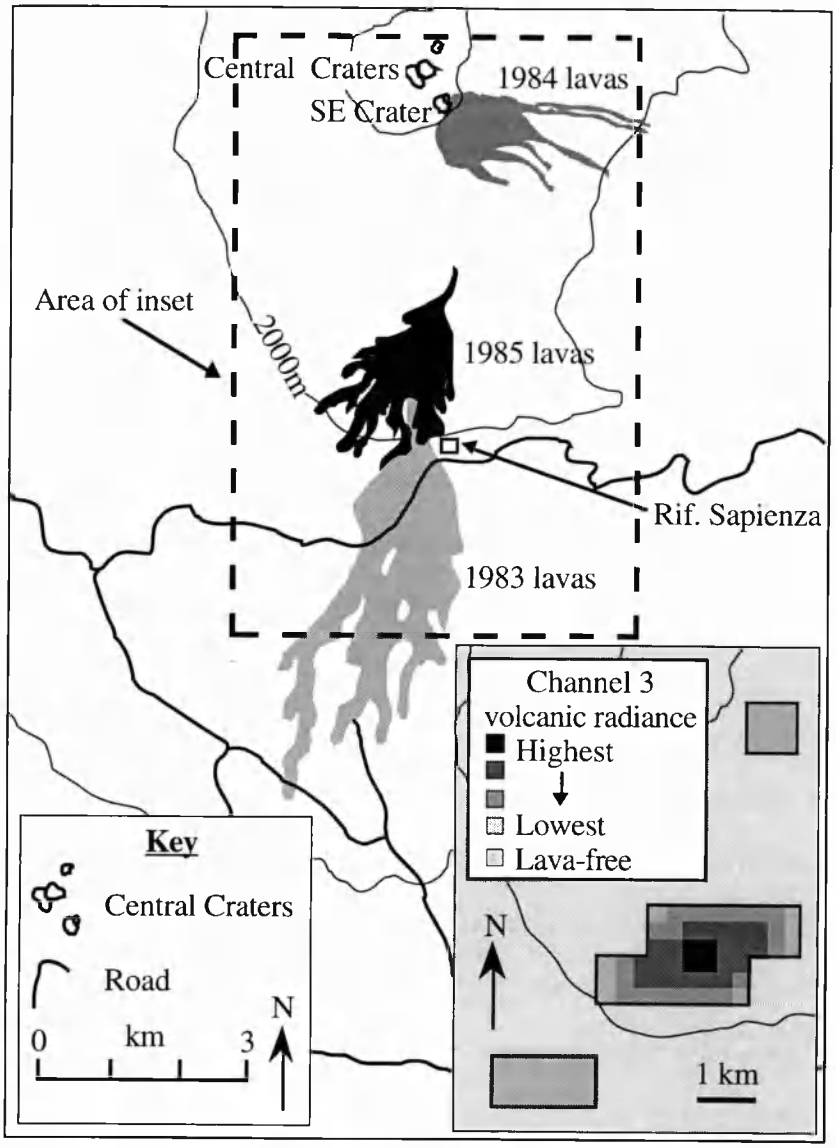

Figure 7.9. *Ground based maps of Etna's 1983, 1984 and 1985 flow fields, with an AVHRR thermal map produced during the 1985 eruption, showing the active flow field and the cooler, inactive, cooling 1983 and 1984 flow fields, inset.*

km^2 flow field, advancing towards the tourist complex at the Rifugio Sapienza and destroying ski-lift pylons. Manually-produced AVHRR radiance maps clearly identify the presence of an active flow field, locating a highly radiant anomaly on Etna's south flank between 2000 and 3000 m (Figure 7.9). Two other anomalies, one to the north and one to the south of the flow field anomaly are also evident. These correspond to cooling flow fields from previous activity, and are distinguishable from the active flow field by their

lower radiance (Figure 7.9). The northern anomaly locates a cooling flow the April-October 1984 SE crater eruption, and the southern anomaly coincides with the thickest portion of the 1983 flow field.

The persistence of cooling anomalies is common on AVHRR images. We measured temperatures up to 220 °C on the 1991-1993 flow field 13 months after activity ceased, with widespread areas of high temperatures (80-100 °C) still apparent at the thickest (75-100 m) areas in September 1995. As a result the cooling 1991-1993 flow field caused a persistent thermal anomaly on many channel 3 images examined up until the end of 1995. It is important not to mistake such cooling anomalies for precursory thermal anomalies.

Analysis of the AVHRR time series identifies two phases characterised by fairly steady active lava area and Q_{tot} levels, punctuated by a low point around 13 June preceded by a month-long decline in both parameters (Figure 7.10a & b). This agrees with ground observations which define two phases of activity (12 March-11 June & 13 June-13 July) during which activity continued at a steady level. These were punctuated by a brief period of quiescence from 11-13 June (Smithsonian Institution, 1989).

The effusion rate time series (Figure 7.10c) shows the same trend, with low (0.5-4.5 $m^3 s^{-1}$) effusion rates throughout the eruption. This compares well with ground-based estimates made between 11 and 13 July of 0.5-2.5 $m^3 s^{-1}$ (Smithsonian Institution, 1989). By integrating effusion rates over time, cumulative volume can be plotted (Figure 7.10d), giving a total flow volume of 16-29 x 10^6 m^3. This suggests that initial ground-based estimates of 30 x 10^6 m^3 (Smithsonian Institution, 1989) were too high, and is in

---

Figure 7.10. *AVHRR time series for (a) active flow area (b) total thermal flux, (c) effusion rates and (d) cumulative volume during the 1985 Etna eruption. In each case white and black symbols define the upper and lower AVHRR estimates, with true value lying in the grey zone, dashed zone is inferred because no images were available during this period. Effusion rates have been calculated using ΔT_{flow} of 150-200 °C (Archambault & Tanguy, 1976) and ϕ of 0.4 to 0.5, allowing for 30 % initial phenocrysts and 20 to 30 % residual glass in solid lava (Armienti et al., 1994).*

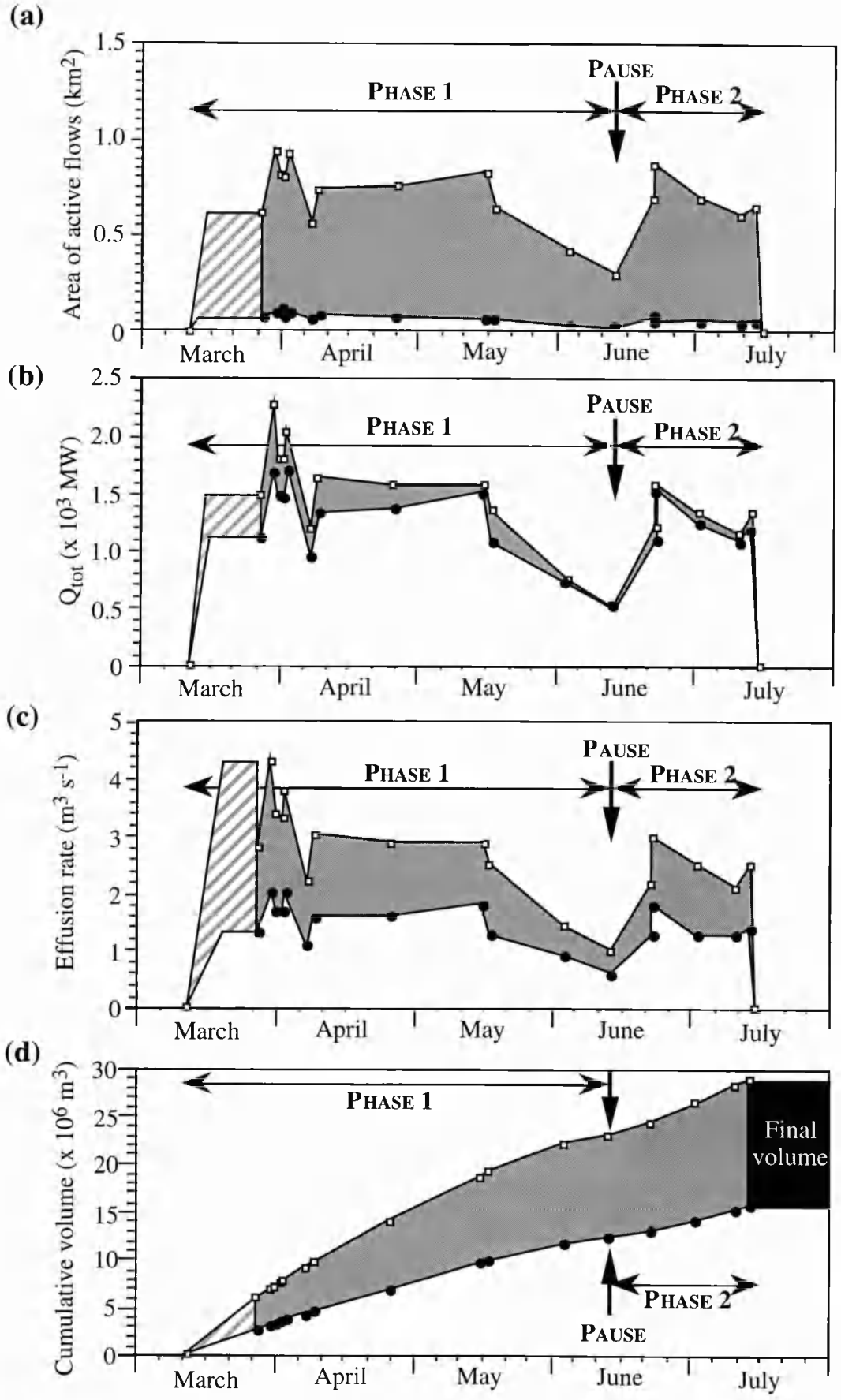
(a)
Area of active flows (km²)
1.5
1.0
0.5
0
PHASE 1
PAUSE
PHASE 2
March
April
May
June
July
(b)
Q_tot (x 10³ MW)
2.5
2.0
1.5
1.0
0.5
0
PHASE 1
PAUSE
PHASE 2
March
April
May
June
July
(c)
Effusion rate (m³ s⁻¹)
5
4
3
2
1
0
PHASE 1
PAUSE
PHASE 2
March
April
May
June
July
(d)
Cumulative volume (x 10⁶ m³)
30
25
20
15
10
5
0
PHASE 1
Final volume
PHASE 2
PAUSE
March
April
May
June
July

agreement with more accurate estimates of 19 x 10^6 m^3 obtained at a later date using Electronic Distance Measurement (J. Murray, personal communication).

Effusion rate and flow volume have been shown to influence flow length and area, higher rates and volumes giving flows of greater length and area (Walker, 1973; Malin, 1980; Pieri & Baloga, 1986), so reliable estimates made during an eruption are extremely important in determining the hazard posed to communities down-flow. At Etna, high effusion rate (>50 m^3 s^{-1}) eruptions in 1928 and 1981 fed flows that rapidly advanced several kilometres causing great damage, the former advancing 8 km in <26 days destroying the town of Mascali, the latter causing costly damage and evacuations (Table 7.1). However, while effusion rates remain low (<10 m^3 s^{-1}) flows are likely to remain short and spatially confined, building a compound field (Walker, 1973), as during the 1985 eruption examined here.

7.8.2. The November to December 1995 eruption of Cerro Negro

Cerro Negro erupted 22 times between 1850 and 1992, causing damage during 9 of these eruptions (Simkin & Siebert, 1994). The 1995 eruption began on 19 November with a Strombolian phase. On 22 November a growing dome emitted the first lava flow, with explosive and effusive activity continuing until 6 December (GVN, 1995e). Humanitarian reports indicated that 12000 people were affected, mainly by tephra fall, of whom 6000 were evacuated. Agricultural damage and evacuation costs totalled US$ 722000 (DHA, 1995a, 1995b). Field observations were impeded by ejection of bombs, which made the upper portions of the active flows dangerous to reach (B. van Wyk de Vries, personal communication), making satellite measurements an attractive option. Fortuitously, the UK Natural Resources Institute had installed an AVHRR receiving station in Managua (Nicaragua) during the preceding summer as part of an Overseas Development Agency supported technical project. From this station the eruptive activity could be imaged, with images showing ash clouds extending mainly to the west and a major hot spot at Cerro Negro itself (Figure 7.11a). Lava area and effusion rate time series (Figure 7.11b & c)

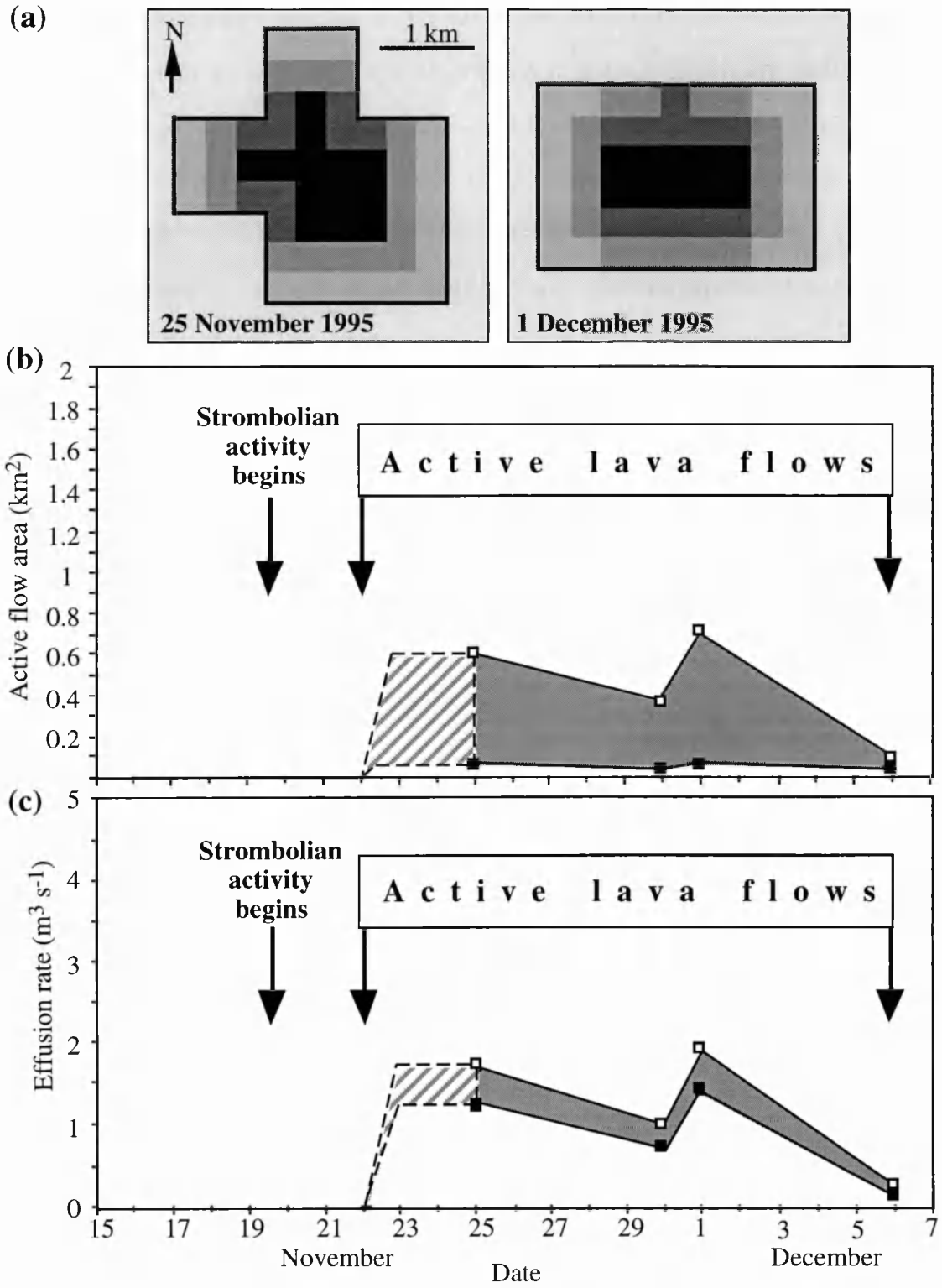

Figure 7.11. *(a) Thermal maps (see Figure 7.8 for key), (b) active area and (c) effusion rates derived from AVHRR data during the 1995 eruption of Cerro Negro. Dashed zones in (b) and (c) are inferred as in Figure 7.10.*

define flows of small area (active areas <0.7 km^2), and low effusion rate (<2 $m^3\ s^{-1}$), indicating that lava flows were unlikely to extend any great distance. Indeed, field reports showed that flows reached no more than 1.5 km from the active dome (GVN, 1995e). Increases in active area and effusion rate are noted around the end of November (Figure 7.11b & c), coincident with a peak in lava emission observed in the field (B. van Wyk de Vries, personal communication). The AVHRR time series gives a mean effusion rate during the eruption of 0.8-1.2 $m^3\ s^{-1}$ and a total volume of 1.0-1.6 x 10^6 m^3. Although Electronic Distance Measurements of the flow field made during April 1996 will be used to obtain a precise volume estimate (N. Stevens, personal communication), at the time of writing the effusion rates and flow volume given here are the only estimates available.

The AVHRR data show that most of the damage caused by this eruption was due to air-fall rather than lava flow activity. Comparison of vegetation maps produced using AVHRR data before and after the eruption showed a ~20 km wide zone of damaged vegetation extending SW to the coast, damage being due to ash-fall during the eruption.

7.8.3. The April to May 1995 eruption of Fogo

On 4 April 1995 a major thermal anomaly in AVHRR channels 3 and 4 within Fogo's Cha Caldera, close to the village Bangaeira, signalled the beginning of a major fissure eruption (Figure 7.12). The eruption had begun during the night of 2-3 April, and on 3 April the ~1300 population living within the caldera left on foot, subsequently being housed in tents, schools or with relations (GVN, 1995f; DHA, 1995c). Fire fountaining and lava effusion continued from a growing scoria cone on the SW flank of the Pico cone until 28 May, building a ~6.3 km^2 lava flow field (Figure 7.13a). Lava flows cut the main caldera road, buried the village of Boca de Fonte (population 56), and covered 5 km^2 or 10% of Fogo's of agricultural land. It destroyed a winery and 5 other houses, stopping ~500 m short of Portela and Bangaeira villages (GVN, 1995f, 1995g, 1995h; DHA, 1995c). Although we were unable to calibrate the AVHRR images and thereby complete a quantitative analysis, the time series of radiance maps clearly charted the development of

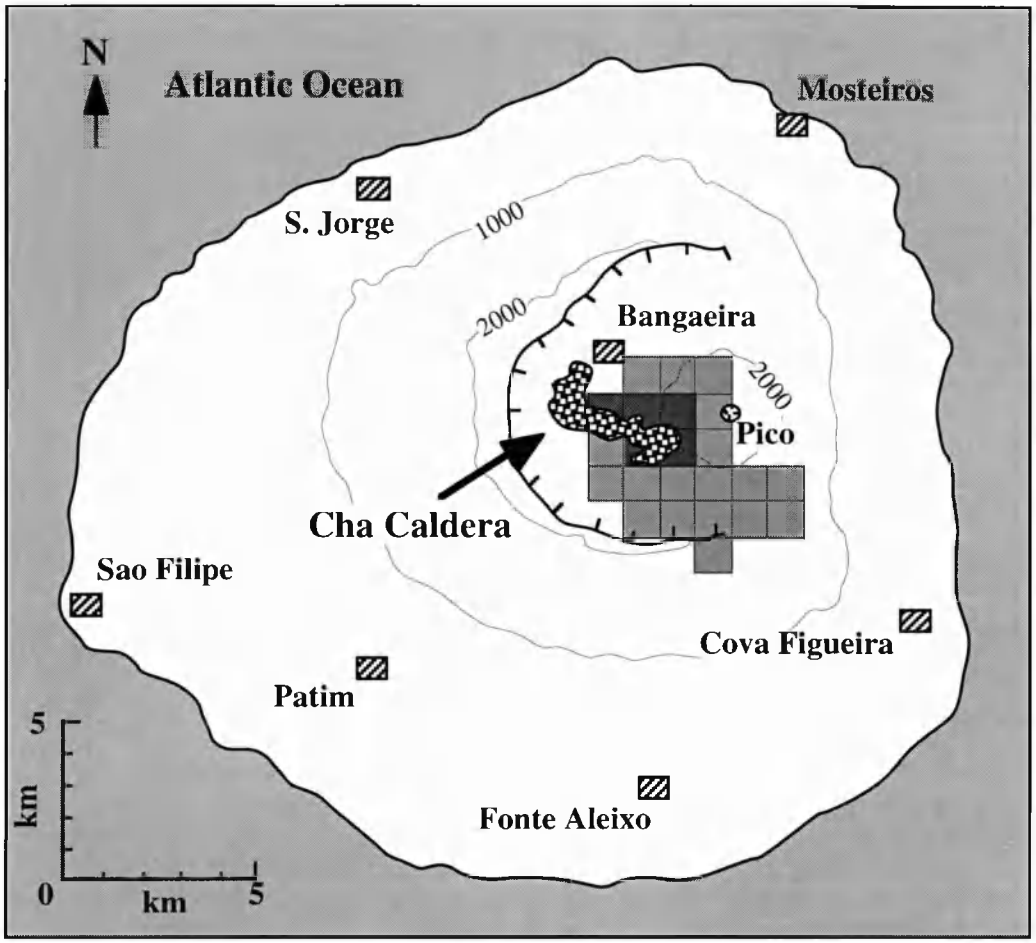

Figure 7.12. *Channel 3 (light grey) and channel 4 (dark grey) thermal anomalies during the first days of the 1995 Fogo eruption located by fitting a map of Fogo to the AVHRR image. Ground-based map of the flow field is overlain in stipple. Channel 3 anomaly is much larger than that of channel 4 due to smearing of radiance along and cross scan into otherwise non-radiant pixels (point spread function pixels). Channel 4, being less effected, gives a more reasonable location and area. The automated thresholding algorithm of Harris et al. (1995b) similarly excludes point spread function pixels, as well as sensor recovery pixels (anomalously cold pixels frequently found on the down scan edge of AVHRR thermal anomalies).*

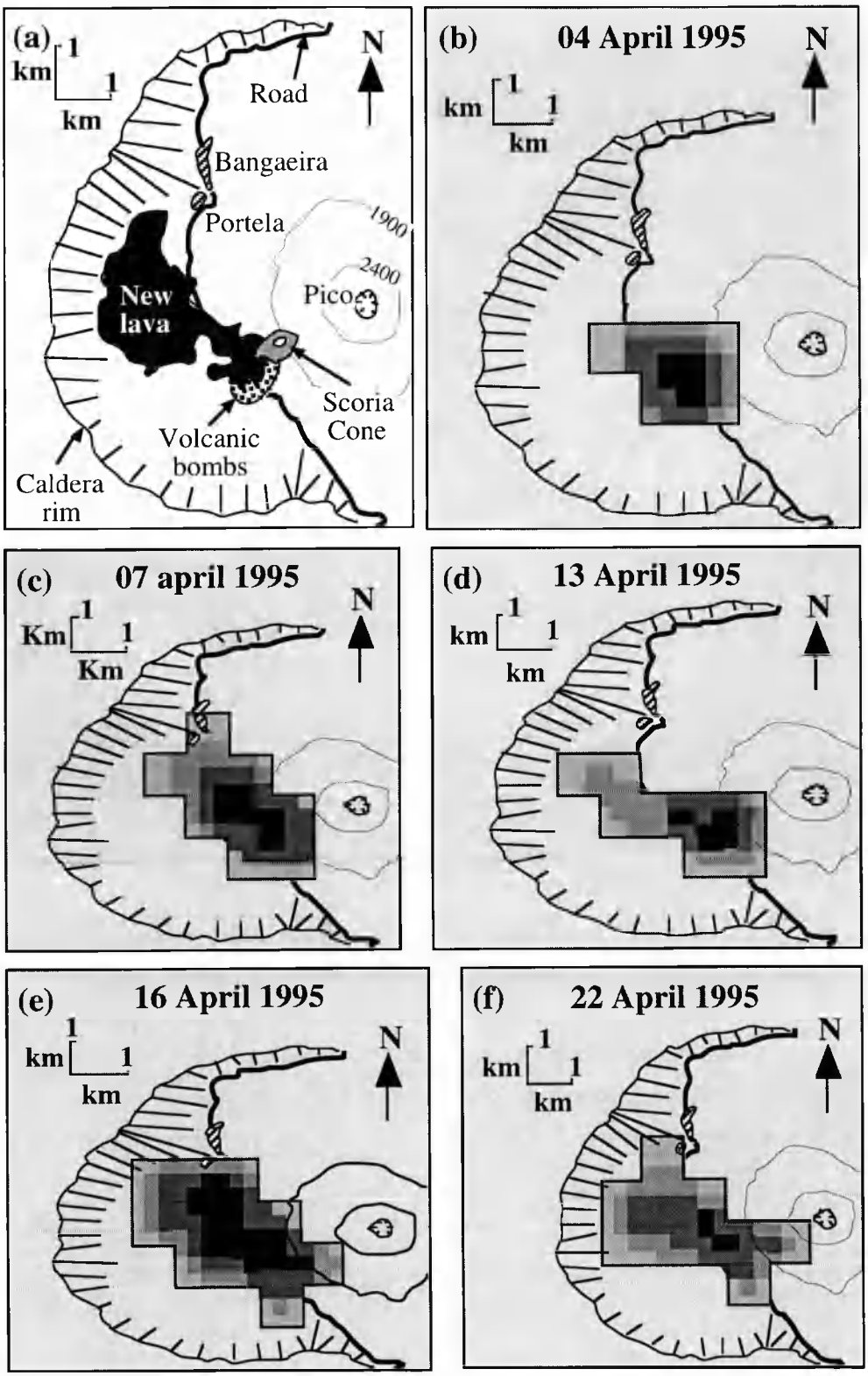

Figure 7.13. *(a) Ground-based map of the flow-field from the 1995 Fogo eruption (GVN, 1995h) and (b) to (f) thermal maps derived from AVHRR time-series acquired during the eruption with base map fitted to the image. The images have not been geometrically corrected, hence the different N-S and E-W scales. Key as for Figure 7.8.*

the eruption through April (Figures 7.13b to f). In agreement with ground observations, all radiance maps show major lava flows advancing from a source on the SW flank of the Pico cone. Figure 13b coincides with the cutting of the main road within a day of the eruption beginning, while subsequent maps (Figures 7.13c to f) show extension of the flow field to the west and north, burying fertile agricultural land and buildings, and illustrating the threat to Portela and Bangaeira.

7.8.4. The April 1993 eruption of Lascar

Current activity at Lascar is characterised dome growth punctuated by explosive eruptions. Lascar is remote, so ground observations are rare. The most complete record of activity since 1984 is from remotely sensed data (e.g. Glaze *et al.*, 1989b; Oppenheimer *et al.*, 1993; Denniss *et al.*, in press; Wooster & Rothery, in press). These have shown how time series of thermal data can be used to monitor lava dome activity within Lascar's summit crater. Wooster & Rothery (in press) demonstrate how cheap, regularly available, 1 km^2 pixel data from the Along Track Scanning Radiometer (ATSR) can be used to detect variations in the state of the dome. Their 1992-1995 time-series shows changes in detected radiance related to dome extrusion, collapse and subsequent explosive events. Here we analyse data for pyroclastic flows emplaced during the April 1993 eruption.

Lascar's largest eruption began late on 18 April 1993 and continued until 21 April, sending ash up to ~25 km (GVN, 1993e). Pyroclastic flows extended 7.5 km to the NW and 4 km to the S, being apparent as a major thermal anomaly on an AVHRR image acquired during the eruption (Figure 7.14). Pyroclastic flow temperature and area were estimated using Equations 7.3 and 7.4. Our assumption that a pyroclastic flow pixel can be described by two thermal components is based on measurements made during the 1980 eruptions of Mount St. Helens by Banks & Hoblitt (1981). These gave pyroclastic flow temperatures which were isothermal in cross-section and approximately uniform along the flow path. Where channel 3 was saturated, T_h derived for the nearest non-saturated flow pixel was used in Equation 7.2. Multiplying p_h by the pixel area, and summing the results

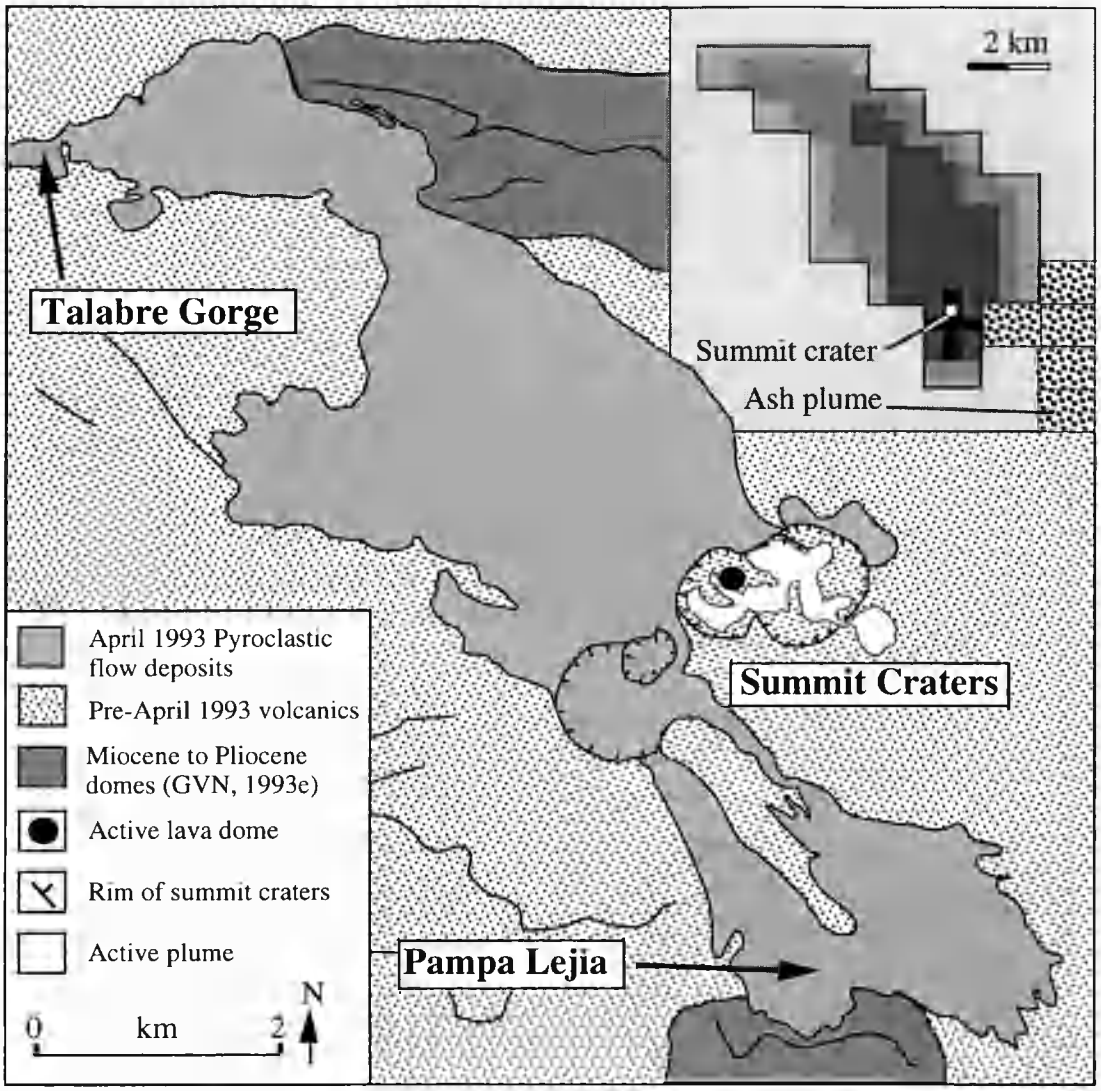

Figure 7.14. *Map of the pyroclastic flows from the April 1993 eruption of Lascar produced from JERS-OPS data (Denniss et al., in press), with thermal map produced from a syn-eruption AVHRR image inset (Key as for Figure 7.8).*

for all pixels, gave an area of recently emplaced hot pyroclastic flow of ~13 km^2. This compares with 18.5 km^2 obtained using a high spatial resolution (324 m^2 pixel) JERS-1 OPS image (Denniss *et al.*, in press). Derived values for T_h were near uniform at 120±20 °C across both the northern and southern flow units. These are somewhat lower than >300 °C emplacement temperatures measured at Mount St. Helens (Banks & Hoblitt, 1981), which could be due to lower emplacement temperatures, surface cooling since emplacement, or mantling by fall-out from a cooler co-ignimbrite ash cloud at Lascar.

The AVHRR radiance map shows (within the limits of its spatial resolution) an identical spatial distribution of pyroclastic flows around the summit crater to that revealed by high spatial resolution mapping (Figure 7.14). The thermal structure, with radiance decreasing very gradually down-flow after an initial rapid decrease, is very different to that seen for fissure-fed (Figure 7.8a) or vent-fed (Figure 7.13) lava eruptions. This is in agreement with Banks and Hoblitt (1981) who note similar thermal structure in pyroclastic flows emplaced during the 1980 Mount St Helens eruptions, suggesting that after initial rapid cooling by adiabatic expansion and incorporation of air, little more cool air is entrained along the remaining flow path. In the absence of ground monitoring, the thermal structure and temperatures obtained from the AVHRR data would have enabled us to identify this flow as a high temperature pyroclastic flow (nuée ardente) rather than a lava flow, which if impacting on a populated area would cause widespread death and injury (Baxter, 1990).

7.8.5. Persistent lava lake activity at Erebus

Two AVHRR images of Erebus were acquired, about one and a half hours apart, during the morning of 13 January 1980. At this time a ~4500 m^2 lava lake was active within the summit crater (Smithsonian Institution, 1989). Area and flux estimates were identical on both images, giving an hot area of ~6-32 x 10^3 m^2. This exceeds the ground estimate, but is less than that given by Glaze *et al.* (1989a) of 35 x 10^3 m^2 using a January 1985 TM image. We suggest both apparent over-estimates are due to the presence a number of hot targets within the pixel in addition to the lava lake, these include ephemeral occasionally incandescent fumaroles (P. Kyle, personal communication) and an active Strombolian vent (Smithsonian Institution, 1989). Our Q_{rad} estimate of 60-70 MW (Q_{tot} = 80-110 MW) is very similar to 58 MW estimated by Glaze *et al.* (1989). Consistency in Q_{rad} between the two AVHRR images and the TM image indicates activity at a steady level. Following Equation 7.12a, thermal loss (Q_{tot}) at the lake surface requires a magma flux of 270-350 kg s^{-1} if all degassed magma is recycled as cumulates to a deeper chamber (δT =

200 K, $\phi = 1$), or 50-70 kg s^{-1} if degassed magma is emplaced as dykes beneath or within the edifice ($\delta T = 1200$ K, $\phi = 0.45$). This will be a minimum estimate since it does not include heat carried by the gas phase, SO_2 flux at Erebus typically being in the range 25-230 t d^{-1} (Kyle *et al.*, 1994).

Sporadic ground observations have shown that similar activity has persisted at Erebus since the discovery of a lava lake in 1972 (Giggenbach *et al.*, 1972). Since 1980 lava lake activity has been punctuated by a period of increased Strombolian activity, burial and re-establishment of the lake and two phreatic eruptions (Smithsonian Institution, 1989; GVN, 1995i). During this period a number of remote sensing assessments have also been made using AVHRR and TM thermal data (Wiesnet & D'Aguanno, 1982; Rothery *et al.*, 1988; Glaze et al, 1989a; Rothery & Oppenheimer, 1994). Such satellite observations offer an ideal means of regularly monitoring Erebus and other remote and inhospitable volcanoes.

7.8.6. Activity at Etna's summit craters 1993-1995

Etna's summit cone or "Central Crater" is occupied by 2 pit craters, La Voragine and the Bocca Nuova. Activity within these reflects magma levels in the main conduit. Low or falling levels causing pit crater collapse and deepening. Rising levels are typified by Strombolian activity and filling with ejecta (Chester *et al.*, 1985). Two lateral cones on the Central Crater's NE and SE flanks, the NE and SE Craters, have also been persistently active since opening in 1911 and 1971 respectively. Although Strombolian activity, lava fountaining and effusive events were common at the NE and SE Craters during 1970s and 1980s (Chester *et al.*, 1985; Calvari *et al.*, 1994a), following the December 1991 - March 1993 flank eruption all craters were active with steady degassing only (GVN, 1994).

These conditions remained characteristic of activity during field work by us in June and October 1994. On both occasions the NE Crater floor was ventless showing fumarolic activity only. However, conduits were open at two 10 x 10 m degassing vents, one each in

Location	Maximum temperature (°C) June 1994	October 1994	Temperature increase (°C)
NE CRATER			
Fumaroles at N rim	65	77	12
Rifts at NW rim	141	246	105
Fumaroles at W rim	97	210	113
Fumaroles at S rim	86	221	135
BOCCA NUOVA			
Fumaroles on N flank	76	79	0
Fumaroles & rifts at N rim	74	74	0
Fumaroles at SW rim	66	72	6
CENTRAL CRATERS			
Fumaroles at S rim	83	82	-1
Between S rim & SE crater	81	83	2
SE CRATER			
Fumaroles & rifts at N rim	312	482	170
Fumaroles & rifts at W rim	208	218	10

Table 7.4. *Changes in maximum fumarole temperatures measured using a Minolta/Land Compac 3 infrared thermometer at Etna's summit craters between June and October 1994.*

La Voragine and the Bocca Nuova at 300-340 °C and 160-170 °C respectively. A third degassing vent was located within the SE Crater. Fumarole temperature increases at the NE Crater (Table 7.4) are interpreted as a thermal precursor to the re-opening of the NE Crater after December 1994. This resulted in sporadic ash and block emission, causing issue of aviation notices when a 4200 m high plume was emitted in June 1995 and termination of guided summit tours (GVN, 1995j). Subsequently, activity has continued to build, with intermittent Strombolian activity resuming from the NE Crater and Bocca Nuova in July-August 1995 and lava fountaining episodes causing ash fall on the city of Catania (30 km SSE) during November (GVN, 1995k; 1995l). As of 11 February 1996 a total of 8 fire fountaining episodes had been observed.

We have examined an AVHRR time series acquired over this period to determine whether the data could have been used to monitor these developments. For hot spots of this nature, (i.e. located at the foot of a shielding feature, in this case 100-120 m high crater

walls), the effect of topographic shielding must be considered (Figure 7.15a). The hot spot will begin to be obscured at a scan angle (α_0) equal to $\sin^{-1}[\Omega\sin(\pi/2-\chi_{in}]$, in which χ_{in} is the angle subtended by a line of sight from the satellite to the hot spot inner edge and the crater floor which just glances the crater rim. This is obtained from $\chi_{in} = \tan^{-1}[H/W]$, H being the height of the shielding feature and W the distance from the foot of the shielding feature to the hot-spot edge. The scan angle at which the hot spot will be completely obscured is obtained by substituting χ_{in} with the angle subtended by a line of sight to the hot spot outer edge and the crater floor which just glances the crater rim (χ_{ou}). Angle χ_{ou} is given by $\tan^{-1}[H/(W+\omega)]$, ω being the hot-spot width. The Bocca Nuova vent, sited at the foot of the crater wall, will become increasingly obscured after α_0 ~0 °, disappearing around α_0 5.5 ° (~100 pixels from nadir). La Voragine vent , roughly central in a ~100 m wide crater, should not begin to be obscured until α_0 ~28 ° (~510 pixels from nadir).

To ensure that a time-series is not affected by scan angle induced radiance variations, (i.e. increased obscuration of the hot vent will cause decreased pixel-integrated radiance), images acquired at similar scan-angles must be used. To monitor Etna's Central Crater we therefore selected all images within 500 pixels of nadir, thereby ensuring an unobscured view of La Voragine vent. Using images between 100 and 500 pixels of nadir also ensured that the Bocca Nuova vent would not be visible, and that variations in radiance would not be due to variations in obscuration of this vent. Equations 7.3 and 7.4 were applied to the selected images to estimate T_h. The resulting variations in T_h for La Voragine vent between 1993 and 1995 are consistent with ground observations (Figure 7.15b). Low values of T_h during 1993 reflect quiet degassing following the 1993 eruption, with a rise during 1994 being a possible precursor to renewal of explosive activity. We interpret low T_h during 1994-1995 as resulting from increases in fume/ash and partial vent blockage by blocks produced during explosive events. The beginning of Strombolian activity in 1995 is marked by a rise in T_h, with highest T_h in the series reached around the time of the first fountaining event. By this time a 15 m wide pit containing spattering magma had developed on the NE Crater floor (GVN, 1995l).

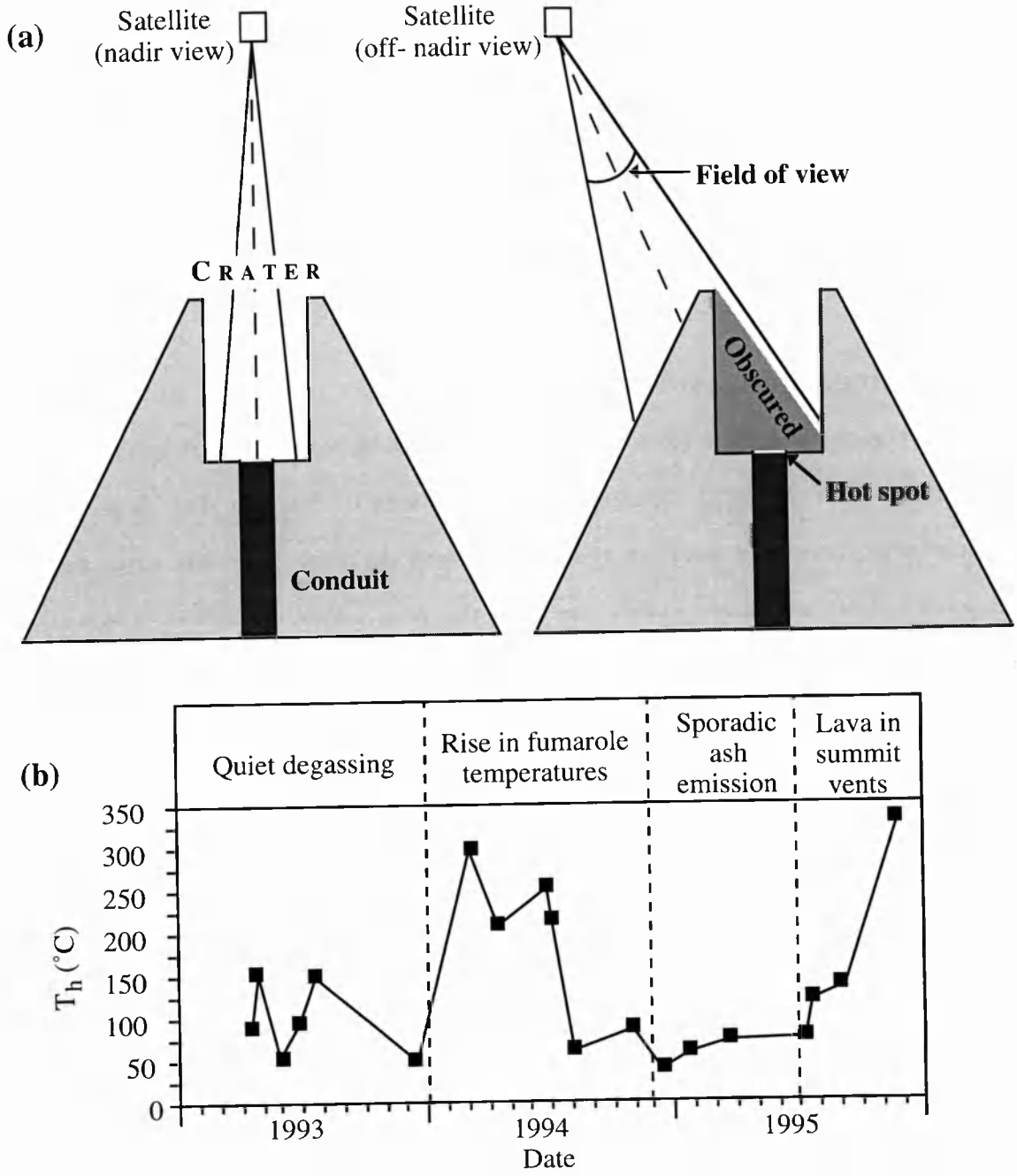

Figure 7.15. *(a) Viewing geometry and effects of topographic shielding for hot-spots located on crater floors in AVHRR data. (b) Variations in approximate vent temperature, T_h, for La Voragine vent produced from 1993-1995 AVHRR time-series, with phases of activity observed from the ground indicated.*

Although activity at Etna's summit craters has produced casualties and damage by tephra fall, as well as being indicative of magma column level (Chester *et al.*, 1984; SEAN, 1987, 1989b, 1989c), published observations of summit activity are scarce (Calvari *et al.*, 1994a). Regular ground observations are impeded by deep snow and harsh conditions. Here, and at other volcanoes, AVHRR data are capable of providing a reliable means of regularly monitoring vent activity when ground observations are impossible or dangerous.

7.9. Distinguishing volcanic hot spots

Mouginis-Mark *et al.* (1994) show how AVHRR viewing geometry can be used to distinguish various hot spot scenarios. For a lava body of constant size, as p_c and p_h decrease with increasing pixel area, so R_i will also decrease. This will bring certain scenarios below saturation if they are near the scan edges, improving chances of discrimination (Figure 7.16). Whether and where this occurs depends on the body size and temperature, background temperatures, waveband, and whether thermal features are isolated or widely separated, allowing each feature to be contained within a single pixel. In practice we were unable to apply the modelled scenarios given in Figure 7.16 to effusive eruption data for Etna or Cerro Negro. Widespread channel 3 saturation occurred on each of ~100 images examined despite utilisation of the full scan width, a result of features being too closely clustered (note the effect of increasing the number of skylights, Figure 7.16).

We present an alternative method which uses the scatter plot of R_{3max} versus R_{4max}, these being the differences between the maximum radiance within the anomaly and the minimum from the background in channels 3 and 4 respectively. For cool or small anomalies such as 100 m^2 vents at 340 °C, as at Etna, or 16 m^2 vents at 900 °C, as at Stromboli, both R_{3max} and R_{4max} will be low. For example, assuming a background at 0 °C for the two cases given above, R_3 and R_4 for the vent pixel will be 0.31 and 72.36 mW/m^2 sr cm^{-1}. R_3 and R_4 for vent-free pixels surrounding the anomaly will be 0.17 and 72.3 mW/m^2 sr cm^{-1}, giving R_{3max} and R_{4max} of 0.14 and 0.06 mW/m^2 sr cm^{-1}.

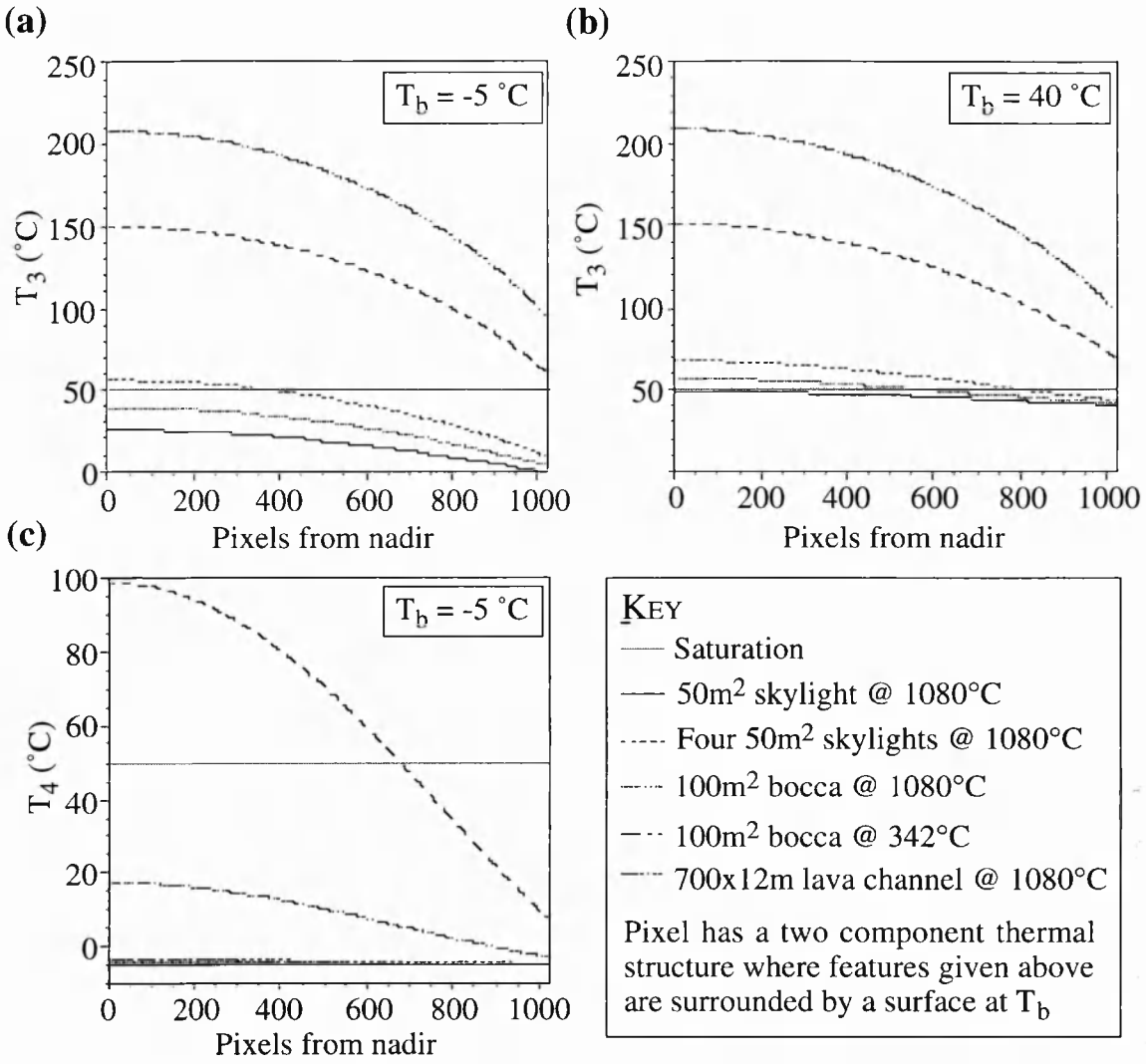

Figure 7.16. *Scan angle induced decrease in channel 3 pixel integrated temperature modelled for a range of sub-pixel hot-spots typical at Etna between 1991 and 1993 against (a) a typical cool winter ambient background and (b) a typical solar-heated summer background. (c) Gives channel 4 variation for a cool winter background. While features remain above saturation they cannot be discriminated.*

However, for small lava bodies such as lava lakes or domes elevation above the background will be higher, resulting in higher R_{3max} and R_{4max}. A 4500 m^2 crusted lava lake at 750 °C, against a background of 0 °C, will give R_{3max} and R_{4max} of 24.39 and 16.61 mW/m^2 sr cm^{-1}. Major effusive eruptions will produce the highest R_{3max} and R_{4max}: a 250000 m^2 lava flow at 750 °C, against a background of 0 °C, will give R_{3max}

and R_{4max} of 1354.85 and 867.07 mW/m^2 sr cm^{-1}. Plotting R_{3max} against R_{4max} should therefore allow each of these features to be distinguished.

We plotted R_{3max} against R_{4max} for 120 images containing lava flows of varying sizes, lava lakes, pyroclastic flows and active vents at Krafla, Etna, Erebus, Lascar and Stromboli (Figure 7.17). The resulting scatter allowed pixels containing active vents to be distinguished from those containing active lava on the basis of radiance alone, even on saturated images. The lava bodies could be further sub-divided into major flows (channel and fissure fed flows extending over >3 km), minor flows (extending <3 km) and small lava bodies (such as lava lakes). At Stromboli, the target pixel will consist of a single of active vents surrounded by ambient ground, but some pixels in a 9x9 pixel box centred on the target pixel will contain sea. By summer sea temperatures are often much lower than ambient land temperatures, selecting a sea surface temperature to use as the minimum background radiance would consequently set the background too low and R_{3max} and R_{4max} too high. Therefore, for the Stromboli data, pixels containing sea were identified and removed and the minimum background value was taken from the remaining land pixels, giving a corrected R_{3max} and R_{4max} (Figure 7.17). Placing radiance data from future eruptions and other volcanoes into this frame should allow the type of feature present to be identified with reasonable confidence.

7.10. Automated real time volcano monitoring from space: a real possibility?

To be of value in monitoring a dynamic and transient hazard, such as a lava or pyroclastic flow, reporting delays must be kept to a minimum. This prompts the question, how quickly could reports similar to those produced here be produced automatically on reception at a dedicated receiving station?

Most results given here were obtained using C++ software written at The Open University. This automatically locates a volcanic hot-spot in an AVHRR image using the procedure given by Harris *et al.* (1995b) and estimates hot spot area and thermal flux by

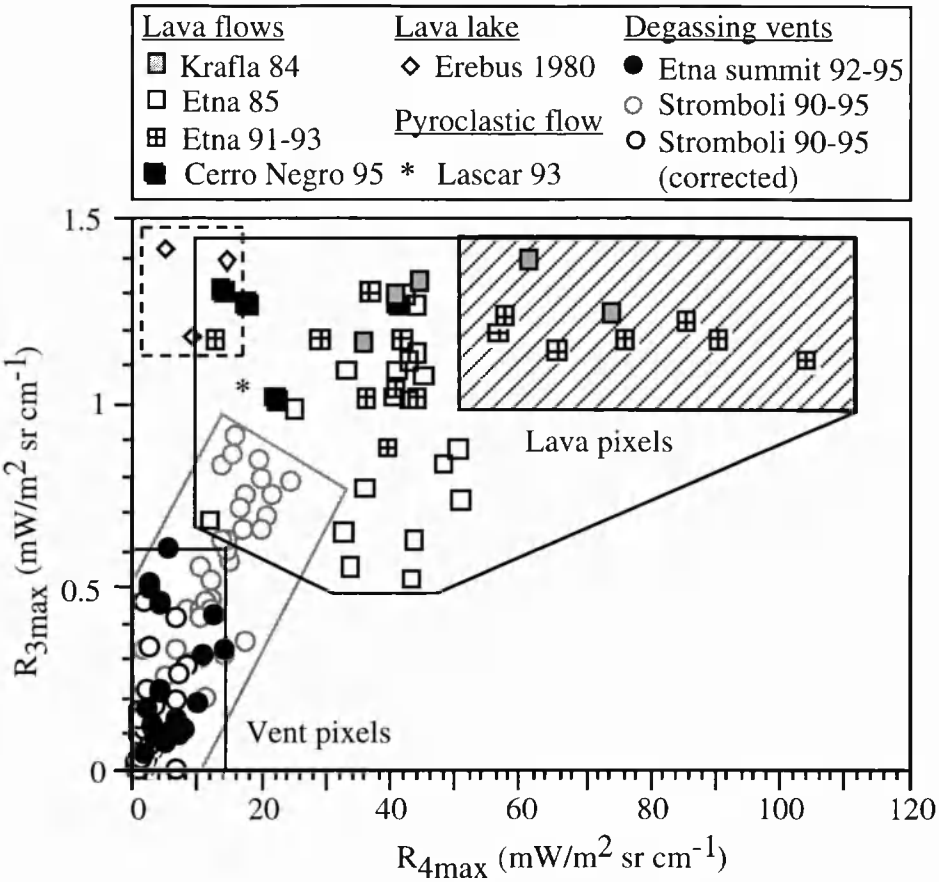

Figure 7.17. *R_{3max} versus R_{4max} scatter graph for a variety of volcanic thermal features, giving the typical space occupied by each feature. Black solid lines delimit feature spaces occupied by vent and lava pixels as indicated, grey lines delimit uncorrected vent pixels, dashed lines delimit lava lake and small area (<0.25 km^2) flows and striped zone marks large area (>5 km^2) flows.*

applying either the two or three component model. Running on 50 x 50 pixel volcano sub-images extracted from 2048 x 2048 full-images, hot spot identification and location is complete within one second, and area and flux estimates are produced within ten seconds. To allow cloud-free volcano sub-images to be located, extracted and examined, other necessary image processing includes geo-location, cloud-screening and extraction. In this study, this was achieved by running the *Panorama* software developed at the NERC Remote Sensing Data Analysis Service. *Panorama* automatically (1) extracts the whole image from the raw satellite data file; (2) geo-locates by applying a satellite orbital model (Sandford & Stephenson, 1992) and fitting image features to a library of ground

landmarks; (3) extracts a sub-image; (4) calculates surface temperature; and (5) cloud-screens by applying a hybrid technique based on Roozekrans & Prangsma (1988), Saunders & Kriebel (1988) and Thiermann & Ruprecht (1992). Sub-images are located and extracted early in the processing so that subsequent computationally intensive operations can be restricted to regions of interest. Run times on a Silicon Graphics Indy 200 MHz workstation are ~4 minutes on a 512 x 512 pixel image and ~10 minutes on a 2048 x 2048 image. Combining these two pieces of software and installing them at a receiving station could therefore produce volcanic hot spot hazard reports within 10 minutes of image reception.

Although automated volcano monitoring software has not yet been installed, the operational AVHRR reception and analysis system installed by the NRI at Managua (Nicaragua) clearly illustrates the cost and logistics of installing such a system for volcano monitoring. All hardware and software (including two PCs, colour printer, antenna and backup power supply) were installed for ~US$ 50000, allowing daily monitoring of ~130 active volcanoes in Central and South America (Figure 7.18). Installation and training can be completed in 2 weeks, and once installed full data are available within 5-10 minutes of a satellite pass, with vegetation and fire monitoring products processed automatically in a further 10 minutes. Currently, active volcanoes are monitored visually, but automatic fire detection algorithms (Flasse & Ceccato, 1996) and production of vegetation fire locations for real time dissemination is a good analogue for the information dissemination time for a similar volcanic hot-spot monitoring system.

Cheap, reliable, real-time automated thermal monitoring of volcanoes on a regional scale is a real possibility. Currently NRI AVHRR stations are in use at 22 countries around the world, including Chile, Ethiopia, Indonesia and Nicaragua. At many, fire monitoring software is already operational. It would take only a small investment of time and money to install reliable, automated volcano hot spot monitoring systems at any of these stations, or to install stations in any volcanic regions which remain poorly monitored from the ground

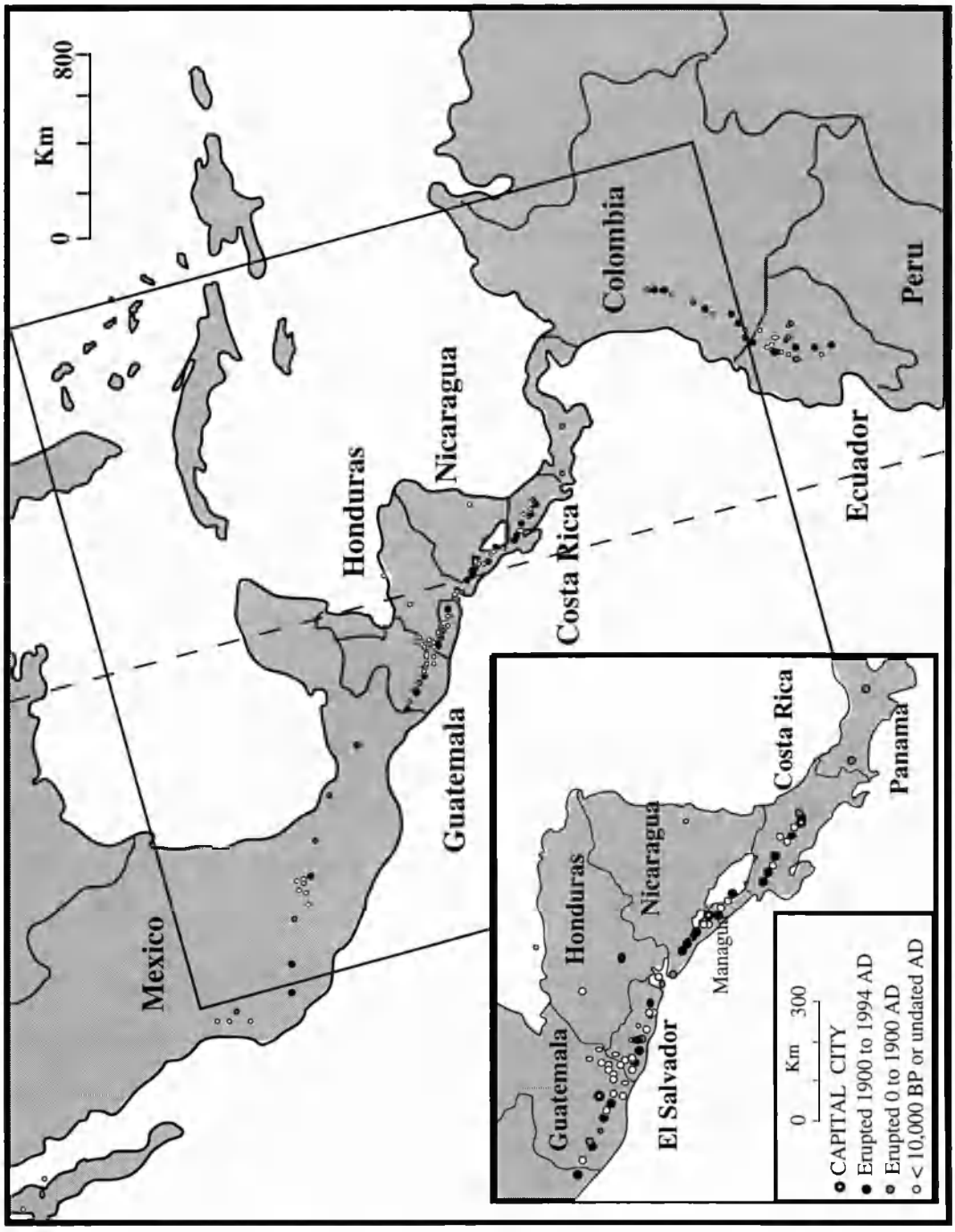

Figure 7.18. *Area covered by a single AVHRR image (solid lines) obtained from an overhead pass (dashed line) at the Managua station, with all active volcanoes given by Simkin & Siebert (1994) located. Nicaragua is enlarged & inset.*

or space. This would allow quantitative and qualitative volcanic hot-spot observations from a safe, re-usable vantage point within 30 minutes of image reception.

7.11. Conclusions

The frequency, ready availability and real-time monitoring capabilities of AVHRR data make them a resource that the volcanological community cannot afford to ignore. It is therefore important to establish the extent to which these data provide useful information on high temperature volcanic features. Our case studies show that reliable information can be extracted for lava flows and lakes, pyroclastic flows and active vents. Extracted information includes location of hot-spots, estimation of hot feature area and thermal flux, and lava effusion rates and cumulative volume. All of these parameters can be obtained automatically within minutes of image acquisition.

7.12. Acknowledgements

Thanks particularly to Jack Salisbury and Dana D'Aria at Johns Hopkins University for running the rock spectra, and to Sonia Calvari (IIV, Catania), Ken Dean and Chris Wyatt (University of Alaska Fairbanks), Philip Kyle (New Mexico Institute of Mining and Technology), Nicki Stevens (Reading University) and Ben Van Wyk de Vries (Open University) for providing details which contributed to this paper. Etna and Krafla AVHRR data were obtained by agreement with the NERC recieving station at the University of Dundee, Fogo data was purchased using an award from the Remote Sensing Society and Cerro Negro data was provided by the ODA supported Land Resource (Fire) Monitoring Project, Nicaragua. Clive Oppenheimer and Lori Glaze are thanked for the Erebus and Lascar data. Field work at Hawaii was funded by an ODA grant and at Etna by kind permission of John Murray. Work was funded by an Open University PhD grant (AJLH) and by the NRI/ODA (ID & PN). *Panorama* software was developed for the OMEX project, EC contract MAS2-CT93-0069 (PM).

Chapter 8. Real-time volcano monitoring from space: a real possibility?

8.1. The ideal volcano monitoring satellite

When designing a sensor for a specific application, the temporal, spatial and spectral features of the target must be considered and the temporal, spatial and spectral resolutions of the instrument chosen accordingly (Mather, 1987; Cracknell & Hayes, 1991). An active lava body presents a dynamic, high temperature (100 to 1200 °C) target, typically extending over tens of metres to many kilometres and developing over hours to months. Conversely, an eruptive ash plume presents a dynamic, low temperature (20 to -80 °C) target, typically extending over tens to tens of thousands of kilometres and developing in seconds to minutes. A satellite-sensor package designed to monitor all types of volcanic activity must therefore meet this range of conflicting spectral, spatial and temporal demands.

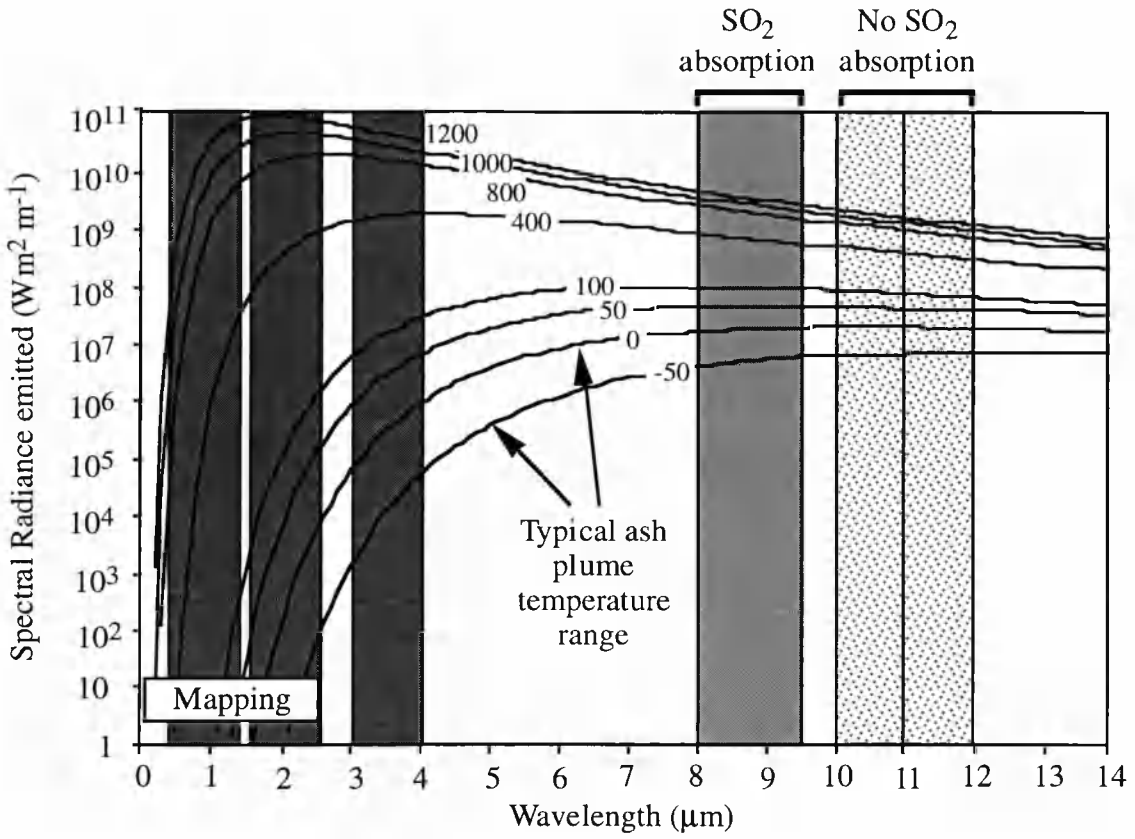

Figure 8.1. *Waveband locations for volcano thermal monitoring (dark grey & stipple), eruption product mapping, and ash and SO_2 plume monitoring (light grey & stipple). Note the coincidence of wavebands <4 µm with peak spectral exitance from blackbodies at typical active lava temperatures (400-1200 °C), and those at 10-12 µm with that from bodies at ambient and high altitude ash plume temperatures. This makes wavebands <4 µm sensitive to sub-pixel lava bodies. Coincidence of 8-9.5 µm and 10-12 µm wavebands with SO_2 absorption and transmission zones make these bands ideal for SO_2 monitoring.*

8.1.1. Spectral resolution for volcano monitoring

8.1.1.1. Wavebands for thermal monitoring

To allow detection, measurement and monitoring of volcanic thermal anomalies, the sensor must provide data in at least four widely spaced wavebands, ideally (1) 1.5 - 1.7, (2) 2.1 - 2.3, (3) 3.5 - 3.9, (4) 10.3 - 11.3 and (5) 11.5 - 12.5 µm (Figure 8.1). Data should also be available in high- and low-gain modes, allowing sufficient sensitivity over low temperature anomalies (e.g. geothermal areas), yet avoiding saturation over high

temperature targets (e.g. active lavas). Data acquired at these wavebands and in these modes would allow (1) hot-spot detection, (2) atmospheric correction and (3) numerical modelling.

(1) Hot spot detection. Bands at 1.6, 2.2 and 3.7 μm are far more sensitive to volcanic hot spots than to sources at ambient temperatures, thus these bands are useful for hot-spot detection. On night-time AVHRR band 2 (0.72-1.10 μm) images, where hot spots have been large enough and hot enough to be detectable they have been evident as bright (highly radiant) spots against a uniformly dark (non-radiant) background, as during the September 1984 Krafla fissure eruption (Harris *et al.*, 1995c). Data acquired at 3.7 and 10.8 μm have allowed automated detection and the filtering out of solar-heated anomalies (Chapters 3, 7 & 8).

(2) Atmospheric correction. Provision of the "split window", i.e., division of the 10-14 μm window into two bands (e.g. 10.3-11.3 and 11.5-12.5 μm), takes advantage of differential atmospheric absorption in theses two bands. This allows atmospheric correction on a pixel-by-pixel basis (Cracknell & Hayes, 1991).

(3) Numerical modelling. Simultaneous acquisition of data at four widely separated bands would improve constraints on pixel thermal structure over an active lava, allowing unique solution of a three thermal component thermal model (Box 8.1 & Figure 8.2). Such models are more realistic than widely-used two component models (e.g. Rothery *et al.*, 1988; Oppenheimer *et al.*, 1993), and are better constrained than current three component models which must work with just two or three widely separated bands of data (e.g. Oppenheimer 1993; Chapters 5 & 7).

8.1.1.2. Wavebands for mapping eruption products

To map eruption products, data at visible and short-wave infrared (SWIR) wavelengths (0.4-2.4 μm) must be available. Numerous studies have shown how data at these wavelengths can be applied to map recently-emplaced pyroclastic and lava flows, pre-historic debris flows, and fissure and cone distributions (e.g. Francis & Wells, 1988;

Use of four bands of thermal data to define sub-pixel thermal sources

For a pixel occupied by three thermal components: a low temperature source at T_b occupying p_b of the pixel, a moderate temperature source at T_c occupying p_c and a high temperature source at T_h occupying $(1-p_b-p_c)$, where thermal radiances are available in 4 wavebands (R_1 to R_4), spectral radiance will be given by:

$$R_1 = p_bL_1(T_b) + p_cL_1(T_c) + (1-p_b-p_c)L_1(T_h) \quad (8.1)$$
$$R_2 = p_bL_2(T_b) + p_cL_2(T_c) + (1-p_b-p_c)L_2(T_h) \quad (8.2)$$
$$R_3 = p_bL_3(T_b) + p_cL_3(T_c) + (1-p_b-p_c)L_3(T_h) \quad (8.3)$$
$$R_4 = p_bL_4(T_b) + p_cL_4(T_c) + (1-p_b-p_c)L_4(T_h) \quad (8.4)$$

in which L_x is the Planck function spectral radiance for channel x (x = 1 to 4). If T_b can be calculated using background pixels and T_h assumed, then p_h (= $1-p_b-p_c$) and p_c can be calculated in terms of p_b, T_b, T_c and T_h by rearranging 8.1 and 8.3 respectively to give

$$p_h = \frac{R_1 - p_b[L_1(T_b)-L_1(T_c)] - L_1(T_c)}{L_1(T_h) - L_1(T_c)} \quad (8.5)$$

and

$$p_c = \frac{R_3 - p_b[L_3(T_b)-L_3(T_h)] - L_3(T_h)}{L_3(T_c) - L_3(T_h)} \quad (8.6)$$

writing A for $[L_1(T_b)-L_1(T_c)]$, B for $[L_1(T_h)-L_1(T_c)]$, C for $[L_3(T_b)-L_3(T_h)]$ and D for $[L_3(T_c) - L_3(T_h)]$, substituting Equations 8.5 & 8.6 into 8.2 & 8.4 and rearranging, p_b can be calculated from

$$p_b = \frac{BR_2 - L_2(T_h)[R_1-L_1(T_c)] - \varphi_2[R_3-L_3(T_h)]}{BL_2(T_b) - AL_2(T_h) - \Psi_2} \quad (8.7)$$

and

$$p_b = \frac{BR_4 - L_4(T_h)[R_1-L_1(T_c)] - \varphi_4[R_3-L_3(T_h)]}{BL_4(T_b) - AL_4(T_h) - \Psi_4} \quad (8.8)$$

in which $\varphi_2 = [Bp_cL_2(T_c)]/D$; $\varphi_4 = [Bp_cL_4(T_c)]/D$, $\Psi_2 = [BCp_cL_2(T_c)]/D$; and $\Psi_4 = [BCp_cL_4(T_c)]/D$. Solving simultaneous Equations 8.7 and 8.8, while ensuring that p_b, p_c and p_h remain positive and sum to 1, will give p_b, p_c, p_h and T_c (Figure 8.2).

Box 8.1. *One possible approach to estimation of the size and temperature of sub-pixel thermal sources using a three band thermal model and four bands of thermal data.*

Munro & Mouginis-Mark, 1990; Rowland & Munro, 1992; Denniss *et al.*, in press). Data acquired at 9-12 μm have also been shown capable of mapping individual flow units within flow pahoehoe fields (Realmuto *et al.*, 1992). My own observations of 8-14 μm Thematic Mapper Simulator images of Mount Etna have shown that solar-heated anomalies, due to

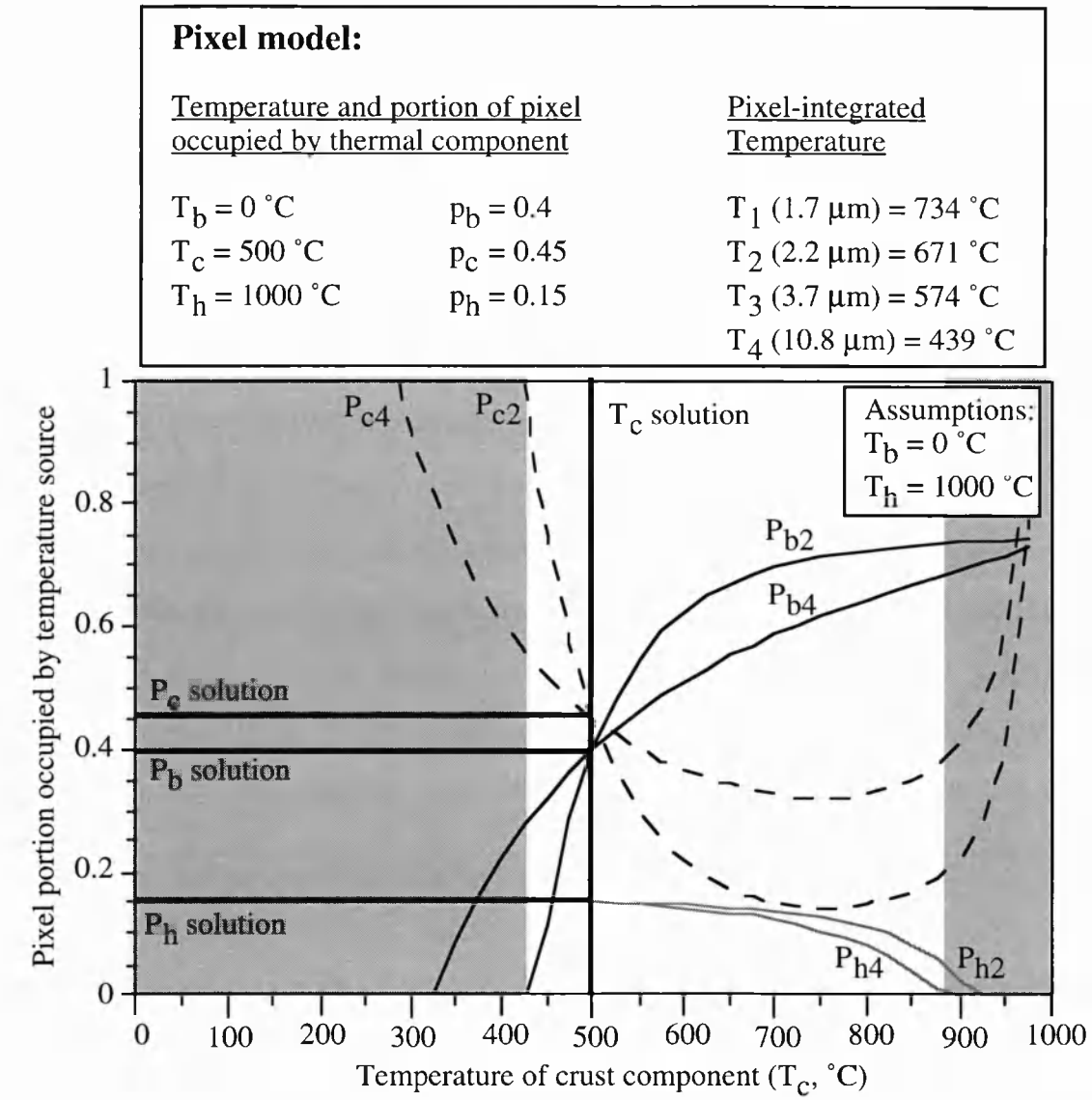

Figure 8.2. *Graphical solution of the three thermal component, four waveband approach given in Box 8.1 on a model pixel containing three temperature sources. The hot temperature and background temperatures (T_h and T_b) are assumed, and all possible combinations of p_h, p_b, p_c and T_c that give the four pixel-integrated temperatures (T_1 to T_4) are plotted. For clarity only the 2.2 and 10.8 μm combinations are given, indicated by subscripts 2 and 4 respectively. Solution occurs where curves cross, giving a single T_c. Convergence also occurs within the grey zones, however these solutions are unreasonable since one of p_h, p_b or p_c must become negative or greater than 1 and are therefore rejected.*

preferential heating of sun-facing slopes, can be used to delimit levéed channels and steep sided aa flow units. Data at 0.73-1.1 and 0.55-0.68 μm can also be used to map the limits of tephra fall, and the impact of volcanic ash and aerosol on vegetation (e.g. Tucker & Matson, 1985; Jeyaseelan & Thiruvengadachari, 1993).

8.1.1.3. Wavebands for ash and gas monitoring

To detect plumes of ash and gas, data must be available at 10-12 μm (Figure 8.1). Data within this waveband have been shown capable of detecting ash plumes and distinguishing them from meteorological clouds (e.g. Prata, 1989; Holasek & Rose, 1991). The coincidence of this waveband with peak spectral emittance from blackbodies at typical plume top temperatures also make these bands suitable for measuring plume temperature, which can in turn be related to plume altitude (e.g. Holasek & Rose, 1991; Holasek & Self, 1995). Inclusion of wavebands coincident with the SO_2 absorption band allows detection and measurement of passive and eruptive SO_2 plumes (e.g. Krueger *et al.*, 1990; Realmuto *et al.*, 1994).

8.1.1.4. Synthetic Aperture radar (SAR)

Inclusion of SAR would complete the volcano monitoring sensor package. A number of studies have shown how SAR data may be used to produce Digital Elevation Models (DEMs), map lava and debris flows and monitor volcano deformation (e.g. Mouginis-Mark & Garbiel, 1993; Rowland *et al.*, 1994; Massonnet *et al.*, 1995; or see Gens & Van Genderen (1996) for review). Observation through cloud means that inclusion of SAR would extend monitoring over cloud-covered periods and volcanoes. SAR products, such as DEMs, could also be used in conjunction with thermal data. For example, fitting a thermal image of a low temperature volcanic feature to a SAR-derived DEM would allow height dependent adiabatic correction (see Chapter 1).

8.1.2. Spatial resolution for volcano monitoring

The lower size limit of a volcanic feature requiring monitoring is set by active fumarole vents which are typically <1-10 cm across, the upper limit by eruptive ash plumes which extend over thousands of kilometres, occasionally encircling the globe. Between these bounds are lava flows, domes and lakes which vary between a few tens of meters to a few kilometres in dimension. However, active lavas also contain highly localised areas of extremely high temperature, such as where the molten (800-1200 °C) core is exposed at centimetre wide cracks in a chilled crust or metre wide lava channels, skylights and breakouts. Therefore, while the accurate identification of small-scale volcanic features and high temperature zones requires pixel sizes of 1-10 m, analysis of entire lava flows and ash plumes requires images tens to thousands of kilometres across.

8.1.3. Temporal resolution for volcano monitoring

Volcanic events are dynamic, and often short-lived. The 13 year effusive eruption at Kilauea, which began on 3 January 1983 and was continuing at the time of writing, progressed through 53 distinct episodes during the first 12 years, each characterised by differences in vent location and eruptive style (USGS, 1995). Conversely, the first 9 explosive events of the 1979 Soufriere of St. Vincent eruption lasted for no more than half an hour each, and an effusive eruption beginning at Krafla around 1100 GMT on 20 December 1975 was over by 1700 on the same day, the main flow being active for just 1 hour (Smithsonian Institution, 1989). To ensure global coverage, capture of short-lived (<1 hour duration) events and identification of changes in eruption location or style during longer eruptions, the sensor must image all volcanoes at least once every 1 to 15 minutes.

8.1.4. A volcano monitoring satellite series

A number of features of an ideal volcano monitoring satellite-sensor package defined in Table 8.1 are incompatible, making such a package an unrealistic proposition. Most importantly there is a trade off between spatial and temporal resolution: higher spatial

Ideal single platform volcano monitoring satellite-sensor

i. Sensor resolution:

Wavelength (μm)		*Application*
0.45 - 0.52		Eruption product mapping
0.52 - 0.60		Eruption product mapping
0.63 - 0.69		Eruption product mapping
0.76 - 0.90		Eruption product mapping
1.55 - 1.75	(High & low gain)	Thermal monitoring & eruption product mapping
2.08 - 2.35	(High & low gain)	Thermal monitoring & eruption product mapping
3.55 - 3.93	(High & low gain)	Thermal monitoring
8.00 - 8.50		SO_2 monitoring
8.50 - 9.00		SO_2 monitoring
9.00 - 9.50		SO_2 monitoring
10.3 - 11.3	(High & low gain)	SO_2, thermal & ash plume monitoring & atmospheric correction
11.5 - 12.5	(High & low gain)	SO_2, thermal & ash plume monitoring & atmospheric correction
Separate SAR sensor		DEM production, eruption product mapping & deformation monitoring

ii.	**Spatial resolution:**	1 to 10 m
	Swath coverage:	3000 x 3000 km
	Coverage:	Global
iii.	**Temporal resolution:**	Once every 10 to 15 minutes

Table 8.1. *Spectral, spatial and temporal capabilities of a volcano monitoring satellite-sensor package.*

resolution systems have to operate at lower temporal resolutions and narrower image swaths (Cracknell & Hayes, 1991). Also, data rates and power necessary to record and transmit the vast amount of data produced would be unmanageable. However, such a package would be possible if the system was split between a number of satellites and sensors, together achieving all the monitoring function of the single package (Table 8.2). High temporal resolution monitoring could be maintained by a low spatial resolution sensors mounted on geostationary platforms and/or a series of polar orbiting platforms (Table 8.2a). High spatial resolution monitoring would be maintained by a sensor mounted on a single polar orbiting low temporal resolution satellite. Giving this satellite a pointable

Ideal volcano monitoring satellite-sensor series

(a) High temporal resolution, low spatial resolution platform/sensor

Prime function & features. High temporal resolution eruption alarm and time-series analysis, either from frequent imaging geostationary platforms or a polar orbiting series.

i. Sensor resolution: *: not feasible from geostationary platform

Wavelength (μm)		*Application*
1.55 - 1.75	(High & low gain)	Thermal monitoring
2.08 - 2.35	(High & low gain)	Thermal monitoring
3.55 - 3.93	(High & low gain)	Thermal monitoring
8.00 - 8.50		SO_2
8.50 - 9.00		SO_2
9.00 - 9.50		SO_2
10.3 - 11.3	(High & low gain)	Thermal, ash plume & atmospheric correction
11.5 - 12.5	(High & low gain)	Thermal, ash plume & atmospheric correction
Separate SAR sensor*		DEM production, mapping & deformation

ii. Spatial resolution: 500-1000 m
Swath width: 3000 km to global
Coverage: global (either through polar orbiting series or geostationary)

iii. Temporal resolution: Once every 5 - 60 minutes

(b) Low temporal resolution, high spatial resolution platform/sensor

Prime function & features: high spatial resolution lava body and plume measurements, from a pointable sensor

i. Sensor resolution:

Wavelength (μm)		*Application*
0.45 - 0.52		mapping
0.52 - 0.60		mapping
0.63 - 0.69		mapping
0.76 - 0.90		mapping
1.55 - 1.75	(High & low gain)	mapping & thermal
2.08 - 2.35	(High & low gain)	mapping & thermal
3.55 - 3.93	(High & low gain)	Thermal
8.00 - 8.50		SO_2
8.50 - 9.00		SO_2
9.00 - 9.50		SO_2
10.3 - 11.3	(High & low gain)	SO_2, thermal, ash plume & atmospheric correction
11.5 - 12.5	(High & low gain)	SO_2, thermal, ash plume & atmospheric correction
Separate SAR sensor		DEM production, mapping & deformation

ii. Spatial resolution: 1-10 m
Swath width / coverage: 200 x 200 km, global

iii. Temporal resolution: Once every 20 days, <20 days in pointable mode

Table 8.2. *Spectral, spatial and temporal capabilities of the ideal satellite-sensor series.*

capability would mean that events located by the geostationary and polar orbiting network could be preferentially targeted (Table 8.2b).

8.1.5. Automated real time satellite data reception and analysis: one function of a model receiving station attached to a volcano observatory?

I envisage remotely sensed data for volcanoes passing through a four stage chain of processing, centred on a volcano observatory. The chain begins with (1) collection of raw data, which is then (2) processed by an expert system and (3) interpreted by a volcanologist who provides (4) information to other scientists, decision makers, media and public. The links between each of these stages are illustrated in Figure 8.3. The volcano observatory is defined as a group of volcanologists whose role is to increase scientific understanding of volcanic processes through relevant research; to monitor activity; prepare hazard maps; produce forecasts, etc. (see Tilling, Figure 1, 1989); and to disseminate information and advice to decision makers, media and public.

For remotely sensed data, stage 1 (raw data collection) is achieved by the satellite which immediately transmits the data to a ground receiving station. Stage 2 (data reception

---

Figure 8.3. *Place of satellite data within the role of a model receiving station and volcano observatory. Collection and analysis of remotely sensed data are fitted into a chain of volcano information dissemination based on Peterson (1988). Data passes through a 4 stage chain of data analysis centred on the volcano observatory, whereby each stage transforms the data passed to it into a form that can be understood by, and is of use to, the next stage. (1) Raw data are collected and (2) processed by an expert individual and/or software. (3) Results of processing are passed to the volcano observatory as data that has some meaning to the volcanologist (e.g. stage 2 converts raw digital numbers to effusion rates and passes these to the volcanologist). (4) The volcanologist passes his interpretation of the data down the chain in a form that makes sense to other scientists, decision makers, media and public (e.g. the volcanologist converts effusion rates to an idea of how far a flow is likely to extend). Note that by the end of each of the 4 stages summarised on the right hand side of Figure 8.3 information should be in a form which the next stage is capable of interpreting.*

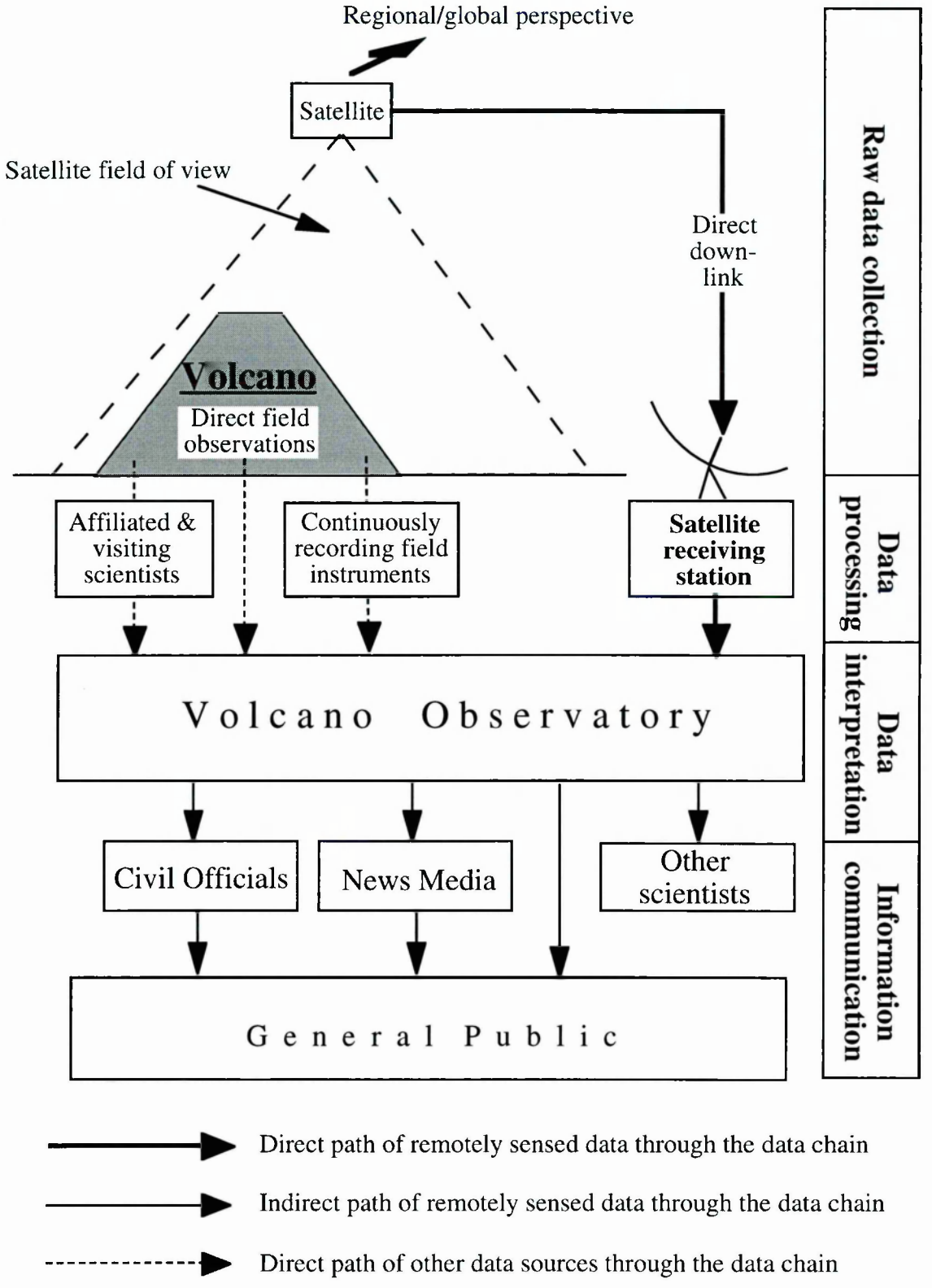
Regional/global perspective
Satellite
Satellite field of view
Direct down-link
Volcano
Direct field observations
Affiliated & visiting scientists
Continuously recording field instruments
Satellite receiving station
Volcano Observatory
Civil Officials
News Media
Other scientists
General Public
Raw data collection
Data processing
Data interpretation
Information communication
Direct path of remotely sensed data through the data chain
Indirect path of remotely sensed data through the data chain
Direct path of other data sources through the data chain

and analysis) occurs at the receiving station, which is either owned by or affiliated to the volcano observatory. At the receiving station remotely sensed data are processed by dedicated software and/or by a remote sensing specialist with expertise in volcanological applications. To be of value for volcano monitoring, results must be made available directly and rapidly to stages 3 and 4, allowing real-time analysis, judgement and reaction. Automation, especially of routine or repetitive tasks, would maximise processing efficiency and speed, and is essential if data for many volcanoes, 4 times an hour, 24 hours a day are to be processed rapidly.

Processed data are passed from stage 2 to stage 3 (the volcanologist at a centralised volcano observatory) in a form that is understandable to, and usable by, the volcanologist. Thus, rather than passing the raw data to the volcanologist, the results of the processing stage are handed on, e.g. lava effusion rates or ash plume heights derived from the remotely sensed data are passed on. The volcanologist is then able to interpret these data and contribute his expertise, possibly in collaboration with the remote sensing expert, to either increase scientific understanding or disseminate information. At this stage integration of the remotely sensed information into the total stream of data passing through the volcano observatory, e.g. seismic, magnetic, gravity, deformation and gas chemistry data gathered for a single volcano or a number of volcanoes on regional or global scale, may allow a fuller understanding of volcanic processes and/or eruption precursors.

Information derived from all data are communicated to stage 4 (the decision makers, media, affiliated bodies, the general public and the wider scientific community) in a form that is understandable by these groups. A useful example of the potential contribution of information derived from remotely sensed data to this stage can be taken from the 1995 eruption of Cerro Negro. During the eruption the local population within 5 to 10 km of the volcano expressed great concern over the potential burial of their crops and houses by lava. Volcanologists monitoring the eruption in the field were convinced that effusion rates were not high enough for flows to advance into cultivated or inhabited areas. However, in the absence of effusion rate data the population remained unconvinced (B.

van Wyk de Vries, personal communication). Although a means of calculating the necessary parameters was not in place at the time, effusion rates derived from AVHRR data received at the Managua receiving station could potentially have been handed to the volcanologists, who in turn could have rapidly communicated the results to the local population, within half an hour of data reception (Chapter 7).

8.2. The ideal volcano monitoring satellite: already available?

We will not have to wait long before the ideal volcano monitoring satellite system is in orbit: some elements of the series described above have been in orbit since Landsat-1 carried the Multispectral Scanner into orbit on 23 June 1972 (Lilliesand & Kiefer, 1987). Currently a number of sensors offer spectral, spatial and temporal resolutions capable meeting many of the requirements outlined above (Table 8.3).

NOAA's Advanced Very High Resolution Radiometer (AVHRR) has been providing for any sub-aerial volcano 4 times a day since 1979. Data are capable of detecting volcanic hot-spots and distinguishing solar heated anomalies (Chapters 3 & 7), measuring the size of, and thermal flux from hot-spots, effusion rates and cumulative volume for active lavas (Chapters 5 & 7) and time series analysis (Chapters 5, 6 & 7). Recent analyses of ERS-1 Along Track Scanning Radiometer data for Etna, Lascar and Fernandina have shown thermal data from this sensor are similarly capable of hot spot detection and time series analysis for lava domes and flows (e.g. Wooster & Rothery, in press). Although thermal data available once every 15 to 30 minutes from geostationary satellites (METEOSAT, GOES-E & -W and GMS) have been applied to automatically detect fires (e.g. Prins & Menzel, 1992), no analysis has yet attempted to locate volcanic hot-spots in such data.

The most common volcanological use of both the AVHRR and geostationary satellite data has been to locate measure and track ash plumes (e.g. Sawada, 1987; Holasek & Rose, 1991; Holasek & Self, 1995). Eruptive SO_2 plumes can be measured and tracked

Current satellite sensors capable of volcano monitoring

i. NOAA-AVHRR

Wavelength (μm)	*spatial resolution*	*Application*
0.55 - 0.9	1 km	
0.73 - 1.0	1 km	
3.55 - 3.93	1 km	Thermal
10.3 - 11.3	1 km	Thermal & ash plume monitoring, & atmospheric correction
11.5 - 12.5	1 km	Thermal & ash plume monitoring & atmospheric correction

Swath width/coverage: 3000 x 3000 km, global coverage.
Temporal resolution: Once every 12 hours, maintaining 2 satellites ensures 4 images/day.

ii. Meteosat

Wavelength (μm)	*spatial resolution*	*Application*
0.4 - 1.1	2.4 km	
10.5 - 12.5	5 km	Thermal & ash plume monitoring
5.7 - 7.1	5 km	Thermal & ash plume monitoring

Swath width/coverage: Earth disc, near global coverage using GOES-E & -W and GMS.
Temporal resolution: Once every 15 minutes.

iii. Landsat-TM

Wavelength (μm)	*spatial resolution*	*Application*
0.45 - 0.52	30 m	Mapping
0.52 - 0.60	30 m	Mapping
0.63 - 0.69	30 m	Mapping
0.76 - 0.90	30 m	Mapping
1.55 - 1.75	30 m	Mapping & thermal monitoring
10.4 - 12.5	120 m	Thermal monitoring
2.08 - 2.35	30 m	Mapping & thermal monitoring

Swath width/coverage: 185 x 185 km, global coverage.
Temporal resolution: Once every 16 days.

iv. Nimbus-TOMS

Wavelength: Six Ultra-Violet bands, including 2 near 0.3 μm capable of SO_2 monitoring.
Spatial resolution: 50 km
Swath width/coverage: 2800 km, Global coverage.
Temporal resolution: Once daily.

v. ERS1-SAR

Wavelength: VV-polarisation, C-band (6 cm) SAR.
Applications: Deformation monitoring, DEM construction, mapping.
Spatial resolution: 30 m
Swath width/coverage: 100 km, Global coverage.
Temporal resolution: Once every 3 or 35 days.

Table 8.3. *Spectral, spatial and temporal characteristics of selected sensors currently capable of volcano monitoring.*

using data from the Total Ozone Mapping Spectrometer (e.g. Krueger *et al.*, 1990; Bluth *et al.*, 1994). Most recently, launches of a number of SAR sensors (e.g. ERS-1 SAR) have meant that, potentially, deformation can now also be monitored from space (e.g. Massonnet *et al.*, 1995).

The work-horse of high resolution thermal analysis has been Landsat's Thematic Mapper. This has provided capable of providing high spatial resolution measurements of lava flows, lakes, domes fumaroles fields and crater lakes, as well as mapping and identification of eruptive products (e.g. Chapter 6; Rothery *et al.*, 1988; Francis & Wells, 1988; Munro & Mouginis-Mark, 1990; Oppenheimer, 1991a; Oppenheimer *et al.*, 1993; Oppenheimer, 1993). Higher spatial resolution thermal analyses are possible using airborne sensors (e.g. Chapter 6; Abrams *et al.*, 1994), as are measurements of SO_2 flux (e.g. Realmuto *et al.*, 1994). However, airborne campaigns are irregular and infrequent.

Using these existing capabilities, a reasonable approach would be to (1) use geostationary satellite data for a coarse thermal or plume alarm, (2) use AVHRR data to provide preliminary low spatial resolution analysis and regularly up-dated high temporal resolution time series, (3) use TM for a detailed survey of targeted eruptions while (4) applying TOMS and SAR data for SO_2 and deformation monitoring.

8.2.1. Automated real time analysis

Data from both the AVHRR and geostationary satellites are freely, directly and immediately available if access to a receiving station is possible. Currently data can be processed automatically within 10 minutes of image receipt, with processing including atmospheric correction, geolocation and extraction of volcano sub-images (P. Miller, personal communication). Automated software to locate hot volcanic pixels and calculate hot spot area and thermal flux can be run on extracted sub-images, taking just 10 seconds to scan a 50 x 50 pixel sub-image (Appendix B). This suggests that routine, automated thermal monitoring at a receiving station is attainable now.

Routine analysis of AVHRR images for eruption plumes and hot-spots currently occurs at University of Alaska Fairbanks, where observations of activity can be released within 10 minutes of image receipt (K. Dean, personal communication). Similar stations are already operational covering many volcanically active areas, such as Central America and Indonesia. In areas still not covered it would cost less than US$ 50000 to install a station, with installation and training taking less than 2 weeks (I. Downey, personal communication).

Automated alarms for SO_2 plume detection have been run on Meteor TOMS data (operational until December 1994). Global data were transmitted once a day, with processed data available ~1 hour after transmission. An eruptive SO_2 alarm took a further minute to run, resulting in a response time of 1 to 25 hours (I. Sprod, personal communication). Data from the Earth Probe TOMS (due for launch on 29 June 1996) will be transmitted as they are collected. This will allow testing of automated, real time SO_2 plume detection and assessment of its utility for air-traffic hazard warning (A. Krueger, personal communication).

However, currently the space-borne volcano monitoring system faces problems due to the cost and availability of high spatial resolution data: single TM scenes cost US$ 3000 and are subject to delivery delays of at least 2 months. The system also lacks (1) thermal data in more than 2 unsaturated wavebands, (2) high-gain capabilities to avoid saturation, (3) high spatial resolution (<30 m) thermal data, and (4) ability to monitor low concentration or passive SO_2 plumes.

8.3. EOS: the way forward

The Earth Observing System (EOS) will be launched from 1998 onwards, with the analysis of volcanic activity and its effects on the atmosphere being one of the 28 interdisciplinary investigations (Mouginis-Mark *et al.*, 1991). EOS will consist of a number of platforms, which together will come closer than any previous combination of satellites to fulfilling the volcano monitoring satellite role (Table 8.4). Using MODIS

EOS sensors

(a) Surface phenomena & plumes

Sensor	Application
GLRS	Deformation rates of volcanoes via laser ranging, topography of eruption plumes, plume height via altimeter.
HIRIS	Visible/near infrared (0.4-2.5 μm). 30m pixel. Used to determine energy output from high temperature bodies (e.g. lava lakes & flows).
ITIR	Analysis of thermal properties of crater lakes, ash plumes and fumaroles & investigation of volcano lithology. Topography of plumes.
MISR	Surface reflectance. Stereo images give surface topography. Time-series of moving flows give velocity of rapidly moving flows (e.g. pyroclastic & mud flows).
MODIS	Low resolution thermal-IR (7.3-12 μm) eruption detection, measurement and search for thermal & SO_2 anomalies. Multi-temporal data to determine plume dispersal.
SAR*	Radar interferometry to determine volcano topography & temporal change in morphology due to eruptions. Multi-temporal SAR to study lava flow advance under any weather conditions, day or night.

(b) Volcanic emissions

Sensor	Application
GOMR	Stratospheric SO_2 from 0.3050, 0.3125 and 0.3175 μm channels.
MLS	Vertical profile of SO_2 (15-30 km altitude), HCl (15-60 km), H_2O (10-90 km) 100 x 6 km spatial resolution, 3 km vertical resolution.
TES	Tropospheric SO_2, CO, OCS, HCl, H_2S (in high concentrations only) and qualitative amounts of H_2O and CO_2.

(c) Volcanic aerosols

Sensor	Application
MISR	Four bands: 0.44, 0.55, 0.67 and 0.86 μm at four look angles fore and aft at 28°, 46°, 60° and 72°. Provides aerosol data. Local spatial resolution 240 m, global 1.9 km.
SAGE III	Tropospheric and stratospheric aerosols, H_20, 1-2 km vertical resolution

Acronyms

GLRS Geodynamics Laser ranging system
HIRIS High-Resolution Imaging Spectrometer
ITIR Intermediate and Thermal Infrared Radiometer
MISR Multiangle Imaging Spectrometer
MODIS Moderate Resolution Imaging Spectrometer
SAR Synthetic Aperture Radar
GOMR Global Ozone Monitoring Radiometer
MLS Microwave Limb Sounder
TES Tropospheric Emission Spectrometer
SAGE III Stratospheric Aerosol & Gas Experiment 3

Table 8.4. *Summary of EOS sensors and their volcanological applications (after Mouginis-Mark et al., 1991). * SAR will no longer be flown aboard EOS, however ENVISAT will provide a future SAR capability, as does RADARSAT currently.*

automated thermal alarms will be run on night-time data within 2 hours of data reception, providing coverage of the entire globe once a day (L. Flynn, personal communication). Data will also be used to produce temperature maps emphasising hot-spot development (Flynn, 1996). High resolution analysis will be possible using ASTER, providing 30 m pixel data in the visible to thermal infrared. MISR, SAGE III and EOSP will be used to study the distribution of volcanic aerosols and MODIS and TES for SO_2 measurement (Mouginis-Mark & Francis, 1992). The real-time use of these new data, in conjunction with existing sources (AVHRR, METEOSAT, ATSR/ENVISAT, SAR and TOMS) offers the potential for a near ideal system.

8.4. Summary and conclusions

This thesis has concentrated on the potential of the AVHRR for monitoring of on-going volcanic eruptions. Algorithms capable of running on the data as they are received have been developed and tested to allow real time volcano monitoring.

In Chapter 2 an unexpected response of the AVHRR was defined and explained, and in chapter 3 an algorithm developed to quickly and automatically locate and extract hot-spot pixels for analysis (see also Appendix B). This algorithm was initially tested using ~100 images acquired during an effusive eruption at Mount Etna, Sicily (Chapter 3) and wild fires in New South Wales, Australia (Chapter 4), showing the cross-applicability of techniques designed for volcano and fire hot-spot analysis. In Chapter 5 techniques were developed to map hot spot radiance and estimate hot-spot area and thermal flux, which were in turn used estimate effusion rates and cumulative volume for active lava flows. The accuracy and potential real time application of these techniques were demonstrated using data for the 1991 to 1993 eruption of Mount Etna. In chapter 6 AVHRR time series were used for time-series analysis of activity at Vulcano and Stromboli between 1986 and 1995. Data from tripod-mounted radiometers, the airborne Thematic Mapper Simulator and Landsat's TM were used to improve the spatial detail of the data set. Chapter 7 provided a synthesis and demonstration of all techniques for monitoring activity at channel- and

fissure-fed lava flows, pyroclastic flows, lava lakes and active vents, giving a demonstration of the potential of AVHRR as a tool for real time thermal volcano monitoring.

One aim of NASA's contribution to natural disaster reduction is to reduce the effects of natural hazard by performing "space-based hazard mapping, risk assessment, and monitoring, detecting minute changes in topography, measuring volcanic inflation and deflation and thermal properties, tracking and modelling volcanic plumes" (U.S. Government Agencies, 1994). Prior to this PhD space-borne plume tracking and modelling and high spatial resolution thermal analyses were already commonplace. During this PhD Massonnet *et al.* (1995) demonstrated the potential of SAR to measure deflation. This PhD, by comparing satellite derived thermal measurements and observations of ongoing volcanic activity, has demonstrated how low spatial resolution data can provide reliable data for real time volcano monitoring.

Where these techniques fall short is that they have been applied and tested only on archived data. To achieve operational real time monitoring, the next step must be to install, test and no doubt further refine techniques at operational AVHRR receiving stations. Hopefully such operational real time data analysis and information dissemination will become increasingly common as the launch of new platform/sensor packages such as EOS moves us closer towards attaining a space-borne volcano monitoring system.

In August 1993 a 30 mm screw a few millimetres too long caused NOAA-13 to short-circuit and fail after just 12 days in orbit. Space-borne volcano monitoring capabilities are improving all the time, let us hope that future missions are not similarly screwed up.

References

Abbruzzese, D., 1937. L'attivita dello Stromboli dal 1934 al 1936. *Bull Volcanol.*, **2**, 205-210.

Abbruzzese, D., 1940. L'attivita dello Stromboli dal 1937 al giugno 1939. *Bull. Volcanol.*, **7**, 57-66.

Abrams, M., Glaze, L., and Sheridan, M., 1991. Monitoring Colima Volcano, Mexico, using satellite data. *Bull. Volcanol.*, **53**, 571-574.

Abrams, M., Buongiorno, F., Realmuto, V., and Pieri, D., 1994. Mt. Etna lava flows analyzed with remote sensing. *EOS*, **75**, 548-551.

Allard, P., Carbonelle, J., Metrich, N., Loyer, H., and Zettwoog, P., 1994. Sulphur output and magma degassing budget of Stromboli volcano. *Nature*, **368**, 326-330.

Andres, R.J., and Rose, W.I., 1995. Description of thermal anomalies on two active Guatemalan volcanoes using Landsat Thematic Mapper Imagery. *Photogram. Eng. & Remote Sensing* **61**, 775-782.

Archambault, C., and Tanguy, J.C., 1976. Comparative temperature measurements on Mount Etna lavas: problems and techniques. *J. Volcanol. & Geotherm. Res.*, **1**, 113-125.

Archambault, C., Stoschek, J., and Tanguy, J.C., 1979. Mise en evidence de zones thermiquement anormales sur le massif de l'etna. Proc. *7e reunion annuelle des sciences de la terre*, Lyon 1979, Soc. Géol. Fr édit Paris, p. 15.

Arino, O., and Melinotte, J.M., 1995. Fire index atlas. *Earth Observation Quart.*, **50**, 11-16.

Armienti, P., Calvari, S., Innocenti, F., Petrini, R., Pompilio, M., and Villari, L., 1990. Petrography and chemical composition. In *Mt. Etna: the 1989 eruption*, edited by F. Barberi, A. Bertabnini & P. Landi, CNR - Gruppo Nazionale per la Vulcanologica, Italy, pp. 30-33.

Armienti, P., Clocchiatti, R., D'Orazio, M., Innocenti, F., Petrini, R., Pompilio, M., Tonarini, S., and Villari, L., 1994. The long-standing 1991-1993 Mount Etna eruption: petrography and geochemistry of lavas, *Acta Vulcanologica,* **4**, 15-28.

Arnaud, N.D., 1988. Stromboli: a morphological study 1984-1988. *Proc. Kagoshima International Conference on Volcanoes*, Kagoshima, Japan, 19-23 July 1988.

Baker, M.C.W., 1981. The nature and distribution of Upper Cenozoic ignimbrite centres in the Central Andes. *J. Volcanol. & Geotherm. Res.*, **11**, 293-315.

Banks, N.G., and Hoblitt, R.P., 1981. Summary of temperature studies of 1980 deposits. In *The 1980 eruptions of Mount St. Helens*, edited by P.W. Lipman & D.R. Mullineaux, U.S. Geological Survey Prof. paper **1250**, pp. 292-313

Barberi, F., 1990. Civil defence implications. In *Mt. Etna: the 1989 eruption*, edited by F. Barberi, A. Bertabnini & P. Landi, CNR - Gruppo Nazionale per la Vulcanologica, Italy, pp. 34-35.

Barberi, F., and Villari, L., 1994, Volcano monitoring and civil protection problems during the 1991 - 1993 Etna eruption. *Acta Vulcanologica,* **4**, 157-164.

Barberi, F., Neri, G., Valenza, M., and Villari, L., 1991. 1987-1990 unrest at Vulcano. *Acta Vulcanol.*, **1**, 95-106.

Barberi, F., Carapezza, M.L., Valenza, M., and Villari, L., 1993a. The control of lava flow during the 1991 - 1992 eruption of Mt. Etna. *Journal of Volcanology & Geothermal Research*, **56**, 1-34.

Barberi, F., Rosi, M. and Sodi, A., 1993b. Volcanic hazard assessment at Stromboli based on review of historical data. *Acta Vulcanol.*, **3**, 173-187.

Barca, D., Crisci, G.M., Di Gregorio, S., and Nicoletta, F., 1993. Cellular automata methods for modelling lava flows: simulation of the 1986-1987 eruption, Mount Etna, Sicily. In *Active Lavas*, edited by C.R.J. Kilburn & G. Luongo, (London: UCL Press), pp. 291-309.

Barrett, E.C., and Curtis, L.F., 1992. *Introduction to environmental remote sensing.* (London: Chapman & Hall).

Baxter, P.J., 1990. Medical effects of volcanic eruptions 1. Main causes of death and injury. *Bull. Volcanol.*, **52**, 532-544.

Bergaust, E., and Beller, W., 1957. *Satellite.* (London: Lutterworth Press).

Bhattacharya, A., Reddy, C.S.S., and Sirvastav, S.K., 1993. Remote sensing for active volcano monitoring in Barren Island, India. *Photogram. Eng. & Remote Sensing*, **59**, 1293-1297.

Bianchi, R., Casacchia, R., Coradini, A., Duncan, A.M., Guest, J.E., Kahle, A., Lanciano, P., Pieri, D.C., and Poscolieri, M., 1990. Remote sensing of Italian volcanoes. *EOS*, **71**, 1780-1791.

Birnie, R.W., 1973. Infrared radiation thermometry of Guatemalan volcanoes. *Bull. Volcanol.*, **37**, 1-36.

Bluth, G.J.S., Casadevall, T.J., Schnetzler, C.C., Doiron, S.D., Walter, L.S., Krueger, A.J., and Badruddin, M., 1994. Evaluation of sulfur dioxide emissions from explosive volcanism: the 1982-1983 eruptions of Galunggung, Java, Indonesia. *J. Volcanol. & Geotherm. Res.*, **63**, 243-256.

Bolognesi, L., and D'Amore, F., 1993. Isotopic variation of the hydrothermal system on Vulcano Island, Italy. *Geochim. et Cosmo. Acta*, **57**, 2069-2082.

Bonneville, A. & Kerr, Y., 1987. A thermal forerunner of the 28th March 1983 Mt. Etna eruption from satellite thermal infrared data. *J. Geodynamics*, **7**, 1-31.

Bonneville, A., and Gouze, P., 1992. Thermal survey of Mount Etna volcano from space. *Geophys. Res. Lett.*, **19**, 725-728.

Bonneville, A., Vasseur, G., and Kerr, Y., 1985. Satellite thermal infrared observations of Mt. Etna after the 17th March 1981 eruption. *J. Volcanol. & Geotherm. Res.*, **24**, 293-313.

Breaker, L.C., 1990. Estimating and removing sensor-induced correlation from Advanced Very High Resolution Radiometer data. *J. Geophys. Res.*, **95**, 9701-9711.

Brivio, P.A., and Tomasoni, R., 1980. Thermal infrared continuous ground measurements in severe environment: a working data collection system. *Proc. .14th International Synopsium on Remote Sensing of Environment*, Ann Arbor, Michigan, 23-30 April 1980, **3**, pp. 1731-1740.

Bruno, N., Caltabiano, T., Grasso, M.F., Porto, M., and Romano, R., 1994. SO_2 flux COSPEC measurements (Vulcano). *Acta Vulcanol.*, **6**, 32.

Bullard, F.M., 1954. Activity of Stromboli in June and December 1952. *Bull. Volcanol.*, **15**, 91-98.

Cahoon, D.R., Levine, J.S., Cofer III, W.R., Miller, J.E., Minnis, P., Tennille, G.M., Yip, T.W., Stocks, B.J., and Heck, P.W., 1991. The Great Chinese fire of 1987: a view from space. In *Global Biomas Burning, Atmospheric, Climatic & Biospheric Implications*, edited by J. S. Levine, (MIT Press), pp. 61-66.

Cahoon Jr., D.R., Stocks, B.J., Levine, J.S., Cofer III, W.R., and Chung, C.C., 1992. Evaluation of a Technique for Satellite-Derived Area Estimation of Forest Fires. *Journal of Geophysical Research*, **97**, 3805-3814.

Cahoon Jr., D.R., Stocks, B.J., Levine, J.S., Cofer III, W.R., and Pierson, J.M., 1994. Satellite analysis of severe 1987 forest fires in northern China and south-eastern Siberia. *Journal of Geophysical Research*, **99**, 18627-18638.

Calvari, S., Coltelli, M., Neri, M., Pompilio, M., and Soribano, V., 1994a. The 1991-1993 Etna eruption: chronology and lava flow-field evolution. *Acta Vulcanologica*, **4**, 1-14.

Calvari, S., Coltelli, M., Muller, W., Pompilio, M., and Scribano, V., 1994b. Eruptive history of South-Eastern crater of Mount Etna, from 1971 to 1994. *Acta Vulcanol.*, **5**, 11-14

Capaldi, G., Guerra, I., Lo Bascio, A., Luongo, G., Pece, R., Rapolla, A., Scarpa, R., Del Pezzo, E., Martini, M., Ghiara, M.R., Lirer, L., Munno, R., and La Volpe, L., 1978. Stromboli and its 1975 eruption. *Bull Volcanol.*, **41**, 259-285.

Capasso, G., Inguaggiato, S., Nuccio, P.M., Pecoraino, G., and Sortino, F., 1994. Chemical variations in the fumarolic gases of La Fossa di Vulcano crater. *Acta Vulcanol.*, **6**, 41-43.

Carapezza, M., Nuccio, P.M., and Valenza, M., 1981. Genesis and evolution of the fumaroles of Vulcano (Aeolian Islands, Italy): a geochemical model. *Bull. Volcanol.*, **44**, 547-563.

Cas, R.A.F., and Wright, J.V., 1987. *Volcanic successions*. (London: Allen & Unwin).

Casadevall, T.J., 1994. The 1989-1990 eruption of Redoubt volcano, Alaska: impacts on aircraft operations. *J. Volcanol. & Geothern. Res.*, **62**, 301-316.

Chester. D., 1993. *Volcanoes and society*. (London: Edward Arnold).

Chester, D.K., Duncan, A.M., Guest, J.E., and Kilburn, C.R.J., 1985. *Mount Etna: the anatomy of a volcano*. (London: Chapman & Hall).

Chrétien, S., and Brousse, R., 1989. Events preceding the great eruption of 8 May, 1902 at Mount Pelée Martinique. *J. Volcanol. & Geotherm. Res.*, **38**, 67-75.

Chiodini, G., Cioni, R., Falsaperla, S., Monalto, A., Guidi, M., and Marini, L., 1992. Geochemical and seismological investigations at Vulcano (Aeolian Islands) during 1978-1989. *J. Geophys. Res.*, **97**, 11025-11032.

Chiodini, G., Cioni, R., Marini, L., Panichi, C., Raco, B. and Taddeucci, G., 1994. Fumarolic gases geochemistry (Vulcano). *Acta Vulcanol.*, **6**, 43-46.

Chiodini, G., Cioni, R., Marini, L., and Panichi, C., 1995. Origin of the fumarolic fluids of Vulcano Island, Italy, and implications for volcano surveillance. *Bull. Volcanol.*, **57**, 99-110.

Chouet, B., Hamisevicz, N., and McGetchin, T.R., 1974. Photoballistics of volcanic jet activity at Stromboli, Italy. *J. Geophys. Res.*, **79**, 4961-4976.

Chuvieco, E., and Martin, M.P., 1994. A simple method for fire growth mapping using AVHRR channel 3 data. *Int. J. of Remote Sensing*, **15**, 3141-3146.

Cioni, R., and D'Amore , F., 1984. A genetic model for the crater fumaroles of Vulcano Island (Sicily, Italy). *Geothermics*, **13**, 375-384.

Clocchiatti, R., Del Moro, A., Giocada, A., Joron, J.L., Mosbah, M., Pinarelli, L., and Sbrana, A., 1994. Assessment of a shallow magmatic system: the 1880-90 eruption, Vulcano Island, Italy. *Bull. Volcanol.*, **56**, 466-486.

Coll, C., Caselles, V., Sobrino, J.A., Valor, E., 1994. On the atmospheric dependence of the split-window equation for land surface temperature. *Int. J. Remote Sensing*, **15**, 105-122.

Colombrita, R., 1984. Methodology for the construction of earth barriers to divert lava flows: the Mt. Etna 1983 eruption. *Bull. Volcanol.*, **47**, 1009-1038.

Coniglio, S., and Dobran, F., 1995. Simulations of magma ascent and pyroclast dispersal at Vulcano (Aeolian Islands, Italy). *J. Volcanol. & Geotherm. Res.*, **65**, 297-317.

Connor, C.B., Clement, B.M., Xiaodan, S., Lane, S.B., and West-Thomas, J., 1993. Continuous monitoring of high-temperature fumaroles on an active lava dome, Volcan Colima, Mexico: evidence of mass flow variation in response to atmospheric forcing. *J. Geophys. Res.*, **98**, 19713-19722.

Cooper, D.I., and Asrar, G., 1989. Evaluating atmospheric correction models for retrieving surface temperatures from the AVHRR over tallgrass Prairie. *Remote Sensing Environ.*, **27**, 93-102.

Cracknell, A.P., and Paithoonwattanakij, K., 1989. Pixel and sub-pixel accuracy in geometrical correction of AVHRR imagery. *Int. J. Remote Sensing*, **10**, 661-667.

Cracknell, A.P., and Hayes, L.B.W., 1991. *Introduction to remote sensing.* (London: Taylor & Francis).

Crisp, J., and Baloga, S., 1990. A model for lava flows with two thermal components. *J. Geophys. Res.*, **95**, 1255-1270.

Danes, Z.F., 1972. Dynamics of lava flows. *J. Geophys. Res.*, **77**, 1430-1432.

De Quervain, F., and Streckeisen, A., 1927. Observations sur le Stromboli. *Bull. Volcanol.*, **1**, 74-82.

Dean, K., Bowling, S.A., Shaw, G., and Tanaka, H., 1994. Satellite analysis of movement and characteristics of the Redoubt volcano plume, January 8, 1990. *J. Volcanol. & Geotherm. Res.*, **62**, 339-352.

Deschamps, P.Y., and Phulpin, T., 1980 Atmospheric correction of infrared measurements of sea surface temperature using channels 3.7, 11 and 12 μm. *Boundary Layer Meteorology*, **18**, 131-143.

Denniss, A.H., Harris, A.J.L., Carlton, R.W., Francis, P.W., and Rothery, D.A., in press. The 1993 Lascar pyroclastic flow imaged by JERS-1. Accepted for publication in *Int. J. Remote Sensing.*

DHA, 1995a. Nicaragua - volcanic eruption. *DHA-Geneva situation report no. 1*, Nicaragua: volcano **DHA-01**.

DHA, 1995b. Nicaragua - volcanic eruption. *DHA-Geneva situation report no. 3*, Nicaragua: volcano **DHA-03**.

DHA, 1995c. Volcanic eruption - Fogo volcano. *DHA-Geneva situation report no. 5*, Cape Verde: volcano **DHA-05**.

Di Palma, S., Drago, F., Galanti, E., and Pennisi, V., 1994. Earthen barriers and explosion tests to delay the lava advance: the 1992 Mt. Etna experience, *Acta Vulcanol.*, **4**, 167-171.

Dousset, B., Flament, P., and Bernstein, R., 1993. Los Angeles Fires Seen from Space. *EOS*, **74**, 33-38.

Dozier, J., 1981. A method for satellite identification of surface temperature fields of subpixel resolution. *Remote Sensing Environ.*, **11**, 221-229.

Dragoni, M., 1989. A dynamic model of lava flows cooling by radiation. *Bull. Volcanol.*, **51**, 88-95.

Dragoni, M., 1993. Modelling the rheology and cooling of lava flows. In *Active Lavas* edited by C.R.J. Kilburn & G. Luongo, (London: UCL Press), pp. 235-261.

Dragoni, M., Piombo, A., and Tallarico, A., 1995. A model for the formation of lava tubes by roofing over a channel. *J. Geophys. Res.*, **100**, 8435-8447.

Falsaperla, S., Frazzetta, G., Neri, G., Velardita, R., and Villari, L., 1989. Volcano monitoring in the Aeolian Islands (southern Tyrrhenian Sea): The Lipari-Vulcano eruptive complex. In *IAVCEI proceedings in Volcanology 1: Volcanic Hazards*, edited by J.H. Latter, (Berlin: Springer-Verlag), pp. 337-356.

Falsaperla, S., Privitera, E., Spampinato, S., and Cardaci, C., 1994. Seismic activity and volcanic tremor related to the December 14, 1991 Mt. Etna eruption, *Acta Vulcanol.*, **4**, 63-73.

Faraone, D., Silvano, A., and Verdiani, G., 1986. The monzogabbroic intrusion in the island of Vulcano, Aeolian Archipelago, Italy. *Bull. Volcanol.*, **48**, 299-307.

Fisher, N.H., 1958. Foreward. In *The 1951 eruption of Mount Lamington, Papua*, by G.A.M. Taylor, Bulletin of the Australian Bureau of Mineral Resources, Ecology & Geophysics Australia, **38**.

Flannigan, M.D., and Vonder Haar, T.H., 1986. Forest fire monitoring using NOAA satellite AVHRR. *Canadian J. Forest Research,* **16**, 975-982.

Flasse, S.P., and Ceccato, P., 1996. A contextual alogrithm for AVHRR fire detection. *Int. J. Remote Sensing*, **17**, 419-424.

Flynn, L., 1996. Thermal anomaly - low spatial resolution. *EOS Volcanology Team Data Product Document*, **MOU81-3292**.

Flynn, L.P. and Mouginis-Mark, P.J., 1992. Cooling rate of an active Hawaiian lava flow from nighttime spectroradiometer measurements. *Geophys. Res. Lett.*, **19**, 1783-1786.

Flynn, L.P., and Mouginis-Mark, P.J., 1994. Temperature of an active lava channel from spectral measurements, Kilauea Volcano, Hawaii. *Bull. Volcanol.*, **56**, 297-301.

Flynn, L.P., Mouginis-Mark, P.J., Gradie, J.C., and Lucey, P.G., 1993. Radiative temperature measurements at Kupaianaha lava lake, Kilauea volcano, Hawaii. *J. Geophysi. Res.*, **98**, 6461-6476.

Flynn, L.P., Mouginis-Mark, P.J., and Horton, K.A., 1994. Distribution of thermal areas on an active lava flow field: Landsat observations of Kilauea, Hawaii, July 1991. *Bull. Volcanol.*, **56**, 284-296.

Foote, R., and Draper, L.T., 1980. TIROS-N Advanced Very High Resolution Radiometer (AVHRR). *Proc. 6th Annual Conference of the Remote Sensing Society*, University of Dundee, UK, 18-19 December 1979, pp. 25-35.

Francis, P.W., 1979. Infra-red techniques for volcano monitoring and prediction - a review. *J. Geol. Soc. Lond.*, **136**, 355-359.

Francis, P.W., and Rothery, D.A., 1987. Using the Landsat Thematic Mapper to detct and monitor active volcanoes: an example from Lascar volcano, Northen Chile. *Geology*, **15**, 614-617.

Francis, P.W., and Wells, G.L., 1988. Landsat Thematic Mapper observations of debris avalanche deposits in the Central Andes. *Bull. Volcanol.*, **50**, 258-287.

Francis, P.W., and De Silva, S.L., 1989. Application of the Landsat Thematic Mapper to the identification of potentially active volcanoes in the Central Andes. *Remote Sensing Environ.,* **28**, 245-255.

Francis, P., Oppenheimer, C., and Stevenson, D., 1993. Endogenous growth of persistently active volcanoes. *Nature*, **266**, 554-557.

Frazzetta, G., and La Volpe, L., 1991. Volcanic history and maximum expected eruption at "La Fossa di Vulcano" (Aeolian Islands, Italy). *Acta Vulcanol.*, **1**, 107-113.

Frazzetta, G., Gilot, P.Y., La Volpe, L., and Sheridan, M.F., 1984. Volcanic hazards at Fossa of Vulcano: data from the last 6,000 years. *Bull. Volcanol.*, **47**, 105-124.

Frazzetta, G., La Volpe, L., and Sheridan, M.F., 1983. Evolution of the Fossa cone, Vulcano. *J. Volcanol. & Geotherm. Res.*, **17**, 329-360.

French, N.H.F., Kasischke, E.S., Bourgeau-Chavez, L.L., and Berry, D., 1995. Mapping the Location of Wildfires in Alaskan Boreal Forests Using AVHRR Imagery. *Int. J. Wildland Fire*, **5**, 55-61.

Frulla, L.A., Milovich, J.A., and Gagliardini, D.A., 1995. Illumination and observation geometry for NOAA-AVHRR images. *Int. J. Remote Sensing*, **16**, 2233-2253.

Gaonac'h, H., Vandemeulebrouck, J., Stix, J., and Halbwachs, M., 1994. Thermal infrared satellite measurements of volcanic activity at Stromboli and Vulcano. *J. Geophys. Res.*, **99**, 9477-9485.

Gauthier, F., 1973. Field and laboratory studies of the rheology of Mount Etna lava. *Phil. Trans. R. Soc. Lond.*, **274**, 83-98.

Gawarecki, S.J., Moxham, R.M., and Morgan, J.O., 1980. An infrared survey of Irazu volcano and vicinity, Costa Rica. *Proc. 14th International synopsium on Remote Sensing of Environment,* Ann Arbor, Michigan, 23-30 April 1980, **3**, 1901-1906.

Gens, R., and Van Genderen, J.L., 1996. SAR interferometry - issues, techniques, applications. *Int. J. Remote Sensing*, **17**, 1803-1835.

Gesell, G., 1989. An algorithm for snow and ice detection using AVHRR data An extension of the APOLLO software package. *Int. J. Remote Sensing*, **10**, 897-905.

Giberti, G., Jaupart, C., and Sartoris, G., 1992. Steady-state operation of Stromboli volcano, Italy: constraints on the feeding system. *Bull. Volcanol.*, **54**, 535-541.

Giggenbach, W.F., Kyle, P.R., and Lyon, G.L., 1973. Present volcanic activity on Mount Erebus, Ross Island, Antarctica. *Geology*, **1**, 135-136.

Glaze, L., Francis, P.W., and Rothery, D.A., 1989. Measuring thermal budgets of active volcanoes by satellite remote sensing. *Nature*, **338**, 144-146.

Glaze, L.S., Francis, P.W., Self, S., and Rothery, D.A., 1989. The September 1986 eruption of Lascar volcano, north Chile: satellite investigations. *Bull. Volcanol.*, **51**, 149-160.

Gönvold, K., 1987. Krafla. *Bull. Volcanic eruptions*, **24**, 51-52.

Goward, S.N., Markham, B., Dye, D.G., Dulaney, W., and Yang, J., 1991. Normalized Difference Vegetation Index measurements from the Advanced Very High Resolution Radiometer. *Remote Sensing Environ.*, **35**, 257-277.

Gower, J.F.R., 1992. Low cost satellite sensor image reception for NOAA HRPT and other compatible data. *Int. J. Remote Sensing*, **14**, 177-181.

Guest, J.E., Kilburn, C.R.J., Pinkerton, H., and Duncan, A.M., 1987. The evolution of lava flow-fields: observations of the 1981 and 1983 eruptions of Mount Etna, Sicily. *Bull. Volcanol.*, **49**, 527-540.

Gupta, R.K., and Badarinath, K.V.S., 1993. Volcano monitoring using remote sensing data. *Int. J. Remote Sensing*, **14**, 2907-2918.

GVN, 1990a. Kelut. *Smithsonian Inst. Bull. Global Volcanol. Net.*, **15**(1), 2-3.

GVN, 1990b. Stromboli. *Smithsonian Inst. Bull. Global Volcanol. Net.*, **15**(4), 16.

GVN, 1991a. Stromboli. *Smithsonian Inst. Bull. Global Volcanol. Net.*, **16**(6), 14.

GVN, 1991b. Stromboli. *Smithsonian Inst. Bull. Global Volcanol. Net.*, **16**(7), 18.

GVN, 1991c. Stromboli. *Smithsonian Inst. Bull. Global Volcanol. Net.*, **16**(8), 13.

GVN, 1991d. Stromboli. *Smithsonian Inst. Bull. Global Volcanol. Net.*, **16**(9), 10-11.

GVN, 1991e. Etna. *Smithsonian Inst. Bull. Global Volcanol. Net.*, **16**(12), 2-3.

GVN, 1991f. Pinatubo. *Smithsonian Inst. Bull. Global Volcanol. Net.*, **16**(6), 2-5.

GVN, 1992a. Etna. *Smithsonian Inst. Bull. Global Volcanol. Net.*, **17**(1), 3-4.

GVN, 1992b. Etna. *Smithsonian Inst. Bull. Global Volcanol. Net.*, **17**(2), 12-16.

GVN, 1992c. Etna. *Smithsonian Inst. Bull. Global Volcanol. Net.*, **17**(3), 6.

GVN, 1992d. Etna. *Smithsonian Inst. Bull. Global Volcanol. Net.*, **17**(4), 10-11.

GVN, 1992e. Etna. *Smithsonian Inst. Bull. Global Volcanol. Net.*, **17**(5), 15-19.

GVN, 1992f. Etna. *Smithsonian Inst. Bull. Global Volcanol. Net.*, **17**(7), 13-17.

GVN, 1993a. Etna. *Smithsonian Inst. Bull. Global Volcanol. Net.* **18**(2), 12-13.

GVN, 1993b. Etna. *Smithsonian Inst. Bull. Global Volcanol. Net.*, **18**(3), 6-7.

GVN, 1993c. Stromboli. *Smithsonian Inst. Bull. Global Volcanol. Net.*, **18**(4), 13-14.

GVN, 1993d. Stromboli. *Smithsonian Inst. Bull. Global Volcanol. Net.*, **18**(10), 6-7.

GVN, 1993e. Lascar. *Smithsonian Inst. Bull. Global Volcanol. Net.*, **18**(4), 2-6.

GVN, 1994a. Stromboli. *Smithsonian Inst. Bull. Global Volcanol. Net.*, **19**(3), 5-7.

GVN, 1994b. Stromboli. *Smithsonian Inst. Bull. Global Volcanol. Net.*, **19**(6), 3-4.

GVN, 1994c. Stromboli. *Smithsonian Inst. Bull. Global Volcanol. Net.*, **19**(10), 13-16.

GVN, 1995a. Stromboli. *Smithsonian Inst. Bull. Global Volcanol. Net.*, **20**(4).

GVN, 1995b. Stromboli. *Smithsonian Inst. Bull. Global Volcanol. Net.*, **20**(5).

GVN, 1995c. Stromboli. *Smithsonian Inst. Bull. Global Volcanol. Net.*, **20**(11/12).

GVN, 1995d, Fernandina. *Smithsonian Inst. Bull. Global Volcanol. Net.*, **20**(2).

GVN, 1995e, Cerro Negro. *Smithsonian Inst. Bull. Global Volcanol. Net.*, **20**(11/12), 2-4.

GVN, 1995f, Fogo. *Smithsonian Inst. Bull. Global Volcanol. Net.*, **20**(3), 2-4.

GVN, 1995g, Fogo. *Smithsonian Inst. Bull. Global Volcanol. Net.*, **20**(4), 2-4.

GVN, 1995h, Fogo. *Smithsonian Inst. Bull. Global Volcanol. Net.*, **20**(5), 5.

GVN, 1995i, Erebus. *Smithsonian Inst. Bull. Global Volcanol. Net.*, **20**(11/12), 12.

GVN, 1995j, Etna. *Smithsonian Inst. Bull. Global Volcanol. Net.*, **20**(6), 12-13.

GVN, 1995k, Etna. *Smithsonian Inst. Bull. Global Volcanol. Net.*, **20**(8), 2-3.

GVN, 1995l, Etna. *Smithsonian Inst. Bull. Global Volcanol. Net.*, **20**(11/12), 8-11.

Hanstrum, B.N., and Watson, A.S., 1983. A case study of two eruptions of Mount Galunggung and an investigation of volcanic eruption cloud characteristics using reote sensing techniques. *Aust. Met. Mag.*, **31**, 171-177.

Hardee, H.C., 1982. Permeable convection above magma bodies. *Tectonophysics*, **84**, 179-195.

Hardee, H.C., 1993. Thermal feedback mechanisms and their potential influence on the emplacement of lavas. In *Active Lavas* edited by C.R.J. Kilburn & G. Luongo, (London: UCL Press), pp. 281-289.

Harris, A.J.L., 1992. *Volcano detection and monitoring using AVHRR: the Krafla eruption, Iceland 1984.* MSc thesis, Department of APEME, University of Dundee, UK.

Harris, A.J.L., and Stevenson, D.S., 1996. Defining the magmatic systems at Vulcano and Stromboli volcanoes. Submitted to *Nature.*

Harris, A.J.L., and Vaughan, R.A., 1993. AVHRR for operational monitoring of volcanic activity - a case study. *Proc. 13th EARSeL symposium,* Dundee, U.K., 28 June - 1 July 1993, pp. 217-224.

Harris, A.J.L. and Rothery, D.A., 1995. Thermal monitoring of volcanoes using data from the AVHRR. *Proc. 21st Annual Conference of the Remote Sensing Society,* University of Southampton, U.K., 11-14 September 1995, pp.528-535.

Harris, A.J.L., Rothery, D.A., Carlton, R.W., Langaas, S., and Mannstein, H., 1995a. Non-zero saturation of AVHRR thermal channels over high temperature targets: evidence from volcano data and a possible explanation. *Int. J. Remote Sensing,* **16**, 189-196.

Harris, A.J.L., Swabey, S.E.J., and Higgins, J., 1995b. Automated thresholding of active lavas using AVHRR data. *Int. J. Remote Sensing,* **16**, 3681-3686.

Harris, A.J.L., Vaughan, R.A., and Rothery, D.A., 1995c. Volcano detection and monitoring using AVHRR data: the Krafla eruption, 1984. *Int. J. Remote Sensing,* **16**, 1001-1020.

Harris, A.J.L., Stevens, N.F., Maciejewski, A.J.H., and Röllin, P.J., 1996. Thermal evidence for linked vents at Stromboli. *Acta Vulcanol.*, in press.

Head III, J.W., and Wilson, L., 1986. Volcanic processes and landforms on Venus: theory, predictions, and observations. *J. Geophys. Res.*, **91**, 9407-9446.

Ho, D., and Asem, A., 1986. NOAA AVHRR image referencing. *Int. J. Remote Sensing,* **7**, 895-904.

Holasek, R.E., and Rose, W.I., 1991. Anatomy of 1986 Augustine volcano eruptions as recorded by multispectral image processing of digital AVHRR weather satellite data. *Bull. Volcanol.*, **53**, 420-435.

Holasek, R.E., and Self, S., 1995. GOES weather satellite observations and measurements of the May 18, 1980, Mount St. Helens eruption. J. *Geophys. Res.*, **100**, 8469-8487.

Hon, K., Kauahikaua, J., Denlinger, R., and Mackay, K., 1994. Emplacement and inflation of pahohoe sheet flows: observations and measurements of active lava flows on Kilauea volcano, Hawaii. *Geol. Soc. Am. Bull.*, **106**, 351-370.

Holben, B., 1986. Characteristics of maximum-value composite images from temporal AVHRR data. *Int. J. Remote Sensing,* **7**, 1417-1434.

Holman, J.P., 1992. *Heat transfer.* (London: McGraw-Hill).

Huppert, H.E., and Sparks, R.S.J., 1988. The generation of granitic magmas by intrusion of basalt into continental crust. *J. Petrology,* **29**, 599-624.

Hurtado. E., Vidal, A., and Caselles, V., 1996. Comparison of two atmospheric correction methods for Landsat TM. *Int. J. Remote Sensing*, **17**, 237-247.

Italiano, F. and Nuccio, P.M., 1992. Volcanic steam output directly measured in fumaroles: the observed variations at Vulcano Island, Italy, between 1983 and 1987. *Bull. Volcanol.,* **54**, 623-630.

Italiano, F., Nuccio, P.M. and Valenza, M., 1984. Geothermal energy and mass release at Vulcano, Aeolian Island, Italy. *Rend. Soc. Ital. Min. Petrol.*, **39**, 379-386.

Italiano, F., Nuccio, P.M. and Pecoraino, G., 1994. Fumarolic gas output at La Fossa di Vulcano crater. *Acta Vulcanol.*, **6**, 39-40.

Jaskolla, F., and Arnason, K., 1989. Applicability of Landsat-TM data for geoscientific purposes in Iceland. *Proc. Workshop on the Earthnet Pilot Project on Landsat Thematic Mapper Applications*, Frascati, December 1987, pp. 127-139.

Jeyaseelan, A.T., and Thiruvengadachari, S., 1993. Suspected Mt. Pinatubo aerosol impact on the NOAA AVHRR NDVI over India. *Int. J. Remote Sensing*, **14**, 603-608.

Kasischke, E.S., and French, N.H.F., 1995. Locating and Estimating the Aerial Extent of Wildfires in Alaskan Boreal Forests Using Multiple-Season AVHRR NDVI Composite data. *Remote Sensing Environ.,* **51**, 263-275.

Kahle, A.B., Gillespie, A R., Abbott, E.A., Abrams, M.J., Walker, R.E., Hoover G., and Lockwood J.P., 1988. Relative dating of Hawaiian lava flows using multispectral thermal infrared images: a new tool for geological mapping of young volcanic terranes. *J. Geophys. Res.*, **93**, 15239-15251.

Kaufman, Y.J., Setzer, A., Justice, C., Tucker, C.J., Pereira, M.C., and Fung, I., 1990. Remote Sensing of Biomass Burning in the Tropics. In *Fires in the Tropical Biota* edited by J.G.Goldammer, (Berlin: Springer-Verlag), pp.371-399.

Kays, W.M. and Crawford, M.E., 1980.*Convective heat and mass transfer.* (New York: McGraw-Hill).

Keller, J., 1980. The island of Vulcano. Rend. *Soc. Ital. Min. Petrol.*, **36**, 369-414.

Kennedy, P.J., Belward, A.S., and Gregoire, J.-M., 1994. An improved approach to fire monitoring in West Africa using AVHRR data. *Int. J. Remote Sensing*, **15**, 2235-2255.

Keszthelyi, L., 1995. A preliminary thermal budget for lava tubes on the Earth and planets. *J. Geophys. Res.*, **100**, 20411-20420.

Khazenie, N., and Richardson, K.A., 1993. Detection of oil fire smoke over water in the Persian Gulf region. *Am. Soc. Photogrammetry & Remote Sensing*, **59**, 1271-1276.

Kidwell, K.B., 1995. *NOAA polar orbiter data users guide.* NOAA/NESDIS, Washington D.C.

Kieffer, H.H., Frank, D., and Friedman, J.D., 1981. Thermal infrared surveys of Mount St. Helens - observations prior to the eruption of May 18. In *The 1980 eruptions of Mount St. Helens*, edited by P.W. Lipman & D.R. Mullineaux, U.S. Geological Survey Prof. paper **1250**, pp. 257-277.

Kilburn, C.R.J., 1993. Lava crusts, aa flow lengthening and the pahoehoe-aa transition. In *Active lavas: monitoring and modelling*, edited by C.R.J. Kilburn & G. Luongo, (London: UCL Press), pp. 263-280.

Kilburn, C.R.J. and Lopes, R.M.C., 1988. The growth of Aa lava flow fields on Mount Etna, Sicily. *J. Geophys. Res.*, **93**, 14759-14772.

Kneizys, F.X., Shettle, E.P., Gallery, W.O., Chetwynd Jr., J.H., Abreu, L.W., Selby, J.E.A., Clough, S.A., and Fenn, R.W., 1983. *Atmospheric transmittance/radiance: computer code LOWTRAN 6.* Air Force Geophysics Laboratory, Environmental Research Paper 846, Hanscom AFB, Massachusetts.

Kokelaar, P., and Romagnoli, C., 1995. Sector collapse, sedimentation and clast population evolution at an active island-arc volcano: Stromboli, Italy. *Bull. Volcanol.*, **57**, 240-262.

Korzhinsky, M.A., Tkachenko, S.I., Shmulovich, K.I., Taran, Y.A., and Steinberg, G.S., 1994. Discovery of a pure rhenium mineral at Kudriavy volcano. *Nature*, **369**, 51-52.

Krueger, A.J., Walter, L.S., Schnetzler, C.C., and Doiron, S.D., 1990. TOMS measurement of the sulfur dioxide emitted during the 1985 Nevado del Ruiz eruptions. *J. Volcanol. & Geotherm. Res.*, **41**, 7-15.

Kyle, P.R., Sybeldon, L.M., McIntosh, W.C., Meeker, K., and Symonds, R., 1994. Sulfur dioxide emission rates from Mount Erebus, Antarctica. In *Volcanological and environmental studies of Mount Erebus, Antarctica*, edited by P.R. Kyle, AGU Antarctic Research Series **66**, 69-82.

Langaas, S., 1992. Temporal and Spatial Distribution of Savanna Fires in Senegal and The Gambia, West Africa, 1989-90, Derived from Multi-temporal AVHRR Night Images. *Int. J. Wildland Fire*, **2**, 21-36.

Langaas, S., 1993. A parametrised bispectral model for savanna fire detection using AVHRR night images. *Int. J. Remote Sensing*, **14**, 2245-2262.

Langaas, S., 1995. *Night-time observations of west-African bushfires from Space.* PhD. thesis, University of Oslo, Norway.

Lauritson, L., Nelson, G.J., and Porto, F.W., 1988. Data extraction and calibration of TIROS-N/NOAA radiometers. *NOAA Technical Memorandum NESS 107,* Washington D.C.

Lee, T.F., and Tag, P.M., 1990. Improved detection of hotspots using the AVHRR 3.7-μm channel. *Bull. Am. Met. Soc.*, **17**, 1722-1730.

Lesage, Ph., Vandemeulebrouck, J., and Halbwachs, M., 1995. Data acquisition and telemetry. In Monitoring Active Volcanoes, edited by B. McGuire, C.R.J. Kilburn & J. Murray, (London: UCL Press), pp. 32-59.

Li (Zhirong), Z.R., and McDonnell, M.J., 1988. Atmospheric correction of thermal infrared images. *Int. J. Remote Sensing*, **9**, 107-121.

Lillesand, T.M., and Kiefer, R.W., 1987. *Remote Sensing and image interpretation.* (New York: John Wiley & Sons).

Llewellyn-Jones, D.T., Minnett, P.J., Saunders, R.W., Zavody, A.M., 1984. Satellite multichannel infrared measurements of sea surface temperature of the N.E.Atlantic Ocean using AVHRR-2. *Quart. J. R. Met. Soc.*, **110**, 613-631.

Malin, M.C., 1980. Lengths of Hawaiian lava flows, *Geology,* 8, 306-308.

Mannstein, H., and Gesell, G., 1991. Deconvolution of AVHRR data. *Proc. 5th AVHRR data users' meeting*, Tromsoe, Norway, 25 June 1991.

Markham, B.L., and Barker, J.L., 1986. Landsat MSS and TM post-calibration dynamic ranges, exoatmosphere reflectances and at-satellite temperatures. *EOSAT Landsat Tech. Note*, Lanham, August 1986, pp. 3-8.

Markham, B.L., and Barker, J.L., 1987. Thematic Mapper bandpass solar exoatmospheric irradiances. *Int. J. Remote Sensing*, **8**, 517-523.

Martini, M., 1986. Thermal activity and ground deformation at Phlegrean Fields, Italy: precursors of eruptions or fluctuations of quiescent volcanism? A contribution of geochemical studies. *J. Geophys. Res.*, **91**, 12255-12260.

Martini, M., Piccardi, G., and Legittimo, P.C., 1980. Geochemical surveillance of active volcanoes: data on the fumaroles of Vulcano (Aeolian Islands, Italy). *Bull. Volcanol.*, **43**, 255-263.

Massonnet, D., Briole, P., and Arnaud, A., 1995. Deflation of Mount Etna monitored by spaceborne radar interferometry. *Nature*, **375**, 567-570.

Mather, P.M., 1987. *Computer processing of remotely-sensed images.* (Chichester: John Wiley & Sons).

Matson, M., and Dozier, J., 1981. Identification of Subresolution High Temperature Sources Using a Thermal IR Sensor. *Photogram. Eng. & Remote Sensing*, **47**, 1311-1318.

Matson, M., and Holben, B., 1987. Satellite detection of tropical burning in Brazil. *Int. J. Remote Sensing*, **8**, 509-516.

Matson, M., Schneider, S.R., Aldridge, B., and Satchwell, B., 1984. Fire detection using the NOAA-series satellites. *NOAA Technical report NESDIS 7*, Washington D.C.

Mazor, E., Cioni, R., Corazza, E., Fratta, M. Magro, G., Matsuo, S., Hirabayashi, J., Shinohara, H., Martini, M., Paccardi, G., and Cellini-Legittimo, P., 1988. Evolution of fumarolic gases - boundary conditions set by measured parameters: case study at Vulcano, Italy. *Bull. Volcanol.*, **50**, 71-85.

McClain, E.P., Pichel, W.G., and Walton, C.C., 1985. Comparative performance of AVHRR-based multichannel sea surface temperatures. *J. Geophys. Res.*, **90**, 11587-11601.

McGetchin, T.R., and Chouet, B.A., 1979. Energy budget of the volcano Stromboli, Italy. *Geophys. Res. Lett.*, **6**, 317-320.

Melson, W.G., and Saenz, R., 1973. Volume, energy and cyclicity of eruptions of Arenal volcano, Costa Rica. *Bull. Volcanol.*, **37**, 416-437.

Menyailov, I.A., 1975. Prediction of eruptions using changes in composition of volcanic gases. *Bull. Volcanol.*, **39**, 112-125.

Menyailov, I.A., Nikitina, L.P., Shapar, V.N. and Pilipenko, V.P., 1986. Temperature increase and chemical change of fumarolic gases at Momotombo volcano, Nicaragua, in 1982-1985: are these indicators of a possible eruption? J. *Geophys. Res.*, **91**, 12199-12214.

Menzel, W.P., Cutrim, E.C., and Prins, E.M., 1991. Geostationary Satellite Estimation of Biomass Burning in Amazonia during BASE-A. In *Global biomass burning, atmospheric, climatic and biospheric implications*, edited by J.S.Levine, (MIT Press), pp.41-46.

Mongillo, M.A., and Wood, C.P., 1995. Thermal infrared mapping of White Island volcano, New Zealand. *J. Volcanol. & Geotherm. Res.*, **69**, 59-71.

Mouginis-Mark, P.J., and Francis, P.W., 1992. Satellite observations of active volcanoes: prospects for the 1990s. *Episodes*, **15**, 46-55.

Mouginis-Mark, P.J., and Garbiel, H., 1993. Digital topography of volcanoes from radar interferometry: an example from Mt. Vesuvius, Italy. *Bull. Volcanol.*, **55**, 566-570.

Mouginis-Mark, P.J., Pieri, D.C., Francis, P.W., Wilson, L., Self, S., Rose, W.I., and Wood, C.A., 1989. Remote sensing of volcanoes and volcanic terrains. *EOS*, **70**, 1567-1575.

Mouginis-Mark, P.J., Rowland, S., Francis, P., Friedman, T., Garbeil, H., Gradie, J., Self, S., Wilson, L., Crisp, J., Glaze, L., Jones, K., Kahle, A., Pieri, D., Zebker, H.,

Krueger, A., Walter, L., Wood, C., Rose, W., Adams, J., and Wolff, R., 1991. Analysis of active volcanoes from the Earth Observing System. *Remote Sensing Environ.*, **36**, 1-12.

Mouginis-Mark, P.J., Garbiel, H., and Flament, P., 1994. Effects of viewing geometry on AVHRR observations of volcanic thermal anomalies. *Remote Sensing Environ.*, **48**, 51-60.

Moxham, R.M., 1967. Changes in surface temperature at Taal volcano, Philippines, 1965-1966. *Bull. Volcanol.*, **31**, 215-234.

Moxham, R.M., 1971. Thermal surveillance of volcanoes. In *The Surveillance & prediction of volcanic activity*, (Paris: UNESCO), pp. 103-124.

Moxham, R.M., Boynton, G.R. and Cote, C.E., 1972. Satellite telemetry of fumarole temperatures, Mount Rainier, Washington. *Bull. Volcanol.*, **36**, 191-199.

Muirhead, K., and Cracknell, A.P., 1984. Identification of gas flares in the North Sea using satellite data. *Int. J. Remote Sensing*, **5**, 199-212.

Munro, D.C., and Mouginis-Mark, P.J., 1990. Eruptive patterns and structure of Isla Fernandina, Galapagos Islands, from SPOT-1 HRV and large format camera images. *Int J. Remote Sensing*, **11**, 1501-1509.

Naboko, S.I., 1960. Change in the fumarole regime of Kliuchevsky volcano. *Bull. Volcanol.*, **23**, 135-140.

Nappi, G., 1976. Recent activity at Stromboli. *Nature*, **261**, 119-120.

Nappi, G., and Renzulli, A., 1989. Stromboli. *Bull. Volcanic Eruptions*, **26**, 1-3.

NASA/AMES, 1991. Airborne Thematic Mapper Simulator tape format. *NASA/AMES Tech. Note*, Moffett Field, California, September 1991.

Neuberg, J., Luckett, R., Ripepe, M., and Braun, T., 1994. Highlights from a seismic broadband array on Stromboli volcano. *Geophys. Res. Lett.*, **21**, 749-752.

Neumann van Padang, M., 1963. The temperatures in the crater region of some Indonesian volcanoes before the eruption. *Bull. Volcanol.*, **26**, 319-336.

Nolan, M.L., 1979. Impact of Parícutin on five communities. In *Volcanic activity and human ecology*, edited by P.D. Payson & D.K. Grayson, (New York: Academic Press), pp.293-338.

NSW Department of Bush Fire Services, 1994. Preliminary report on the January bushfires in N.S.W. 27th December 1993 to 16th January 1994. Report prepared by *NSW Department of Bush Fire Services*, New South Wales, Australia, 20 January 1994.

Ntepe, N., and Dorel, J., 1990. Observations of seismic volcanic signals at Stromboli volcano (Italy). *J. Volcanol. & Geotherm. Res.*, **43**, 235-251.

O'Hanlon, L., 1995. Fighting fire with fire. *New Scientist*, **1986**, 29-33.

Oppenheimer, C., 1989. AVHRR volcano hotspot monitoring. *Proc. 4th AVHRR Data Users' Meeting*, Rothenberg, Germany, 3-5 September 1989, pp. 335-338.

Oppenheimer, C., 1991a. Lava flow cooling estimated from Landsat Thematic Mapper infrared data: the Lonquimay eruption (Chile, 1989). *J. Geophys. Res.*, **96**, 21865-21878.

Oppenheimer, C., 1991b. *Volcanology from space: applications of infrared remote sensing*. PhD. thesis, Department of Earth Sciences, The Open University, UK.

Oppenheimer, C., 1993. Thermal distributions of hot volcanic surfaces constrained using three infrared bands of remote sensing data. *Geophys. Res. Lett.*, **20**, 431-434.

Oppenheimer, C., 1993b. Infrared surveillance of crater lakes using satellite data. *J. Volcanol & Geotherm. Res.*, **55**, 117-128.

Oppenheimer, C.M.M. and Rothery, D.A., 1989. Infrared remote sensing of hot volcanoes assessed by field observations. *Proc. 15th Annual Conference of the Remote Sensing Society*, Bristol, U.K., 13-15 September 1989, pp. 317-322.

Oppenheimer, C.M.M., and Rothery, D.A., 1991. Infrared monitoring of volcanoes by satellite. *J. Geol. Soc. Lond.*, **148**, 563-569.

Oppenheimer, C., Francis, P.W., Rothery, D.A., Carlton, R.W.T., and Glaze, L.S., 1993. Infrared image analysis of volcanic thermal features: Lascar volcano, Chile, 1984-1992. *J. Geophys. Res.*, **98**, 4269-4286.

Paltridge, G.W., and Barber, J., 1988. Monitoring Grassland Dryness and Fire Potential in Australia with NOAA/AVHRR Data. *Remote Sensing Environ.*, **25**, 381-394.

Parker, D.R., 1992. The Oakland-Berkeley Hills Fire: An Overview. In: *Response of the San Francisco Fire Department to the Oakland-Berkeley Conflagration of October 20 and 21, 1991* (by F.F.Postel & edited by D.Fowler), San Francisco Fire Department, U.S.A, pp.3-5.

Pereira, M.C., and Setzer, A.W., 1993. Spectral characteristics of deforestation fires in NOAA/AVHRR images. *Int. J. Remote Sensing*, **14**, 583-597.

Peterson, D.W., 1988. Volcanic hazards and public response. *J. Geophys. Res.*, **93**, 4161-4170.

Pieri, D.C., and Baloga, S.M., 1986. Eruption rate, area, and length relationships for some Hawaiian lava flows. *J. Volcanol. & Geotherm. Res.*, **30**, 29-45.

Pieri, D.C., Glaze, L.S., and Abrams, M.J., 1990. Thermal radiance observations of an active lava flow during the June 1984 eruption of Mount Etna. *Geology,* **18,** 1018-1022.

Pinkerton, H., and Wilson, L., 1994. Factors controlling the lengths of channel-fed lava flows. *Bull. Volcanol.*, **56**, 108-120.

Prata, A.J., 1989. Observations of volcanic ash clouds in the 10-12 μm window using AVHRR/2 data. *Int. J. Remote Sensing*, **10**, 751-761.

Price, J.C., 1984. Land surface temperature measurements from the split window channels of the NOAA 7 Advanced Very High Resolution Radiometer. *J. Geophys. Res.*, **89**, 7231-7237.

Prins, E.M., and Menzel, W.P., 1992. Geostationary satellite detection of biomass burning in South America. *Int. J. Remote Sensing*, **13,** 2783-2799.

Ruapehu Surveillance Group, 1996. Volcanic eruption at a New Zealand ski resort prompts reevaluation of hazards. *EOS*, **77**, 189-191.

Realmuto, V.J., Hon, K., Kahle, A.B., Abbott, E.A., and Pieri, D.C., 1992. Multispectral thermal infrared mapping of the 1 October 1988 Kupaianaha flow field, Kilauea volcano, Hawaii. *Bull. Volcanol.*, **55**, 22-44.

Realmuto, V.J., Abrams, M.J., Buongiorno, M.F., and Pieri, D.C., 1994. The use of multispectral thermal infrared image data to estimate the sulfur dioxide flux from volcanoes: a case study from Mount Etna, Sicily, July 29, 1986. *J. Geophys. Res.*, **99**, 481-488.

Reddy, C.S.S., Bhattacharya, A., and Srivastav, S.K., 1993. Night-time TM short wavelength infrared data analysis of Barren Island volcano, South Andaman, India. *Int. J. Remote Sensing*, **14**, 783-787.

Rees, J.D., 1979. Effects of the eruption of Parícutin volcano on landforms, vegetation and human occupancy. In *Volcanic activity and human ecology*, edited by P.D. Payson & D.K. Grayson, (New York: Academic Press), pp.293-338.

Ripepe, M., and Braun, T., 1994. Air-wave phases in Strombolian explosion-quake seismographs: a possible indicator for the magma level? *Acta Vulcanol.*, **5**, 201-206.

Robinson, J.M., 1991. Fire from space: Global fire evaluation using infrared remote sensing. *Int. J. Remote Sensing*, **12**, 3-24.

Robock, A., and Matson, M., 1983. Circumglobal transport of the El Chichon volcanic dust cloud. *Science*, **221**, 195-197.

Romano, R. and Sturiale, C., 1992. The historical eruptions of Mount Etna (volcanological data). *Mem. Soc. Geol. It.*, **23**, 75-97.

Roozekrans J.N., and Prangsma, G.J., 1988. Processing and application of digital AVHRR imagery for land and sea surfaces. *Final Report of the BCRS project*, no: **TO-3.1**, Royal Netherlands Meteorological Institute (KNMI).

Rose Jr., W.I., and Stoiber, R.E., 1969. The 1966 eruption of Izalco Volcano, El Salvador. *J. Geophys. Res.*, **74**, 3119-3130.

Rosi, M., 1980. The island of Stromboli. Rend. *Soc. Ital. Min. Petrol.*, **36**, 345-368.

Rosi, M., and Sbrana, A., 1988. Stromboli. *Bull. Volcanic Eruptions*, **25**, 7-8.

Rothery, D.A., 1989. Volcano monitoring by satellite. *Geology Today*, Jul-Aug 1989, 128-132.

Rothery, D.A., 1992. Monitoring and warning of volcanic eruptions by remote sensing. In *Geohazards: Natural and Man-made*, edited by G.J.H. McCall, D.J.C. Laming, & S.C Scott, (London: Chapman & Hall), pp. 25-32.

Rothery, D.A., and Francis, P.W., 1987. Detection and monitoring of volcanic activity using short wavelength infrared TM and MSS imagery. *Proc. 13th Annual Conference of the Remote Sensing Society*, University of Nottingham, 8-11 September 1987, pp. 204-213.

Rothery, D.A., and Francis, P.W., 1990. Short wavelength infrared images for volcano monitoring. *Int. J. Remote Sensing*, **11**, 1665-1667.

Rothery, D.A., and Pieri, D.C., 1993. Remote sensing of active lava. In *Active Lavas: Monitoring & Modelling*, edited by CRJ Kilburn & G. Luongo, (London: UCL Press), pp. 203-232.

Rothery, D.A., and Oppenheimer, C., 1991. Monitoring volcanoes using short wavelength infrared images. Proc. 5th International Colloquium - Physical Measurements & Signatures in Remote Sensing, Courchevel, France, 14-18 January 1991, pp. 513-516.

Rothery, D.A., and Oppenheimer, C., 1994. Monitoring Mount Erebus by remote sensing. In *Volcanological and environmental studies of Mount Erebus, Antarctica*, edited by P.R. Kyle, AGU Antarctic Research Series 66, pp. 51-56.

Rothery, D.A., Francis, P.W., and Wood, C.A., 1988. Volcano monitoring using short wavelength infrared data from satellites. *J. Geophys. Res.*, **93**, 7993-8008.

Rothery, D.A., Borgia, A., Carlton, R.W., and Oppenheimer, C., 1992. The 1992 Etna lava flow imaged by Landsat TM. *Int. J. Remote Sensing*, **13**, 2759-2763.

Rothery, D.A., Oppenheimer, C., and Bonneville, A., 1995. Infrared thermal monitoring. In: *Monitoring active volcanoes,* edited by B. McGuire, C.R.J. Kilburn & J. Murray (London: UCL Press) pp. 184-216.

Rowland, S.K., and Munro, D.C., 1992. The caldera of Volcan Fernandina: a remote sensing study of its structure and recent activity. *Bull. Volcanol.*, **55**, 97-109.

Rowland, S.K., Smith, G.A., and Mouginis-Mark, P.J., 1994. Preliminary ERS-1 observations of Alsakan and Aleutian volcanoes. *Remote Sensing Environ.*, **48**, 358-369.

Sakellariou, N.K., and Leighton, H.G., 1988. Identification of cloud-free pixels in inhomogeneous surfaces from AVHRR radiances. *J. Geophys. Res.*, **93**, 5287-5293.

Salisbury, J.W., 1986. Preliminary measurements of leaf spectral reflectance in the 8-14 μm region. *Int. J. Remote Sensing*, **7**, 1879-1886.

Salisbury, J. W., and Milton, N. M., 1988. Thermal infrared (2.5- to 13.5-μm) directional hemispherical reflectance of leaves. *Photogram. Eng. & Remote Sensing*, **54**, 1301-1304.

Salisbury, J.W., and D'Aria, D.M., 1992. Emissivity of terrestrial materials in the 8-14 μm atmospheric window. *Remote Sensing Environ.*, **42**, 83-106.

Salisbury, J.W., and D'Aria, D.M., 1994. Emissivity of terrestrial materials in the 3-5 μm atmospheric window. *Remote Sensing Environ.*, **47**, 345-361.

Salisbury, J. W., D'Aria, D. M., and Wald, A., 1994. Measurements of thermal infrared spectral reflectance of frost, snow and ice. *J. Geophys. Res.*, **99**, 24235-24240.

Sandford, T.D.G., and Stephenson. J., 1992. Orbital prediction for the NOAA satellite series. *Proc. Remote Sensing Society Annual Conf*erence, University of Dundee, September 1992, pp. 424-433.

Saunders, R.W., 1986. An automated scheme for the removal of cloud contamination from AVHRR radiances over Western Europe. *Int. J. Remote Sensing*, **7**, 867-886.

Saunders, R.W., and Kriebel, K.T., 1988. An improved method for detecting clear sky and cloudy radiances from AVHRR data. *Int. J. Remote Sensing*, **9**, 123-150.

Sawada, Y., 1987. Analyses of volcanic eruptions based on eruption cloud image obtained by geostationary meteorological satellite (GMS). *Technical Report of the Meteorological Institute*, **22**, Meteorological Research Institute, Japan.

Sawada, Y., 1989. The detection capability of explosive eruptions using GMS imagery, and the behaviour of dispersing eruption clouds. In *IAVCEI Proceedings in Volcanology 1*, edited by J.H. Latter, (Berlin: Springer-Verlag), pp. 233-245.

Schick, R., and Mueller, W., 1988. Volcanic activity and eruption sequences at Stromboli during 1983-1984. In *Modelling of volcanic processes*, edited by Chi-Yu King & R. Scarpa, (Wiesbaden: Fr. Vieweg & Son), pp. 120-139.

Schnetzler, C.C., Doiron, S.D., Walter, L.S., and Krueger, A.J., 1994. Satellite measurements of sulfur dioxide from the Redoubt eruptions of 1989-1990. *J. Volcanol. & Geotherm. Res.*, **62**, 353-357.

Schwalb, A., 1978. The TIROS-N/ NOAA A-G satellite series. *NOAA Technical Memorandum NESS 95*, Washington D.C.

Scorer, R.S., 1986. Etna: the eruption of christmas 1985 as seen by meteorological satellite. *Weather*, **41**, 378-384.

Setzer, A.W., and Malingreau, J.P., 1993. Temporal variation in the limit of fires in AVHRR's channel 3. *Proc. 6th AVHRR data user's meeting*, Belgirate, Italy, May 1993.

SEAN, 1987. Etna. *Smithsonian Inst. Scientific Event Alert Net. Bull.*, **12**(4), 2-3.

SEAN, 1989a. Stromboli. *Smithsonian Inst. Scientific Event Alert Net. Bull.*, **14**(3), 4.

SEAN, 1989b. Etna. *Smithsonian Inst. Scientific Event Alert Net. Bull.*, **14**(8), 14-15.

SEAN, 1989c. Etna. *Smithsonian Inst. Scientific Event Alert Net. Bull.*, **14**(10), 16-26.

Sekioka, M. and Yuhara, K., 1974. Heat flux estimation in geothermal areas based on the heat balance of the ground surface. *J. Geophys. Res.*, **79**, 2053-2058.

Settle, M. and McGetchin, T.R., 1980. Statistical analysis of persistent explosive activity at Stromboli, 1971: implications for eruption prediction. *J. Volcanol. & Geotherm. Res.*, **8**, 45-58.

Setzer, A.W., and Verstraete, M.M., 1994. Fire and glint in AVHRR's channel 3: a possible reason for the non-saturation mystery. *Int. J. Remote Sensing*, **15**, 711-718.

Sheridan, M.F., and Malin, M.C., 1983. Application of computer-assisted mapping to volcanic hazard evaluation of surge eruptions: Vulcano, Lipari, and Vesuvius. *J. Volcanol. & Geotherm. Res.*, **17**, 187-202.

Sicardi, L., 1940. Il recente ciclo dell' attivita fumarolica dell' isola di Vulcano. *Bull. Volcanol.*, **7**, 85-139.

Simkin, T., and Siebert, L., 1994, *Volcanoes of the world*, (Tucson: Geoscience Press).

Singh, S.M., 1984. Removal of atmospheric effects on a pixel by pixel basis from the thermal infrared data from instruments on satellites. The Advanced Very High Resolution Radiometer (AVHRR). *Int. J. Remote Sensing*, **5**, 161-183.

Singh, S.M., 1985. Evaluation of atmospheric for SPOT stereoscopic modelling using AVHRR data. *Proc. Remote Sensing Workshop*, Nottingham, U.K., 22 May 1985, pp. 101-137.

Singh, S.M., and Warren, D.E., 1983. Sea surface temperatures from infrared measurements. In *Remote Sensing Applications in Marine Science and Technology*, edited by A. P. Cracknell, (Reidel), pp. 231-262.

Smithsonian Institution, 1989. Etna. In *Global volcanism 1975-1985*, edited by L. McClelland, T. Simkin, M. Summers, E. Nielson and T. C. Stein, (New Jersey: Prentice Hall), pp. 52-76.

Sobrino, J.A., Coll, C., Caselles, V., 1991. Atmospheric correction for land surface temperature using NOAA-11 AVHRR channels 4 & 5. *Remote Sensing Environ.*, **38**, 19-34.

Stephens, G., 1993. Mt. Spurr ash plume. *Int. J. Remote Sensing*, **14**, 2905-2906.

Stephens, G., 1995. Mt. Pinatubo ash plume. *Int. J. Remote Sensing*, **16**, 407-408.

Stevenson, D.S., 1993. Physical models of fumarolic flow. *J. Volcanol. & Geotherm. Res.*, **57**, 139-156.

Suwa, A., and Tanaka., Y., 1959. The changes in the temperatures of the fumaroles in the crater of Miharayama, Oshima, in connection with the activities of the volcano. *Bull. Volcanol. Soc. Jap.*, **3**, 107-118.

Tabbagh, A., Tabbagh, J., and Dechambenoy, C., 1987. Mapping of the surface temperature of Mount Etna and Vulcano using an airborne scanner radiometer. *J. Volcanol. & Geotherm. Res.*, **34**, 79-88.

Tanguy, J.C., 1973. The 1971 Etna eruption: petrography of lavas. *Phil. Trans. R. Soc. Lond.*, **274**, 45-53

Taran, Y.A., Hedenquist, J.W., Korzhinsky, M.A., Tkachenko, S.I., and Shmulovich, 1995. Geochemistry of magmatic gases from Kudriavy volcano, Kuril Islands. *Geochim. et Cosmo. Acta*, **59**, 1749-1761.

Taylor, G.A.M., 1958. The 1951 eruption of Mount Lamington, Papua. *Bulletin of the Australian Bureau of Mineral Resources, Ecology & Geophysics Australia*, **38**.

Tedesco, D., Toutain, J.P., Allard, P., and Losno, R., 1991. Chemical variations in fumarolic gases at Vulcano Island (Southern Italy): seasonal and volcanic effects. *J. Volcanol. & Geotherm. Res.*, **45**, 325-334.

Tedesco, D., Miele, G., Sano, Y., and Toutain, J.P., 1995. Helium isotopic ratio in Vulcano island fumaroles: temporal variations in shallow level mixing and deep magmatic supply. *J. Volcanol. & Geotherm. Res.*, **64**, 117-128.

Thiermann, V., and Ruprecht, E., 1992. A method for the detection of clouds using AVHRR infrared observations. *Int. J. Remote Sensing*, **13**, 1829-1849.

Thorarinsson, S., Steinthorsson, S., Einarsson, T.H., Kristmannsdottir, H., and Oskarsson, N., 1973. The eruption on Heimaey, Iceland. *Nature*, **241**, 372-375.

Tilling, R.I., 1989. Volcanic hazards and their mitigation: progress and problems. *Rev. Geophys.*, **27**, 237-269.

Tilling, R.I., 1995. The role of monitoring in forecasting volcanic events. In *Monitoring Active Volcanoes*, edited by B. McGuire, C.R.J. Kilburn & J. Murray, (London: UCL Press), pp. 369-402.

Time Life, 1982. The Fiery Ordeal of Heimaey. In *Volcano*, (USA: Time Life Books), pp. 134-139.

Tucker, C.J., and Matson, M., 1985. Determination of volcanic dust deposition from El Chichon using ground and satellite data. *Int. J. Remote Sensing*, **6**,619-627.

Tucker, C.J., Gatlin, J.A., and Schneider, S. R., 1984. Monitoring vegetation in the Nile Delta with NOAA-6 and NOAA-7 AVHRR imagery. *Photogram. Eng. & Remote Sensing*, **50**, 53-61.

U.S. Government Agencies, 1994. United States activities on natural disaster reduction. *World Conference for Natural Disaster Reduction*, Yokohama, Japan, 23-27 May 1994.

USGS, 1995. The first 12 years of Pu'u 'O'o-Kupaianaha eruption. *Volcano Watch*, 6 Januray 1995, USGS, Hawaiian Volcano Observatory.

Vassale, R., 1994. The use of explosive for the diversion of the 1992 Mt. Etna lava flow. *Acta Vulcanol.*, **4**, 173-177.

Vidal, A., 1991. Atmospheric and emissivity correction of land surface temperature measured from satellite using ground measurements or satellite data. *Int J Remote Sensing*, **12**, 2449-2460.

Vidal, A., Pinglo, F., Durand, H., Devaux-Ros, C., and Maillet, A., 1994. Evaluation of a Temporal Fire Risk Index in Mediterranean Forests from NOAA Thermal IR. *Remote Sensing Environ.*, **49**, 269-303.

Wadge, G., 1978. Effusion rate and the shape of aa lava flow-fields on Mount Etna. *Geology,* **6**, 503-506.

Wadge, G., 1981. The variation of magma discharge during basaltic eruptions. *J. Volcanol. & Geotherm. Res.*, **11**, 139-168.

Wadge, G., Walker, G. P. L., and Guest, J. E., 1975. The output of Etna volcano. *Nature*, **255**, 385-387.

Wadge, G., Francis, P.W., and Ramirez, C.F., 1995. The Socompa collapse and avalanche event, *J. Volcanol. & Geotherm. Res.*, **66**, 309-336.

Walker, G.P.L., 1972. Compound and simple lava flows and flood basalts. *Bull. Volcanol.*, **35**, 579-590.

Walker, G.P.L., 1973. Lengths of lava flows. *Phil. Trans. R. Soc. Lond.*, **274**, 107-118,.

Washington, H.S., 1917. Persistence of vents at Stromboli and its bearing on volcanic mechanism. *Bull. Geol. Soc. Am.*, **28**, 249-278.

Weinreb, M.P., Hamilton, G., Brown, S., and Koczor, R.J., 1990. Nonlinearity corrections in calibration of Advanced Very High Resolution Radiometer infrared channels. *J. Geophys. Res.*, **95**, 7381-7388.

Weisel, D., and Stapleton, F., 1992. *Aloha O Kalapana*, (Honolulu: Bishop Museum Press).

Weisnet, D.R., and D'Aguanno, J., 1982. Thermal imagery of Mount Erebus from the NOAA-6 satellite. *Antarctic J. U.S.*, **17**, 32-34.

Williams Jr., R.S., and Friedman, J.D., 1970. Satellite observation of effusive volcanism. *J. Brit. Interplan. Soc.*, **23**, 441-450.

Wooster, M.J., Sear, C.B., Patterson, G., and Haigh, J., 1994. Tropical lake surface temperatures from locally received NOAA-11 AVHRR data - comparison with in situ measurements. *Int. J. Remote Sensing*, **15**, 183-189.

Wooster, M.J., and Rothery, D.A., (in press). Thermal monitoring of Lascar Volcano, Northern Chile, using infrared data at high temporal resolution: a 1992 to 1995 time-series using the Along Track Scanning Radiometer. Submitted to *Bull. Volcanol.*

Yamamoto, T., Takarado, S., and Suto, S., 1993. Pyroclastic flows from the 1991 eruption of Unzen volcano. *Japan. Bull. Volcanol.*, **55**, 166-175.

Yamanouchi, T., and Kawaguchi, S. , 1992. Cloud distribution in the Antarctic from AVHRR data and radiation measurements at the surface. *Int. J. Remote Sensing*, **13**, 111-127.

Yokoyama, I., 1964. Seismometrical observation of the 1962 eruption of Volcano Tokati, Hokkaido, Japan. *Bull. Volcanol.*, **27**, 217-223.

Yokoyama, R., and Tanba, T., 1991. Estimation of sea surface temperature via AVHRR of NOAA-9 - comparison with fixed buoy data. *Int. J. Remote Sensing*, **12**, 2513-2528.

Young, P., and Wadge, G., 1990. Flowfront: simulation of a lava flow. *Computers & Geoscience*, **16**, 1171-1191.

Zettwoog, P., and Tazieff, H., 1972. Instrumentation for measuring and recording mass and energy transfer from volcanoes to atmosphere. *Bull. Volcanol.*, **26**, 1-19.

Appendix A. Mount Etna: the view from above

A.J.L. Harris, M.F. Buongiorno, D.C. Pieri, D.A. Rothery, and N.F. Stevens

Paper published in Etna 15 Years On, P. Gravestock & W. McGuire (eds.), 40-46, 1996.

A.1. Abstract

The first observation of thermal emission from volcanic activity using civilian satellite data was made during the 1966 eruption of Surtsey. Thirteen years later in 1979 the first satellite remote sensing analysis of Mount Etna was published. Since these observations, the technology available and the data interpretation techniques applied have both developed considerably, and Etna has become a major target for remote sensing studies. Here we consider the increasing contribution of remote sensing to monitor active lavas and other thermal anomalies, passive gas plumes and ground deformation at Etna. The complementary use of multiple data sets accurately to document an eruption is demonstrated by producing a chronology of the 1991 to 1993 eruption using data of various temporal and spatial resolutions.

A.2. Introduction

In 1979 the first satellite remote sensing analysis of Mount Etna was published, revealing a thermal anomaly believed to be due to shallow level magma storage (SEAN,

1989). To date at-least 20 published studies have shown how data from space and air-borne platforms can be used to monitor Mount Etna. That Etna has become the focus of so many remote sensing studies has been the result of four main factors. (1) Synoptic view: using just one image the whole of the volcano or volcanic feature can be analysed, including remote, inaccessible or dangerous points, as opposed to isolated point measurements possible from the ground. This has allowed construction of thermal maps (e.g. Bianchi *et al.* 1990; Bonneville & Gouze, 1992; Harris *et al.*, 1995), estimation of SO_2 flux using data for the entire plume (Realmuto *et al.*, 1994) and attempts to measure volcano-wide deformation (Massonnet *et al.*, 1995). (2) Thermal capabilities: measurements in a number of spectral bands permit temperature estimates and thermal modelling. For lava flows, thermal parameters can be used in models for mass production rate and flow behaviour (Pieri *et al.*, 1990). For gas plumes, thermal data allow SO_2 flux to be measured (Realmuto *et al.*, 1994). (3) Repeat coverage: data are available at regular intervals, once every 16 days for Landsat Thematic Mapper (TM) and four times a day for NOAA's Advanced Very High Resolution Radiometer (AVHRR). This allows time series analysis, so that lava flow, plume or deformation developments can be monitored through time (e.g. Harris *et al.*, 1995; Massonnet *et al.*, 1995; Pieri *et al.*, 1995). (4) Surface activity: Etna is the site of a constant passive gas plume and frequent lava activity, making it a profitable target for analysis. Activity is also well documented, providing "ground truth" against which the accuracy of remotely sensed results can be assessed.

The principles of thermal remote sensing of active volcanoes are given in Rothery *et al.* (1995) and elsewhere. Here we review published studies which have used air and space-borne remote sensing to monitor Mount Etna's thermal, plume and deformation activity. We use a case study of the 1991 to 1993 eruption to show how data sets from multiple sensors can be used to monitor an event.

A.3. Monitoring of low temperature thermal anomalies

The first published image to show a thermal anomaly on Etna was one from the Very High Resolution Radiometer (VHRR) acquired in September 1978, which had pixels 900 m across. This showed a N-S elongated thermal anomaly, of a few degrees above the background, 10 km in length on Etna's upper eastern flank. The presence of this anomaly was confirmed by field measurements and interpreted as being due to storage of magma at a shallow depth (Archambault *et al.*, 1979; SEAN, 1989). Subsequently image processing, atmospheric corrections and thermal models were developed allowing low temperature thermal anomalies to be located using 1 km pixel data from the VHRR's successor, the AVHRR (Bonneville *et al.*, 1985; Bonneville & Kerr, 1987). On the images analysed, low temperature anomalies were interpreted as being due to cooling lava from the March 1981 flank eruption, fumarolic and persistent activity at the summit, and an intrusive event prior to the March 1983 eruption. Bonneville and Gouze (1992) used AVHRR data jointly with TM data to locate five anomalous zones. Two were due to summit activity and cooling flows from the 1984 eruption respectively, a third correlated with the location of the October 1986 eruption which began one week after the image was acquired, the final two coincided with fissure zones and recent lava flow fields.

Low temperature anomalies have also been observed in thermal data from airborne scanners. ARIES images acquired from 5 aircraft passes during September 1983 were used to map surficial temperature, showing elevated temperatures from the cooling March 1983 flow field and Central Crater activity (Tabbagh *et al.*, 1987). A further 3 zones of elevated temperatures were mapped, one of which was postulated as being due the dyke which produced the 1983 flow.

A.4. High Spatial resolution monitoring of active lava

The first published lava flow analysis using airborne thermal data at Mount Etna was by Bianchi *et al.* (1990) using data acquired 10 days after the end of the October 1989 eruptive activity by the Thermal Infrared Multispectral Scanner (TIMS). This provides 6 to

14 m pixel data in six wavebands between 8.2 and 12.2 μm. Bianchi *et al.* (1990) used this data to produce a temperature map of the October 1989 lava flow, and demonstrated the value of such data for discriminating lithological units and mapping lava flows.

In the same year Pieri *et al.* (1990) used spaceborne TM data to analyse an active lava flow from the SE crater on 20 June 1984. On the basis of this image, they suggested that the flow consisted of a main stalled body, from which a narrower forward lobe extended for ~500 m eastwards into the Valle del Bove. Pieri *et al.* (1990) also used the data for quantitative analysis by applying a technique known as the "dual-band method", first applied for the analysis of active lavas in TM data by Rothery *et al.* (1988). The method allows analysis of the thermal structure of the flow surface, giving estimations for the size and temperature of crusted and molten surface areas. It uses a two component thermal model in which a hot spot is surrounded by a cooler background. By assuming the temperature of either of the two components and using two thermal bands of data, commonly TM bands 5 (1.55-1.75 μm) and 7 (2.08-2.35 μm), the size of both components and the temperature of the unassumed component can be estimated. For the 1984 flow, this method gave temperatures for hot fractures in the crusted flow surface of 177 to 830 °C. Using the thermal observations as boundary conditions, Pieri *et al.* (1990) constructed a thermal model of flow interior temperature, and calculated a maximum difference between initial eruption temperature (1050 °C) and internal flow temperature of ~20 °C. They concluded that for this flow 10-20% of the total radiated thermal output was emitted by hot fractures, which constituted <1% of the observed surface area. Only where hot fractures occupy >1% of the flow surface area will losses from such features significantly reduce internal temperatures. For the 1984 flow they inferred that boundary layer and flow thickness effects dominated over radiant zones in controlling the depression of core temperature.

Oppenheimer (1993) was able to use radiance measurements in three bands of airborne Thematic Mapper Simulator (TMS) data to extend the two component thermal model on which the dual band method is based to include a more realistic three component

thermal surface. The image, acquired during an aircraft overflight on 19 July 1991, showed the largest thermal anomaly within the NE crater. La Voragine contained a smaller anomaly, and the Bocca Nuova and SE crater both contained two anomalies. Using the hottest pixel within La Voragine, given a background temperature of 16 °C and the presence of fresh magma at 1070 °C, Oppenheimer's (1990) model suggested that a crusted surface at ~350 °C occupied ~5% of the pixel, with fresh magma occupying ~0.02%.

A different approach was taken Oppenheimer *et al.* (1993). During the summer of 1991 Etna was overflown by the Airborne Visible/Infrared Imaging Spectrometer (AVIRIS). This provided data at a nominal spatial resolution of 20 m in 224 spectral channels. Using a curve fitting algorithm to match the 224 channel spectra with Planck radiation models, Oppenheimer *et al.* (1993) attempted to derive information on the size and temperatures of the thermal anomalies within the Central Craters. As on the TMS image, the NE crater and La Voragine contained one hot spot each, and the Bocca Nuova and SE crater contained 2 each, with the most intense being in the NE crater. Although the method allowed a ~15m^2 hot spot at ~600 °C to be identified within Stromboli's crater terrace, an "unusual" spectrum for the NE crater anomaly could not be interpreted in terms of any realistic Planck model.

Rothery *et al.* (1992) and a report to the Global Volcanism Network (GVN, 1992) used a TM image acquired on 2 January 1992, just over two weeks after the beginning of the 1991 to 1993 eruption, for a qualitative interpretation of activity. The image showed lava flowing from a source in the SW back wall of the Valle del Bove for 6.5 km into the Val Calanna. Radiance for 700 m downstream in band 4 (0.76-0.90 μm) was interpreted to be from a 10-15 m wide open channel. TMS images for this flow field were acquired 3 months later during an overflight on 29 April 1992 (Abrams *et al.*, 1994). This provides 4-12 m pixel data depending on ground elevation and aircraft altitude. Abrams *et al.* (1994) fitted the image to a Digital Elevation Model (DEM) of Etna to give a 3D view showing active surface flows south of Monte Calanna fed by a complex braided tube system from

the fissure vent. Pieri *et al.* (1995) used a sequence of four TM scenes to show the progression of the lava flows across and out of the Valle del Bove during this eruption. A comparison of scenes acquired in February and May 1992 with scenes acquired in August and September 1992 showed a progression of most intense activity from the distal flow field area to the proximal area. This change corresponded with the successful upstream diversion by the Italian authorities between 27 and 29 May 1992.

A.5. Low Spatial resolution monitoring of active lava

Although the first low spatial resolution thermal image of Mount Etna was published in 1979, the first report of a thermal anomaly due to an active lava flow was not published until 1986 (Scorer, 1986). Scorer (1986) used 1 km pixel AVHRR images to show thermal anomalies caused by the December 1985 eruption. Two images acquired on 25 and 27 December 1985 showed a hot spot due to the 25 to 28 December activity. A major plume was also evident on a Coastal Zone Colour Scanner (CZCS) image, showing up brightly in the visible channel for ~100-150 km to the ESE (Scorer, 1986).

It was not until 1995 that any attempt to go further than simple visual detection of thermal anomalies in AVHRR data was made. Given the AVHRR's poor spatial resolution compared with TM and TMS this may not appear too surprising. However, AVHRR offers 3 major advantages over data of higher spatial resolution. AVHRR data are far more frequently available. AVHRR images are received at least 4 times a day, compared with once every 16 days for TM and the infrequent occasions when an airborne campaign is organised for TIMS, TMS or AVIRIS. This greatly increases the chances of coinciding with a cloud-free period. As a result, during the December 1991 to March 1993 eruption 308 cloud-free AVHRR images were available on which activity could be detected, as opposed to just 10 TM images and 1 TMS sortie. Secondly, AVHRR data are freely available at cheap to install receiving stations. A quarter TM image can cost over US$3000 and has to be recorded by a major receiving station, but degraded AVHRR data can be received by a simple antenna costing <US$1000 (Rothery *et al.*, 1995). Finally, AVHRR

data can be interpreted as they are received by the user, allowing real time monitoring and cutting out data delays. In contrast the January 1992 TM scene used by Rothery *et al.* (1992) took more than two months to arrive.

Due to these advantages a number of studies are now developing algorithms capable of locating and measuring volcanic thermal anomalies in AVHRR and similar data. Harris *et al.* (1995) used AVHRR data for Mount Etna develop and test an automated method capable of locating thermal anomalies. The algorithm was successfully tested on 90 images acquired during and since the 1991 to 1993 eruption, locating Central Crater and flank activity. Harris and Rothery (1995) analysed 308 cloud-free AVHRR images of the 1991 to 1993 eruption to produce a time series of thermal maps, lava flow area and thermal flux estimates for this eruption. As with the TM time series given by Pieri *et al.* (1995), the AVHRR thermal maps showed a transition of most intense activity from the distal to proximal areas of the flow-field following the successful diversion. Area and flux estimates use AVHRR bands 3 (3.55-3.93 μm) and 4 (10.3-11.3 μm) in the dual-band method. However the two component thermal surface assumed by the method is unreasonable for a 1 km AVHRR pixel. As a result Harris and Rothery (1995) and Harris *et al.* (in press) chose to assume three components: molten lava, chilled crust and lava-free land, to produce area and thermal flux estimates for a range of assumed lava crust temperatures. Active lava area estimates derived were in agreement with ground based estimates. Ridley and Vaughan (1995) used AVHRR data for the March 1981 and April-May 1984 eruptions to produce flow field thermal maps and area estimates based on pixel counts. Their best estimate for the 1981 eruption lava area was 3-9 km^2, compared with a ground estimate of 6 km^2.

A.6. Plume monitoring

Although plumes of gas and/or ash are frequently apparent in TM and AVHRR images of Mount Etna, such data have not yet been used for any quantitative analysis. However, Realmuto *et al.* (1994) used airborne TIMS data acquired during a July 1986

over-flight to estimate SO_2 plume concentrations. TIMS has three bands in the SO_2 absorption band (8.0-9.5 μm), as well as three bands beyond the absorption band (9.5-12.0 μm). Using radiance data from these six bands Realmuto *et al.* (1994) developed a technique capable of measuring SO_2 flux for the entire plume, estimating a flux of 6700 t d^{-1}, as well as producing SO_2 abundance profiles across the plume.

A.7. Ground deformation monitoring

With the launch of ERS-1 (European Remote Sensing Satellite-1) in July 1991, routine observations of centimetre-size changes in ground surface became possible using data from the Synthetic Aperture Radar (SAR). This was demonstrated by Massonnet *et al.* (1995) who used pairs of SAR images, along with a DEM constructed using data from the SPOT satellite, to produce interferograms apparently revealing volcano wide deformation. Twelve interferograms were used in this study, produced spanning the period 17 May 1992 and 24 October 1993. Analysis of the interferograms suggested a deflation of the volcano, with a maximum displacement of ~11 cm. By fitting their results to theoretical displacements derived from a model of pressure change in a sphere located in an elastic half space, they found the best fit was given by a sphere located 2±0.5 km east of the Central Craters at a depth of 16±3 km. Massonnet *et al.* (1995) concluded that the rate of volume change deduced from their observations (3.4×10^7 m^3 per month) was not balanced by the production of lava (1.9×10^7 m^3 per month).

A.8. The 1991 to 1993 eruption: a case study

On 14 December 1991 the most prolonged and volumetrically significant Etnean eruption for the last 300 years began (Calvari *et al.*, 1994). Here we use high and low spatial resolution satellite data acquired during this eruption to show how remotely sensed data can be used together to produce a spatially and temporally detailed chronology of an eruption.

The last pre-eruption cloud-free TM image was acquired during September 1991. Although it showed thermal anomalies due to activity at the Central Craters, no flank activity was apparent. The last pre-eruption cloud-free AVHRR image was acquired on 8 December, also showing no eruption related anomaly.

An intense thermal anomaly on an AVHRR image acquired at 14:12 (GMT) on 14 December, 12 hours after the eruption began, revealed the onset of activity. By the 15 December thermal maps derived from AVHRR data showed two anomalies, Fig. A1a. The less intense northern anomaly located inactive, cooling flows from activity in the vicinity of the SE crater during the previous day, the southern anomaly located active flows extending across the southern floor of the Valle del Bove. By 26 December the inactive flows were no longer detectable, however extension of the active flow field towards Monte Calanna was evident from the thermal map, Fig. A1b.

The first eruption TM image was acquired on 2 January 1992, the spatial detail allowed an extensive channel fed flow field to be mapped. This extended for 6.5 km down the Valle del Bove and across the Val Calanna, Fig. A2a. The next TM image acquired, during March, revealed a change to tube fed flows. The line of the main tube was identifiable from the location of sky-lights and surface break-outs, Fig. A2b. The Valle del Bove was now the site of only minor surface break-outs. Major surface activity occurred from tube fed vents between Monte Calanna and Monte Zoccolaro. The effectiveness of the earth barrier, constructed to impede the flows advance towards Zafferana Etnea, was apparent from the straight line defining the toe and from the concentration of surface activity in Val Calanna.

Tube fed surface flows in the vicinity of Monte Calanna were also shown by AVHRR thermal maps, the location of surface flows being located by the most intense radiation, Fig. A1c. The threat to Zafferana following the over-flow of the barrier in early April was indicated by the proximity of the toe pixel to Zafferana, Fig. A1c. However, by the 3 June the AVHRR thermal map had identified another change in the thermal structure. Active flows had returned to high within the SW Valle del Bove, with the toe isolated and

cooler, Fig. A1d. This was the result of the artificial diversion just 6 days earlier. The effects of the diversion were also apparent in the next available TM image, acquired during August. Although cloud-contaminated, the image located active flows within the Valle del Bove. Flows were fed by a tube marked by a line of 6 skylights. The absence of radiance in bands 5 and 7 within the Val Calanna indicated that the distal portion of the flow field was no longer active, Fig. A2c.

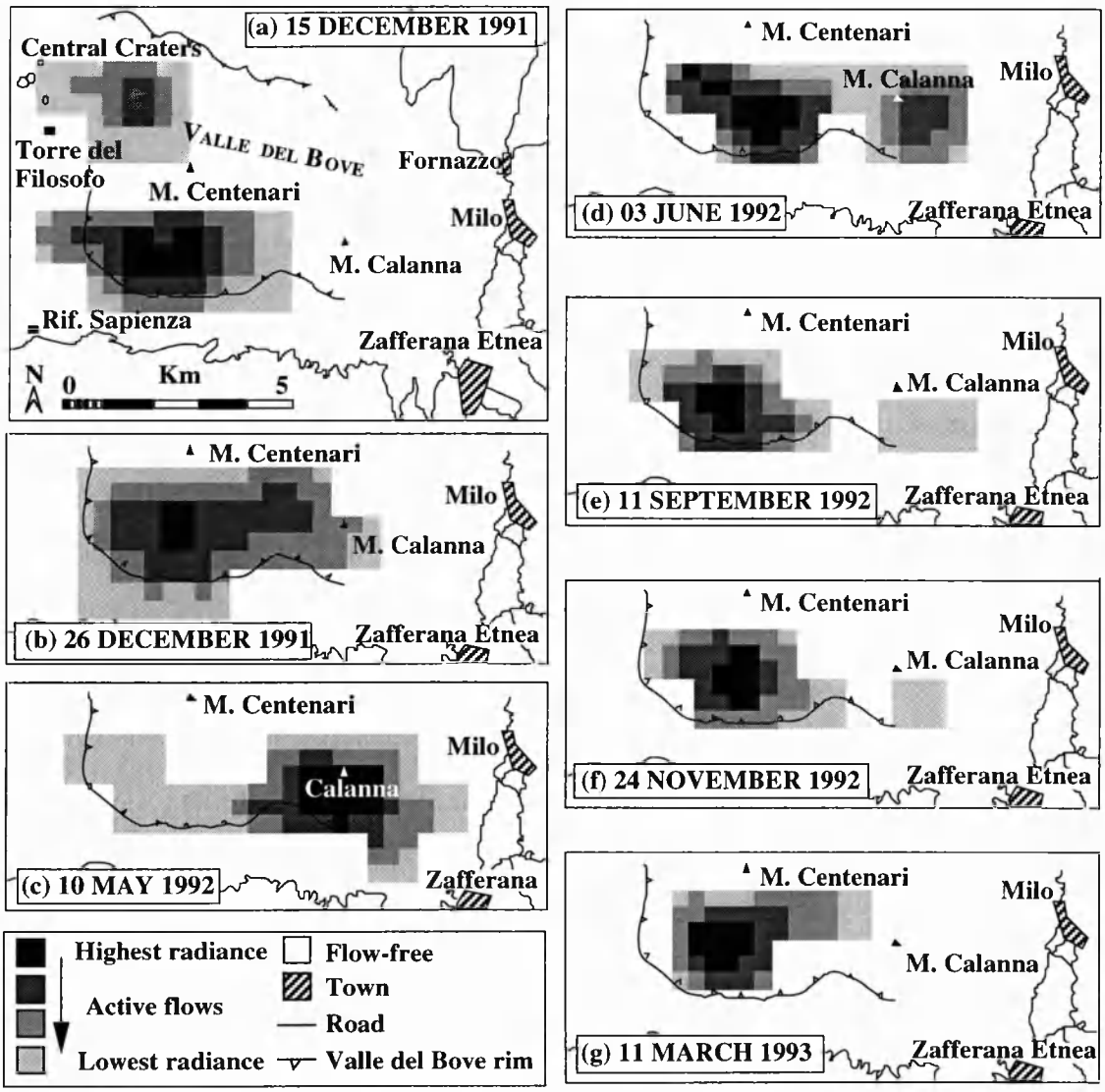

Figure A1. *Time series of thermal maps produced from AVHRR data using the method given by Harris and Rothery (1995) showing the evolution of the 1991 to 1993 flow field. The location of active surface flows are indicated by highest radiances (darkest tones).*

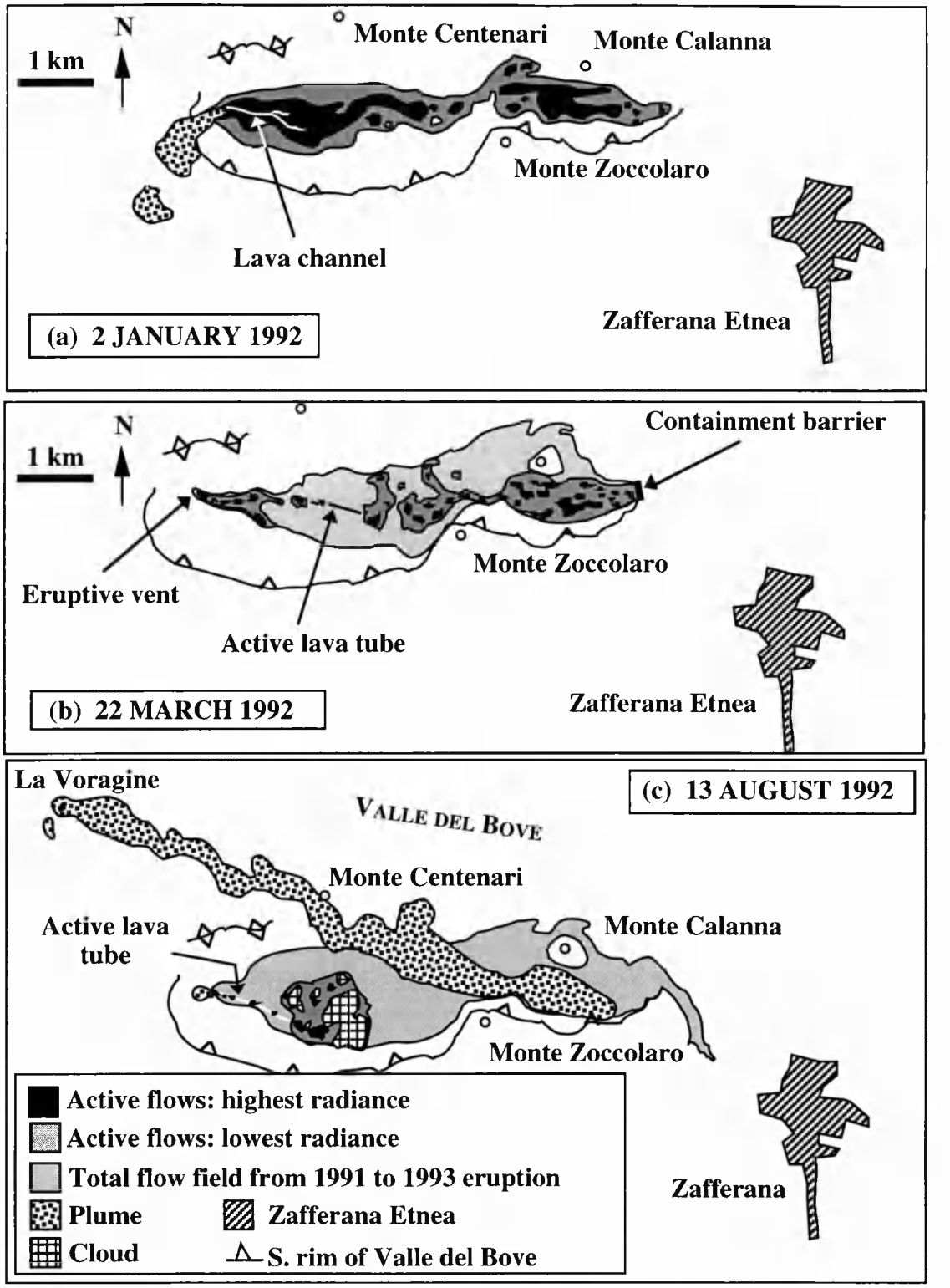

Figure A2. *Thermal maps produced from 3 TM images. Active flow areas are mapped using emitted radiation in bands 5 and 6: pixels saturated in band 5 are used to indicate highest radiance, and pixels radiant in band 7 only to indicate lowest radiance. Location of lava channels are mapped using radiance in band 4, and lava tubes using skylight lines and breakouts. Total flow field is mapped from reflected radiation in all bands.*

AVHRR images acquired during the final months of the eruption showed that active flows remained confined to the SW corner of the Valle del Bove, with the toe isolated and cooling, Figs. A1e to A1g.

Estimates for the flow field area were made using AVHRR, TM and 10 m pixel SPOT satellite data. Area estimates using the AVHRR data were made over a range of values following the method given by Harris and Rothery (1995). Using 35 cloud-free images this allowed a time series of area estimates to be produced, Fig. A3a. Estimates were in agreement with ground based estimates for total flow field area (Calvari *et al.*, 1994) during the first three months, but were lower there-after. This is a result of the AVHRR estimate being for active areas only, and the Calvari *et al.* (1994) estimate being for the total flow field, active and inactive areas. Using the 3 TM images more accurate, but less frequent, estimates were obtained for (1) the total flow field area, by counting those pixels covered by fresh lava (very dark tones in TM bands 4, 5 and 7) and (2) active flow areas, by counting radiant pixels in bands 5 and 7. Total flow field estimates are in agreement with ground based estimates, and active flow estimates fall within, and validate, the AVHRR range, Fig. 3a. An initial estimate for the final flow field area, derived using pixel counts from a SPOT image acquired 28 months after the activity ended, gives 7.0 ± 0.2 km^2. This does not include the flows erupted in the vicinity of the SE crater, and is therefore lower than the ground based estimate of ~7.6 km^2 given by Calvari *et al.* (1994) which includes these.

Following Harris and Rothery (1995) a thermal flux estimated using the AVHRR data, Fig. A3b, giving a total flux from the flow field of 1.40×10^{11} to 2.23×10^{11} MJ

Figure A3. *Time series estimates for (a) flow field area, (b) thermal flux from active flows, (c) effusion rates and (d) cumulative volume for the 1991 to 1993 eruption. In each case the range of estimates derived from AVHRR data are given by the grey area. In (a) the dashed line, black squares and white squares give ground based total flow field area, TM total flow field area and TM active flow area estimates respectively; the black diamond gives the initial SPOT final flow field area estimate. On (c) and (d) ground based estimates are given by white circles.*

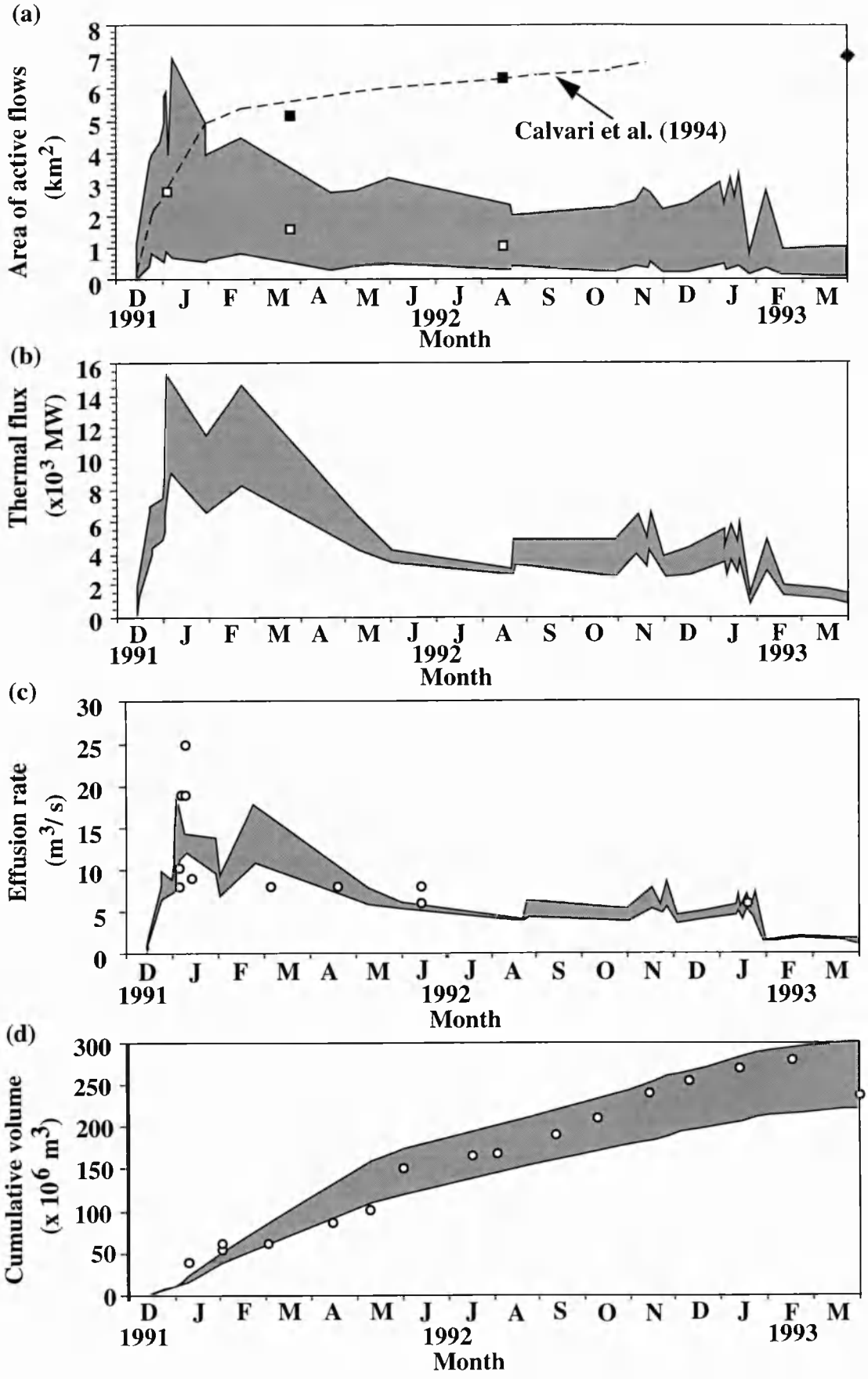
(a)
Area of active flows (km²)
Calvari et al. (1994)
D J F M A M J J A S O N D J F M
1991
1992
1993
Month
(b)
Thermal flux (x10³ MW)
D J F M A M J J A S O N D J F M
1991
1992
1993
Month
(c)
Effusion rate (m³/s)
D J F M A M J J A S O N D J F M
1991
1992
1993
Month
(d)
Cumulative volume (x 10⁶ m³)
D J F M A M J J A S O N D J F M
1991
1992
1993
Month

over 473 days. Using our AVHRR area and flux estimates in the model given by Pieri and Baloga (Equation 4b, 1986), effusion rates were estimated, Fig. A3c. These are in agreement with ground based estimates, and give an eruption rate of 5.6 to 7.6 m^3/s. By integrating our measured effusion rate over time, we also estimate cumulative lava flow volume, Fig 3d. These too are in agreement with ground based estimates, and give a total volume of 220 x 10^6 m^3 to 300 x 10^6 m^3. Taking this volume range and the SPOT derived area, we estimate an average thickness for the flow field of 31 to 44 m. A fuller report of this study is given in Harris *et al.* (in press).

A.9. Conclusions

Remote sensing offers a wide range of data of variable spatial, temporal and spectral resolutions. Together these data sets offer a means of monitoring thermal anomalies, lava flows, summit crater activity, gas flux and deformation at Etna. By using a number of complementary data sets together, an accurate spatially and temporally detailed chronology of eruption events can be produced. Future sensors will add to these capabilities.

A.10. References

Abrams, M., Buongiorno, F., Realmuto, V., and Pieri, D., 1994. Mt. Etna lava flows analyzed with remote sensing. *EOS*, 75(47), 545-551.

Archambault, C., Stoschek, J., and Tanguy, J. C., 1979. Mise en evidence de zones thermiquement anormales sur le massif de l'Etna. *Proc. 7e Reunion annuelle des sciences de la terre*, Lyon, France, 1979, 15.

Bianchi, R., Casacchia, R., Picchiotti, A., Poscolieri, M., and Salvatori, R., 1990. Airborne thermal IR survey. In Mount Etna: the 1989 eruption. F. Barberi, A. Bertagnini & P. Landi (eds.), (Italy: Giardini), pp. 69-72.

Bonneville, A., Vasseur, G, and Kerr, Y., 1985. Satellite thermal infrared observations of Mt. Etna after the 17th March 1981 eruption. *J. Volcanol. Geotherm. Res.*, 24, 293-313.

Bonneville, A., and Kerr, Y., 1987. A thermal forerunner of the 28th March 1983 Mt. Etna eruption from satellite thermal infrared data. *J. Geodynamics*, 7, 1-31.

Bonneville, A., and Gouze, P., 1992. Thermal survey of Mount Etna from space. *Geophys. Res. Lett.*, 19(7), 725-728.

Calvari, S., Coltelli, M., Neri, M., Pompilio, M., and Scribano, V., 1994. The 1991-1993 Etna eruption: chronology and lava-field evolution. *Acta Vulcanologica*, 4, 1-14.

GVN, 1992. Etna. Bulletin of the Global Volcanism Network, 17(5), 15-19.

Harris, A. J. L., and Rothery, D. A., 1995. Thermal monitoring of volcanoes using data from the AVHRR. In *Proceedings of the 21st Annual conference of the Remote Sensing Society*, 11-14 September 1995, Southampton University, pp.528-535.

Harris, A. J. L., Swabey, S. E. J., and Higgins, S. E. J., 1995. Automated thresholding of active lavas using AVHRR data. *Int. J. Remote Sensing*, 16(18), 3681-3686.

Harris, A. J. L., Blake, S., Rothery, D. A., and Stevens, N. F., in press. A chronology of the 1991 to 1993 Etna eruption using AVHRR data: implications for real time thermal volcano monitoring. Submitted to *J. Geophys. Res.*

Massonnet, D., Briole, P., and Arnaud, A., 1995. Deflation of Mount Etna monitored by spaceborne radar interferometry. *Nature*, 372, 567-570.

Oppenheimer, C., 1993. Thermal distributions of hot volcanic surfaces constrained using three infrared bands of remote sensing data. *Geophys. Res. Lett.*, 20(6), 431-434.

Oppenheimer, C., Rothery, D. A., Pieri, D. C., Abrams, M. J., and Carrere, V., 1993. Analysis of Airborne Visible/Infrared Imaging Spectrometer (AVIRIS) data of volcanic hot spots. *Int. J. Remote Sensing*, 14(16), 2919-2934.

Pieri, D. C., and Baloga, S. M., 1986. Eruption rate, area, and length relationships for some Hawaiian lava flows, *J. Volcanol. & Geotherm Res.*, 30, 29-45.

Pieri, D. C., Glaze, L. S., and Abrams, M. J., 1990. Thermal radiance observations of an active lava flow during the June 1984 eruption of Mount Etna. *Geology*, 18, 1018-1022.

Pieri, D. C., Crisp, J., and Kahle, A. B., 1995. Observing volcanism and other transient events with ASTER. *J. Remote Sens. Soc. Japan*, 15(2), 56-61.

SEAN, 1989. Etna. In *Global volcanism 1975-1985* , McClelland, L., Simkin, T., Summers, M., Nielsen, E., and Stein , T. C., (eds.), (New Jersey: Prentice-Hall), pp.57-58.

Realmuto, V. J., Abrams, M. J., Buongiorno, M. F., and Pieri, D. C., 1994. The use of multispectral thermal infrared image data to estimate the sulfur dioxide flux from volcanoes: a case study from Mount Etna, Sicily, July 29, 1986. *J. Geophys. Res.*, 99(B1), 481-488.

Ridley, I. K., and Vaughan, R. A., 1995. Use of AVHRR to detect and monitor volcanic eruptions of Mount Etna in 1981 and 1984. In *Proceedings of the 21st Annual conference of the Remote Sensing Society*, 11-14 September 1995, Southampton University, pp.536-543.

Rothery, D. A., Francis, P. W., and Wood, C. A., 1988. Volcano monitoring using short wavelength infrared data from satellites. *J. Geophys. Res.*, 93(B7), 7993-8008.

Rothery, D. A., Borgia, A., Carlton, R. W., and Oppenheimer, C., 1992. The 1992 Etna lava flow imaged by Landsat TM. *Int. J. Remote Sensing*, 13(15), 2759-2763.

Rothery, D. A., Oppenheimer, C., and Bonneville, A., 1995. Infrared thermal monitoring. In *Monitoring active volcanoes*, B. McGuire, C. R. J. Kilburn & J. Murray (eds.), (London: UCL Press), pp. 184-216.

Scorer, R. S., 1986. Etna: the eruption of Christmas 1985 as seen by meteorological satellite. *Weather*, 41(12), 378-384.

Tabbagh, A., Tabbagh, J., and Dechambenoy, 1987. Mapping of the surface temperature of Mount Etna and Vulcano island using an airborne scanner radiometer. *J. Volcanol. Geotherm. Res.*, 34, 79-88.

Appendix B. VAST: a program to automatically locate and analyse volcanic thermal anomalies in remotely sensed data

---

Jez Higgins and Andy Harris

Paper submitted to Computers and Geoscience, 1996.

B.1. Abstract

VAST is a program to calibrate thermal data for active volcanoes from the Advanced Very High Resolution Radiometer (AVHRR), locate thermally anomalous pixels containing active volcanic features, and produce output capable of monitoring activity at the target volcano. Testing the software on sub-images of active volcanic features at Mount Etna Volcano, Sicily, showed that VAST was capable of rapidly providing reliable data for lava flow location, dimensions and thermal flux. Installation of similar software at cheap direct read-out stations may allow near-real-time thermal monitoring of many of the world's otherwise unmonitored volcanoes.

B.2. Introduction

On 10 January 1977, a draining lava lake at Nyiragongo (eastern Zaire) fed lava flows which swept down the volcano at speeds of up to 60 km/hr leaving around 70

people dead, 800 homeless and 1200 hectares of agricultural land destroyed (SEAN, 1989). Between this event and 1994 at least 1935 deaths and 61465 evacuations have resulted from lava and pyroclastic flows alone (Simkin & Siebert, 1994). Such high temperature volcanic features are easy to detect using Advanced Very High Resolution Radiometer (AVHRR) channel 3 (3.55 to 3.93 μm) images (Rothery *et al.*, 1995). This is a scanning radiometer flown on-board the National Oceanographic and Atmospheric Administration (NOAA) series of polar orbiting satellites. Since AVHRR images are available for any cloud-free sub-aerial volcano at least 4 times a day, can be received free of charge in near-real-time at direct receiving stations, and are available in two other thermal channels, channels 4 (10.3 to 11.3 μm) and 5 (11.5 to 12.5 μm), the data are of great potential for monitoring volcanic thermal phenomena (Harris *et al.*, 1995b). This has been demonstrated at the Alaskan Volcano Observatory where images covering more than 50 active Alaskan, Aleutian and Kamchatkan volcanoes are checked twice a day for thermal anomalies or ash plumes (Chris Wyatt, personal communication). If reliable detection and monitoring in near-real-time can be achieved, then satellite data could serve a role in hazard monitoring at otherwise unmonitored volcanoes. At well monitored volcanoes, satellite monitoring has the benefit of providing regular, synoptic, monitoring from a safe distance even in times of crisis, using equipment that will not be destroyed by the activity being observed.

If near-real-time volcano monitoring is to be achieved using satellite data, images must be routinely received and analysed rapidly. The most time and labour-efficient way to do this is by automating the three main steps in the satellite volcano monitoring process: calibration, detection and analysis. To this end we have developed VAST (Volcanic Anomaly SofTware), an ANSI C program which, after calibrating the data, automatically detects and analyses hot-spots in AVHRR images. This has been tested as a stand-alone package using 13 AVHRR images acquired during the December 1991 to March 1993 eruption at Etna (Sicily).

B.3. The program

A simplified flow diagram summarising the program is given in Figure B1. There are a number of parameters required for the analysis, listed in Table B1, and the function GetSetup reads these from a configuration file specified on the command line. The user is prompted for the values of any parameters still unspecified once the configuration file has been parsed.

Two data sets are used in the analysis, the raw channel 3 and 4 digital number (DN) images. Since the location of most sub-aerial volcanoes are known (Simkin & Siebert, 1994), to minimise processing time we extract ~30 x 30 DN pixel sub-images covering the volcano only from the full 2048 x 2048 pixel image. The files containing the sub-images can be specified on the command line, or alternatively multiple pairs of sub-images can be specified in a list file, which is also parsed by GetSetup. This allows many images with the same parameters to be processed in one batch.

VAST notation	Description
V3, V4	Channel 3 and 4 central wavenumbers (cm^{-1})
DN3, DN4	Channel 3 and 4 DN (DN_i, i=3,4)
DN3Slope, DN4Slope	Channel 3 and 4 slope (S_i, i=3,4)
DN3Intercept, DN4Intercept	Channel 3 and 4 intercept (I_i, i=3,4)
DN3MinSat	Minimum channel 3 saturation DN (DN=0)
DN3Max	Maximum channel 3 saturation DN (Defined in Chapter 2)
MaskSize	Size of mask to be searched for hot pixels
MaskHow	Method of centring mask (i.e. on saturated pixels, maximum T_3 or maximum ΔT)
AreaOfPixel	Pixel area (m^2)
BroadBandEmissivity	Emissivity integrated over all wavelengths (ε)
Emissivity3, Emissivity4	Emissivity in channels 3 and 4 (ε_3 and ε_4)
Tau3, Tau4	Transmissivity in channels 3 and 4 (τ_3 and τ_4)
CrustedLavaTemp	Temperature of crusted lava (T_c, °C)
MoltenLavaTemp	Temperature of molten lava (T_h, °C)
MinThermalFeatureTemp	Lower limit to crusted lava temperature range
MaxThermalFeatureTemp	Upper limit to crusted lava temperature range

Table B1: *Input parameters into VAST.*

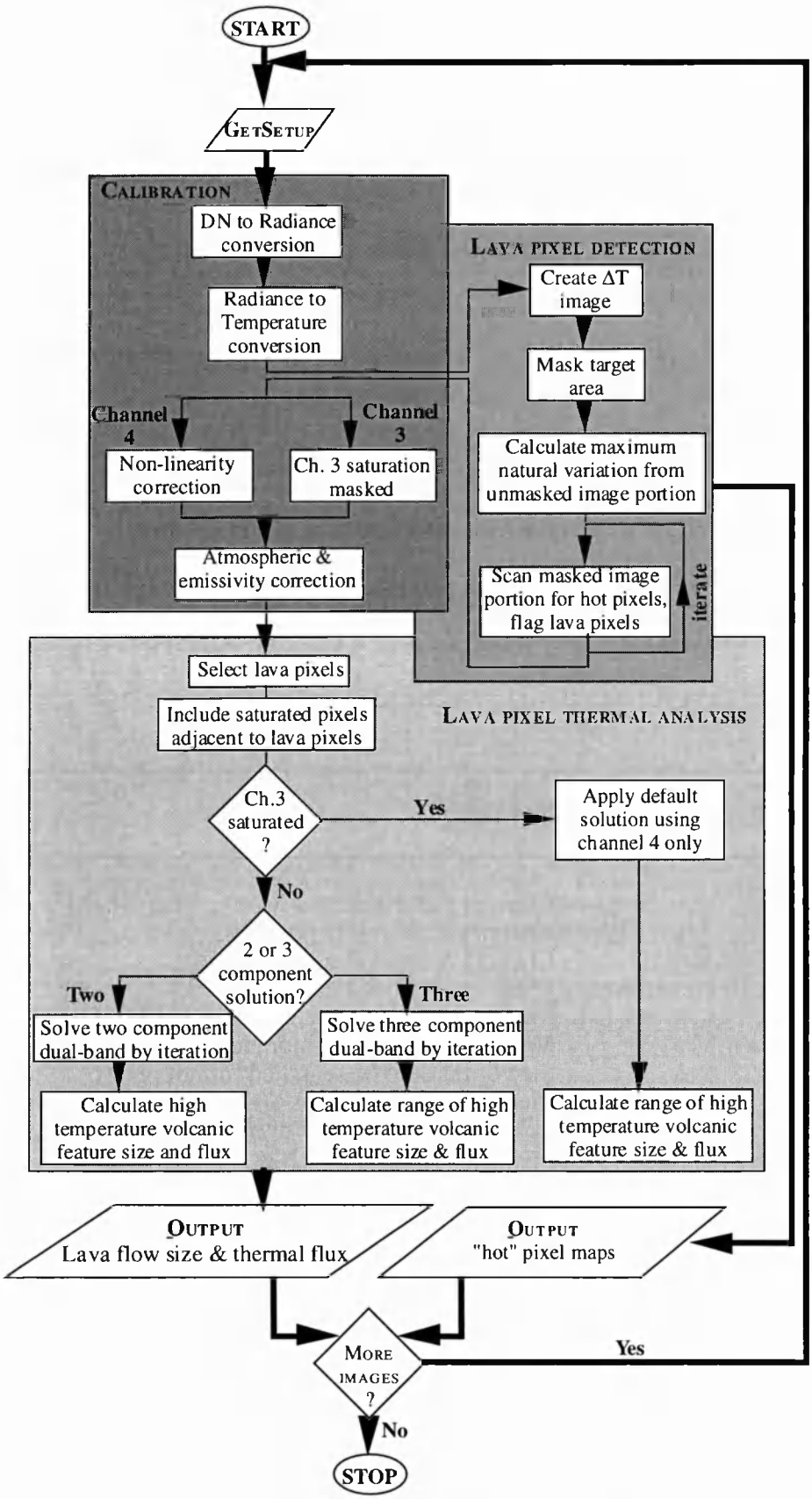

Figure B1. *Simplified flow diagram of VAST*

B.3.1. Calibration

In the AVHRR thermal channels radiance emitted from the Earth's surface is detected at the sensor and converted to a DN by an analogue to digital converter. DN is related to radiance in the linear relationship,

$$R_i = S_i\, DN_i + I_i \qquad \text{(B1)},$$

where R_i, S_i and I_i are radiance, slope and intercept in channel i. The conversion is carried out by the DNToRad subroutine. Slope and intercept are input parameters, and can be calculated using the procedure given by Lauritson *et al.* (1988). Conversion from radiance (in units of mW/m^2 sr cm^{-1}) to brightness temperature (in K) in channel i (T_i) is then achieved by inverting Planck's radiation equation:

$$R_i = c_1\, \upsilon^3 / [\exp(c_2\, \upsilon / T_i) - 1] \qquad \text{(B2)},$$

to give

$$T_i = \frac{c_2 \upsilon}{\ln\left(1 + \frac{c_1 \upsilon^3}{R_i}\right)} \qquad \text{(B3)},$$

in which c_1 and c_2 are universal constants (1.1910659×10^{-5} mW/m^2 sr cm^{-4} and 1.438833 cm K respectively) and υ is the central wavenumber (in cm^{-1}) of the channel filter. The central wavenumbers for the AVHRR thermal channels vary from instrument to instrument and are given by Kidwell (1995) and Wooster *et al.* (1995). Planck's equation is defined in the subroutine TempToRad, and the inverse in RadToTemp.

Since the response of channel 4 is not linear, to give the true channel 4 brightness temperature (T_4) a non-linearity correction must be applied. Therefore VAST applies the non-linearity corrections given by Weinreb *et al.* (1990) and Kidwell (1995), whereby a non-linearity correction is added to T_4, depending on the AVHRR internal blackbody calibration target temperature and T_4.

At the same time, VAST checks channel 3 pixels for saturation, this being a cut-off in the analogue to DN conversion which occurs at the maximum recordable signal. This occurs at a DN of zero, equivalent to a channel 3 brightness temperature (T_3) of ~50 °C. However, due to the design of the analogue-to-digital converter, it is impossible to define a single saturation DN, instead saturation occurs over a range of DN which varies from instrument to instrument (Harris *et al.*, 1995a; Setzer & Verstraete, 1995). VAST therefore locates and masks saturated pixels by comparing each pixel DN with the saturation DN range given by Harris *et al.* (1995a): pixels within this range are masked.

Finally, VAST applies an atmospheric and emissivity correction to pixel radiances using

$$RC_i = R_i / \varepsilon_i \tau_i \qquad \text{(B4)},$$

in which RC_i is the corrected radiance, ε_i is emissivity of the surface in channel i and τ_i is atmospheric transmissivity in channel i. Emissivities for a variety of surfaces, including typical volcanic surfaces, can be obtained from Salisbury and D'Aria (1994), and transmissivities can be obtained using the LOWTRAN 7 atmospheric model (Kneizys *et al.*, 1988).

B.3.2. Lava pixel detection

To locate thermal anomalies automatically in the AVHRR data a contextual approach is applied, which compares a pixel with its neighbours and a threshold calculated from within the image, to define whether or not a pixel is "hot".

The hot pixel detection technique uses the difference between brightness temperature in channel 3 (T_3) and in channel 4 (T_4), defined as ΔT (= T_3 - T_4). Although channels 3 and 4 are equally sensitive to solar heated surfaces, channel 3 is more sensitive to high temperature (>500 °C) surfaces (Kennedy *et al.*, 1994). Therefore, ΔT allows pixels that are hot due to solar heating, and those that are hot due to their containing a high

temperature volcanic feature, to be distinguished. For pixels containing high temperature volcanic features, ΔT will be greater than for those containing solar-heated surfaces.

To identify hot pixels within volcanic areas of the image, the variation in ΔT between a pixel and its background is calculated using the mean ΔT of the 8 pixels (excluding saturated pixels) surrounding the target pixel. This variation is then compared with the maximum natural variation for the image. The maximum natural variation is defined as the greatest variation between a pixel and its background among those pixels beyond the volcanic area. Pixels within the volcanic area with a difference in ΔT greater than the maximum natural variation area flagged as "hot" and are assumed to contain a high temperature volcanic feature.

VAST breaks this technique down into a 4 step process. In step 1, the ΔT image is created, i.e. the ΔT for each pixel is calculated. Step 2 defines the volcanic area by locating the hottest pixels and placing a mask around them. The user defines the mask size and is given the option to place the mask around either saturated pixels, pixels with the highest T_3 or pixels with the greatest ΔT. The mask is placed using the MaskIt function. Step 3 calls the NatVariation function for each pixel in the unmasked area of the image. The maximum value encountered is stored. Finally step 4 searches the masked area searching for "hot" pixels. NatVariation is called for each pixel in the masked area to calulate the difference between a pixel's ΔT and the mean ΔT of its surrounding pixels. If this is greater than the stored maximum variation, the pixel is flagged as being "hot". However, pixels which have an elevated ΔT, but which also have neighbouring "hot" pixels may not be detected, due to the influence of the high ΔT values in their background. To detect all "hot" pixels, step 4 is iterated, with pixels flagged as "hot" in previous passes being excluded from background ΔT calculations until no further pixels are flagged as "hot". Outputs are the number of iterations and pixel maps showing pixels flagged as "hot" after (1) the first iteration and (") all iterations (Figure B2).

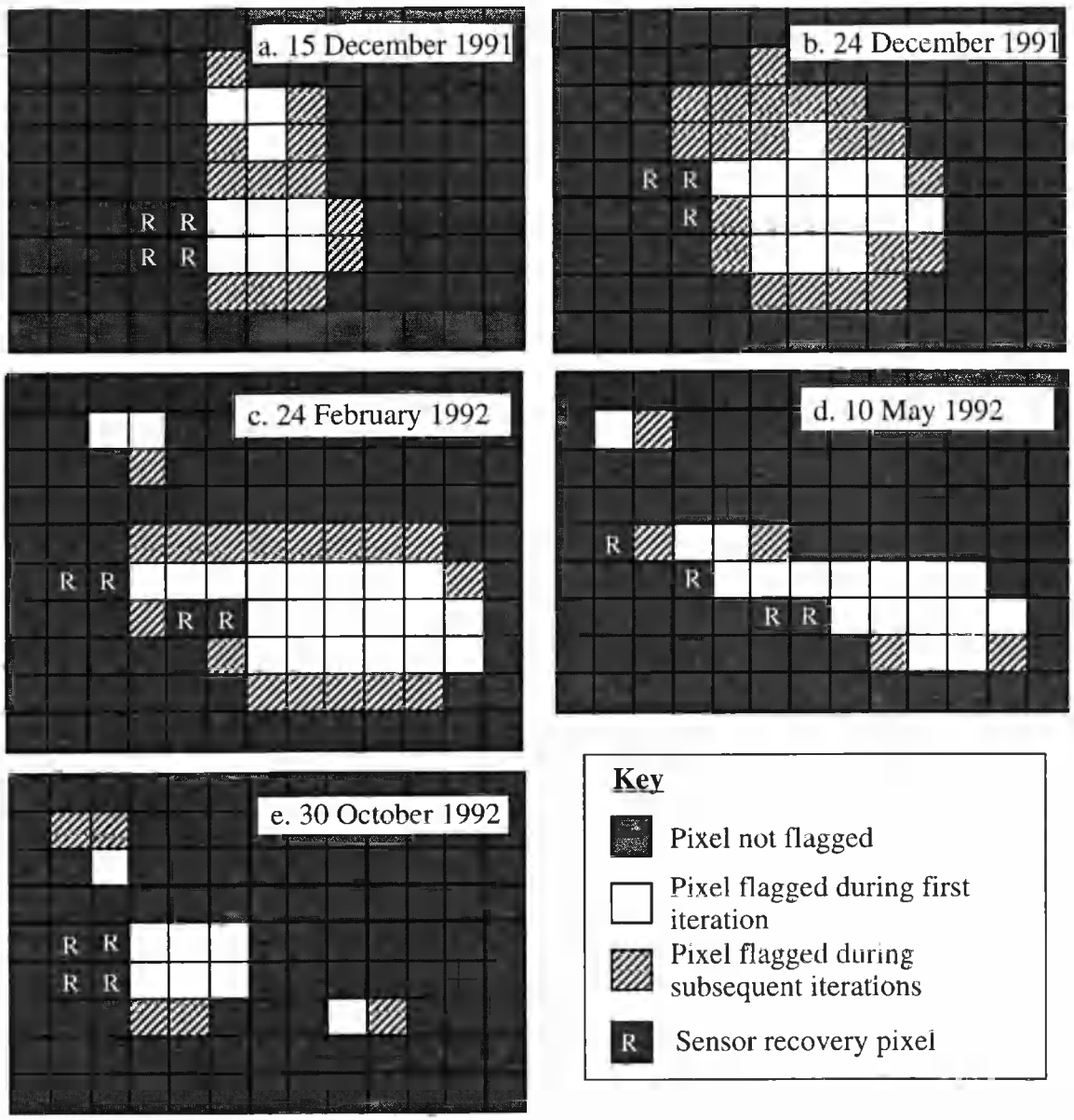

Figure B2. *"Hot pixels" flagged by VAST during the first and all iterations of the hot pixel detection algorithm. (See Chapter 3 for definition of sensor recovery).*

B.3.3. Hot pixel thermal analysis

Thermal analysis is carried out for each "hot" pixel located to give an estimate for the size of, and thermal flux from, the thermal feature contained within the pixel. The analysis uses the dual-band method, originally proposed by Dozier (1981), as a starting point. This method assumes that a pixel is occupied by two temperature components, a low temperature component at temperature T_b occupying portion p of the pixel, and a high

temperature component at T_h occupying the remaining portion, p_h (= 1 - p), of the pixel. For a 1 km AVHRR pixel over a volcano we assume that this thermal structure relates to a high temperature volcanic feature surrounded by a cooler background at ambient temperatures. If thermal measurements are available in two widely separated wavebands, as with AVHRR channels 3 and 4, and any one of T_h, T_b or p is known, then the method allows the two remaining unknowns to be calculated by solving the following simultaneous equations:

$$RC_3 = p\, L_3(T_b) + (1\text{-}p)\, L_3(T_h) \qquad \text{(B5)},$$

$$RC_4 = p\, L_4(T_b) + (1\text{-}p)\, L_4(T_h) \qquad \text{(B6)},$$

in which RC_3 and RC_4 are the corrected channel 3 and 4 radiances and $L_3(T)$ and $L_4(T)$ are the Planck function radiances for a blackbody at temperature T at the channel 3 and 4 central wavelengths. To solve Equations B5 and B6 VAST estimates T_b using the mean channel 4 brightness temperature of the nearest lava-free pixels in any direction. This is calculated within the ApplyTwoComponent function. However, the equations will be unsolvable if $L_4(T_b) > RC_4$. Therefore a trap is included whereby T_b is set equal to the minimum channel 4 brightness temperature from the nearest lava-free pixels in such cases. If $L_4(T_b)$ is still greater than RC_4 then no solution is possible and VAST will display a "Cannot solve" message. Otherwise ApplyTwoComponent continues to solve Equations B5 and B6 by iteration. Once solved, the calculated parameters (p and T_h) are used to estimate the ground area occupied by, and thermal flux from, the high temperature component. The ground area occupied by the high temperature component (A_h) is estimated by multiplying p_h by the pixel area. Pixel area is an input parameter and can be calculated using the methodology set out in Cahoon *et al.* (1992). Thermal flux from the high temperature component (Q_h) is estimated from

$$Q_h = \varepsilon \sigma (T_h^4 A_h) \quad \text{(B7)},$$

where ε is the emissivity of the surface integrated over all wavelengths and σ is the Stefan-Boltzmann constant. Emissivity is an input parameter, and can be obtained for a variety of surfaces, including typical volcanic surfaces, from Salisbury and D'Aria (1992). All calculated values (T_b, T_h, p, p_h, A_h and Q_h) are output.

The two component pixel model is only applicable where the high temperature component has a uniform surface temperature. This will apply to a pixel occupied by active volcanic features where the surface is broadly isothermal, such as a hot mud or ash flow or a high temperature degassing vent. However, many volcanic features do not have isothermal surfaces, as is the case for an active lava body, such as a lava dome, lake or flow. The surface of these features is commonly composed of at least two thermal components: a chilled crust at temperature T_c broken by areas where the molten core at T_h is exposed (Crisp & Baloga, 1990). In this case the thermal structure of a 1 km pixel is more accurately described by a three component model with a cool lava-free background at T_b occupying portion p of the pixel, surrounding an area of crusted lava at T_c occupying p_c of the pixel and an area of molten lava at T_h occupying the remainder of the pixel [$p_h = (1 - p - p_c)$]. The user is therefore given the option to apply a three component solution if this is more reasonable. In such a case, Equations B5 and B6 are modified in the ApplyThreeComponent function to include the third thermal component:

$$RC_3 = p\, L_3(T_b) + p_c\, L_3(T_c) + (1-p-p_c)\, L_3(T_h) \quad \text{(B8)},$$

$$RC_4 = p\, L_4(T_b) + p_c\, L_4(T_c) + (1-p-p_c)\, L_4(T_h) \quad \text{(B9)},$$

ApplyThreeComponent estimates T_b as in the two component case and prompts the user to input T_h, which can be approximated using field measurements for the incandescent

portions of the flow (Oppenheimer, 1991). However, crustal temperatures will vary between a few degrees above ambient background temperatures to a few degrees below molten temperatures. As a result the ApplyThreeComponent subroutine solves Equations B8 and B9 by iteration for a range of crustal temperatures, between a reasonable minimum crust temperature input by the user and a maximum crust temperature defined by the highest crust temperature for which Equations B8 and B9 are still solvable. Typical crust temperatures for lava flows and lakes in Hawaii have been calculated from multiple component modelling of spectrometer data by Flynn & Mouginis-Mark (1992) and Flynn *et al.* (1993). The results of ranging Equations B8 and B9 between the two bounds will give the upper and lower limits for a range of solutions within which the true solution is assumed to lie.

In the three component case the ground area and flux calculations for the high temperature volcanic feature must be modified to take into account the two component temperature structure of its surface. The ground area occupied by the high temperature volcanic feature (A_{lava}) will now be estimated by multiplying the sum of p_h plus p_c by the pixel area. Thermal flux (Q_{lava}) is estimated from

$$Q_{lava} = \varepsilon \sigma [(T_h^4 A_h) + (T_c^4 A_c)] \qquad (B10),$$

in which A_h and A_c are the ground areas occupied by the molten and crust components respectively.

Two lines of output are displayed on screen. The first line gives the maximum crust temperature calculated, with all parameters estimated using this value (p, p_c, p_h, A_{lava} and Q_{lava}). The second line gives the same output but with the minimum crust temperature used and the parameters estimated using this. These two lines define the upper and lower limits of a range for each parameter, within which the true value will lie.

In cases where channel 3 is saturated it will not be possible to use the channel 3 radiance. In this case a default solution is applied using the channel 4 radiance only. Two

component lava flow models and analysis of Landsat Thematic Mapper data for lava flows and domes have shown that the exposed molten core occupies between 0.0001 and 0.1 of the flow surface (Crisp & Baloga, 1990; Pieri *et al.*, 1990; Oppenheimer 1991; Oppenheimer *et al.*, 1993). Therefore, since the fraction of the pixel occupied by the molten component at temperature T_h is small, and the sensitivity of channel 4 to this component is low, the contribution of this component to the channel 4 radiance is assumed to be negligible. This allows the pixel portion occupied by the crusted component (p_c) to be estimated from

$$p_c = [RC_4 - L_4(T_b)] / [L_4(T_c) - L_4(T_b)] \qquad \text{(B11)},$$

To solve Equation B11 a reasonable lower and upper limits for the crust temperature must be supplied by the user to give a range of solutions within which the true solution will lie. Multiplying p_c by the pixel area will give the area occupied by the crusted component (A_c). Thermal flux is calculated by substituting T_c and p_c into Equation B7. For such pixels VAST will give a saturated pixel warning along with two lines of output, one for parameters calculated using the minimum crust temperature (p, p_c, A_c and Q_c), and one for those calculated using the maximum crust temperature. The true value for each parameter will lie between these upper and lower limits.

B.4. Results

The program has been tested using 13 cloud-free AVHRR images acquired during the 15 December 1991 to 29 March 1993 eruption at Mount Etna, Sicily. This eruption built a lava flow field of 7.6km^2 on the eastern flank of the volcano and fed flows which extended to within 850 m of Zafferana Etnea, a village of 7000 inhabitants (Barberi *et al.*, 1993; Calvari *et al.*, 1994). For each image a 30 x 30 pixel sub-image centred on Mount Etna (37.73°N, 15.00°E) was extracted and input into VAST.

The hot pixel detection algorithm successfully located the volcanic thermal anomalies associated with the active lava flow field and summit craters, and distinguished these from solar heated anomalies on all 13 sub-images (Figure B2). The main flow field was located as a major thermal anomaly on the east flank of the volcano, and the active summit vents were located as smaller, 2 to 3 pixel, anomalies to the NW of the flow field. The size and structure of the flow field anomalies located by the first iteration of the detection algorithm agreed with those expected from ground observations. On the 15 December 1991 image, Figure B2a, lava pixels flagged during the first iteration show two anomalies. The northern anomaly is due to flows which extended eastwards for about 500 m from fissures in the vicinity of the summit craters on 14 December (Calvari *et al.*, 1994). The southern anomaly is the main flow which reached 2 km from the eruptive fissure during 15 December (Calvari *et al.*, 1994). By 24 December extension of the flow, observed to have reached 4.5 km from the eruptive fissure on 23 December (GVN, 1991), is apparent from the increased anomaly dimensions identified by the first iteration (Figure B2b). Between January and May 1992 the upper portions of the flow tubed over to feed surface flows at lower elevations on the volcano (Calvari *et al.*, 1994). This is evident from the first iteration lava area on Figures B2c and B2d, where a one pixel wide tubed section feeds a 1 to 3 pixel wide surface flow section. On both of these images the entire flow field anomaly is 9 pixels east to west, corresponding with ground reports which observed the flow front at 7.5 km from the eruptive fissure during April 1992 (GVN, 1992a). All anomalies located after June 1992 show the same structure: a main anomaly separated by 1 to 2 pixels from a smaller anomaly to the NW. This is a result of the successful diversion attempt that was carried out between 27 and 29 May 1992, which returned the active flow front to within 1 km of the eruptive fissure (Barberi *et al.*, 1993; GVN, 1992b). Subsequently, flows extended for no more than 1.5 km until the final day of the eruption on 29 March 1993 (Calvari *et al.*, 1993). This left the toe of the flow, starved of supply, isolated and cooling (Figure B2e).

Although the dimensions of the flow field indicated by the first iteration were in close agreement with those expected from ground reports, the inclusion of lava pixels located by all iterations gave far too large an area (Figure B2). This is a result of the inclusion of point spread function pixels around the flow field by subsequent iterations. These pixels do not contain active lava, but are anomalous due to radiance being spread into them from adjacent lava pixels. Inclusion of such pixels would give lava flow field dimension, area and flux estimates that were too large. We therefore only considered the first iteration pixels in the thermal analysis.

For each image, the lava area and thermal flux was summed for each pixel located by the first iteration of the lava detection algorithm. The results were used to produce a time series plot for the lava area and thermal flux during the eruption (Figure B3). Both plots are in close agreement with ground observations, showing a rapid increase in flow area and flux during December 1991 and January 1992, falling away to a lower and steady level which lasted from July 1992 until the end of the eruption. Observations of flow lengths and effusion rates during the same period show longest flows and highest effusion rates between December 1991 and May 1992. During this period flows reached up to 7.5 km from the active vent (GVN, 1992a) and effusion rates were 30 m^3/s (Barberi & Villari, 1994). However, following the lava diversion at the end of May 1992 flow lengths did not exceed 1.5 km (Calvari *et al.*, 1994) and effusion rates halved to 15 m^3/s (Barberi & Villari, 1994).

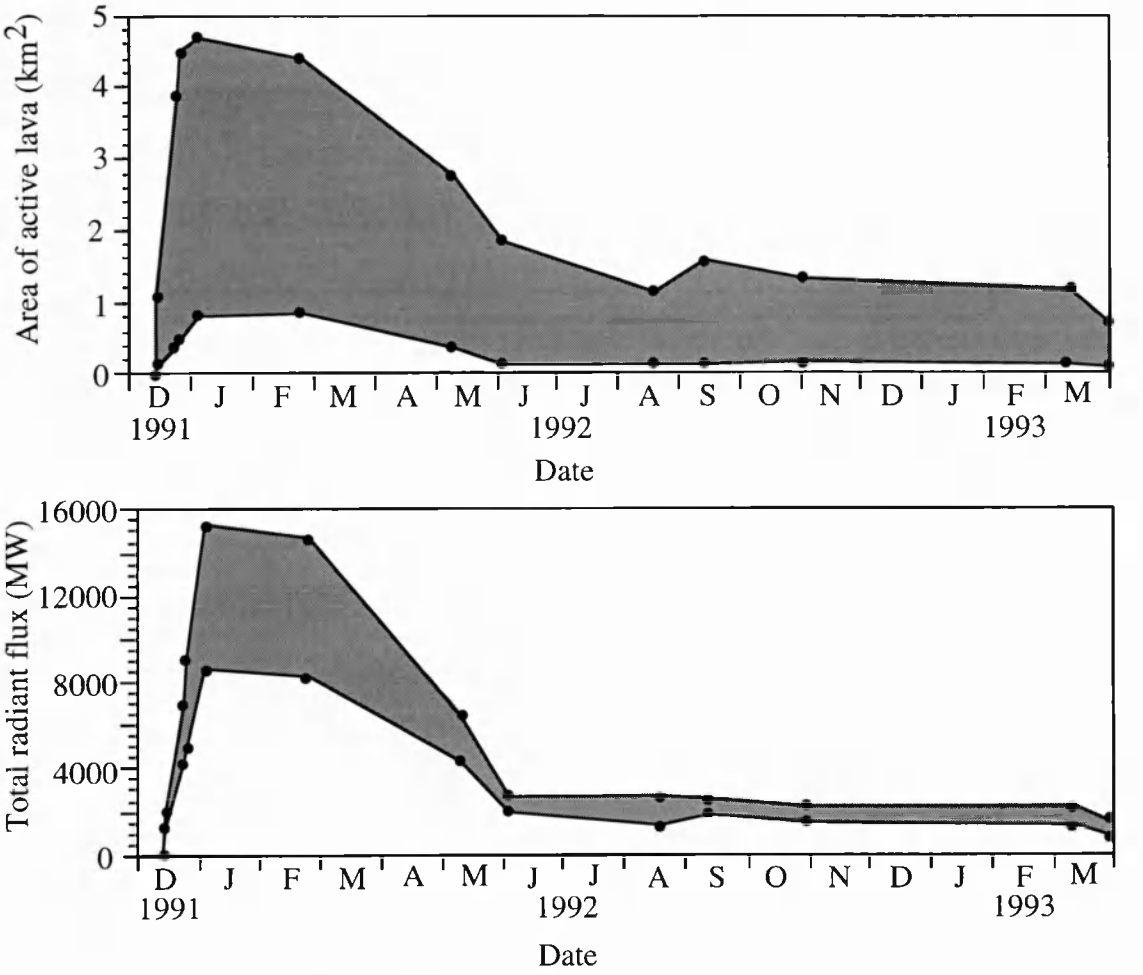

Figure B3. *Lava area and thermal flux variations during the 1991 to 1993 Etna eruptions, produced using the lava area and thermal flux output given by VAST for 13 AVHRR images acquired during the eruption.*

B.5. Conclusion

For the 30 x 30 pixel sub-images tested, VAST was able to locate active lava flows and vents in less than a second, and apply a thermal analysis to the lava pixels located in less than 10 seconds. Both analyses produced results which were in close agreement with ground observations. If volcano sub-images can be located, extracted and cloud-screened just as rapidly, there is no reason why software such as VAST should not be capable analysing images as they are received, and provide the operator with reliable information about activity at the target volcano within seconds of image acquisition.

B.6. References

Dozier, J., 1981, A method for satellite identification of surface temperature fields of subpixel resolution: Remote Sensing of Environment, v. 11, p. 221-229.

Calvari, S., Coltelli, M., Neri, M., Pompilio, M., and Scribano, V., 1994, The 1991-1993 Etna eruption: chronology and lava flow-field evolution: Acta Vulcanologica, v. 4, p. 1-14.

Barberi, F., Carapezza, M. L., Valenza, M., and Villari, L., 1993, The control of lava flow during the 1991 - 1992 eruption of Mt. Etna: J. Volcanol. & Geotherm. Res., v.56, p. 1-34.

Barberi, F., and Villari, L., 1994, Volcano monitoring and civil protection problems during the 1991 - 1993 Etna eruption: Acta Vulcanologica, v. 4, p. 157-165.

Crisp, J., and Baloga, S., 1990, A model for lava flows with two thermal components: J. Geophys. Res., v. 95, no. B2, p. 1255-1270.

Flynn, L. P., and Mouginis-Mark, P. J., 1992, Cooling rate of an active Hawaiian lava flow from nighttime spectroradiometer measurements: Geophys. Res. Lett., v. 19, no. 17, p. 1783-1786.

Flynn, L. P., Mouginis-Mark, P. J., Gradie, J. C., and Lucey, P. G., 1993, Radiative temperature measurements at Kupaianaha Lava Lake, Kilauea volcano, Hawaii: J. Geophys. Res., v. 98, n. B4, p. 6461-6476.

GVN, 1991, Etna: Bulletin of the Global Volcanism Network, v. 16, no. 12, p. 2-3.

GVN, 1992a, Etna: Bulletin of the Global Volcanism Network, v. 17, no. 3, p. 6.

GVN, 1992b, Etna: Bulletin of the Global Volcanism Network, v. 17, no. 5,p. 15-19.

Harris, A. J. L., Rothery, D. A., Carlton, R. W., Langaas, S., and Mannstein, H., 1995a, Non-zero saturation of AVHRR thermal channels over high temperature targets: evidence from volcano data and a possible explanation: Int. J. Remote Sensing, v. 16, no., 1, p. 189-196.

Harris, A. J. L., Vaughan, R. A., and Rothery, D. A., 1995b, Volcano detection and monitoring using AVHRR data: the Krafla eruption, 1984: Int. J. Remote Sensing, v. 16, no. 6, p. 1001-1020.

Kennedy, P. J., Belward, A. S., and Gregoire, J.-M., 1994, An improved approach to fire monitoring in West Africa using AVHRR data: Int. J. Remote Sensing, v. 15, no. 11, p. 2235-2255.

Kidwell, K. B., 1995, NOAA polar orbiter data users guide: NOAA/NESDIS, Washington D.C.

Kneizys, F. X., Shettle, E. P., Abreu, L. W., Chetwynd, J. H., Anderson, G. P., Gallery, W. O., Selby, J. E. A., and Clough, S. A., 1988, Users' guide to Lowtran 7: Air Force Geophysics Laboratory Environmental Research Paper 1010, Hanscom AFB, Massachusetts, 137 pp.

Oppenheimer, C., 1991, Lava flow cooling estimated from Landsat Thematic Mapper Infrared Data: the Lonquimay Eruption (Chile, 1989): J. Geophys. Res., v. 96, no. B13, p. 12865-21878.

Oppenheimer, C., Francis, P. W., Rothery, D. A., Carlton, R. W., and Glaze, L. S., 1993, Infrared image analysis of volcanic thermal features: Lascar Volcano, Chile, 1984 - 1992: J. Geophys. Res., v. 98, no. B3, p. 4269-4286.

Pieri, D. C., Glaze, L. S., and Abrams, M. J., 1990, Thermal radiance observations of an active lava flow during the June 1984 eruption of Mount Etna: Geology, v. 18, p. 1018-1022.

Rothery, D. A., Oppenheimer, C., and Bonneville, A., 1995, Infrared thermal monitoring: Monitoring active volcanoes, McGuire, B., Kilburn, C., & Murray, J. (eds.), UCL Press, London, p.184-216.

Salisbury, J. W., and D'Aria, D. M., 1994, Emissivity of terrestrial materials in the 3 - 5 μm atmospheric window: Remote Sensing of Environment, v. 47, p. 345-361.

Salisbury, J. W., and D'Aria, D. M., 1992, Emissivity of Terrestrial materials in the 8 - 14 μm atmospheric window: Remote Sensing of Environment, v. 42, p. 83-106.

SEAN, 1989. Global Volcanism 1975-1985: McClelland, L., Simkin, T., Summers, M., Nielsen, E., & Stein, T.C. (eds.), Prentice Hall, New Jersey, 656 pp.

Setzer, A.W., and Verstraete, M. M., 1994, Fire and glint in AVHRR's channel 3: a possible reason for the non-saturation mystery: Int. J. Remote Sensing, v. 15, no. 3, p. 711-718.

Simkin, T., and Siebert, L., 1994, Volcanoes of the world: Geoscience Press, Tucson, 349 pp.

Wooster, M. J., Richards, T. S., and Kidwell, K., 1995, NOAA-11 AVHRR/2 - Thermal channel calibration update: Int. J. Remote Sensing, v. 16, n. 2, p. 359-363.

Weinreb, M. P., Hamilton, G., Brown, S., and Koczor, R. J., 1990, Nonlinearity corrections in calibration of Advanced Very High Resolution Radiometer Infrared channels: J. Geophys. Res., v. 95 no. C5, p. 7381-7388.

B.7. Appendix A

C++ code for VAST

```
/* ------------------------------------------------------------------------------*/
/*VAST    -  Automatically calibrates AVHRR thermal data in channels 3 and 4, locates  */
/* hot pixels in the image data set and calculates temperature, size and thermal flux from  */
/* located hot feature.                                                          */
/* ------------------------------------------------------------------------------*/


/* ------------------------------------------------------------------------------*/
/* AVHRR.c: module to process the image                                          */
/* ------------------------------------------------------------------------------*/

#include "vast.h"

float T3MinSat = 0, T3MaxSat = 0;
float MaxT3=-999, MaxNaturalVariation=-999, MaxDeltaT = -999;

/* pointers to image array */
float *DN3, *DN4;                                   /* pointers to raw DN data */
float *T3, *T4;                                     /* pointers to T3 and T4 images */
float *Delta;                                       /* pointer to ΔT (T3-T4) image */
float *Rad3, *Rad4;                                 /* pointers to radiance images */
char *Mask, *ResultMask, *MaskAfterFirstIteration;  /* pointers to image masks */
```

```
int ImageWidth, ImageDepth;                    /* hold size of image */

float NatVariation(const int x, const int y);
void SmackResult(char *c, char *name);
float DNToRad(float slope, float intercept, float DN);
float RadToDN(float slope, float intercept, float Rad);
float RadToTemp(float v, float e);
float TempToRad(float v, float t);
int MaskIt(int x, int y);
void ApplyTwoComponent(int x, int y);
void ApplyThreeComponent(int x, int y);

int main(int argc, char* argv[])
{
    int y, x;
    int change, iteration = 0;
    char    key, name[MAX_PATH_LENGTH];
    int left=9999, top = 9999, right=0, bottom=0;

    int DN3Width, DN3Depth, DN4Width, DN4Depth;

    printf("\nAVHRR Hot Pixel Thresholding. \nCopyright Andy Harris, Jez Higgins, The Open
University\n");

    /* loop until GetSetup fails, i.e. until there are no more files to process */
    while(GetSetup(argc, argv))
    {
        /* load the source data */
        if((DN3 = LoadArray(DN3Filename, &DN3Width, &DN3Depth))==NULL)
        {
            printf("\nCouldn't open \'%s\'", DN3Filename);
            return -1;
        }
        if((DN4 = LoadArray(DN4Filename, &DN4Width, &DN4Depth))==NULL)
        {
            printf("\nCouldn't open \'%s\'", DN4Filename);
            return -1;
        }

        /* check images are the same size */
        if((DN3Width != DN4Width) || (DN3Depth != DN4Depth))
        {
            /* fail if they are not */
            printf("\n\'%s\' & \'%s\' Images are not the same size", DN3Filename, DN4Filename);
            return -1;
        }
        else
        {
            /* otherwise allocate and zero memory for the various arrays */
            int size;

            ImageWidth = DN3Width;
            ImageDepth = DN4Depth;

            size = ImageDepth * ImageWidth;

            T3 = (float *)malloc(size * sizeof(float));
            memset(T3, 0, size*sizeof(float));
            T4 = (float *)malloc(size * sizeof(float));
```

```
    memset(T4, 0, size*sizeof(float));
    Delta = (float *)malloc(size * sizeof(float));
    memset(Delta, 0, size*sizeof(float));
    Rad3 = (float *)malloc(size * sizeof(float));
    memset(Rad3, 0, size*sizeof(float));
    Rad4 = (float *)malloc(size * sizeof(float));
    memset(Rad4, 0, size*sizeof(float));
    Mask = (char *)malloc(size * sizeof(char));
    memset(Mask, '.', size*sizeof(char));
    ResultMask = (char *)malloc(size * sizeof(char));
    memset(ResultMask, '.', size*sizeof(char));
    MaskAfterFirstIteration = (char *)malloc(size * sizeof(char));
    memset(MaskAfterFirstIteration, '.', size*sizeof(char));
}

/* image processing starts, at this point DN3 and DN4 point to the source data arrays,  */
/* and the variables declared in vast.h have been assigned                              */

/* calculate brightness temperature equivalent of channel 3 saturation radiances */
T3MinSat = RadToTemp(V3, DNToRad(DN3Slope, DN3Intercept, DN3MinSat));
T3MaxSat = RadToTemp(V3, DNToRad(DN3Slope, DN3Intercept, DN3MaxSat));
/* check the saturation range is minimum to maximum */
if(T3MinSat > T3MaxSat)
{
    float m = T3MaxSat;

    T3MaxSat = T3MinSat;
    T3MinSat = m;
}

/* convert DN to temperature, calculate ΔT for each pixel */
/* and find maximum value of T3 and ΔT                    */
for(y = 0; y < ImageDepth; y++)
    for(x = 0; x < ImageWidth; x++)
    {
        T4[x+(y*ImageWidth)]=RadToTemp(V4, DNToRad(DN4Slope,
  DN4Intercept,DN4[x+(y*ImageWidth)]));
        if(DN3[x+(y*ImageWidth)]==SENSOR_RECOVERY)
        {
            T3[x+(y*ImageWidth)]=SENSOR_RECOVERY;
            Delta[x+(y*ImageWidth)]=SENSOR_RECOVERY;
            ResultMask[x+(y*ImageWidth)]='R';
        }
        else
        {
            T3[x+(y*ImageWidth)]=RadToTemp(V3, DNToRad(DN3Slope,
      DN3Intercept,DN3[x+(y*ImageWidth)]));
            Delta[x+(y*ImageWidth)]=T3[x+(y*ImageWidth)] - T4[x+(y*ImageWidth)];
            ResultMask[x+(y*ImageWidth)]='.';
            if(T3[x+(y*ImageWidth)] > MaxT3)
                MaxT3=T3[x+(y*ImageWidth)];
            if(Delta[x+(y*ImageWidth)] > MaxDeltaT)
                MaxDeltaT=Delta[x+(y*ImageWidth)];
        }
    }


/* search image for 'hot' pixels and create image mask */
change = 0;
```

```
while(!change)
{
    for(y = 0; y < ImageDepth; y++)
        for(x = 0; x < ImageWidth; x++)
        {
            if(MaskIt(x,y))                    /* check if pixel is 'hot' */
            {
                /* if pixel is 'hot', mark the mask around that pixel */
                int dy, dx;

                for(dy = y - MaskSize; dy <= y+MaskSize; dy++)
                    for(dx = x - MaskSize; dx <= x+MaskSize; dx++)
                    {
                        if((dy>=0) && (dy<ImageDepth) && (dx>=0) && (dx<ImageWidth))
                        {
                            if(ResultMask[dx+(dy*ImageWidth)]!='R')
                                ResultMask[dx+(dy*ImageWidth)]='M';
                            change++;          /* indicate that a 'hot' pixel has been located */
                        }
                    }
                /* and mark the pixel as 'hot' */
                ResultMask[x+(y*ImageWidth)]='H';
            }
        }

    /* If MaskHow == 2 or 3 (MaxT3 or MaxDelta) then a mask will have been created, */
    /* in which case the while loop will terminate.                                  */
    /* If MaskHow == 1 (mask on saturated pixels) a mask may not have been placed,   */
    /* so change masking method to 2.                                                */
    /* If no mask had been placed the while loop will not terminate, causing a mask  */
    /* to be placed around the hottest pixel.                                        */
    if(MaskHow == 1)
        MaskHow = 2;
}

/* find the maximum natural variation for unmasked portion of the image */
for(y = 0; y < ImageDepth; y++)
    for(x = 0; x < ImageWidth; x++)
    {
        if(ResultMask[x+(y*ImageWidth)]=='.')
        {
            float NV = NatVariation(x, y);

            if(fabs(NV) > MaxNaturalVariation)
                MaxNaturalVariation = fabs(NV);
        }
    }

/* find and process lava pixels, i.e. located 'hot' pixels */
do
{
    change = 0;
    iteration++;
    for(y = 0; y < ImageDepth; y++)
        for(x = 0; x < ImageWidth; x++)
        {
            if(ResultMask[x+(y*ImageWidth)]=='M' ||
              ResultMask[x+(y*ImageWidth)]=='H')
            {
                /* pixel is masked or 'hot' */
```

```
                float NV = NatVariation(x, y);

                if(NV - MaxNaturalVariation > 0)
                {
                    /* if pixel ΔT is greater than background and maximum natural      */
                    /* variation, then flag as 'lava'                                  */
                    Mask[x+(y*ImageWidth)] = 'L';
                    change++;
                }
            }
        }

    /* first iteration */
    if(iteration == 1)
    {
        /* create result file of first iteration */
        sprintf(name, "%s.1", ResultFilename);
        printf("\nWriting result file : %s",name);
        SmackResult(Mask, name);

        /* copy Mask for use later */
        memcpy(MaskAfterFirstIteration, Mask, ImageWidth*ImageDepth*sizeof(char));

        /* iterate lava pixel search */
        for(y = 0; y < ImageDepth; y++)
            for(x = 0; x < ImageWidth; x++)
                if(Mask[x+(y*ImageWidth)]=='L')
                {
                    if(x<left)
                        left = x;
                    if(x>right)
                        right = x;
                    if(y<top)
                        top = y;
                    if(y>bottom)
                        bottom = y;
                }
        left--;
        top--;
        right+=2;
        bottom+=2;

        /* (left, top) and (right,bottom) define the smallest rectangle which includes  */
        /* all the lava pixels                                                           */
    }

    /* flag lava pixels in the result mask */
    for(y = 0; y < ImageDepth; y++)
        for(x = 0; x < ImageWidth; x++)
            if(Mask[x+(y*ImageWidth)] == 'L')
                ResultMask[x+(y*ImageWidth)] = Mask[x+(y*ImageWidth)];

}                                           /* iterate until no more lava pixels are found */
while(change);

/* write final result to file */
sprintf(name, "%s.%d",ResultFilename,iteration);
printf("\nWriting result file : %s",name);
SmackResult(ResultMask, name);
printf("\nFinished after %d iterations.", iteration);
```

```
if(!DontDoDualComp)
{
    /* restore result after first iteration */
    memcpy(ResultMask, MaskAfterFirstIteration, ImageWidth*ImageDepth*sizeof(char));

    printf("\n\nApply dual band?");
    do
        key = getch();
    while((key!='N')&&(key!='n')&&(key!='y')&&(key!='Y'));

    if((key=='Y')||(key=='y'))
    {
        /* apply dual band calculations to lava pixels */
        float correction[14];

        /* load channel 4 non-linearity correction values */
        printf("\nBlack body temp\n1) 9.2\n2) 13.9 \n3) 19.0");
        do
            key = getch();
        while((key!='1')&&(key!='2')&&(key!='3'));

        {
            /* reads the appropriate non-linearity correction file */
            FILE *file;
            char line[13];
            int i;

            sprintf(line, "a:\\correct%c",key);
            if((file = fopen(line, "rt")) == NULL)
            {
                printf("\nCannot open file \"%s\".", line);
                return -1;
            }
            for(i=0; i< 14; i++)
            {
                fgets(line, 13, file);
                correction[i] = atof(line);
            }
            fclose(file);
        }

        /* apply non-linearity correction to channel 4 and saturation mask to channel 3 */
        for(y = top; y < bottom; y++)
            for(x = left; x < right; x++)
            {
                int k;

                /* mask pixel saturated in channel 3 */
                MaskHow = 1;
                if(MaskIt(x,y))
                    ResultMask[x+(y*ImageWidth)] = 'S';

                /* apply non-linearity correction to channel 4 */
                for(k = 0; k < 14; k++)
                {
                    int u, l;

                    if(k <= 3)
                    {
```

```
            u = k*5;
            u -= 2.5;
            l = u+5;
        }
        else
        {
            u = 10 + ((k-3)*10);
            l = u+10;
        }
        if((T4[x+(y*ImageWidth)]-KCconv) > 46.85)
            T4[x+(y*ImageWidth)] += correction[0];
        if((T4[x+(y*ImageWidth)]-KCconv) < -68.15)
            T4[x+(y*ImageWidth)] += correction[13];
        if(((T4[x+(y*ImageWidth)]-KCconv) <= 46.85-u) &&
   ((T4[x+(y*ImageWidth)]-KCconv) > 46.85-l))
        {
            T4[x+(y*ImageWidth)] += correction[k];
            break;
        }
    }
}

{
/* apply emissivity and atmospheric correction */

    /* convert corrected temperature to radiance */
    for(y = top; y < bottom; y++)
        for(x = left; x < right; x++)
        {               /* x + (y*ImageWidth) */
            if(T3[x+(y*ImageWidth)] != SENSOR_RECOVERY)
            {
                Rad3[x+(y*ImageWidth)] = (TempToRad(V3,
      T3[x+(y*ImageWidth)]) / (Emissivity3 * Tau3));
            }
            Rad4[x+(y*ImageWidth)] = (TempToRad(V4,
  T4[x+(y*ImageWidth)]) / (Emissivity4 * Tau4));
        }

    /* search through all pixels, picking out lava and saturated pixels */
    for(y = top; y < bottom; y++)
        for(x = left; x< right; x++)
            switch(ResultMask[x+(y*ImageWidth)])
            {
                case 'L':
                {
                    /* apply two or three component solution */
                    printf("\nPixel (%d, %d) - apply 2) or 3) component
            solution?", x, y);
                    do
                        key = getch();
                    while((key!='2')&&(key!='3')&&(key!='\27'));
                                                /* '\27' is escape character */

                    if(key == '2')
                        ApplyTwoComponent(x,y);
                    if(key == '3')
                        ApplyThreeComponent(x,y);
                }
                break;
            case 'S':
```

```
                                {
                                    printf("\nPixel (%d, %d) is saturated.  Dual band not possible -
                                  default solution applied", x, y);
                                    ApplyTwoComponent(x,y);
                                }
                            }
                        }
                    }
                }

                /* free everything */
                free(T3);
                free(T4);
                free(DN3);
                free(DN4);
                free(Delta);
                free(Rad3);
                free(Rad4);
                free(ResultMask);
                free(Mask);
                free(MaskAfterFirstIteration);
            }

            return 0;
        }


        /* NatVariation:  Calculates the difference between pixel and its background for          */
        /* pixel (x,y) in the ΔT image. Lava and sensor recovery pixels are excluded from the     */
        /* calculation.                                                                           */
        float NatVariation(const int x, const int y)
        {
            int dy, dx, count=0;
            float Total=0, AverageBackground;

            /* for each pixel around the target pixel, add it to the total */
            for(dy = y-1; dy<=y+1; dy++)
                for(dx = x-1; dx<=x+1; dx++)
                {
                    if((dy>=0)&&(dy<ImageDepth)&&(dx>=0)&&(dx<ImageWidth))  /* checks image  */
                                                                            /* edge has not  */
                                                                            /* been reached  */
                    {
                        if((ResultMask[dx+(dy*ImageWidth)] != 'R') &&
              (ResultMask[dx+(dy*ImageWidth)] != 'L') && !((dy==y) && (dx==x)))
                        {                       /* pixel is not the target pixel, lava or sensor recovery */
                            Total += Delta[dx+(dy*ImageWidth)];
                            count++;
                        }
                    }
                }

            if(count == 0)                      /* avoids divide by zero errors */
                count++;
            AverageBackground = Total/count;

            return Delta[x+(y*ImageWidth)] - AverageBackground;
        }

        /* SmackResult:  Write the result mask pointed at by c to a file given the name in the    */
```

```
/* string pointed at by name. The result is a character array of the same size as the original   */
/* image. A non-lava pixel is denoted by a '.' and a lava pixel by an 'L'                        */
 void SmackResult(char *c, char *name)
{
    int y, x;
    char line[512];
    FILE *file;

    file = fopen(name, "wt");
    for(y=0; y<ImageDepth; y++)
    {
        for(x=0; x<ImageWidth; x++)
        {
            if(c[x+(y*ImageWidth)]!='L')
                line[x] = '.';
            else
                line[x] = 'L';
        }
        line[ImageWidth]='\n';
        line[ImageWidth+1]='\0';
        fputs(line, file);
    }
    fclose(file);
}

/* DNToRad:      Converts a raw DN to a radiance */
float DNToRad(float slope, float intercept, float DN)
{
    return (slope*DN)+intercept;
}

/* RadToDN:      Converts a radiance to DN equivalent */
float RadToDN(float slope, float intercept, float Rad)
{
    return (Rad-intercept)/slope;
}

/* RadToTemp:    Converts a radiance to brightness temperature */
float RadToTemp(float v, float e)
{
    float divisor = log(1 + ((C1*v*v*v)/e));
    return (C2*v)/divisor;
}

/* TempToRad:    Converts brightness temperature to radiance */
float TempToRad(float v, float t)
{
    float divisor = exp((C2*v)/t) - 1;
    return (C1*v*v*v)/divisor;
}

/* MaskIt:       Checks that a pixel matches the mask criteria. Returns 1 if it does, 0 if not.*/
int MaskIt(int x, int y)
{
    int maskit = 0;

    switch(MaskHow)
    {
        case 1:
            if((T3[x+(y*ImageWidth)] >= T3MinSat) && (T3[x+(y*ImageWidth)] <= T3MaxSat))
```

```
                maskit = 1;
            break;
        case 2:
            if(T3[x+(y*ImageWidth)] == MaxT3)
                maskit = 1;
            break;
        case 3:
            if(Delta[x+(y*ImageWidth)] == MaxDeltaT)
                maskit = 1;
            break;
    }

    return maskit;
}

/* ApplyTwoComponent: solves the two component dual-band solution for the      */
/* specifed pixel to find the size and temperature of the hot feature within the pixel      */
void ApplyTwoComponent(int x, int y)
{
    int masksize = 1;    /* size around target pixel to use to calculate background temperature */
    int dy,dx;           /* loop variables */
        int n = 0;       /* iteration counter */
        float  Rmin =9999;
    float Rb3= 0, Rb4 = 0;      /* radiance of pixel background in channel 3, 4 */
    float Tu3, Tu4;      /* temperture of hot feature */
        float p;         /* portion of pixel occupied by background */
        float prevratio; /* ratio of feature (hot or background) temperature in each channel */
    float Ru3, Ru4;

    /* calculateRb4 - the background radiance around the target pixel */
    while(Rb4 == 0)
    {
        for(dy = y - masksize; dy <= y+masksize; dy++)
            for(dx = x - masksize; dx <= x+masksize; dx++)
            {
                if(ResultMask[dx+(dy*ImageWidth)]=='.')
                {
                    Rb4 =Rb4 + Rad4[dx+(dy*ImageWidth)];
                    if(Rad4[dx+(dy*ImageWidth)] < Rmin)
                        Rmin = Rad4[dx+(dy*ImageWidth)];
                    n++;
                }
            }
        masksize++;              /* increase masksize if RB4 calculation has to be repeated   */
    };                           /* repeat if Rb4=0, i.e. all surrounding pixels are lava      */
    Rb4 /= n;
        if(Rad4[x+(y*ImageWidth)] <Rb4)
        Rb4 = Tmin;

    if(Rad4[x+(y*ImageWidth)] <Rb4)     /* should not fail in the normal course of events*/
    {
        printf("\n   Cannot solve, background hotter than target !?!?!");
        return;
    }

    if(ResultMask[x+(y*ImageWidth)] != 'S')
    {                                   /* not saturated */
            long count = 0;
        /* convert background radiance from channel 4 to channel 3 equivalent radiance */
        Rb3 = TempToRad(V3, RadToTemp(V4,Rb4));
```

```
    p = 0.9;                        /* arbitrary initial value of p */

        /* calculate initial values of the hot feature radiance and equivalent temperature (Th) */
        Ru3 = (p*Rb3 - Rad3[x+(y*ImageWidth)]) / (p - 1);
        Ru4 = (p*Tb4 - Rad4[x+(y*ImageWidth)]) / (p - 1);
        Tu3 = RadToTemp(V3, Ru3);
        Tu4 = RadToTemp(V4, Ru4);

    /* find the hot feature temperature and portion of the pixel it occupies */
    /* iterate on p until Tu3 and Tu4 converge                               */
    do
    {
        prevratio = Tu3/Tu4         /* calculate temperature ratio */

        /* recalculate p from Ru3 or Ru4 depending on which is dominating the ratio */
        if(prevratio < 1)
        {
            Ru3 = TempToRad(V3, Tu4);
            p = (Rad3[x+(y*ImageWidth)] - Ru3) / (Rb3 - Ru3);
        }
        else
        {
            Ru4 = TempToRad(V4, Tu3);
            p = (Rad4[x+(y*ImageWidth)] - Ru4) / (Tb4 - Ru4);
        }

        /* recalculate hot feature radiance in each channel for the new value of p */
        Ru3 = (p*Rb3 - Rad3[x+(y*ImageWidth)]) / (p - 1);
        Ru4 = (p*Tb4 - Rad4[x+(y*ImageWidth)]) / (p - 1);
        Tu3 = RadToTemp(V3, Ru3);
        Tu4 = RadToTemp(V4, Ru4);

        count++;
    }
    /* terminate loop if new temperature ratio and previous temperature ratio are  */
    /* arbitrarily close or program has looped a very large number of times (indicating  */
    /* that the solution is not converging): ordinarily converges very quickly     */
    while((fabs((Tu3/Tu4) - prevratio) > 0.000005) && (count < 4096));

    /* print results: Th, Tb, ph, pb, lava area and thermal flux from lava area*/
    printf("\n Th=%d Tb=%d, Ph=%f Pb=%f, Lava area=%ld, Flux=%.8f", (int)(Tu3-KCconv),
  (int)(Tb4-KCconv), 1-p, p, (long)(AreaOfPixel*(1-p)),
((BroadBandEmissivity*SBC*pow(Tu3,4))*(AreaOfPixel*(1-p)))/1e6);
                                    /* and calucluates lava area and thermal flux */
  }
  else
  {
    /* saturated, so solve for supplied maximum and minimum tempertures to give a range */
    /* of possible feature sizes                                                        */
    float pmin,pmax;
    float RadMax = TempToRad(V4, MaxThermalFeatureTemp);
    float RadMin = TempToRad(V4, MinThermalFeatureTemp);

    pmin = (Rad4[x+(y*ImageWidth)] -Rb4) / (RadMax -Rb4);
    pmax = (Rad4[x+(y*ImageWidth)] -Rb4) / (RadMin -Rb4);
    printf("\n Sat. pixel: Tc = 100 Pb=%f Pc=%f, Lava area=%ld, Flux=%.8f", 1-pmax, pmax,
      (long)(AreaOfPixel*pmax),
  ((BroadBandEmissivity*SBC*pow(MinThermalFeatureTemp,4))*(AreaOfPixel*pmax))/1e6);
printf("\n     Tc = 500 Pb=%f Pc=%f, Lava area=%ld, Flux=%.8f", 1-pmin, pmin,
```

```
(long)(AreaOfPixel*pmin),
((BroadBandEmissivity*SBC*pow(MaxThermalFeatureTemp,4))*(AreaOfPixel*pmin))/1e6);
    }
}

/* ApplyThreeComponent:  solve the three component dual-band solution for the   */
/* given pixel, to calculate size and temperature of the hot feature and the feature at an   */
/* intermediate temperature (ie crusted lava)                                   */
void ApplyThreeComponent(int x, int y)
{
    int masksize = 1;                       /* size around target pixel used to calculate */
                                            /* background temperature                     */
    int dy,dx;                              /* loop variables */
    int n = 0;                              /* iteration counter */
    float Rmin = 9999;
    float Rb3 = 0, Rb4 = 0;                 /* radiance of pixel background in channel 3, 4 */
    float R3 = Rad3[x + (y*ImageWidth)];    /* channel 3 radiance of target pixel */
    float R4 = Rad4[x + (y*ImageWidth)];    /* channel 4 radiance of target pixel */
    float Tc;                               /* intermediate (crusted lava) temperature */
    float Rh3,Rh4;                          /* hot feature radiance */
    float Rc3, Rc4;                         /* intermediate feature radiance */
    float pc3, pc4 = 0;                     /* portion of pixel occupied by intermediate  */
    float pb;                               /* portion of pixel occupied by background */
    float prevratio;
    int solved = 0;                         /* state variable */
    int step = 5;                           /* temperature step */

    Tc = CrustedLavaTemp;

    /* calculateRb4 */
    while(Tb4 == 0)
    {
        for(dy = y - masksize; dy <= y+masksize; dy++)
            for(dx = x - masksize; dx <= x+masksize; dx++)
            {
                if(ResultMask[dx+(dy*ImageWidth)]=='.')
                {
                    Tb4 =Rb4 + Rad4[dx+(dy*ImageWidth)];
                    if(Rad4[dx+(dy*ImageWidth)] < Tmin)
                        Tmin = Rad4[dx+(dy*ImageWidth)];
                    n++;
                }
            }
        masksize++;
    };
    Rb4 /= n;
    if(R4 <Rb4)
        Rb4 = Tmin;
    if(R4 <Rb4)
    {
        printf("\n   Cannot solve, background hotter than target !?!?!");
        return;
    }

    /* convert from channel 4 radiance to channel 3 radiance equivalent */
    Rb3 = TempToRad(V3, RadToTemp(V4,Rb4));

    /* calculate initial values of hot feature radiance in each channel */
    Rh3 = TempToRad(V3, MoltenLavaTemp);
    Rh4 = TempToRad(V4, MoltenLavaTemp);
```

```
while(solved!=2)
{
    /* calulate radiance of intermediate feature in each channel */
    Rc3 = TempToRad(V3, Tc);
    Rc4 = TempToRad(V4, Tc);

    /* set initial value of pb */
     pb = 0.2;
    n = 0;

    /* calculate initial values for pixel portion occupied by intermediate temperature feature */
    /* (pc) from the radiance of the feature in each channel                                    */
    pc3 = (R3 - (pb*(Rb3 - Rh3)) - Rh3) / (Rc3 - Rh3);
    pc4 = (R4 - (pb*(Rb4 - Rh4)) - Rh4) / (Rc4 - Rh4);

    /* iterate, so that pc3 and pc4 converge to the same value */
    do
    {
        prevratio = pc3/pc4;

        /* adjust pb, depending on whether pc3 or pc4 is dominant in ratio (pc3/pc4) by     */
        /* cross- substition                                                                */
        if(prevratio > 1)
            pb = (R3 - Rh3 - (pc4*(Rc3-Rh3))) / (Rb3 - Rh3);
        else
            pb = (R4 - Rh4 - (pc3*(Rc4-Rh4))) / (Rb4 - Rh4);

        /* recalculate pc3 and pc4 based on new value of pb */
        pc3 = (R3 - (pb*(Rb3 - Rh3)) - Rh3) / (Rc3 - Rh3);
        pc4 = (R4 - (pb*(Rb4 - Rh4)) - Rh4) / (Rc4 - Rh4);

        /* increment iteration counter */
        n++;
    }
    /* terminate loop if new temperature ratio and previous temperature ratio are       */
    /* arbitrarily close or program has looped a very large number of times (indicating */
    /* that the solution is not converging): ordinarily converges very quickly          */
    while((fabs((pc3/pc4) - prevratio) > 0.000005) && (n < 4096));

    if(solved ==1)
    {                                   /* this is the final pass, when Tc has been increased */
                                        /* to its maximum solvable value                      */
        solved = 2;                     /* set solved state to 2 so that loop terminates      */
        printf("\n Th=%d Tcmax=%d Tb=%d, Pb=%f Pc=%f Ph=%f, Lava area=%ld,
Flux=%.8f", (int)(MoltenLavaTemp-KCconv),(int)(Tc-KCconv),(int)(Rb4-KCconv),                pb,
pc3, 1-  (pb+pc3), (long)(AreaOfPixel*(1-pb)),
((SBC*BroadBandEmissivity*(AreaOfPixel*pc3)*pow(Tc,4)) +
(SBC*BroadBandEmissivity*(AreaOfPixel*(1-
(pb+pc3))*pow(MoltenLavaTemp,4))))/1e6);
    }

    if(CrustedLavaTemp == Tc)     /* true if this is the first pass, when Tc is at minimum */
        printf("\n Th=%d Tcmin=%d Tb=%d, Pb=%f Pc=%f Ph=%f, Lava area=%ld,
Flux=%.8f", (int)(MoltenLavaTemp-KCconv),(int)(Tc-KCconv),(int)(Rb4-KCconv),                pb,
pc3, 1-  (pb+pc3), (long)(AreaOfPixel*(1-pb)),
((SBC*BroadBandEmissivity*(AreaOfPixel*pc3)*pow(Tc,4)) +
                (SBC*BroadBandEmissivity*(AreaOfPixel*(1-
          (pb+pc3))*pow(MoltenLavaTemp,4))))/1e6);
```

```
        /*  increase crusted lava temperature */
        if((pb+pc3) > 0.999999)     /* arbitrary maximum size of background and crusted feature */
        {
            /* set solved state to 1, so terminate on next iteration */
            solved = 1;
            /* back off Tc, one step */
            Tc-=step;
        }
        else                                /* otherwise increase crusted lava temperture */
            Tc+=step;
    }       /* repeat while solved state is not 2 */
}
```

```
/* ------------------------------------------------------------------------------------------*/
/* vast.c:   This module parses the command line and loads the configuration file and data   */
/*  files                                                                                    */
/* ------------------------------------------------------------------------------------------*/

#include "vast.h"

float V3;                                   /* channel 3 central wave number */
int bV3 = 0;
float V4;                                   /* channel 4 central wave number */
int bV4 = 0;

float DN3Slope, DN3Intercept;               /* channel 3 slope and intercept */
int bDN3Slope = 0, bDN3Intercept = 0;
float DN4Slope , DN4Intercept;              /* channel 4 slope and intercept */
int bDN4Slope = 0, bDN4Intercept = 0;

float DN3MinSat, DN3MaxSat;                 /* limits of channel 3 saturation range */
int bDN3MinSat = 0, bDN3MaxSat = 0;

int MaskSize;                               /* size of masked area to be searched for hot pixels */
int bMaskSize = 0;
int MaskHow;                                /* method by which mask is to be centred */
int bMaskHow = 0;

float AreaOfPixel;                          /* pixel area */
int bAreaOfPixel = 0;
float BroadBandEmissivity;                  /* Emissivity (ε) used in thermal flux calculations */
int bBroadBandEmissivity = 0;
float Emissivity3, Tau3;                    /* channel 3 emmissivity and transmissivity (ε3,τ3) */
int bEmissivity3 = 0, bTau3 = 0;
float Emissivity4, Tau4;                    /* channel 4 emmissivity and transmissivity (ε4,τ4) */
int bEmissivity4 = 0, bTau4 = 0;

int DontDoDualComp = 0;

int CrustedLavaTemp;                    /* lowest expected intermediate (crust) temperature */
int bCrustedLavaTemp = 0;
int MoltenLavaTemp;                     /* hot (molten lava) component temperature */
int bMoltenLavaTemp = 0;
int MinThermalFeatureTemp;              /* lower limit set for intermediate (crust) temperature */
int bMinThermalFeatureTemp = 0;
int MaxThermalFeatureTemp;              /* upper limit set for intermediate (crust) temperature */
int bMaxThermalFeatureTemp = 0;
```

```
char DN3Filename[MAX_PATH_LENGTH];      /* array to hold channel 3 DN data */
int bDN3Filename = 0;
char DN4Filename[MAX_PATH_LENGTH];      /* array to hold channel 4 DN data */
int bDN4Filename = 0;
char ResultFilename[MAX_PATH_LENGTH];   /* array to hold results */
int bResultFilename = 0;
char FilelistFilename[MAX_PATH_LENGTH];

int UseFilelist = 0;

/* local file handling functions */
int FileLength;
int FilePosition;
char *FileContents;
int file_open(const char *filename);
char *read_file_line(char *buffer, int buffersize);
void file_close(void);
void ProcessConfigFile(char *ConfigurationFilename);
int isexcelfile(char *line);
int countcolumns(char *line);
int GetNextFilenames(void);

/* GetSetup:  Parses command line and ensures all required variables are assigned.   */
/* Valid cl arguments are [-c <config file>] [-f <list file>]||[<dn3 file> <dn4 file> <result  */
/* file>]. Returns 1 if parsed successfully, 0 if it failed. The function can be called  */
/* repeatedly until it returns 0, making it possible to specify multiple sets of source  */
/* filenames e.g. vast -c config dn3.1 dn4.1 result1 dn3.2 dn4.2 result2  */
int GetSetup(int argc, char* argv[])
{
    static args = 1;

    if((args != 1) && (UseFilelist == 0))
        return 0;

    /* search for command line arguments */
    if(args == 1)
    {
        int i;

        for(i=1; i<argc; i++)
        {
            if(!strcmp(argv[i], "-c"))
            {
                /* config file specified, so process it */
                ProcessConfigFile(argv[i+1]);
                args+=2;
            }
            if(!strcmp(argv[i], "-f"))
            {
                /* list file specified, so store name */
                strcpy(FilelistFilename, argv[i+1]);
                UseFilelist = 1;
                args+=2;
            }
        }
    }

    if(!UseFilelist)
    {
```

```
    /* a list file has not been specified so get filenames from command line */
    if(args<argc)
    {
        strcpy(DN3Filename, argv[args++]);
        bDN3Filename = 1;
        if(args<argc)
        {
            strcpy(DN4Filename, argv[args++]);
            bDN4Filename = 1;
        }
    }

    if(args<argc)
    {
        strcpy(ResultFilename, argv[args++]);
        bResultFilename = 1;
    }
}
else
{
    /* list file specified so try to get filenames from it */
    if(!GetNextFilenames())
        return 0;
}
if(bDN3Filename != bDN4Filename)
{
    printf("Wrong number of arguments.");
    return 0;
}

/* get items not specified in config file from the user */
if(!bV3)
{
    printf("Central wave number in channel 3 : ");
    scanf("%f",&V3);
    bV3 = 1;
}
if(!bV4)
{
    printf("Central wave number in channel 4 : ");
    scanf("%f",&V4);
    bV4 = 1;
}
if(!bDN3Slope)
{
    printf("DN3 Slope        : ");
    scanf("%f",&DN3Slope);
    bDN3Slope = 1;
}
if(!bDN3Intercept)
{
    printf("DN3 Intercept : ");
    scanf("%f",&DN3Intercept);
    bDN3Intercept = 1;
}
if(!bDN4Slope)
{
    printf("DN4 Slope : ");
    scanf("%f",&DN4Slope);
    bDN4Slope = 1;
```

```
}
if(!bDN4Intercept)
{
    printf("DN4 Intercept : ");
    scanf("%f",&DN4Intercept);
    bDN4Intercept = 1;
}
if(!bDN3MinSat)
{
    printf("DN3 Minimum saturation value : ");
    scanf("%f",&DN3MinSat);
    bDN3MinSat = 1;
}
if(!bDN3MaxSat)
{
    printf("DN3 Maximum saturation value : ");
    scanf("%f",&DN3MaxSat);
    bDN3MaxSat = 1;
}
if(!bMaskSize)
{
    printf("Mask size : ");
    scanf("%d",&MaskSize);
    bMaskSize = 1;
}
if(!bMaskHow)
{
    printf("Select 1) center on saturated pixels\n      2) center on hottest pixel\n");
    printf("       3) center on max delta T\n");
    scanf("%d",&MaskHow);
    bMaskHow = 1;
}
if(!DontDoDualComp)
{
    /* these values are not needed if no thermal calculations are to be carried out */
    if(!bAreaOfPixel)
    {
        printf("Area of pixel : ");
        scanf("%f",&AreaOfPixel);
        bAreaOfPixel = 1;
    }
    if(!bBroadBandEmissivity)
    {
        printf("Broad band emissivity : ");
        scanf("%f",&BroadBandEmissivity);
        bBroadBandEmissivity = 1;
    }
    if(!bEmissivity3)
    {
        printf("Emissivity in channel 3 : ");
        scanf("%f",&Emissivity3);
        bEmissivity3 = 1;
    }
    if(!bTau3)
    {
        printf("Tau of channel 3                : ");
        scanf("%f",&Tau3);
        bTau3 = 1;
    }
    if(!bEmissivity4)
```

```
    {
        printf("Emissivity in channel 4 : ");
        scanf("%f",&Emissivity4);
        bEmissivity4 = 1;
    }
    if(!bTau4)
    {
        printf("Tau of channel 4                    : ");
        scanf("%f",&Tau4);
        bTau4 = 1;
    }
    if(!bCrustedLavaTemp)
    {
        printf("Crusted lava temperature : ");
        scanf("%d",&CrustedLavaTemp);
        CrustedLavaTemp += KCconv;
        bCrustedLavaTemp = 1;
    }
    if(!bMoltenLavaTemp)
    {
        printf("Molten lava temperature : ");
        scanf("%f",&MoltenLavaTemp);
        MoltenLavaTemp += KCconv;
        bMoltenLavaTemp = 1;
    }
    if(!bMinThermalFeatureTemp)
    {
        printf("Minimum thermal feature temperature : ");
        scanf("%f",&MinThermalFeatureTemp);
        MinThermalFeatureTemp += KCconv;
        bMinThermalFeatureTemp = 1;
    }
    if(!bMaxThermalFeatureTemp)
    {
        printf("Maximum thermal feature temperature : ");
        scanf("%f",&MaxThermalFeatureTemp);
        MaxThermalFeatureTemp += KCconv;
        bMaxThermalFeatureTemp = 1;
    }
}

if(!bDN3Filename)
{
    /* if data file names have not been specified get them now */
    printf("DN3 File          : ");
    scanf("%s", DN3Filename);
    bDN3Filename = 1;
    printf("DN3 File          : ");
    scanf("%s", DN4Filename);
    bDN4Filename = 1;
}
else
    printf("\nDN3 File    : %s\nDN4 File    : %s\n", DN3Filename, DN4Filename);

if((!bResultFilename) && (!UseFilelist))
{
    /* if result filename has not been specified, get it */
    printf("Result file : ");
    scanf("%s", ResultFilename);
    bResultFilename = 1;
```

```
    }
    else
        printf("Result file : %s\n", ResultFilename);
    return 1;
}

/* ProcessConfigFile:      Reads through the configuration file, pulling out values and    */
/* storing them in the appropriate variables                                               */
void ProcessConfigFile(char *ConfigurationFilename)
{
    char line[512];

    if(file_open(ConfigurationFilename) == 0)
    {
        printf("\nCannot open configuration file \"%s\".", ConfigurationFilename);
        return;
    }

    while(read_file_line(line, 512) != NULL)
    {
        char VariableName[128], VariableValue[484];
        int i=0, j=0;

        /* split line into name and value    */
        /* strip leading spaces, etc         */
        while(((line[i] == ' ') || (line[i] == '\t')) && (line[i] != '\0'))
            i++;
        /* get variable name (everything up to next whitespace or = )*/
        while((line[i] != ' ') && (line[i] != '\t') && (line[i] != '\0') && (line[i] != '='))
            VariableName[j++] = line[i++];
        VariableName[j]='\0';
        /* strip whitespaces and = */
        while(((line[i] == ' ') || (line[i] == '\t') || (line[i] == '=')) && (line[i] != '\0'))
            i++;
        /* get value string (everything up to next whitespace) */
        j = 0;
        while((line[i] != ' ') && (line[i] != '\t') && (line[i] != '\0'))
            VariableValue[j++] = line[i++];
        VariableValue[j]='\0';

        /* store value in appropriate variable */
        strlwr(VariableName);

        if((!bV3) && (!strncmp(VariableName, "v3", 2)))
        {
            V3 = atof(VariableValue);
            bV3 = 1;
        }
        if((!bV4) && (!strncmp(VariableName, "v4", 2)))
        {
            V4 = atof(VariableValue);
            bV4 = 1;
        }
        if((!bDN3Slope) && (!strncmp(VariableName, "dn3slope", 8)))
        {
            DN3Slope = atof(VariableValue);
            bDN3Slope = 1;
        }
        if((!bDN3Intercept) && (!strncmp(VariableName, "dn3intercept", 12)))
        {
```

```
    DN3Intercept = atof(VariableValue);
    bDN3Intercept = 1;
}
if((!bDN4Slope) && (!strncmp(VariableName, "dn4slope", 8)))
{
    DN4Slope = atof(VariableValue);
    bDN4Slope = 1;
}
if((!bDN4Intercept) && (!strncmp(VariableName, "dn4intercept", 12)))
{
    DN4Intercept = atof(VariableValue);
    bDN4Intercept = 1;
}
if((!bDN3MinSat) && (!strncmp(VariableName, "dn3minsat", 8)))
{
    DN3MinSat = atof(VariableValue);
    bDN3MinSat = 1;
}
if((!bDN3MaxSat) && (!strncmp(VariableName, "dn3maxsat", 8)))
{
    DN3MaxSat = atof(VariableValue);
    bDN3MaxSat = 1;
}
if((!bMaskSize) && (!strncmp(VariableName, "masksize", 8)))
{
    MaskSize = atoi(VariableValue);
    bMaskSize = 1;
}
if((!bMaskHow) && (!strncmp(VariableName, "maskhow", 7)))
{
    MaskHow = atoi(VariableValue);
    bMaskHow = 1;
}
if((!bAreaOfPixel) && (!strncmp(VariableName, "areaofpixel", 11)))
{
    AreaOfPixel = atof(VariableValue);
    bAreaOfPixel = 1;
}
if((!bBroadBandEmissivity) && (!strncmp(VariableName, "broadbandemissivity", 19)))
{
    BroadBandEmissivity = atof(VariableValue);
    bBroadBandEmissivity = 1;
}
if((!bEmissivity3) && (!strncmp(VariableName, "emissivity3", 11)))
{
    Emissivity3 = atof(VariableValue);
    bEmissivity3 = 1;
}
if((!bTau3) && (!strncmp(VariableName, "tau3", 4)))
{
    Tau3 = atof(VariableValue);
    bTau3 = 1;
}
if((!bEmissivity4) && (!strncmp(VariableName, "emissivity4", 11)))
{
    Emissivity4 = atof(VariableValue);
    bEmissivity4 = 1;
}
if((!bTau4) && (!strncmp(VariableName, "tau4", 4)))
{
```

```
            Tau4 = atof(VariableValue);
            bTau4 = 1;
        }
        if((!bCrustedLavaTemp) && (!strncmp(VariableName, "crustedlavatemp", 15)))
        {
            CrustedLavaTemp = atoi(VariableValue) + KCconv;
            bCrustedLavaTemp = 1;
        }
        if((!bMoltenLavaTemp) && (!strncmp(VariableName, "moltenlavatemp", 14)))
        {
            MoltenLavaTemp = atoi(VariableValue) + KCconv;
            bMoltenLavaTemp = 1;
        }
        if((!bMinThermalFeatureTemp) && (!strncmp(VariableName, "minthermalfeaturetemp",
    20)))
        {
            MinThermalFeatureTemp = atoi(VariableValue) + KCconv;
            bMinThermalFeatureTemp = 1;
        }
        if((!bMaxThermalFeatureTemp) && (!strncmp(VariableName, "maxthermalfeaturetemp",
    20)))
        {
            MaxThermalFeatureTemp = atoi(VariableValue) + KCconv;
            bMaxThermalFeatureTemp = 1;
        }
        if((!DontDoDualComp) && (!strncmp(VariableName, "dontdodualcomp", 14)))
        {
            DontDoDualComp = 1;
        }
    }
    file_close();
}


/* LoadArray: Reads a DN data file. The data file should be in rows and columns (like      */
/* a spreadsheet) and may be space, comma or tab separated. Sensor recovery pixels should  */
/* be marked by the single letter 'R'. If the rows and columns are labelled (like a Excel file) */
/* then this is detected. The lines can be CR, LF or CR/LF terminated (ie Mac, Unix or     */
/* DOS type). The function returns a pointer to a floating point array containing the DN   */
/* data, and also sets the width and depth parameters.                                     */
float* LoadArray(const char *filename, int *width, int *depth)
{
/* This will need modification if file format is not space/tab separated and newline delimited */

    float *f;
    char line[1024];
    int x = 0, wid, y = 0;
    int excelfile;

    if(file_open(filename) == 0)
    {
        printf("\nCannot open file \'%s\'", filename);
        return NULL;
    }
    else
        printf("\nReading \'%s\'", filename);

    read_file_line(line, 1024);
    y = 0;
    /* check if the file has row and column names like an Excel-type text file */
```

```
    excelfile = isexcelfile(line);

    /* count number of data columns */
    wid = countcolumns(line) - excelfile;

    /* if an Excel-type file, discard first line as it contains no data */
    if(excelfile)
        read_file_line(line, 1024);

    /* just malloc f to something, so we can realloc it later */
    f = malloc(sizeof(float));

    do
    {
        int i=0;

        /* realloc array to have room for next line */
        f = (float* )realloc((void *)f, wid*(y+1)*sizeof(float));

        /* if Excel-type file, ignore first column, as it contains the row number */
        if(excelfile)
            x = -1;
        else
            x = 0;

        /* work along the line, picking out each data value in turn */
        do
        {
            int j = 0;
            char number[20];

            /* strip white space and commas */
            while(((line[i] == ',')||(line[i]==' ')||(line[i]=='\t'))&&(line[i]!='\0'))
                i++;
            /* get number */
            while((line[i] != ',')&&(line[i]!=' ')&&(line[i]!='\t')&&(line[i]!='\0'))
                number[j++]=line[i++];
            if(x!=-1)
            {
                /* store the number in the array */
                number[j]='\0';
                if(number[0]=='R')                                  /*sensor recovery pixel*/
                    f[x+(y*wid)] = SENSOR_RECOVERY;
                else
                    f[x+(y*wid)] = (float)atof(number);
            }
            x++;
        }
        while(line[i]!='\0');
        y++;
    }
    while(read_file_line(line, 1024));
    file_close();

    *width = wid;
    *depth = y;

    return f;
}
```

```
/* isexcelfile:     Checks if the file contains row and column labels by running along the  */
/* line until a non-white space  is encountered.  If first cell is a letter then assume excel  */
/* type spreadsheet - this will obviously return a false positive if the very first pixel is a  */
/* sensor recovery pixel, however this is highly unlikely if the image is centred on the  */
/* volcano properly. Returns 1 if the file is  Excel-type, 0 if not.  */
int isexcelfile(char *line)
{
    int i = 0;

    while((line[i]==' ')||(line[i]=='\t'))
        i++;
    return ((line[i]>='A')&&(line[i]<='Z')) || ((line[i]>='a')&&(line[i]<='z'));
}

/* countcolumns: Count the number of data items in the line passed to it (including  */
/* any label that may be present). Returns number of items.  */
int countcolumns(char *line)
{
    int i = 0, cols = 0;

    while(line[i]!='\0')
    {
        while((line[i]==' ')||(line[i]=='\t')||(line[i]==','))
            i++;
        while((line[i]!=' ')&&(line[i]!='\t')&&(line[i]!=',')&&(line[i]!='\0'))
            i++;
        cols++;
    }

    return cols;
}

/* GetNextFilenames:  Reads through a list file, and pulls out a pair of source  */
/* filenames and the result filename.  Each time it is called it reads the next line in the list.  */
/* Returns 1 if it successfully read the filenames, 0 otherwise.  */
int GetNextFilenames(void)
{
    static int linecount = 0;
    int i = 0, ok = 1;
    char line[512];

    linecount++;

    /* open file */
    if(file_open(FilelistFilename) == 0)
    {
        printf("\nCannot filelist file \"%s\".", FilelistFilename);
        return 0;
    }

    /* read line */
    while((i < linecount) && (ok))
    {
        i++;
        ok = (int)read_file_line(line, 512);
    }

    file_close();

    if(ok)
```

```
    {
        /* if next line has been read ok, then get filenames from it */
        int i = 0, j, s = 0;
        char str[256];

        while((line[i]!='\0') && (s!=3))
        {
            j = 0;
            /* strip whitespace */
            while((line[i]==' ') || (line[i]=='\t'))
                i++;
            /* copy nonwhitespace */
            while((line[i]!=' ') && (line[i]!='\t')&&(line[i]!='\0'))
                str[j++]=line[i++];
            str[j]=0;

            /* fill appropriate variable */
            switch(s)
            {
                case 0:
                    strcpy(DN3Filename, str);
                    break;
                case 1:
                    strcpy(DN4Filename, str);
                    break;
                case 2:
                    strcpy(ResultFilename, str);
                    break;
            }
            s++;
        }
        /* if there is a missing name, return 0 */
        if(s!=3)
        {
            printf("Missing filename at line : %d", linecount);
            return 0;
        }
    }
    else
    {
        /* there are no more lines */
        return 0;
    }

    return 1;
}


/* file_open:  Reads entire file into memory, which can then be read using      */
/* read_file_line. The file should be discarded using file_close.  This has been implemented  */
/* since the file functions used here (open, lseek and close) while widely supported, are not  */
/* ANSI standard and so may not be available.  If this is the case, only this function would  */
/* need to be rewritten. Returns 1 if successful, 0 otherwise.                 */
int file_open(const char *filename)
{
    int file;

    FileLength = 0;
    FilePosition = 0;
```

```
    /* open file */
    if((file = open(filename, O_RDONLY|O_BINARY)) == -1)
        return 0;

    /* find out file size */
    FileLength = lseek(file, 0, SEEK_END);

    /* return file pointer to beginning of the file */
    lseek(file, 0, SEEK_SET);

    /* allocate memory for entire file */
    FileContents = (char *)malloc((FileLength+1) * sizeof(char));

    read(file,FileContents,FileLength);


    FileContents[FileLength]=EOF;

    close(file);

    return 1;
}

/* read_file_line:    Reads the next line of the file buffered into memory by a previous   */
/* call to file_open. The returned string is null terminated. The line in the file can be   */
/* terminated by CR, LF or CR\LF (ie Mac, Unix or DOS type files). The buffer should        */
/* be big enough to accomondate the line, but it will not be overrun if it is too small.    */
/* Returns a pointer to buffer if successful and the line read stored in buffer, or a NULL  */
/* pointer if no line was read (ie at EOF).                                                 */
char *read_file_line(char *buffer, int buffersize)
{
    int count = 0;
    int ch;
    char *returnpointer;

    /* advance position in file */
    ch = FileContents[FilePosition++];

    /* copy everything into the buffer until CR, LF or EOF is found */
    while((ch != '\n') && (ch != '\r') && (ch != EOF) && (count < buffersize))
    {
        buffer[count++] = (char)ch;
        ch = FileContents[FilePosition++];
    }
    buffer[count] = '\0';

    /* skip over CRs and LFs */
    while(((ch == '\n') || (ch == '\r')) && (ch != EOF))
    {
        ch = FileContents[FilePosition++];
    }
    /* rewind in the file one character */
    FilePosition--;

    if(count == 0)
        returnpointer = NULL;
    else
        returnpointer = buffer;

    return returnpointer;
```

```
}

/* file_close:      Discards the file previously buffered into memory by a call to file_open */
void file_close(void)
{
    free(FileContents);
}


/* ------------------------------------------------------------------------------------------*/
/* VAST.H:    Variables used by AVHRR.c and vast.c                                          */
/* ------------------------------------------------------------------------------------------*/


 #include <stdio.h>
#include <string.h>
#include <conio.h>
#include <stdlib.h>
#include <math.h>
#include <io.h>
#include <fcntl.h>

#define C2  1.438833                    /* Constant c1 */
#define C1  1.1910659e-5                /* Constant c2 */
#define KCconv  273                     /* Degrees centigrade to Kelvin conversion */
#define SBC  5.67e-8                    /* Stefan-Boltzmann constant */

#define MAX_PATH_LENGTH  256

#define SENSOR_RECOVERY -999

extern float V3;                        /* channel 3 central wave number */
extern float V4;                        /* channel 4 central wave number */

extern float DN3Slope, DN3Intercept;    /* channel 3 slope and intercept */
extern float DN4Slope, DN4Intercept;    /* channel 4 slope and intercept */

extern float DN3MinSat, DN3MaxSat;      /* limits of channel 3 saturation range */


extern int MaskSize;                    /* size of masked area to be searched for hot pixels */
extern int MaskHow;                     /* method by which mask is to be centred */

extern float AreaOfPixel;               /* pixel area */
extern float BroadBandEmissivity;       /* Emissivity (ε) used in thermal flux calculations */
extern float Emissivity3, Tau3;         /* channel 3 emmissivity and transmissivity (ε3,τ3) */
extern float Emissivity4, Tau4;         /* channel 4 emmissivity and transmissivity (ε4,τ4) */
extern char DN3Filename[MAX_PATH_LENGTH];       /* channel 3 input data file name */
extern char DN4Filename[MAX_PATH_LENGTH];       /* channel 4 input data file name */
extern char ResultFilename[MAX_PATH_LENGTH];    /* Result file name */

extern int DontDoDualComp;          /* do dual-band and thermal calculations? */

extern int CrustedLavaTemp;         /* lowest expected intermediate (crust) temperature */
extern int MoltenLavaTemp;              /* hot (molten lava) temperature */
extern int MinThermalFeatureTemp;       /* lower limit for intermediate (crust) temperature */
extern int MaxThermalFeatureTemp;       /* upper limit set for intermediate (crust) temperature */

int GetSetup(int argc, char* argv[]);
float *LoadArray(const char *filename, int *width, int*depth);
```

B.8. Appendix B

Inputs into VAST

B.8.1. Configuration file

An example configuration file:

Free text can be placed anywhere in the file, providing that the line does not begin with one of the variable names.

V3 = 2671.40	Channel 3 central wave number (cm^{-1})
V4 = 927.83	Channel 4 central wave number (cm^{-1})
DN3Slope = -0.001493	Channel 3 slope
DN3Intercept = 1.478117	Channel 3 intercept
DN4Slope = -0.177511	Channel 4 slope
DN4Intercept = 176.374839	Channel 4 intercept
DN3MinSat = 0	Minimum DN for channel 3 saturation range
DN3MaxSat = 47	Maximum DN for channel 3 saturation range
MaskSize = 5	Size of pixel masked area to be searched for hot pixels
MaskHow = 1	Method by which mask is to be centred (i.e. on saturated pixels, or on the pixel with the maximumT_3 or maximum ΔT
'DontDoDualComp	Remove the leading ' to turn off dual band calculations, and to stop VAST from carrying out any thermal calculations
AreaOfPixel = 1100000	Pixel area (m^2)
BroadBandEmissivity = 0.9887	Emissivity for thermal flux calculations
Emissivity3 = 0.96	Channel 3 emissivity
Tau3 = 0.9387	Channel 3 transmissivity
Emissivity4 = 0.9	Channel 4 emissivity
Tau4 = 0.9612	Channel 4 trasnmissivity
CrustedLavaTemp = 100	Minimum expected crusted lava temperature (°C)
MoltenLavaTemp = 1000	Temperature of molten lava thermal component (°C)
MinThermalFeatureTemp = 100	Lower limit of crusted lava temperature range (°C)
MaxThermalFeatureTemp = 500	Upper limit of crusted lava temperature range (°C)

B.8.2. List file

The list file takes the form:

<dn3 image filename> <dn4 image filename> <output filename>

For example:

a:\dn3 a:\dn4 a:\image1

B.8.3. Input data

Input data used here were tab separated and line delimited. Sensor recovery pixels were located and masked using "R" prior to input. In each case the first cell gives the file name, the first line contains column numbers and the first column contains line numbers. All other cells contain channel 3 (first file) or 4 (second file) DN or sensor recovery pixels.

DN3	10	11	12	13	14	15	16	17	18	19	20	21	22
5	834	843	857	886	900	914	908	903	886	865	853	822	797
6	835	845	858	884	894	914	917	899	868	855	853	836	807
7	834	847	852	881	899	918	925	897	866	856	853	838	817
8	831	844	842	868	894	917	926	900	872	859	855	835	817
9	829	836	845	861	888	919	927	905	870	847	837	819	814
10	839	836	825	840	857	902	907	909	881	841	821	804	788
11	828	848	840	854	608	303	834	885	863	826	817	798	786
12	843	853	830	836	772	564	828	854	828	806	806	798	793
13	840	838	824	820	785	752	797	816	812	811	801	791	800
14	826	824	R	R	45	47	46	752	783	799	805	784	779
15	819	836	R	R	211	47	36	788	794	796	798	780	772
16	811	835	836	829	782	765	783	813	811	800	798	788	765
17	808	818	815	807	815	811	811	815	810	785	790	788	773
18	788	791	789	776	779	801	806	811	802	781	784	785	781
19	775	777	773	780	781	802	816	812	804	781	776	784	775
20	778	774	769	774	771	784	801	809	799	786	787	782	781
21	773	770	765	770	782	793	790	787	789	784	780	775	777
22	760	766	769	773	794	796	795	785	785	787	787	776	769
23	750	761	751	766	779	781	778	775	776	782	786	778	759
24	759	763	742	756	757	765	772	773	774	780	788	775	764

DN4	10	11	12	13	14	15	16	17	18	19	20	21	22
5	566	574	591	611	626	632	628	617	594	576	560	539	523
6	566	580	596	616	634	647	643	613	581	570	562	545	526
7	566	576	592	614	636	654	645	604	575	568	563	550	530
8	569	574	589	614	640	657	646	607	582	572	562	546	528
9	566	571	582	609	643	665	654	619	588	568	554	539	525
10	566	568	572	584	619	652	648	626	588	560	547	532	518
11	565	572	570	574	588	610	617	605	571	551	540	526	513
12	565	569	566	571	574	587	603	581	555	541	533	525	513
13	562	563	565	570	575	588	590	559	544	536	528	521	513
14	555	559	567	571	548	517	538	541	533	532	525	513	506
15	554	561	569	568	550	522	560	551	536	530	523	509	503
16	550	557	562	563	569	576	570	554	536	526	520	510	503
17	547	549	550	550	557	557	551	544	531	520	516	510	505
18	534	536	535	529	533	542	543	540	529	517	514	508	503
19	526	526	526	525	527	539	540	536	525	516	510	506	501
20	521	520	519	519	520	528	531	529	522	515	508	505	499
21	517	516	515	516	520	525	523	521	517	513	507	503	496
22	513	514	514	517	524	525	522	516	515	513	509	502	493
23	504	509	510	514	517	517	515	512	510	512	508	500	489
24	505	506	503	507	510	513	513	510	508	509	507	496	482

B.8.4. Channel 4 non-linearity correction file (Correct%)

Non-linearity corrections, in Kelvin, are entered for each range of scene temperatures and internal blackbody temperature, n.b. each range of scene temperatures has a unique correction, which depends on scene and blackbody temperature. Three correction files (Correct%, % = 1, 2 or 3) should be set up one for each of the three blackbody temperatures: (1) 9.2 °C (Correct1), (2) 13.9 °C (Correct2) and (3) 19.0 °C (Correct3). The example given is taken from the corrections in Weinreb *et al.* (1990) for a NOAA-11 blackbody temperature of 19.0 °C (Correct3).

3.25	Correction for scene temeperture 320 K
2.55	Correction for scene temeperture 315 K
1.91	Correction for scene temeperture 310 K
1.32	Correction for scene temeperture 305 K
0.22	Correction for scene temeperture 295 K
-0.67	Correction for scene temeperture 285 K
-1.15	Correction for scene temeperture 275 K
-1.66	Correction for scene temeperture 265 K
-2.03	Correction for scene temeperture 255 K
-2.22	Correction for scene temeperture 245 K
-2.28	Correction for scene temeperture 235 K
-2.36	Correction for scene temeperture 225 K
-2.20	Correction for scene temeperture 215 K
-1.98	Correction for scene temeperture 205 K

Appendix C. Thermal evidence for linked vents at Stromboli

A.J L. Harris, N.F. Stevens, A.J.H. Maciejewski, P.J. Röllin

Accepted for publication in Acta Vulcanologica, 1996.

C.1. Abstract

Near-continuous thermal measurements of a degassing vent within Stromboli's crater terrace showed that gas flux from this vent was reduced during eruptions from other vents within the crater terrace. This provides strong evidence that vents within the Stromboli crater terrace are linked at a shallow level. We propose that linkage is via a shared magma chamber or feeder conduit, to which the surface vents are linked via narrow conduits.

C.2. Introduction

Current activity at Stromboli volcano is characterised by repeated mildly explosive eruptions from a variable number of active vents (Fig. C1). Explosive events typically propel incandescent ejecta and brown or black ash to heights of up to 300 m above the crater terrace (GVN, 1990; GVN, 1994). This explosive activity is driven by the bursting

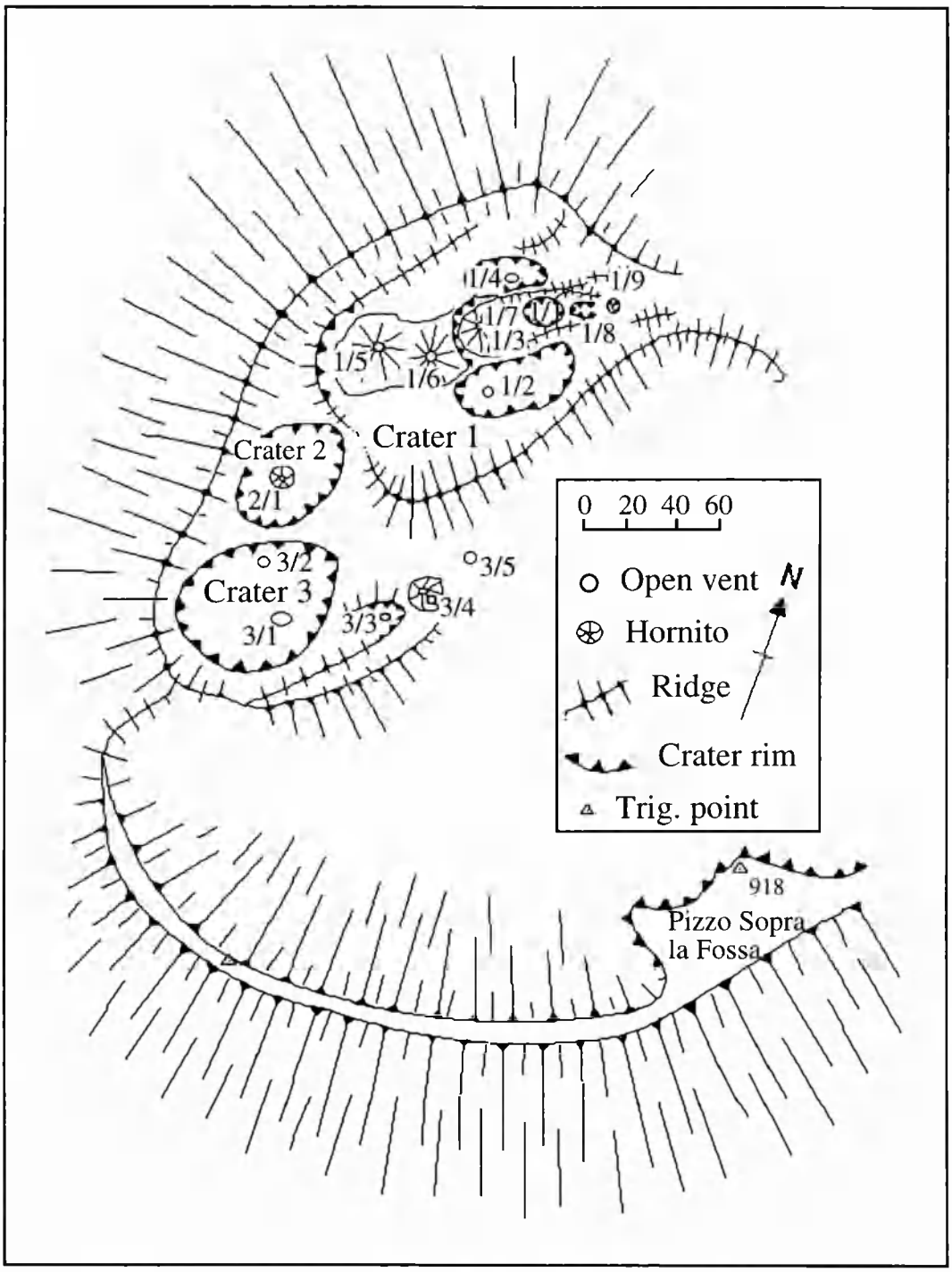

Figure C1a. *Stromboli Crater Terrace, October 1994.*

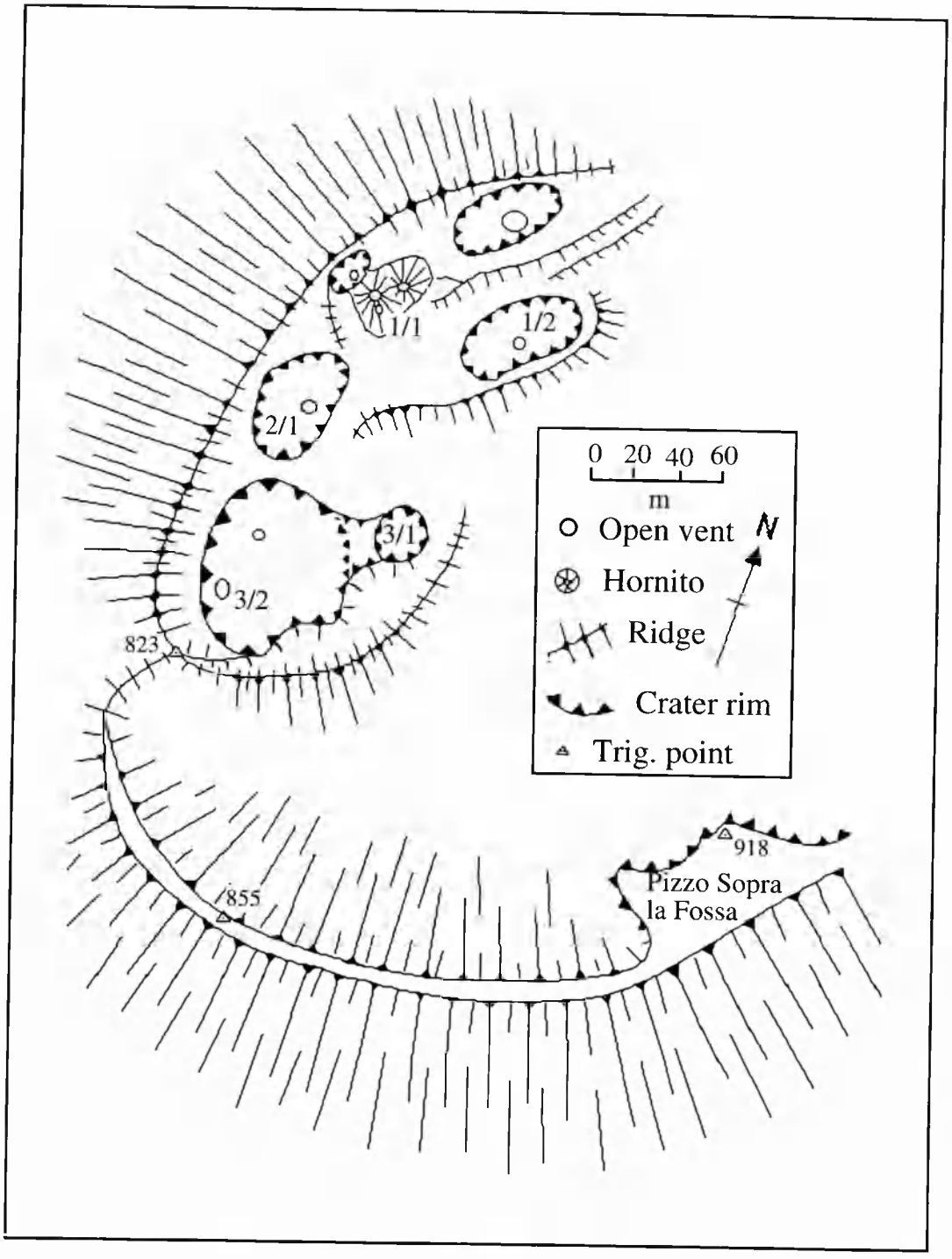

Figure C1b. *Stromboli Crater Terrace, September 1995.*

of large gas pockets at the magma-air interface (Blackburn *et al.*, 1976; Vergniolle & Brandeis, 1994). Experiments by Jaupart and Vergniolle (1988; 1989) indicate that the formation of the gas pockets may be the result of the collapse of a foam layer, formed by gas bubbles rising through the degassing magma chamber to gather at the chamber roof. Intermittent collapse of the foam layer generates gas pockets which flow into the conduit. Ntepe and Dorel (1990) speculate that such a foam layer collapse could explain seismic signals recorded at Stromboli during 1986. Ripepe *et al.* (1993) use this mechanism to explain the types of explosive events evident from the temporal flux of ejected matter. They distinguish three types of event: (1) "single shot" explosions resulting from the explosion of a single pocket, (2) single shot explosions followed by secondary outbursts, caused by the rise of a large pocket followed by several smaller ones and (3) "fountain-like explosions", reproduced by simulating many gas pockets of equal size exploding at regular intervals with increasing depth. The possibility that vents are fed by a system of linked conduits was suggested by Settle and McGetchin (1980) to explain the strong correlation they found between the eruption of one vent and the repose period of two other vents.

We present thermal data showing that explosive events at one vent correlate with changes in the de-gassing from another. This is strong evidence that the conduits are linked at a shallow level, presumably by a common magma chamber, feeder conduit or dyke.

C.3. Visual observations

We made visual observations of the activity within the crater terrace during October 1994 and September 1995. On both occasions morphological maps were made of the crater terrace (Fig. C1). The September 1995 map was drawn from Electronic Distance Measurement (EDM) and triangulation measurements using a Wild TC-1600 (Fig. C1b). The October 1994 map was initially drawn using compass bearings and field sketches, and then fitted to the September 1995 map using common ground control points (Fig. C1a). Crater and vent numbering corresponds to the naming convention described by Schick and Mueller (1988). The three permanent craters, Zolfo, Sciara and Torrione described by

Washington (1917), are ascribed numbers 1, 2 and 3 respectively. Vents within the craters are then named using numbers following the crater number. Since few of the vents were identifiable on both dates, vent numbers do not usually correspond to the same features.

During October 1994 we observed recurrent eruptions expelling incandescent ejecta and ash to heights of up to 300 m from 6 vents within craters 1 and 3 (Fig. C2a). It was possible to view some way into vents 3/4 and 1/5 (Fig. C1a). The walls of these vents were incandescent and the vents themselves were estimated to be around 4 and 1 meters in diameter respectively. Vent 3/4 was the source of regular (~1 per second) gas puffs, but no eruptions were observed. Vent 1/5 was the source of vigorous gas jet eruptions sending incandescent gas with small amounts of ejecta to 50 m (Fig. C2a). Gas jet eruptions, characterised by long lasting (>10 seconds), high pressure degassing events carrying little or no ejecta, were observed during April 1990 (Boris Behncke, personal communication) and are noted by other workers, including Neuberg *et al.* (1994) and Chouet *et al.* (1974). Such gas jet eruptions appear to be as much a feature of persistent activity at Stromboli as pyroclastic loaded eruptions.

Between 19 and 20 September 1995 eruptions occurred from vents within craters 1, 2 and 3, sending incandescent ejecta and brown ash clouds up to 100 m (Fig. C2b). From Pizzo Sopra la Fossa it was possible to view directly into vent 1/1 (Fig. C1b). The vent walls were incandescent and the vent itself was the source of ~50 m high incandescent gas jet eruptions containing small numbers (1-10) of bombs. Using triangulation measurements we estimate the diameter of vent 1/1 to have been ~4 m. Since no lava was observed within the vent, we infer that incandescence was due to high temperature gas heating the vent walls. Incandescence within vents that were visible in 1994 (vents 3/4 and 1/5) is similarly attributable to the same process. The site of the 1994 incandescent vent 3/4 was occupied by a collapse crater. This was the source of constant night glow and gas emission. By night 1 to 10 bombs were frequently observed to reach up to 10 m above the crater 3 rim, but these ejections were not accompanied by audible explosions.

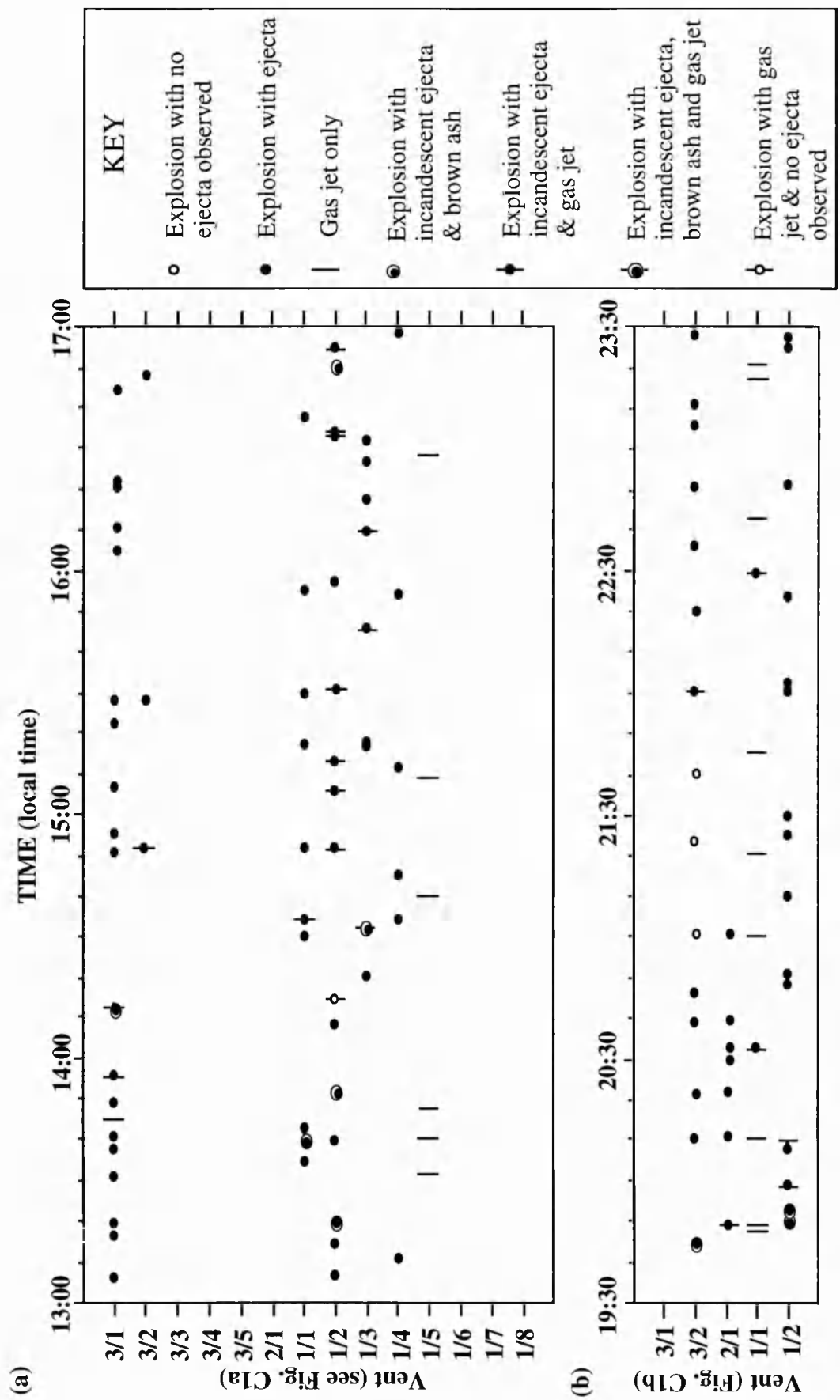

Figure C2. Eruptive activity within the Stromboli crater terrace during 4-hour observation periods on (a) 5/10/94 and (b) 19/9/95.

C.4. Thermal observations

During the night of 19 to 20 September 1995 near continuous measurements were made of incandescent vent 1/1 from a distance of 290 m. Over a 5 hour period 35 measurements were made with a hand-held Minolta/Land Cyclops 152 infrared (0.8 to 1.1 μm) thermometer (Fig. C3). This is capable of measuring temperatures in the range 600 to 3000 °C, and at a distance of 290 m has a field of view (FOV) 1.7 m in diameter. Near continuous measurements were also made over shorter (5 to 20 minute) periods using a Minolta/Land Cyclops 330 infrared (8 to 14 μm) thermometer mounted on a tripod. This measures temperature between -50 and 500 °C, and at a distance of 290 m will have a FOV of 8.6 m in diameter. The use of such instruments to produce time-temperature curves for a small lava pond at Stromboli and temperature profiles across a fumarole fissure at Vulcano has been documented by Oppenheimer and Rothery (1991).

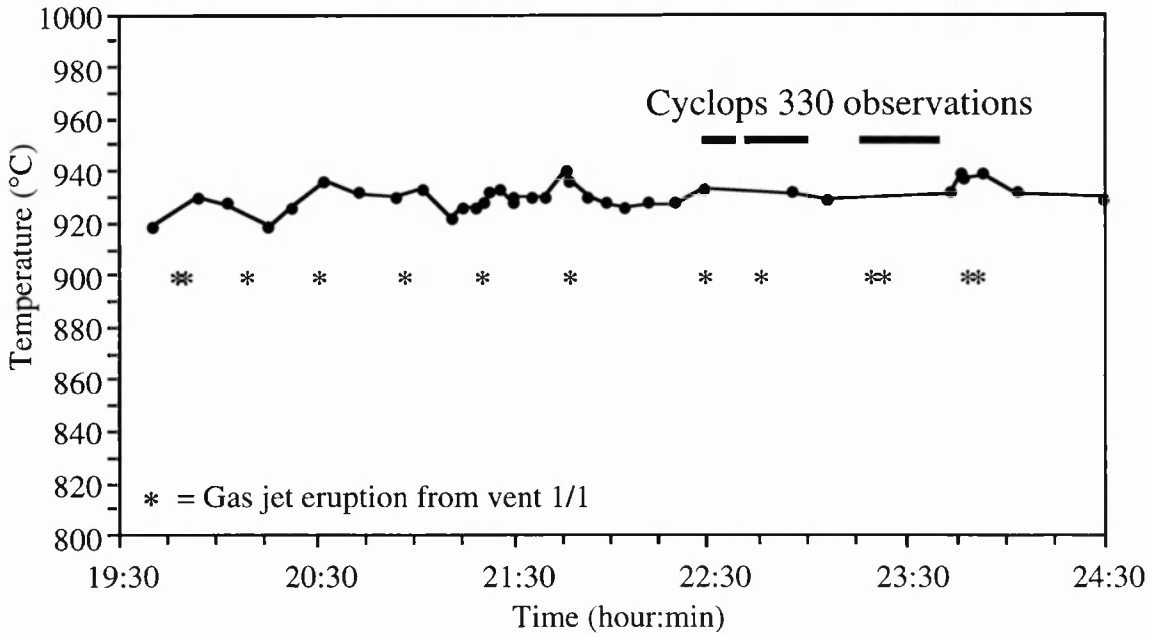

Figure C3. *Temperature variation at vent 1/1 on 19 September 1995 recorded using a Minolta/Land Cyclops 152 infrared thermometer. Each gas jet eruption occurring from vent 1/1 during the measurement period is marked by an * and the three Cyclops 330 observation periods (Figs. C4a to C4c) are indicated by thick horizontal lines.*

In spite of 13 gas jet eruptions during the measurement period, temperatures obtained using the Cyclops 152 remained stable (Fig. C3). The small variations that did occur may have been due to variable amounts of fume drifting between the vent and the instrument or due to slightly different points within the vent being measured each time. Since the incandescent vent easily filled the Cyclops 152 FOV, we believe that the vent temperature was more or less constant during the measurement period at ~940 °C.

Temperature measurements using the Cyclops 330 were lower and far more variable (Fig. C4). This is a result of the Cyclops 330 FOV being much larger, such that the incandescent vent filled only ~20 % of the FOV. The Cyclops 330 temperature is therefore an integrated temperature composed of three thermal components: (1) the incandescent vent, (2) the cooler background, measured at 27 °C just below the vent and (3) high temperature gas, which was observed to be incandescent for 1 to 2 m above the vent. Since the measurements made with the Cyclops 152 show that vent temperature was stable, variations in temperature in Fig. C4 cannot be due to changes in the vent temperature, but to variations in the area of the high temperature gas.

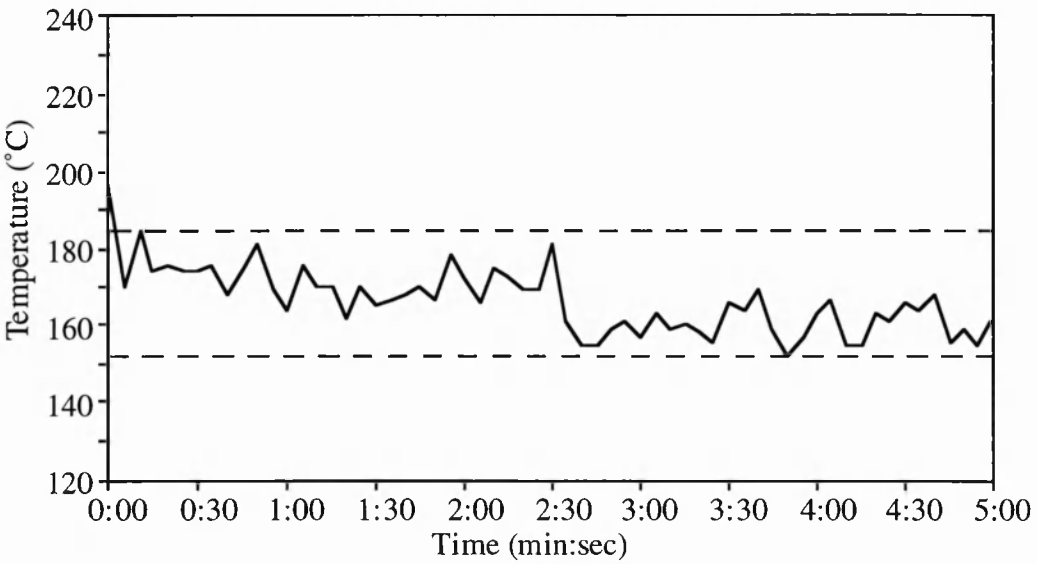

Figure C4. *Temperature variation at vent 1/1 on 19 September 1995 recorded during the first measurement period (Fig. C3) using the Cyclops 330. Steady state limits are marked by the horizontal dashed lines.*

The start of the time-temperature measurement series given in Fig. C4 coincided with the end of a gas jet eruption from vent 1/1. By increasing the area of the high temperature source, such gas jet eruptions will increase the Cyclops 330 integrated temperature, as is evident from the initial high temperature of 196 °C which was recorded as the vent 1/1 eruption ended. Two trends can be identified in the temperature time series following the vent 1/1 eruption: an initial higher temperature trend is replaced by a lower temperature trend, following a sharp decline in temperature just after 2 minutes 30 seconds. Although no event was detected visually or audibly during the sharp decline at 2 minutes 30 seconds, it appears that the high temperature gas flux decreased at this time to a lower level. Constant variation in the Cyclops 330 integrated temperature around these two trends show that the high temperature area was constantly changing. This area variation is explained by high temperature gas exiting the vent in puffs, which were observed to exit the vent at regular (~1 per second) intervals. Temperature fluctuations may also be the result of variations in the amount of fume between the instrument and the vent or events that were undetected by visual observations.

Following the eruption from vent 1/1, no major eruptions occurred from any vent during the 5 minute measurement period given in Fig. C4. Therefore, for our measurements, we use the temperature range given in Fig. C4 to define the upper and lower limits of the steady state temperature range of the hot target (vent and gas).

During longer measurement periods, observations coincided with eruptions from vent 1/1 and other vents, and a direct relationship was observed between eruptions and the Cyclops 330 integrated temperature for vent 1/1 (Figs. C5a and C5b). Gas jet eruptions from vent 1/1 elevated the Cyclops 330 integrated temperature by >30 °C above the steady state. However, eruptions from either vent 1/2 or 3/2 caused the Cyclops 330 temperature to drop by up to 12 °C below the lowest steady state value. This relationship was an immediate one, with temperature decreasing the instant vent 1/2 or 3/2 erupted. The temperature would then remain depressed for the duration of the eruption, and return to within the steady state level at the end of the eruption. In all 14 eruptions occurred during

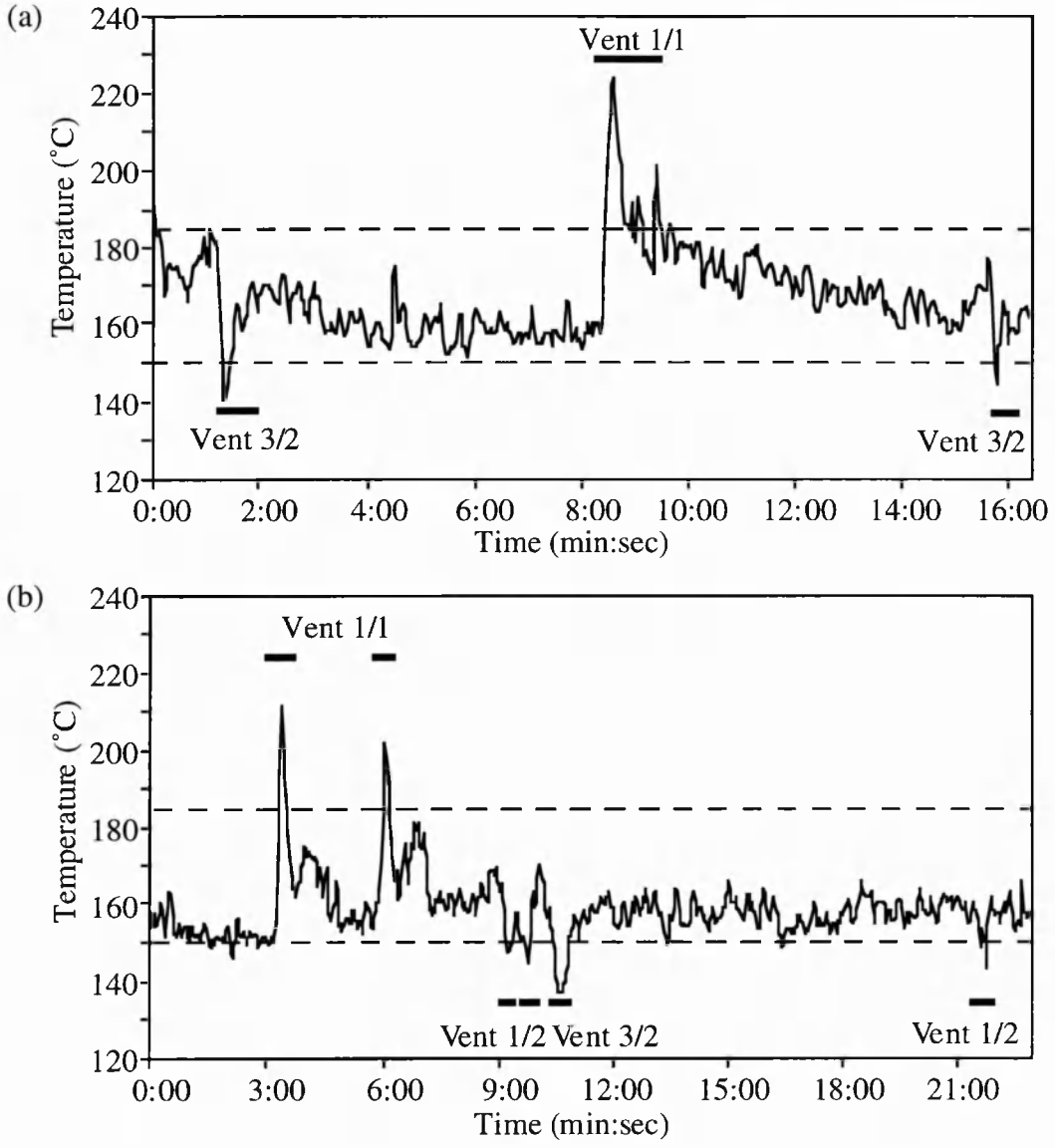

Figure C5. *Temperature variation at vent 1/1 on 19 September 1995 recorded during (a) the second and (b) third measurement periods (Fig. C3) using the Cyclops 330, showing a direct relationship between eruptive events and temperature, which in turn is related to gas flux. Steady state limits defined in Fig C4 are marked by the dashed lines and eruptive periods using solid lines.*

simultaneous Cyclops 330 measurements, and this relationship held for 100 % of these eruptions: eruptions from vent 1/1 would raise the temperature above steady state, eruptions from any other vent would depress the temperature below steady state.

Since the temperature of the vent was stable, it follows that variations in the integrated temperature measured by the Cyclops 330 during eruptions were the result of variations in the gas flux causing the area of the high temperature component to vary accordingly. During eruptions from vent 1/1 the gas jet increased the high temperature area within the Cyclops 330 FOV increasing the integrated temperature. During eruptions from vents 1/2 or 3/2 gas flux from vent 1/1 was reduced to well below the minimum steady state flux for the duration of the eruption, thereby decreasing the integrated temperature.

We note two other trends in the integrated temperature time series given in Fig. C5a. First, immediately preceding the two eruptions from vent 3/2, an increase in the integrated temperature is recorded, indicating an increase in the gas flux from vent 1/1 before the two eruptions at vent 3/2. Second, following the eruption of vent 1/1, the integrated temperature steadily declines over the 5 minute period until the eruption at vent 3/2, indicating a steady decline in gas flux from vent 1/1 following the initial eruption. Again, other variations in the time series will be due to visually or audibly undetected events, the gas exiting the vent in regular puffs and variable amounts of fume between the instrument and the target.

C.5. Implications of the observations

The thermal observations give direct evidence for a linkage between vent 1/1 and vents 1/2 and 3/2, the linkage causing a decrease in gas flux from vent 1/1 whenever vent 1/2 or 3/2 erupts. That the relationship is instant and direct indicates that this link is a simple one and occurs at a shallow level within the volcanic edifice. We assume that this link is via a common magma chamber, conduit or dyke, to which each vent is linked by a narrow conduit. Since eruptions were only observed from three vents, it is impossible to determine whether all other vents are similarly linked.

We assume that the shallow linkage is at, or slightly below, the magma level, which photoballistic, thermal flux and seismic analyses have already shown to be at a shallow depth of 100 to 400 m within the volcanic edifice (Chouet *et al.*, 1974; Giberti *et al.*, 1992;

Chouet & Dawson, 1995). This shallow level is confirmed by Ripepe and Braun (1994). They use the difference in the arrival time between the seismic-wave and air-wave generated by an explosion to show that the magma level is shallow and variable, varying between 50 and 130 m below the crater terrace over a 24 hour measurement period.

One possible mode of linkage is through a shallow (100 to 600 m deep) magma chamber to which all three vents are linked via narrow conduits. When an eruption occurs from one vent, decreased gas flux occurs at the other vents due to their being fed by a common chamber. A similar model is proposed by Settle and McGetchin (1980), who suggest that the strong correlation of the repose periods at two vents with the eruption frequency at a third may be due to each being directly connected to a near-surface magma chamber. This fits with evidence from a broadband seismic survey carried out by Neuberg *et al.* (1994). This showed eruption epicentres to be situated NW of the craters beneath the Sciara del Fuoco at a depth between 100 and 600 m. They suggest that this indicates a confined source region common to all craters. Other possible evidence for such a shallow magma chamber is given by the formation of a pit crater 60 m deep and 100 m in diameter following the 1986 effusive eruption, which has been interpreted as resulting from the draining of such a chamber and may give an idea of the chamber dimension (Ntepe & Dorel, 1990). Instability resulting from a shallow chamber within the edifice is also one of the proposed causes of sector collapse which episodically occur at Stromboli, the latest of which formed the Sciara del Fuoco <5000 years ago (Kokelaar & Romagnoli, 1995). However, it is also possible that linkage is via the branching of a main feeder conduit or dyke, or due to a branching conduit system in which small magma chambers occur in some branches.

C.6. Conclusions

Vents, or clusters of vents, at Stromboli are fed by a system of linked conduits, presumably joined via a shared magma chamber or feeder conduit. Any model for the Stromboli feeder system must therefore be built on the premise that the system is linked at a

shallow depth, i.e. within the volcano itself. However, definition of the true nature of the feeder system is not possible given the available data. Proving how the system is linked and operates would benefit greatly from simultaneous thermal, acoustic, seismic and photoballistic observations over an extended time (~1 month) period.

C.7. Acknowledgements

Field-work by Andy Harris and Nicki Stevens was funded by the Remote Sensing Society's Shackleton Award. The content of this paper benefited from an open discussion by the Open University's Volcano Geophysics Group. We also thank John Murray and Clive Oppenheimer for the loan of essential equipment, Dave Rothery, Steve Blake and Peter Francis for constructive reviews. David Stevenson, John Taylor and Boris Behncke are also thanked for discussions and input.

C.8. References

Blackburn, E.A., Wilson, L. & Sparks, R.S.J. (1976): Mechanisms and dynamics of strombolian activity. J. Geol. Soc. Lond., 132, 429-440.

Chouet, B.A. & Dawson, P.B. (1995): Array measurements of explosions and tremor at Stromboli volcano, Italy. Abstracts week A, IUGG XXI General Assembly, Boulder, Colorado, July 2-14 1995, A64.

Chouet, B., Hamisevicz, N. & McGetchin, T.R. (1974): Photoballistics of volcanic jet activity at Stromboli, Italy. J. Geophys. Res., 79, 4961-4976.

Giberti, G., Jaupart, C. & Sartoris, G. (1992): Steady-state operation of Stromboli volcano, Italy: constraints on the feeding system. Bull. Volcanol., 54, 535-541.

GVN (1990): Stromboli. Bull. Global Volcanism Network, 19(4), 16.

GVN (1994): Stromboli. Bull. Global Volcanism Network, 19(10), 13-15.

Jaupart, C. & Vergniolle, S. (1988): Laboratory models of Hawaiian and Strombolian eruptions. Nature, 331, 58-60.

Jaupart, C. & Vergniolle, S. (1989): The generation and collapse of a foam layer at the roof of a basaltic magma chamber. J. Fluid Mech., 203, 347-380.

Kokelaar, P. & Romagnoli, C. (1995): Sector collapse, sedimentation and clast population evolution at an active island-arc volcano: Stromboli, Italy. Bull. Volcanol., 57, 240-262.

Neuberg, J., Luckett, R., Ripepe, M. & Braun, T. (1994): Highlights from a seismic broadband array on Stromboli volcano. Geophys. Res. Lett., 21, 749-752.

Ntepe, N. & Dorel, J. (1990): Observations of seismic volcanic signals at Stromboli volcano (Italy). J. Volcanol. & Geotherm. Res., 43, 235-251.

Oppenheimer, C.M.M. & Rothery, D.A. (1991): Infrared monitoring of volcanoes by satellite. J. Geol. Soc. Lond., 148, 563-569.

Ripepe, M., Rossi, M. & Saccorotti, G. (1993): Image processing of explosive activity at Stromboli. J. Volcanol. & Geotherm. Res., 54, 335-351.

Ripepe, M. & Bruan, T. (1994): Air-wave phases in strombolian explosion-quake seismograms: a possible indicator for the magma level? Acta Vulcanol., 5, 201-206.

Schick, R. & Mueller, W. (1988): Volcanic activity and eruption sequences at Stromboli during 1983-1984. In: "modelling of volcanic processes", Chi-Yu King & R. Scarpa (Eds.), Fr. Vieweg & Son, Wiesbaden, 120-139.

Settle, M. & McGetchin, T.R. (1980): Statistical analysis of persistent explosive activity at Stromboli, 1971: implications for eruption prediction. J. Volcanol. & Geotherm. Res., 8, 45-58.

Vergniolle, S. & Brandeis, G. (1994): Origin of the sound generated by Strombolian explosions. Geophys. Res. Lett., 21, 1959-1962.

Washington, H.S. (1917): Persistence of vents at Stromboli and its bearing on volcanic mechanism. Bull. Geol. Soc. America, 28, 249-278.

Appendix D. Defining the magmatic systems at Vulcano and Stromboli volcanoes

---

A.J.L. Harris and D.S. Stevenson

Paper submitted to Geophysical Research Letters, June 1996.

D.1. Abstract

Explosive activity at Vulcano poses a serious threat to settlements near the active crater. At Stromboli activity has injured tourists gathering close to the active craters and damaged the island's villages. Defining the magmatic systems which drive activity at these two volcanoes and understanding their operation are essential for assessing possible eruption precursors and hazard. To this end, we present three generally applicable models of the magma budget during steady-state activity. Using thermal and gas flux data we apply these models at Vulcano to calculate cooling, crystallisation and degassing of magma at a rate of 10-100 kg s^{-1} of magma from an intrusion at ~2 km depth. This intrusion feeds a currently active fumarole field. At Stromboli a steady supply of 300 - 1300 kg s^{-1} magma to shallow depths (<1 km) feeds continuous gas emission and frequent explosions within the summit crater and episodic effusive eruptions on the flank. The principles of these models may be adapted to volcanoes with similar systems.

D.2. Defining the magmatic systems at Vulcano and Stromboli volcanoes

Vulcano and Stromboli (Aeolian Islands, Italy) are currently characterised by persistent, steady-state, activity. Since the most recent explosive eruption at Vulcano (1888-1890), activity has been characterised by continuous gas discharge from low to moderate temperature fumaroles (80-700 °C). Stromboli's activity is characterised by continuous gas discharge and frequent explosions from a variable number of vents (5 - 15), which has persisted at least since first observations were made 2000 years ago.

For volcanoes characterised by persistent non-eruptive degassing, total thermal flux ($Q_{non\text{-}erupt}$) will be the sum of radiative and convective heat losses from the active vents (Q_{rad} and Q_{conv}), heat loss by conduction through the conduit and chamber walls (Q_{cond}) and heat carried by the gas phase (Q_{negas}). At intermittently erupting systems, heat will also be carried by gas and ejecta expelled during eruptions, $Q_{egas}+Q_{ejecta} = Q_{erupt}$. Mass flux of magma through the system (M) can then be calculated from $M = Q_{tot} / (c_L\Delta f + c\Delta T)$, where $Q_{tot} = Q_{non\text{-}erupt}+Q_{erupt}$ and c_L, Δf, c_p and ΔT are latent heat of crystallisation, crystallised mass fraction, specific heat capacity and the temperature through which magma cools before removal from the system.

During September 1995 we measured temperatures at Vulcano at over 500 vents (Figure D1). By applying a porous pipe model for gas flow at a fumarole field[1], we were able to estimate the depth of the magma source and Q_{tot} (Table D1). To estimate depth, we divide the field into 6 (N) porous conduits of radius (r_0) 5 m (from the total exhalative area,

---

Figure D1. *Maximum temperature distribution for the Vulcano Fossa fumarole field, mapped using electronic distance measurement and radiometer-derived temperatures in September 1995. Temperatures refer to the maximum obtained within each 10 x 10 m cell, and cover the entire active area. Maximum vent temperature was 531 °C, with a mean of 203±4 °C. By dividing the field into 6 porous conduits, these measurements are used to constrain inputs to a fumarolic flow model[1], which together with gas flux data, give source magma depths.*

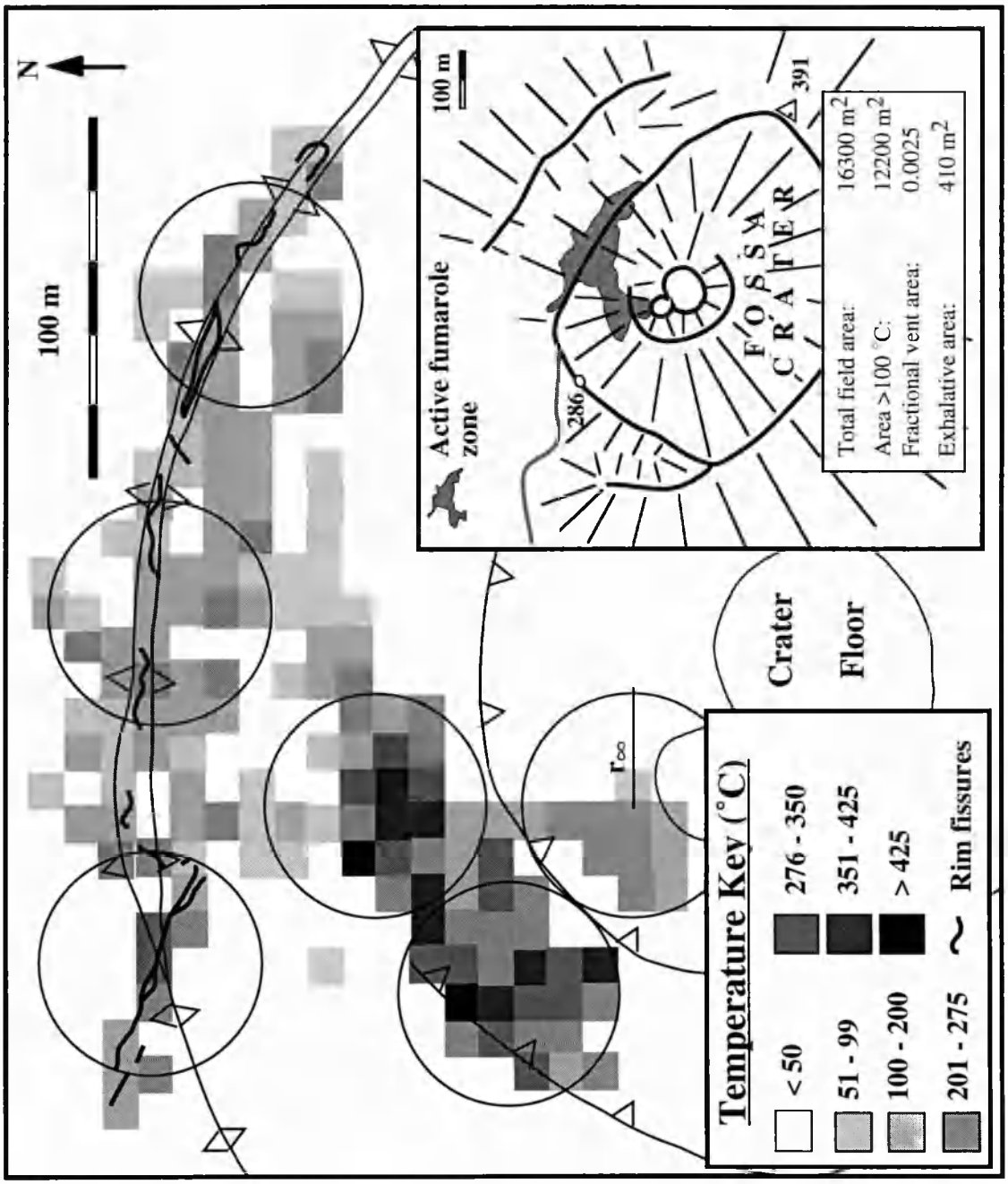
N
100 m
Temperature Key (°C)
< 50
51 - 99
100 - 200
201 - 275
276 - 350
351 - 425
> 425
Rim fissures
Crater Floor
r∞
100 m
Active fumarole zone
286
391
FOSSA CRATER
Total field area: 16300 m²
Area >100 °C: 12200 m²
Fractional vent area: 0.0025
Exhalative area: 410 m²

A_{exhal}: $r_o = \sqrt{A_{exhal}/[N\pi]}$), which cool to ambient temperatures at a radius (r_∞) of 25 m (based on the total area > 100 °C, A_{field}: $r_\infty = \sqrt{A_{field}/[N\pi]}$). Total gas fluxes of 5 - 15 and 15 - 45 kg s^{-1} are derived respectively from the direct condensation method[2], and from COSPEC measurements of SO_2 flux[3] in tandem with gas chemistry[4]. These data yield depths to magma of 0.2 - 2 km, the lower limit giving a deeper source consistent with borehole evidence[5].

We used these data to constrain the magmatic system which drives persistent activity at the fumarole field. Three magma budget models were used to estimate magma flux (M) through the magma system: a dyke model, a cumulate model and an intrusion model (Figure D2). These respectively give M of 250, 180 and 85 kg s^{-1}. The results are equivalent to emplacement of 0.3 km^3 of dykes, production of 0.2 km^3 of cumulates, or cooling and crystallisation of an intrusion of volume 0.1 km^3 since the last eruption. All these have errors of ±80 %, mainly due to uncertainty in the gas flux (25±20 kg s^{-1}).

Table D1. *Heat flux from Stromboli and Vulcano. Values for all input parameters were obtained using field measurements made in 1995 or using airborne thermal Thematic Mapper Simulator data (TMS) acquired in 1991. For Stromboli T_{exit} and r_o were estimated for each vent area identified in the TMS data and fluxes derived for each vent area were summed[6], and r_∞ to the maximum distance to fumaroles > 100 °C (~120 m). At Vulcano T_{exit} and r_o were estimated using vent temperature measurements collected in 1995 (Figure D1). The fumarole field was divided into 100 m^2 cells and for each cell T_{exit} was set to the mean temperature of all fumaroles within the cell; πr_o^2 was substituted with total vent area for all fumaroles within the cell. Fluxes derived for each cell were then summed. D was calculated using the model given by Stevenson[1]. For Stromboli M_e of 6 kg s^{-1} was calculated from data for explosive and effusive eruptive activity over the last 100 years[7-14]. Gas and water fluxes for Stromboli were calculated from Allard et al.[15] and for Vulcano were taken from references 2 to 4. Constants k, α, p, μ and κ were taken from tables in Kays & Crawford[16], ε, k_w, c, L_v, C_p and c_L were set to 0.9887, 3 W m^{-1} K^{-1}, 1600 J kg^{-1} K^{-1} (a mixture of 50 % H_2O and 50 % CO_2 at 700 K), 2.26 x 10^6 J kg^{-1}, 1150 J kg^{-1} K^{-1} and 3 x 10^5 J kg^{-1} respectively. Magmatic and eruption temperatures of 1000 °C, the near solidus temperature for magma at Stromboli and Vulcano, were used with an ambient air and surface temperature of 0 °C.*

Heat flux from Vulcano and Stromboli 1890 - 1995

Mode of heat loss	Flux (MW) Vulcano	Stromboli	Derivation
Q_{rad}	1	2	$Q_{rad} = \pi r_o^2 \sigma \varepsilon T_{exit}^4$ (r_o = conduit radius, σ = Stefan-Boltzmann constant, ε = Emissivity, T_{exit} = conduit exit or vent temperature)
Q_{conv}	1	1	$Q_{conv} = 0.14\ \pi r_o^2\ k\ (g\alpha p/\mu\kappa)^{1/3}\ (T_{exit} - T_{air})^{4/3}$ (T_{air} = ambient air temperature, g = acceleration due to gravity, k, α, p, μ and κ are thermal conductivity, density, cubic expansivity, dynamic viscosity and thermal diffusivity for gas at a mean temperature of $[T_{air}+T_{exit}]/2$)
Q_{cond}	24±10	11±6	$Q_{cond} = [2\pi k_w D(T_{gas} - T_{amb})] / \ln(r_\infty/r_o)$ (k_w = wall rock thermal conductivity, D = magma depth, T_{gas} = gas temperature in the conduit [approximated from $[T_{magma}+T_{exit}]/2$, in which is the magma surface temperature], T_{surf} = ambient temperature and r_∞ = distance to ambient temperatures)
Q_{negas}	92±74	400±220	$Q_{negas} = Fc_g\Delta T_g + F_w L_v$ (F = total non-eruptive gas flux, c_g = specific heat capacity of gas, ΔT_g is gas cooling from magmatic to ambient temperature, F_w = water flux, L_v = latent heat of water condensation)
Q_{egas}	0	1	$Q_{egas} = F_e c_g \Delta T_g + F_{we} L_v$ (F_e = total erupted gas flux, F_{we} = total erupted water flux)
Q_{ejecta}	0	8	$Q_{ejecta} = (c_e \Delta T_e + c_L)\ M_e$ (c_e = specific heat capacity of ejecta, ΔT_e is ejecta cooling from eruption to ambient temperature, c_L latent heat of crystallisation, M_e = mass flux of erupted material)
Q_{tot}	118±84	423±226	$Q_{tot} = Q_{nonerupt} + Q_{erupt}$, where $Q_{nonerupt} = Q_{rad} + Q_{conv} + Q_{cond} + Q_{negas}$ and $Q_{erupt} = Q_{egas} + Q_{ejecta}$

Current areal contraction of the crater, probably an effect of magma cooling at a shallow depth[17], indicates the intrusion model is most likely at Vulcano, with heat flux from this cooling body fuelling the surface activity.

Observations at Stromboli during 1995 defined two types of explosive eruption: pyroclast-laden eruptions ejecting pyroclasts and gas to heights of 50-300 m, and gas jet eruptions expelling incandescent gas flares up to 50 m. Data from the University of Udine summit seismic station give a mean rate for both types of explosive event of 8.8 explosions per hour between 1992 and 1996, varying between 1-2 and >30 (R. Carniel, personal communication). Our own vent temperature measurements gave a maximum temperature of 940 °C, and triangulation gave a vent diameter of 4 m. Using these parameters and the 150±90 kg s^{-1} time-averaged gas flux for Stromboli[15] in a model for gas flow through rough pipes[1] gives a magma surface depth of 600±350 m.

As at Vulcano, we use these measured and derived parameters to constrain the magmatic system which drives persistent activity. For a steady-state system, such as Stromboli, which displays persistent magmatic activity at the surface, the intrusion model can be rejected and the dyke and cumulate models must be adapted to take into account direct connection of the magma system to the surface. At Stromboli, magma at a shallow

---

Figure D2. *Three schematic models for a steady-state degassing magma system. In the dyke (a) and cumulate (b) models, a sealed or blocked pipe is connected to a magma chamber. Buoyant, volatile rich magma rises from the chamber up the pipe. Above the saturation depth gas is exsolved from the magma and lost to the surrounding system. Gas and heat rise to be released at the surface. Denser degassed magma sinks back down the conduit. This convection cools the magmatic system, eventually leading to the formation of dykes or cumulates. In the dyke model, chamber magma (taken to be 1200 °C, 0 % crystals) is assumed to release its gas, cool to 900 °C and crystallise 45 % before emplacement; the magma's remaining heat is lost from the dyke in situ, and is not released through the active crater. In the cumulate model, convecting magma releases gas and progressively cools (to 900 °C), depositing crystalline cumulates within the chamber; hence all of the available latent heat is released to the remaining chamber magma. In (c), the intrusion model, all magma cools to 250 °C and crystallises fully in place.*

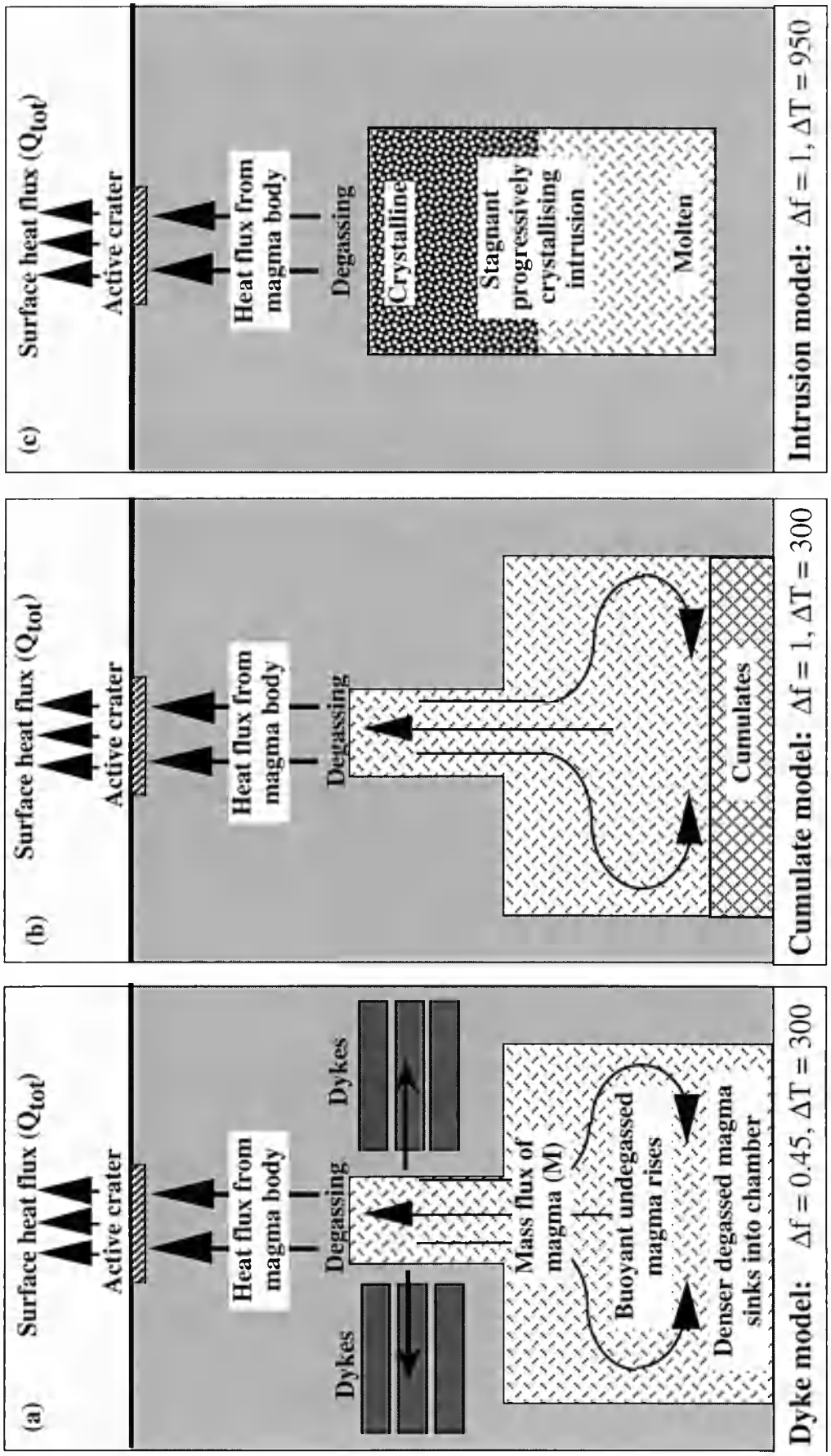
(a)
Surface heat flux (Q_{tot})
Active crater
Heat flux from magma body
Degassing
Dykes
Dykes
Mass flux of magma (M)
Buoyant undegassed magma rises
Denser degassed magma sinks into chamber
Dyke model: Δf = 0.45, ΔT = 300
(b)
Surface heat flux (Q_{tot})
Active crater
Heat flux from magma body
Degassing
Cumulates
Cumulate model: Δf = 1, ΔT = 300
(c)
Surface heat flux (Q_{tot})
Active crater
Heat flux from magma body
Degassing
Crystalline
Stagnant progressively crystallising intrusion
Molten
Intrusion model: Δf = 1, ΔT = 950

level is connected to the surface via a system of linked, open conduits. Linkage is apparent from our continuous thermal observations of the high temperature gas plume above these vents, which show reduced gas flux from non-erupting vents whenever another vent erupts, the effect lasting for the exact duration of the eruption[18]. That this relationship is instantaneous and occurred during all observed eruptions shows that certain vents must be linked directly to the same shallow source. This shallow source is in turn linked to a deeper chamber (Figure D3).

$Q_{non\text{-}erupt}$ from Stromboli's linked shallow system is more than an order of magnitude greater than Q_{erupt} (Table D1). To maintain $Q_{non\text{-}erupt}$, 860 kg s^{-1} must be intruded as dykes within or beneath the edifice, equivalent to injection of 22 km^3 during the 2000 years that persistent activity has been observed. This compares with a total edifice volume of 230 km^3. Alternatively, 640 kg s^{-1} of cumulates must be formed, equivalent to emplacement of 16 km^3 of cumulates in 2000 years. Both estimates have errors of ±55 %. Such endogenous growth of Stromboli has previously been postulated[23], and our estimate of 0.004 - 0.016 km^3 yr^{-1} is in good agreement with two existing estimates, based on

---

Figure D3. *Schematic model for the magma system at Stromboli. Buoyant, volatile rich magma rises from a deep (10-15 km) chamber evident from geochemical and seismic data[8,24]. Gas rises to form a foam layer at the roof of a shallow (<1 km deep) chamber[19]. Effusive vents for the 1975 and 1985-1986 eruptions located 100-120 m[11,13,14] below the active craters indicate feeding from this shallow source. The shallow source could equally be a dyke or a widening of the main feeder conduit. The 4 x 10^5 m^3 collapse pit formed after the 1985-1986 effusive eruption[20] may approximate typical shallow source volume. Collapse of the foam layer feeds gas slugs which rise up subsidiary conduits to drive explosive activity at the surface[19]. Pyroclast-laden and gas jet eruptions occur. The latter are characterised by lower energy explosions, carrying little or no pyroclasts, and are separated by periods of continuous high temperature gas release. Vents rarely exhibiting eruptions may be connected directly to the main feeder pipe or to a separate source, in which case lower gas flux or formation of a frozen cap on the magma column could explain the low frequencies of eruptions. Degassed magma descends, and is emplaced as dykes (a) or cumulates (b) at depth. This necessitates convection in the main feeder conduit, as envisaged or by the rise of buoyant spheres through the sinking medium[21,22].*

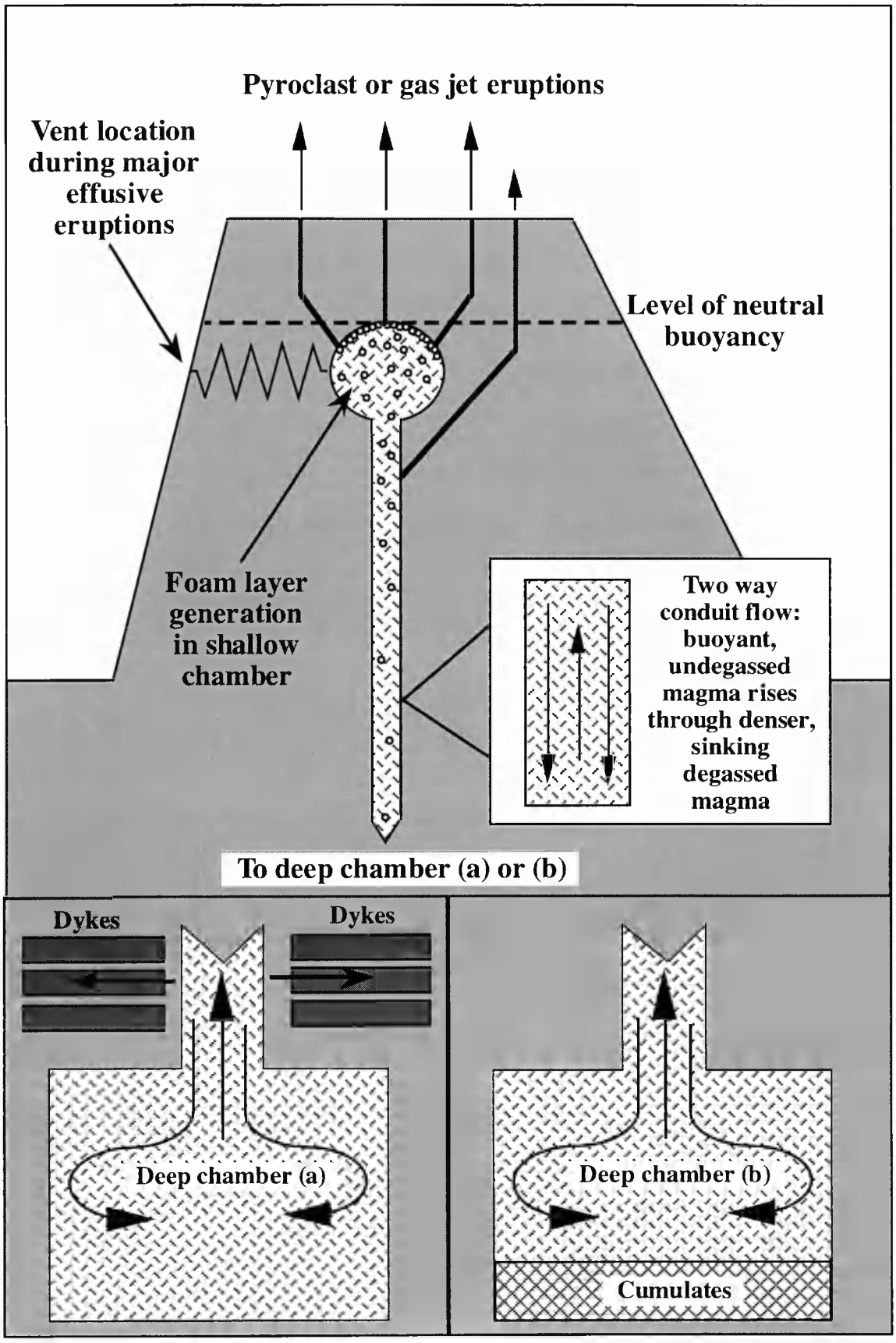
Pyroclast or gas jet eruptions
Vent location during major effusive eruptions
Level of neutral buoyancy
Foam layer generation in shallow chamber
Two way conduit flow: buoyant, undegassed magma rises through denser, sinking degassed magma
To deep chamber (a) or (b)
Dykes
Dykes
Deep chamber (a)
Deep chamber (b)
Cumulates

magma sulphur budgets, for intrusive or sub-edifice growth[15,23].

Our calculations indicate current activity at Stromboli can be modelled by internal or sub-edifice growth by dyking and/or cumulate formation. This occurs within a system where a deep chamber is linked, by two-way conduit flow, to a high level chamber, located at <1 km depth, to which a number of vents are linked (Figure D3).

Using Vulcano and Stromboli as worked case studies, we show how thermal and gas flux measurements can be used to constrain an active magma system. Such constraint is an essential step in understanding the operation of an active volcano and potential eruption hazard. Variations in any of the measured parameters will have implications for the operation of the system and thereby hazard posed. Principles on which the three schematic steady-state models are based have been kept simple and general to allow application to volcanoes with similar feeder systems and activity including, fumarolic (e.g. Kudriavy and Nisyros) and crater lake systems (e.g. Poas and Ruapehu) or degassing conduit systems (e.g. Etna and Masaya).

D.3. Acknowledgements

We thank Nicki Stevens and Adam Maciejewski for field assistance and discussions. Dave Rothery, Peter Francis, Paul Röllin, the Open University's Volcano Geophysics Group and Roberto Carniel provided valuable input. Fieldwork was funded by the Remote Sensing Society's Shackleton Award.

D.4. References

1. Stevenson, D.S. *J. Volcanol. & Geotherm. Res.*, **57**, 139-156 (1993).
2. Italiano, F., Nuccio, P.M. & Pecoraino, G. *Acta Vulcanol.*, **6**, 39-40 (1994).
3. Bruno, N., Caltabiano, T., Grasso, M.F., Porto, M. & Romano R. *Acta Vulcanol.*, **6**, 32 (1994).
4. Chiodini, G., Cioni, R., Marini, L., Panichi, C., Raco, B. & Taddeucci G. *Acta Vulcanol.*, **6**, 43-46 (1994).
5. Faraone, D., Silvano, A. & Verdiani, G. *Bull. Vulcanol.*, **48**, 299-307 (1986).
6. Harris, A.J.L. & Stevenson, D.S. *J. Volcanol. & Geotherm. Res.*, **submitted**, (1996).
7. Chouet, B., Hamisevicz, N. & McGetchin, T.R. *J. Geophys. Res.*, **79**,4961-4976 (1974).

8. Blackburn, E.A., Wilson, L. & Sparks, R.S.J. *J. Geol. Soc. Lond.*, **132**, 429-440 (1976).
9. Napoleone, G., Ripepe, M., Saccorotti, G., Totti, L. & Albianelli, A. *Acta Vulcanol.*, **3**, 163-171 (1993).
10. Ripepe, M., Rosi, M. & Saccorotti, G. *J. Volcanol. & Geotherm. Res.*, **54**, 335-351 (1993).
11. Rosi, M. & Sbrana, A. *Bull. Volcanic Eruptions*, **25**, 7-8 (1988).
12. Barberi, F., Rosi, M. & Sodi, A. *Acta Vulcanol.*, **3**, 173-187 (1993).
13. Capaldi, G., Guerra, I., Lo Bascio, A., Luongo, G., Pece, R., Rapolla, A., Scarpa, R., Del Pezzo, E., Martini, M., Ghiara, M.R., Lirer, L., Munno, R. & La Volpe, L. *Bull. Volcanol.*, **41**, 259-285 (1978).
14. Nappi, G. & Renzulli, A. *Bull. Volcanic Eruptions*, **26**, 1-3 (1989).
15. Allard, P., Carbonnelle, J., Metrich, N., Loyer, H. & Zettwoog, P. *Nature*, **368**, 326-330 (1994).
16. Kays, W.M. & Crawford, M.E. (McGraw-Hill, London, 1980).
17. Montalto, A. Bull. Volcanol., **57**, 483-492 (1996).
18. Harris, A.J.L., Stevens, N.F., Maciejewski, A.J.H. & Röllin, P.J. *Acta Vulcanol.*, **in press**, (1996).
19. Jaupart, C. & Vergniolle, S. Nature, **331**, 58-60 (1988).
20. Arnaud, N.D. *Proc. Kagoshima International Conference on Volcanoes* (19-23 July 1988).
21. Kazahaya, K., Shinohara, H. & Saito, G. *Bull. Volcanol.*, **56**, 207-216 (1994).
22. Stevens, D. & Blake, S. Bull. Volcanol., **submitted**.
23. Francis, P., Oppenheimer, C. & Stevenson, D. *Nature*, **366**, 554-557 (1993).